



**HAL**  
open science

**Fabrication of Opto-microfluidic Circuits of the "Lab on Chip" Type, by 2D and 3D Laser Writing of Organic-inorganic Hybrid Materials**  
**Fabrication de Circuits Opto-microfluidiques de Type**

Jinane Elias

► **To cite this version:**

Jinane Elias. Fabrication of Opto-microfluidic Circuits of the "Lab on Chip" Type, by 2D and 3D Laser Writing of Organic-inorganic Hybrid Materials. *Fabrication de Circuits Opto-microfluidiques de Type*. Mechanics of materials [physics.class-ph]. Université Montpellier, 2021. English. NNT : 2021MONT114 . tel-03934745

**HAL Id: tel-03934745**

**<https://theses.hal.science/tel-03934745>**

Submitted on 11 Jan 2023

**HAL** is a multi-disciplinary open access archive for the deposit and dissemination of scientific research documents, whether they are published or not. The documents may come from teaching and research institutions in France or abroad, or from public or private research centers.

L'archive ouverte pluridisciplinaire **HAL**, est destinée au dépôt et à la diffusion de documents scientifiques de niveau recherche, publiés ou non, émanant des établissements d'enseignement et de recherche français ou étrangers, des laboratoires publics ou privés.

# THÈSE POUR OBTENIR LE GRADE DE DOCTEUR DE L'UNIVERSITÉ DE MONTPELLIER

En Physique et Astrophysique

École doctorale Information, Structure, Systèmes

Unité de recherche Laboratoire Charles Coulomb (L2C)

## Fabrication of Opto-microfluidic Circuits of the "Lab on Chip" Type, by 2D and 3D Laser Writing of Organic- Inorganic Hybrid Materials

Présentée par Jinane ELIAS

Le 15 Decembre 2021

Sous la direction de Pascal ETIENNE  
et Sylvie CALAS-ETIENNE

Devant le jury composé de

Benoit CLUZEL  
Mohamed OUBAHA  
Jihane JABBOUR  
Csilla Gegerly  
Pascal ETIENNE  
Sylvie CALAS-ETIENNE  
Laurent DUFFOURS

Maître de conférences, Université Bourgogne-Franche Comté  
Directeur de recherche, Technological University Dublin  
Professeur des universités, Université Libanaise  
Professeur des universités, Université de Montpellier  
Professeur des universités, Université de Montpellier  
Maître de conférences, Université de Montpellier  
Docteur ingénieur, PRIMEVerre

Rapporteur  
Rapporteur  
Examinatrice  
Présidente du Jury  
Directeur de thèse  
Co-directrice de thèse  
Invité



UNIVERSITÉ  
DE MONTPELLIER



# Acknowledgments

First of all I would like to thank M. Benoit CLUZEL and M. Mohamed OUBAHA, for accepting to evaluate this work, and for their kind and constructive remarks.

I wish to extend my special thanks to the other members of the committee: Mme Jihane Jabbour and Mme. Csilla Gergerly, for their meticulous reading of the manuscript and for their much appreciated feedback.

I would like to express my gratitude to my supervisors, M, Pascal ETIENNE and M. Sylvie CALAS-ETIENNE, who guided me throughout this project, and transferred to me their experience, and accumulated knowledge after years of experimental research.

My biggest thank you goes to M. Laurent DUFFOURS and Mme. Pascale COLOMBEL, for their help and support. Without them a great part of this work would not have been possible. Thank you for all the fruitful discussions.

This project would not have been possible without the assistance of M. Laurent BONNET: a true master of the art, Laurent, thank you.

I would also like to thank M. Ahmad MEHDI for his suggestions and the discussions we had, and Mme Karine PARRA for her help with the NMR spectra analysis.

My warmest thank you to my fellow labmates (in the order of appearance): Aurelien, Sami, Lena, Harry, Adrian, Theo, and Nour, with whom I shared good and bad days, during these 3 years. Bruno and Clara even though we were not in the same group, you guys are a blessing.

To all the friends in Montpellier: Alain, Louise, Nadine, Bastien, Rodolphe, Johnny, Laure, Bachar, Nour, Talal; to those scattered around the globe: Lilas, Anna, Joelle, Stephanie, Roger, Sahar, Sarah, Sary, Caroline, and Priscilla; and to all the people I accidentally forgot to mention: thank you.

Last but not least, my endless gratitude to my dearest Hassan for all the support throughout these years. To **my parents**: Hala and Edmond; **my sisters**: Joelle, Jana and Therese; **my brother** Joseph; **my aunts** and **uncles**; whose support is usually taken for granted: this would not have been possible without you all. To the grand-parents, those who left us and those who still are with us: all the love and appreciation.

# Contents

Contents	iv
List of Figures	viii
List of Tables	xvi
General Introduction	1
<b>I Literature Review</b>	<b>3</b>
<b>1 Optofluidic Lab on Chip</b>	<b>5</b>
1.1 Introduction . . . . .	5
1.2 Microfluidic Lab on Chip . . . . .	6
1.2.1 Dimension consideration . . . . .	7
1.2.2 Fluid characteristics . . . . .	7
1.2.3 Flow characteristics . . . . .	8
1.3 Integrated optical circuits . . . . .	10
1.3.1 Propagation in rectangular dielectric waveguides . . . . .	13
1.3.1.1 Marcatili's analytical solution . . . . .	13
1.3.1.2 Goell's circular harmonic analysis . . . . .	16
1.3.1.3 The effective index method . . . . .	18
1.3.1.4 Comparison of Marcatili's approximation with other methods . . . . .	19
1.3.2 Losses in optical waveguides . . . . .	22
1.3.2.1 Propagation losses . . . . .	22
1.3.2.2 Coupling losses . . . . .	23
1.3.2.3 Bending losses . . . . .	24
1.3.3 Single mode propagation . . . . .	25
1.3.3.1 The interest in single mode propagation . . . . .	25
1.3.3.2 Waveguide dimension requirements for single mode propagation . . . . .	26
1.4 Optofluidics: the interaction between optics and fluidics . . . . .	26
1.4.1 Optics Enabled LoC Manipulation . . . . .	28
1.4.2 Theory: Analytical Solutions and Numerical Simulations . . . . .	30
1.4.2.1 Rayleigh regime . . . . .	31
1.4.2.2 Mie Regime . . . . .	32
1.4.2.3 Lorentz-Mie Regime . . . . .	33
1.4.3 2D Optical Manipulation: Actuators . . . . .	36

1.4.4	3D Optical Traps/Tweezers . . . . .	38
1.4.4.1	Waveguide traps (WGT) . . . . .	39
1.4.4.2	Resonant cavity traps (RCT) . . . . .	39
1.4.4.3	Plasmonic Optical Traps (POT) . . . . .	40
1.4.5	Deformation of Liquid-Liquid ( <i>L2</i> ) Interfaces and membranes . . . . .	41
1.5	Summary . . . . .	43
<b>2</b>	<b>Materials for OM-LoC</b>	<b>45</b>
2.1	Introduction . . . . .	45
2.2	Materials requirement for OM-LoC . . . . .	45
2.3	Existing materials and associated fabrication techniques . . . . .	46
2.3.1	Silicon based platforms . . . . .	47
2.3.2	Glass Platforms . . . . .	50
2.3.3	Organic polymer Platforms . . . . .	53
2.3.3.1	Non photosensitive polymers . . . . .	53
2.3.3.2	Photosensitive polymers . . . . .	55
2.3.4	Hybrid organic-inorganic platforms . . . . .	58
2.3.4.1	Non photosensitive hybrids . . . . .	59
2.3.4.2	Photosensitive hybrids . . . . .	61
2.4	Hybrid organic-inorganic materials for optofluidics . . . . .	62
2.4.1	Definition of hybrid materials . . . . .	63
2.4.2	The sol-gel process: formation of the inorganic network . . . . .	65
2.4.3	The formation of the organic network . . . . .	66
2.4.3.1	Photoinitiators . . . . .	66
2.4.3.2	The radical photopolymerisation of methacrylates . . . . .	68
2.4.3.3	The thermal crosslinking of VEs and carboxylic acids . . . . .	69
2.4.3.4	The photoinduced decrosslinking of hemiacetals . . . . .	69
2.4.4	Applications . . . . .	70
2.4.4.1	Negative working photoresist for integrated optics . . . . .	70
2.4.4.2	Positive working photoresist for microfluidics . . . . .	72
2.5	Polyamic acid positive resists . . . . .	77
2.6	Processing methods of photoresists . . . . .	77
2.6.1	Deposition by spin coating . . . . .	78
2.6.2	The Laser writing model for photoresists . . . . .	79
2.6.2.1	Small truncation: Gaussian beam . . . . .	81
2.6.2.2	Large truncation: uniform irradiance . . . . .	82
2.7	Conclusion . . . . .	84
<b>II</b>	<b>Experimental study</b>	<b>85</b>
<b>3</b>	<b>Fabrication and characterisation of waveguides using an established hybrid photoresist</b>	<b>91</b>
3.1	Introduction . . . . .	91
3.2	Photosensitive resist development . . . . .	91
3.2.1	Precursors and process . . . . .	92
3.2.2	The addition of the photoactive compound . . . . .	95

3.2.3	The solid content . . . . .	96
3.3	Deposition of the photoresist . . . . .	96
3.4	Refractive index measurement . . . . .	99
3.4.1	MZ10-2.5 with Irgacure 184 . . . . .	100
3.4.2	MZ10-2.5 with Irgacure 189 . . . . .	104
3.4.3	MZ10-1 refractive index . . . . .	105
3.5	Laser writing . . . . .	107
3.5.1	The Dilase laser writer piloting . . . . .	107
3.5.2	Laser writing parameters for MZ10-2.5 . . . . .	108
3.6	Waveguides morphological characterisation . . . . .	110
3.6.1	Dimensions and geometry of revealed waveguides . . . . .	110
3.6.2	Dimension and geometry of unrevealed waveguides . . . . .	112
3.7	Power transmission and optical losses . . . . .	114
3.7.1	Light propagation in unrevealed waveguides . . . . .	114
3.7.2	Propagation Losses at 365nm . . . . .	115
3.7.3	Coupling losses at the connections . . . . .	118
3.8	Conclusion . . . . .	118
<b>4</b>	<b>The positive working resist</b>	<b>121</b>
4.1	Introduction . . . . .	121
4.2	The requirements for a resist used to fabricate microchannels . . . . .	122
4.3	Statement of the problem . . . . .	123
4.4	Transmittance spectrum of PMDA-ODA . . . . .	123
4.4.1	Spin coating deposition of PMDA-ODA . . . . .	123
4.4.2	Spectrophotometry measurements . . . . .	124
4.5	Characterization of the “as received” polyamic acid . . . . .	127
4.5.1	The choice of the characterisation method . . . . .	127
4.5.2	Assignment of the chemical shifts to the corresponding protons . . . . .	128
4.5.3	Chain length and molecular mass estimation . . . . .	131
4.5.4	Evolution of PMDA-ODA at room temperature . . . . .	133
4.6	Increasing the solid content of the photoresist . . . . .	134
4.6.1	The physical route . . . . .	134
4.6.2	The chemical route . . . . .	136
4.6.2.1	Characterization of the reactants: PMDA and ODA . . . . .	137
4.6.2.2	Study of the PMDA-ODA reaction to form the polyamic acid . . . . .	138
4.7	Reactivity of PMDA-ODA with the VE . . . . .	140
4.7.1	TVEB $H^1$ NMR spectrum . . . . .	140
4.7.2	Co-polymerisation kinetics . . . . .	141
4.7.3	The reactive model: Benzoic acid and TVEB . . . . .	144
4.7.4	Copolymerisation of TVEB and PMDA-ODA: Dissolution in TMAH . . . . .	146
4.7.5	Discussion and perspective . . . . .	147
4.8	Conclusion . . . . .	147
<b>5</b>	<b>The optofluidic integration</b>	<b>149</b>
5.1	Introduction . . . . .	149
5.2	PDMS chip fabrication . . . . .	149
5.2.1	The mold fabrication . . . . .	149

5.2.2	PDMS Molding . . . . .	151
5.3	The bonding step . . . . .	153
5.3.1	Selective transfer of the adhesive . . . . .	154
5.3.2	The bonding of the two layers . . . . .	155
5.3.3	The adhesive layer thickness . . . . .	156
5.4	The alignment step . . . . .	158
5.5	Conclusion . . . . .	160
	<b>General Conclusion</b>	<b>163</b>
	<b>Appendix A</b>	<b>167</b>
	<b>Appendix B</b>	<b>171</b>
	<b>Appendix C</b>	<b>173</b>
	<b>Appendix D</b>	<b>181</b>
	<b>Bibliography</b>	<b>183</b>

# List of Figures

1.1	(a)The OraQuick In-Home HIV test kit [9], (b)A microfluidic LoC equipped with a laser emitting diode ( <b>LED</b> ) and a photodiode ( <b>PD</b> ) to be integrated in a field test kit for Arsenic detection in water. Edited from [11]. . . . .	6
1.2	Schematic drawing of flow under shear stress. . . . .	8
1.3	A typical but simplified microfluidic setup. No dispense reservoir is connected to the chip for the sake of clarity. The flow controller is connected to an external pressure source, and the flow sensor provides a feedback loop to adjust the pressure in order to keep a stable flow rate on the chip. Edited from [14] . . . . .	9
1.4	Schematic drawing of a 2D pressure driven flow in a microchannel. . . . .	10
1.5	Light confinement in a high refractive index medium: (a) 1D confinement: planar waveguide, (b) 2D confinement: fiber or channel waveguide, (c) 3D confinement: cavity. . . . .	11
1.6	The level of integration allowed by photonic integrated circuits [15] . . . . .	11
1.7	Schematic representation of various channel waveguides. . . . .	12
1.8	Schematic representation of the implemented waveguides . . . . .	12
1.9	Geometry of the rectangular dielectric waveguide immersed in different dielectrics. Field distribution of the first order mode $E_{11}^y$ , in blue $H_x$ and in orange $E_y$ . . . . .	14
1.10	Dimension and coordinates system for Goell's method. . . . .	16
1.11	Intensity profiles of $E_{11}^y$ (up) and $E_{22}^y$ (bottom) for unity aspect ratio (left) and $a = 2b$ waveguides (right), $\Delta n = 0.01$ and $\mathcal{B} = 3$ [18]. . . . .	17
1.12	Propagation curves for the first modes in a waveguide of (a) unity aspect ratio, and (b) for $a = b/2$ , when $\Delta n \rightarrow 0$ . . . . .	18
1.13	(a) Configuration of the rectangular dielectric waveguide. (b) A 1-D waveguide with equivalent confinement in the y direction. (c) An equivalent 1-D waveguide with confinement in the x direction. $n_{eff}$ is the effective index of the mode in waveguide (b). . . . .	19
1.14	(a) Comparison between different approximations, of the dispersion curves for a square dielectric rod in air with $n_1 = 1.5$ and (b) Comparison between Marcatili's approximation and other methods for a rectangular waveguide with $a = 2b$ and surrounded by different media [20]. . . . .	20
1.15	Propagation constant for different modes and waveguides geometry: (a) $a = 2b$ and (b) $a = b$ . Solid lines represent Marcatili's transcendental equation solutions. Dashed lines represent Marcatili's closed form solutions. The dot-dashed lines represent Goell's computer results. $n_1^2/n_4^2 = 1.1$ . Edited from [17]. . . . .	21
1.16	Intrinsic attenuation of silica optical fibers, edited from [27]. . . . .	22
1.17	Geometry of a 3D linear waveguide taper. Edited from [29]. . . . .	23
1.18	illustration of a curved dielectric guide. . . . .	24
1.19	Roadmap to optofluidics. L2 is Liquid-Liquid, L-S is Liquid-Solid, SPR is Surface Plasmon Resonance and finally ATR is Attenuated Total Reflection. . . . .	27
1.20	An example of an experimental setup of a traditional optical tweezer. . . . .	29

1.21	Schematic comparison between far field and near field optical manipulation. . . . .	30
1.22	Schematic drawing of a sphere of radius $a$ in the evanescent field of an optical waveguide.	30
1.23	Schematic definition of the variables used in tracing the path of a ray through the dielectric sphere [80]. . . . .	32
1.24	Schematic drawing of a sphere of radius $a$ in the evanescent field of an optical waveguide.	34
1.25	Outline of the model by Hellesø with (a) sphere 100 nm above strip waveguide and (b) the fundamental TE mode used to excite the waveguide with 1 mW power as shown in (c) as well. . . . .	35
1.26	A comparison between MST and optical pressure for simulation [83]: Simulation results: Radiation force $F_z$ on 1 and 3 $\mu m$ spheres for (a) $n_{water} < n_s < 2$ and (b) $n_s < 1.4$ , that is, zoom of (a). . . . .	36
1.27	Examples of near field actuators: (a)The setup for Ng's experiment (on the left) and a time lapse showing the propulsion of gold nanoparticles (on the right) [77] and (b) a setup for the manipulation of dielectric nanoparticles on the surface of a silicon nitride waveguide [87]. . . . .	37
1.28	(a) Schematic illustrating the transport in a slot waveguide and (b) Mode profile for a SOI 40-nm slot waveguide [89] . . . . .	37
1.29	A schematic view of a Y branched sorter implemented by Grujic [92]. one of the two branches is directed towards the waste disposal and the other towards the sample outlet.	38
1.30	A scale roughly showing micro and nanometric organisms with the most convenient optical trapping techniques. . . . .	38
1.31	Different types of waveguide implemented traps: (a) standing wave trap [98], (c) mode beating optical trap [28] . . . . .	39
1.32	Examples of resonant cavity traps:(a) Nanoparticle navigating in the direction that light takes within the WGM. The red arrow represents the light path in the cavity [100] (b) a count of particles position in a photonic crystal resonator for different bead diameter [101] and (c) photonic crystal resonators architecture and field confinement [95]	40
1.33	Low power plasmonic nano-traps examples: (a) View of the resonant coaxial nanoaperture traps, (b) Au nano-antennas traps: (1) is a schematic view of the trap [108], (2) is the calculated spectrum of the electric field intensity enhancement and (3) is the calculated electric field distribution around the structure exited at 980nm [109] . . . . .	41
1.34	Near field optical forces applied to studies on the elasticity of RBC's: (a) Timelapse of RBC squeezed as they are propelled towards the waveguide taper. Edited from [50] and (b) Sequential images of an RBC repeatedly stretched with laser diode. Scale bar= $4\mu m$ . Edited from [114] . . . . .	42
2.1	(a) Steps of silicon waveguide fabrication in a SOI wafer [132], (b) nSWAT waveguides fabricated in SOI wafers [98] . . . . .	48
2.2	(a) CMOS-compatible fabrication process of an optofluidic chip. (b) Schematic of the optofluidic chip cross-section. (c) Optical micrograph of the fabricated optofluidic chip with air-cladding. PR: photoresist, RIE: reactive ion etching, LTO: low-temperature oxide [133]. . . . .	49
2.3	Ion exchange for the fabrication of channel waveguides. . . . .	51
2.4	(a)The steps for the fabrication of a microfluidic channel in a soda lime glass substrate with an integrated waveguide. (b) The final product, channel and waveguides of this process [139]. . . . .	52

2.5	Femto second fabricated optofluidic platform for parallel multiple sensing at different positions in the micro channel. Adapted from [143] and [144], with the permission of AIP Publishing. . . . .	53
2.6	The microfluidic channels and the waveguides fabricated by hot embossing in PMMA [150]. . . . .	54
2.7	Positive and negative photoresist response to selective UV treatment. . . . .	55
2.8	(a) Photograph of the lab-on-chip before sealing: with integrated microfluidic dye laser, optical waveguides in SU-8, microfluidic network and photodiodes. (b) a cross section of the fabricated device showing the same components. [156] . . . . .	57
2.9	Mask design of the device in [154]. All optical structures as well as the channel walls and defined in the same layer. The dark regions correspond to the remaining SU-8 layer after structuring which will be used for channel sealing. . . . .	58
2.10	Principle of waveguides fabrication in PDMS by multiphoton polymerization: (a, b, c and d) in their respective order illustrate the four steps of fabrication. (e) Absorption spectrum of 0.01 mM phenylacetylene in acetonitrile. Violet arrows indicate energies of two-photon absorption (2PA) and three-photon absorption (3PA). Inset illustrates the reaction of multiphoton polymerization of phenylacetylene [158]. . . . .	59
2.11	The measured values of refractive index for PDMS in different mixing ratios of the base to curing agent . . . . .	60
2.12	Schematic procedures to fabricate the PDMS waveguide [160]. . . . .	60
2.13	Typical interactions in hybrid materials and their relative strength [171]. . . . .	63
2.14	The two classes of hybrid materials, and their respective network formations. Connected filled in circles are polymeric chains, and empty octahedrons are inorganic entities [171].	64
2.15	Jablonsky diagram, energy levels vs. time [172] . . . . .	67
2.16	The thermal polymerisation reaction of VE and carboxylic acid to form hemiacetal groups, . . . . .	69
2.17	Acid catalysed addition reaction of VEs and carboxylic acid to form hemiacetal groups.	69
2.18	The acidolitic de-crosslinking of hemiacetal groups . . . . .	70
2.19	The refractive index increase as a function of the $Zr(OPr)_4$ molar loading as per multiple references [164, 183, 184]. . . . .	71
2.20	The steps for processing the positive photoresist based on PMDA-ODA and a VE crosslinker. The changes in the material chemistry are highlighted at each step. The green coded material is the only one soluble in an aqueous solvent. . . . .	73
2.21	The protection and deprotection of $COOH$ groups with VE groups. The green and red squares around the different groups indicate that they are either soluble or insoluble in an aqueous solvent. . . . .	74
2.22	The precursors used for the elaboration of the co-polymer, used in the positive photoresist composition. . . . .	74
2.23	Polymerisation of PMDA-ODA and (a)TVEB, (b)VEPTES, via VE and $COOH$ functions, resulting in an insoluble copolymer. This is followed by the UV depolymerisation of the resulting copolymers, leading to deprotection of the $COOH$ groups of the PMDA-ODA. The green and red squares around the different compounds indicate that they are either soluble or insoluble in an aqueous solvent. The functional groups are highlighted in grey. . . . .	75
2.24	The process flow for the photosensitive resist elaboration. . . . .	76
2.25	The four stages of the spin coating process: (a)dispense, (b) ramping up, (c) spinning at constant rate, (d) solvent evaporation [197] . . . . .	78

2.26	Schematic of the laser spot profile (Gaussian profile) and the line drawn on the photoresist film, together with the reference system used [199]. . . . .	80
2.27	Experimental results showing, irradiance distribution of the focal spot for several values of $\gamma$ . [199]. . . . .	81
2.28	Plot of the first order Struve function (continuous curve) together with that which describes its asymptotic behavior, $\frac{2}{\pi z^2}$ (dashed curve). Inset, the region containing the secondary maxima plotted on a different scale for clarity. [199] . . . . .	83
2.29	Linewidth versus $\Omega$ for the two limiting cases of a nontruncated laser beam (Gaussian spot profile) and a strongly truncated beam (uniform illumination), together with the respective fits to the corresponding theoretical functions. A $20\times$ microscope objective was used, with $f = 8.3mm$ and $NA = 0.40$ . The line $\lambda = 475.9nm$ from an $Ar^+$ laser is used as the light source. . . . .	84
2.30	The 3D design of the cell sorter. The substrate is not illustrated and the drawing is not to scale. . . . .	87
2.31	The process for the vertical integration of a optical layer and a microfluidic layer using photolithography of hybrid materials. The baking steps are not illustrated. . . . .	88
3.1	Schematic illustration of the precursors used for the sol. $Zr(OPr)_4$ is illustrated as complexed to MAA in a 1:1 ratio. . . . .	92
3.2	Schematic representation of the hydrolysis and polycondensation of both precursors. The $Zr(OPr)_4$ is illustrated as complexed to MAA in 1:1 ratio. . . . .	93
3.3	Schematic representation of the photopolymerisation reaction of both precursors. . . . .	93
3.4	Process flow chart for the MZ10-X photoresists . . . . .	94
3.5	Striation effects on the surface of an MZ10-2.5 layer . . . . .	97
3.6	Film thickness as a function of spin speed for MZ10-X photoresists with different solid content: (a) the MZ10-2.5 with 50% solid content and (b) the MZ10-1 with 80% solid content, and their corresponding fits. . . . .	98
3.7	The working principle of an Abbe refractometer, illustrated here in the case where the sample is a thin film deposited on a substrate. . . . .	99
3.8	The refractive indices of uncured samples of $MZ10 - 2.5+$ . All samples are hard baked at $110^\circ C$ for 2h. . . . .	100
3.9	The refractive indices of UV cured samples of $MZ10 - 2.5+$ . All samples are hard baked at $110^\circ C$ for 2h. . . . .	101
3.10	A plot representing the mean values of refractive indices of the UV cured and uncured MZ10-2.5 samples presented in Figures 3.8 and 3.9, and the refractive index step induced by the UV curing (Inset). . . . .	102
3.11	The Cauchy model's fit of the cured samples of MZ10-2.5+ experimental results and the corresponding parameters. . . . .	103
3.12	A comparison of the extrapolated value for MZ10-2.5+ with the existing literature. . . . .	103
3.13	Refractive index of cured and uncured MZ10-2.5 formulation, along with the Cauchy model fit of each one of them . . . . .	104
3.14	The associated refractive index step for the MZ10-2.5 composition with Irgacure 189 and 184 as photoinitiators. . . . .	105
3.15	The refractive index of MZ10-1 with the associated cauchy model fit. Marked on the graph is the expected refractive index of the layer at 633 nm . . . . .	106
3.16	Validation of the extrapolated values for MZ10-1 with the existing literature. . . . .	106

3.17	The cured linewidth as a function of the dose for the MZ10-2.5, for different combinations of filter's ODs and laser scanning speeds $V$ . . . . .	108
3.18	The cured linewidth as a function of the dose for the MZ10-2.5, with the corresponding fit. . . . .	109
3.19	Summary of the waveguide's core and surrounding media refractive indices. . . . .	110
3.20	Waveguides fabricated with different combinations of modulation and speed using a Filter with an O.D.=1.3. On the top is the front view of the waveguides, on the bottom left is a zoom into each of the 3 waveguides, and finally the bottom right shows the top view of the waveguides. All the dimensions are indicated as well as the scale bars. . . . .	111
3.21	Optical microscope photos of the revealed waveguide structures, taken by optical microscope Keyence VHX7000. Writing parameters are $M = 5\%$ , $v = 1\text{mm/s}$ , $OD = 1.3$ . . . . .	112
3.22	Optical microscope photos of the written waveguides, by refractive index increase in MZ10-2.5, at different power modulation, at a scanning velocity of 1mm/s and using an OD=0.6. Seen under a) partial coaxial illumination, and b) the using the HD functionality of the optical microscope Keyence VHX700. . . . .	113
3.23	Far field photos of the different propagating modes that can be excited in the fabricated waveguides. . . . .	114
3.24	The setup used to measure the power transmission along the waveguides. The upper photo shows the exit facet coupling. . . . .	115
3.25	The power transmission plot in dBm for refractive index contrast waveguides. . . . .	116
3.26	The power transmission plot in dBm for revealed waveguides. . . . .	117
3.27	Schematic illustration of the setup used to measure the power at different levels of the equipment . . . . .	118
4.1	Thickness versus spin speed for PMDA-ODA, with a 15% wt. in NMP. . . . .	124
4.2	UV-Visible reflectance and transmittance spectra of PMDA-ODA films of different thickness. . . . .	125
4.3	UV-Visible absorptance spectra of PMDA-ODA films of different thickness, as well as that of the glass slide used as a substrate. 354 nm and 381 nm are the wavelengths that correspond to maximum absorptance for the 2 $\mu\text{m}$ and the 12 $\mu\text{m}$ thick films respectively. . . . .	126
4.4	UV-Vis absorptances of PMDA-PDA films as a function of the film thickness for different wavelengths of interest. . . . .	127
4.5	PMDA-ODA configurations, the meta-PMDA-ODA configuration, which will also be called isomer A (top) and the para-PMDA-ODA configuration, which will also be called isomer B (bottom). The hydrogen atoms are annotated ( $H_0 - > H_5$ ) and color coded depending on their electromagnetic equivalence. The atoms numbering (1 - > 64) refers to non hydrogen atoms such as carbon, oxygen and hydrogen. . . . .	129
4.6	Proton NMR spectrum of the as received PMDA-ODA and chemical shifts assignment . . . . .	130
4.7	Possible chain ends in PMDA-ODA:(a)Type 1 chain end, resulting from excess PMDA. (b)Type 2 chain end, resulting from excess ODA. . . . .	131
4.8	NMR spectrum showing the assignment of the end of chains of PMDA-ODA. . . . .	132
4.9	The structure of a PMDA-ODA polymer having n repetitive units and terminated with oxidianiline. The repetitive unit is illustrated as a para-PMDA-ODA, but in fact it should indeed be a combination of both configuration. This will not affect the molecular mass estimation. . . . .	133
4.10	Evolution of PMDA-ODA sample:(a)received sample, (b)same sample after 15 days . . . . .	134

4.11	NMR spectra of a commercial PMDA-ODA sample and the extracted polymer from the same sample . . . . .	135
4.12	Evolution of PMDA-ODA chain length:(a)commercial sample, (b)extracted sample . . .	136
4.13	NMR proton spectrum of ODA purchased from abcr chemicals . . . . .	137
4.14	NMR proton spectrum of PMDA purchased from abcr chemicals . . . . .	137
4.15	NMR proton spectrum of PMDA-ODA mixture compared to purchased reactants from abcr chemicals: in green the spectrum of the resulting PMDA-ODA sampled at $t = 0 h$ in red that of PMDA and in blue that of ODA. . . . .	138
4.16	A zoom into the region of interest of Figure 4.15. . . . .	138
4.17	The $H^1$ NMR spectrum of the resulting PMDA-ODA sampled at $t = 0 h$ . . . . .	139
4.18	$H^1$ NMR spectrum of TVEB. The atoms N, O, and C are indicated by a number. The protons are coloured coded and indexed from 0 to 4. . . . .	140
4.19	A schema illustrating the changes in the proton NMR spectrum of the PMDA-ODA and TVEB composition upon polymerisation of the VE and the COOH groups. . . . .	141
4.20	Proton NMR spectrum of the TVEB and PMDA-ODA mixture at $25^\circ C$ (in blue) , $130^\circ C$ (in red) and $165^\circ C$ (in green). Total disappearance of the vinyl proton peak at $6.56 ppm$ and the shift of the aromatic proton peak at $6.16 ppm$ . . . . .	142
4.21	A comparison of the $H^1$ NMR spectra of PMDA-ODA and TVEB thermally treated at $25^\circ C$ (in red) and $130^\circ C$ (in blue). . . . .	143
4.22	The NMR proton spectrum of the resulting molecule due to the hydrolysis of the TVEB. 143	
4.23	A schematic illustration showing four benzoic acid modules as functional group in the PMDA-ODA. Benzoic acid modules are highlighted in grey and blue. . . . .	144
4.24	The $H^1$ NMR spectra of the TVEB and benzoic acid reactive mixture at $25^\circ C$ (blue) and $110^\circ C$ (red), and $130^\circ C$ (green). . . . .	145
5.1	The 2D computer assisted design to be imprinted on SU-8, along with the laser writing parameters for the writing process. . . . .	150
5.2	An optical microscope photo of the SU-8 mold fabricated, the width of the channel is indicated in the figure on the right. . . . .	151
5.3	The crosslinking reaction between the PDMS prepolymer and the crosslinking agent, illustrated here as polymethylhydrosiloxane ( <b>PMHS</b> ), the most simple form that the curing agent may take. . . . .	152
5.4	Optical microscope photo of the PDMS channel:(a) top view, (b) channel profile . . . . .	152
5.5	The plasma treatment effect on the MZ layer: (a) before and (b) after plasma treatment of the same location. The observation spot is marked by the UV imprint of a cross. . . . .	153
5.6	The adhesive transfer and bonding process. . . . .	154
5.7	Plasma treatment and baking time effect . . . . .	155
5.8	Optical microscope photo of the bonded PDMS channels: (a) with a $5 \mu m$ , and (b) $2 \mu m$ adhesive layer. . . . .	156
5.9	Fluid (in blue) injection in the bonded PDMS chip. . . . .	157
5.10	Two adhesive bonded chips that passed the dismantling test. . . . .	157
5.11	An alternative to a desktop aligner for PDMS/PDMS or PDMS/MZ: on the left, a photo of the setup that is the optical microscope and the upper layer mount, and on the right the same setup with the mounts dimensions in mm. . . . .	158
5.12	The alignment process steps. . . . .	159
5.13	A schema explaining the method we use to assess the alignment quality. The $(\Delta x, \Delta y, \Delta \theta)$ model proposed by [229] . . . . .	160

5.14	Photos taken of the alignment marks, before and after the alignment . . . . .	160
5.15	Cationic polymerisation mechanism of Vinyl groups. For VEs the R is an OR' [181]. . .	171
5.16	(a) ODA and (b) PMDA terminations. . . . .	173
5.17	$H^1 - H^1$ COSY spectrum of PMDA-ODA . . . . .	174
5.18	PMDA-ODA configurations, the meta-PMDA-ODA configuration, which will also be called isomer A (top) and the para-PMDA-ODA configuration, which will also be called isomer B (bottom). The hydrogen atoms are annotated ( $H_0 - > H_5$ ) and color coded depending on their electromagnetic equivalence. The atoms numbering (1 - > 64) refers to non hydrogen atoms such as carbon, oxygen and hydrogen. . . . .	175
5.19	2D HSQC NMR of PMDA-ODA. Protons on horizontal axis and carbons on the vertical one. . . . .	176
5.20	PMDA-ODA configurations, the isomer A (top) and isomer B (bottom). The Carbon atoms are annotated depending on their electromagnetic equivalence. . . . .	176
5.21	2D HMBC NMR of PMDA-ODA. Protons on horizontal axis and carbons on the vertical one. . . . .	177
5.22	$C^{13}$ NMR spectrum of PMDA-ODA. . . . .	179
5.23	The cured linewidth as a function of the dose applied for SU-8. . . . .	181



# List of Tables

1.1	From conventional optics to integrated optical circuits . . . . .	11
1.2	Dimensions for different values of $\Delta$ assuming that the height $b$ is infinite and $n_3 = n_1(1 - \Delta)$ . Reproduced from [30] . . . . .	25
2.1	Bonds refractions at 587.56 nm, based on data given in Landolt-Bornstein, as they appeared in reference [152]. . . . .	56
3.1	A summary of the photoinitiators characteristics . . . . .	95
3.2	Values of the waveguide width $a$ for different refractive index contrast and waveguide ratio. . . . .	110
3.3	Possible combinations for writing single mode waveguides. . . . .	111
4.1	Chemical shifts assignment of PMDA-ODA protons . . . . .	129
4.2	Relative integrals of the peaks that appear in the PMDA-ODA spectrum . . . . .	130
4.3	Assignment of end of chains protons according to carbon numbers in figure 4.8. The relative integral of the proton $H_5$ is also mentioned because it is going to be used in the calculation of the molecular mass. The normalisation of the integrals is done with respect to $H'_5$ . . . . .	132
4.4	Average estimation of the polymers molecular weight . . . . .	135
4.5	Chemical shifts assignment and relative intensities (integrals) of TVEB protons . . . .	140
4.6	The ratio of the vinylic to aromatic proton intensities for the reactive model, benzoic acid and TVEB . . . . .	146
4.7	Dissolution in TMAH in of different copolymer reactants at 3 different temperatures. (+) is soluble (-) is insoluble. . . . .	147
5.2	COSY protons correlations and assignments . . . . .	173
5.3	Carbon assignment according to HSQC correlation. Carbon annotation is done according to Figure 5.20. . . . .	175
5.4	Carbon assignment according to HMBC correlation . . . . .	178
5.5	Carbon NMR assignment . . . . .	179



# General Introduction

The lab-on-chip (*LoC*) domain has demonstrated to be particularly beneficial for life sciences, and especially for point of care diagnostics. Moreover, the integration of optical components into these devices has resulted in a new era of potential, in terms of both sample manipulation and detection at the micro-scale. Since on-chip optical add-ons increase both control and analytical capabilities of LOCs, while reducing reliance on expensive laboratory optical equipment. One way to combine microfluidics and photonics on the same platform, is through the vertical integration of a photonic circuit and a microfluidic one. As such, this enables the interaction between the evanescent field of the photonic circuit, and the fluids in the microfluidic system. Therefore, allowing the implementation of both evanescent field sensing and manipulation, on chip.

Many fields of research will remain dormant, until an associated technological revolution occurs. The same applies to optofluidic miniaturised platforms. The rise in the research around this topic did not occur until the early 2000's, when the fabrication of miniaturised systems was revolutionised with the soft lithography techniques and materials. Since then, multiple challenges in the fabrication and development of such devices has been surpassed, yet many more remain due to the complexity involved in combining photonic with micro-fluidic systems.

The optical layer is the active component of the chip. Thus, it plays an important role in ensuring an effective performance, maintaining good signal delivery and collection. An ideal waveguide material should be able to confine light and have low propagation losses. The different materials usually used for the elaboration of the optical layer have both their advantages and inconveniences:

- while the performance of silicon photonic circuits cannot be doubted, their extremely reduced dimensions renders them unfit for the use with microfluidic systems,
- glass and specifically quartz is transparent in the UV and the visible domain, however the realization of waveguides in glass is a complicated process,
- polymer waveguides are attractive, because they can be easily processed, either by soft lithography or photolithography. Nevertheless, they are usually less performant than other types of waveguides.

In addition to the type of materials used for the fabrication of the waveguides, one should be able to pattern and integrate a microfluidic layer within the device, and to seal it properly. The fluidic channel or pool can be implemented in the same material as the waveguide or using other materials as long as they are compatible. For the research and development (R&D) of these devices, many prototypes are produced before one final design gets to production. Therefore, in this context, the materials used for R&D must be compatible with rapid prototyping techniques. At the same time they should also be transferable to the production phase. Since any change in the

materials might generate problems and may lead to redesigning the device. The use of a negative resist for the optical circuit, and a positive resist for the fluidic layer, is particularly adapted for this task. They are a perfect fit for rapid prototyping using laser writing. Moreover, once a design gets to production they can be easily and rapidly patterned using UV masking systems.

This work is an exploration of the potential of organic-inorganic photoresists, for the fabrication of optofluidic miniaturised systems. This class of materials presents the advantages of both glass and photopolymerisable polymers. They are suitable candidates for the use in the R&D of optofluidic chips.

This manuscript is divided into two parts. The first consists of the literature review and is composed of two chapters. They are dedicated to optofluidic chips, from the conception to the materials and the fabrication techniques. In the first chapter, microfluidic chips and optical circuits along with their respective governing laws, are introduced. Afterwards, we will present a general overview of optofluidic systems, with a particular emphasis on optofluidic chips for evanescent field manipulation. The second chapter is fully dedicated to the materials and methods used for the fabrication of optofluidic systems for manipulation. After presenting the material requirements for the fabrication of these chips, we will go through the conventional ones while presenting their processing methods and discussing their advantages and disadvantages. In the end we will investigate the potential of organic-inorganic materials to perform this integration. For this purpose the details of their chemistry will be thoroughly studied. In addition we will discuss their use for the implementation of optical waveguides as well as microfluidic channels.

The second part is composed of three chapters (Chapters 3, 4, and 5) that summarize the experimental work. This starts with a brief introduction tackling the application that will be implemented and the different materials that will be used. The third chapter will address the negative photoresist used for the implementation of the optical circuit. This includes the resist fabrication and deposition, as well as the refractive index measurements. In addition to the elaboration of the solid film, we present the patterning of the waveguides using laser writing. Finally we characterise their morphology as well as their propagation losses.

The fourth chapter constitutes a major part of the experimental work. It will be dedicated to adapt a hybrid positive photoresist, in order to use it for the fabrication of microfluidic channels.

Finally, in the fifth and last chapter we accomplish the integration of the optical layer and the microfluidic layer. For that we shift the work towards using PDMS, because the positive resist needs further optimisation. We describe in details how the PDMS chip is fabricated, from the mixing of the reagents to the fabrication of the mold and the molding step. We investigate the bonding of the PDMS to the optical layer by the use of an adhesive, and we propose a simple setup in order to align these two components.

Part I  
Literature Review



# Chapter 1

## Optofluidic Lab on Chip

### 1.1 Introduction

Optofluidics, Light-Fluid interaction is nothing but a subdivision of Light-Matter interaction, and this is mainly an exchange of energy and momentum between these two systems. This exchange clearly depends on the energies, and scales at stake. So from the less energetic IR to the most energetic UV the possibilities of manifestation of these interactions on the molecular and atomic levels, are greater than we can ever imagine, even the absence of an interaction is a phenomenon in itself: transparency.

Optofluidics refer to a wide range of applications in which a symbiotic relationship between optics and fluidics is utilised to synthesize creative, novel and highly versatile functionalities. On the other hand the Lab on Chip (*LoC*) domain, thriving for further integration, has found a special interest in optical "add-ons" on a microfluidic device, thus paving the way for a new generation of LoC which we will baptise as **Opto-Microfluidic Lab-on-Chip** (*OMLoC*).

These OMLoC have demonstrated to be beneficial on multiple levels, mainly: biosensing and particle manipulation. Therefore, we wish to address this subject due to its increasing importance for novel nano-biotechnologies. In fact this approach would enable contactless, single and multiple particle manipulation as well as mass transport in order to implement an on chip control functionalities.

Thus, our goal in this chapter is to focus on the near field optical forces for particle manipulation on a chip, a task that is only possible through the interaction of the fluid with the evanescent field of an optical waveguide. Moreover, in order to understand the importance of these optics enabled manipulation we will be looking first into the concept of microfluidic lab on chip in Section 1.2 to understand its utility and development. We will then address the propagation of electromagnetic waves in dielectric waveguides in Section 1.3. And finally, in Section 1.4 we will go through the main functionalities that were enabled by optical integration, and extend to the implementation of near field optical manipulation on chip, from theory to application.

## 1.2 Microfluidic Lab on Chip

Microfluidics is defined as the study of fluids in microchannels, whose dimensions are roughly less than 1 millimeter and greater than 1 micron [1]. It found a true realm in the LoC paradigm, the concept of incorporating several classical **Lab** functionalities (from synthesis to analysis) **on** one miniaturised platform, **a Chip**. This model offers many advantages over classical lab equipment like minimized consumption of reagents, portability, increased automation and reduced costs.

Trivially linked to life sciences, microfluidic LoCs originally known as **Micro Total Analysis Systems** ( $\mu$ -**TAS**), were the fruitful result of the work of analytical chemists in their quest for miniaturisation. As early as the 1970s, Stephen Terry miniaturized and integrated a complete gas chromatography system [2] on a 2 inches silicon wafer by micro-machining. These efforts didn't get any echo until the 90's where two major events happened: soft lithography techniques were born and a conceptual paper [3] by Manz et al. was published. This paper theoretically concluded that such approach enhances the analytical performance of total analysis systems by allowing: a faster and more efficient chromatographic separation, faster electrophoretic separation, shorter transport time, dramatically small reagent consumption, and as a consequence parallel performance of large number of measurements on the same device. Revisited 10 years later [4], the advantages of such down scaling, were once again confirmed, and it was added to them increased automation and low manufacturing cost. The latter two were enabled by the development of on-chip control elements such as valves, pumps [5] and mixers [6], and much simpler fabrication techniques and materials [7].

Hence it is clear that the miniaturisation was not a goal in itself, but an improvement that was later used to increase portability, this is why they became attractive for point of care application (on site diagnosis and detection) especially that their low fabrication and operation cost makes them disposable and adequate for self testing [8,9] (Figure 1.1a) and rapid screening in resource poor settings (Figure 1.1b) [10,11] and in periods of biological crisis [12]. After having stated the importance and relevance of LoCs, we can now explore the basic physical principles that govern the microfluidic realm.

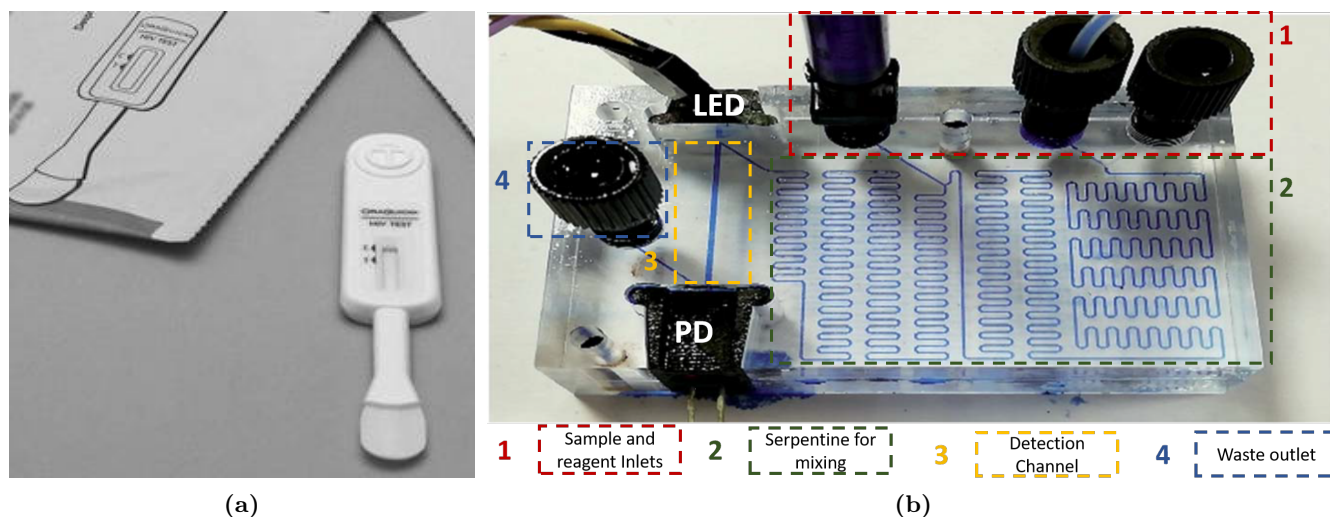


**Figure 1.1:** (a)The OraQuick In-Home HIV test kit [9], (b)A microfluidic LoC equipped with a laser emitting diode (**LED**) and a photodiode (**PD**) to be integrated in a field test kit for Arsenic detection in water. Edited from [11].

### 1.2.1 Dimension consideration

The dimension of a microchannel should be adjusted to its content. This sets what we call a characteristic length scale<sup>1</sup>  $L$ , that is the ratio of the cross sectional surface  $A_{cs}$  to the perimeter of the cross section  $P_{cs}$ .

$$L = \frac{A_{cs}}{P_{cs}} \quad (1.1)$$

It allows us to treat any channel morphology as a cylindrical one with diameter  $L$ .  $L$  typically ranges between  $20 \mu m$  and  $200 \mu m$ .

Generally, transport processes are classified into three categories according to  $L$ , of the systems:

- Nanoscale systems:  $L < 100 nm$  covering the realm of small molecules (around  $0.1 nm$ ), to lipids (around  $1 nm$ ) and finally proteins at around  $10 nm$  as well as some viruses ( $> 20 nm$ ).
- Microscale systems:  $100 nm < L < 200 \mu m$  covering the realm of bacteria ( $1 - 10 \mu m$ ), animal and plant cells ( $10 - 100 \mu m$ ), and organoids.
- Macroscale systems:  $L > 200 \mu m$  covering the realm of tissues, organs and organisms.

The characteristics of the transport processes change significantly as the characteristic dimension of the system changes from one category to another. The fluid behavior on this scales is not very intuitive to us as that of macroscopic fluids, it is marked by a strongly laminar flow, an extremely weak inertial forces, a greater relevance of both surface tension and capillary forces, an ability to exploit electrokinetic effects, optical and acoustic forces, whose impacts are rarely observable on a bigger scale.

### 1.2.2 Fluid characteristics

A fluid is defined as a system that rearranges and flows in response to external shear stress, such as liquids, gases, and plasma. To define such a system three quantities need to be set:

- Its specific mass  $\rho$  in  $[kg/m^3]$  defined as the mass  $m$  to volume  $V$  ratio.
- The pressure  $P$  in  $[Pa]$  at a certain position in the fluid. In microchannels, this pressure reduces to the externally applied one integrally transmitted through the fluid and inducing its flow.
- Its viscosity  $\eta$  in  $[Pa.s]$ , the internal resistance to an imposed flow.

As illustrated in Figure 1.2, two parallel plates are set on top of each other with a liquid film of thickness  $2b$  between them. The upper plate can be set into motion by a surface force,  $\vec{F}$ , resulting in a velocity,  $\vec{v}$  relative to the lower one regarded as stationary. The applied surface force  $\vec{F}$  acts on an area,  $A$ , of the liquid surface containing  $\vec{F}$ , inducing a shear stress  $F/A$ , while the displacement of liquid at the top plate,  $\Delta x$ , relative to the thickness of the film is the shear strain  $\Delta x/2b$ .

---

<sup>1</sup>or a hydraulic diameter

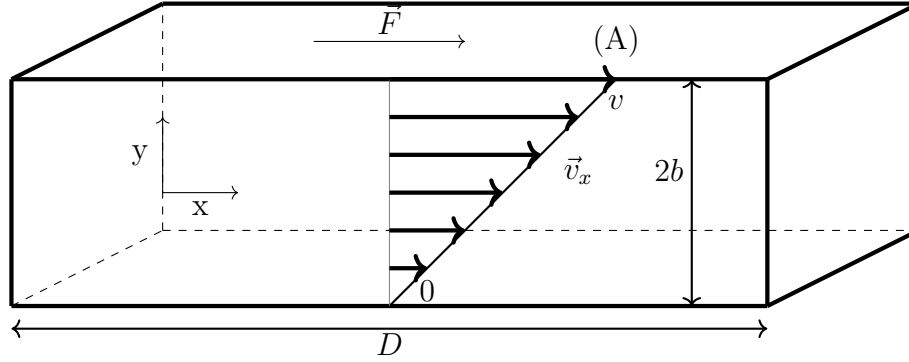


**Figure 1.2:** Schematic drawing of flow under shear stress.

The coefficient of viscosity,  $\eta$  in  $[Pa.s]$ , can then be defined as the ratio of the shear stress to the shear rate:

$$\eta = \frac{F/A}{v/2b} \quad (1.2)$$

if  $\eta$  is constant (i.e the shear stress of a fluid is directly proportional to the velocity gradient) the fluid is a Newtonian one, otherwise it is a non Newtonian fluid.

### 1.2.3 Flow characteristics

Fluid transport on the micro scale is governed by continuum mechanics and by the Navier-Stokes equation similarly to classical fluid dynamics. The only difference is the order of scale of the flow parameters.

The ratio of the magnitudes of inertial to viscous forces defined as the dimensionless Reynolds number  $R_e$  and expressed in terms of fluid characteristics and the characteristic dimension as:

$$R_e = \frac{\rho L v_0}{\eta} \quad (1.3)$$

is extremely low where  $v_0$  is the characteristic velocity of the fluid.

For Reynolds numbers below 2300, we can expect the flow to be laminar. For values above 4000 approximately, the flow will be turbulent. In between these two limits, the flow is termed “transition flow”. To get a sense of the scale of magnitude of the  $R_e$  in microfluidic channels, we evaluate it in the case of a channel having a hydraulic diameter of  $10 \mu m$ , filled with water flowing at a characteristic velocity of  $100 \mu m/s$ . We can find an extremely low  $R_e$  number of the order of  $10^{-3}$ . Thus we can clearly expect a laminar flow.

The equations of continuity and the Navier-Stokes equation for a viscous incompressible and homogeneous Newtonian fluids are [13]:

$$\vec{\nabla} \cdot (\vec{v}) = 0 \quad (1.4)$$

$$\rho \left( \frac{\partial(\vec{v})}{\partial t} + (\vec{v} \cdot \vec{\nabla})\vec{v} \right) = -\vec{\nabla} p + \eta \vec{\nabla}^2 \vec{v} \quad (1.5)$$

Where  $\vec{v}$  is the velocity of the fluid, and  $p$  is the fluid pressure. Within these conditions of extremely low Reynolds number the Navier Stokes equation reduces to Stokes equation:

$$\vec{0} = -\vec{\nabla}p + \eta\vec{\nabla}^2\vec{v} \quad (1.6)$$

This differential equation is solved on a domain  $\Omega \subset R^n$  (here we will consider  $n = 1$ ), having a boundary  $\delta\Omega$ . This time independent equation physically means that any change in the input pressure will be translated as instant change in the flow velocity. We can also note that the Navier-Stokes equation does not account for surface tension, as this later only acts on boundaries and not on elementary volumes in the fluid. As a result it only appears when solving for  $\vec{v}$ , and it is formulated in the Dirichlet type boundary condition  $v(\delta\Omega) = 0$ , commonly known as the no slip boundary condition.

Even though multiple flow control techniques exist, pressure driven flow is the most robust and commonly used method for fluid actuation. It imposes a certain flow velocity to fluids in microchannels without having much regard to its properties, nor to those of the channels surface. It only requires a pump which provides a simple setup as it can be seen in Figure 1.3. The only drawback is its inability to adapt to submicronic channel dimensions, since the flow velocity is proportional to the square of the channel size as we will later clarify.

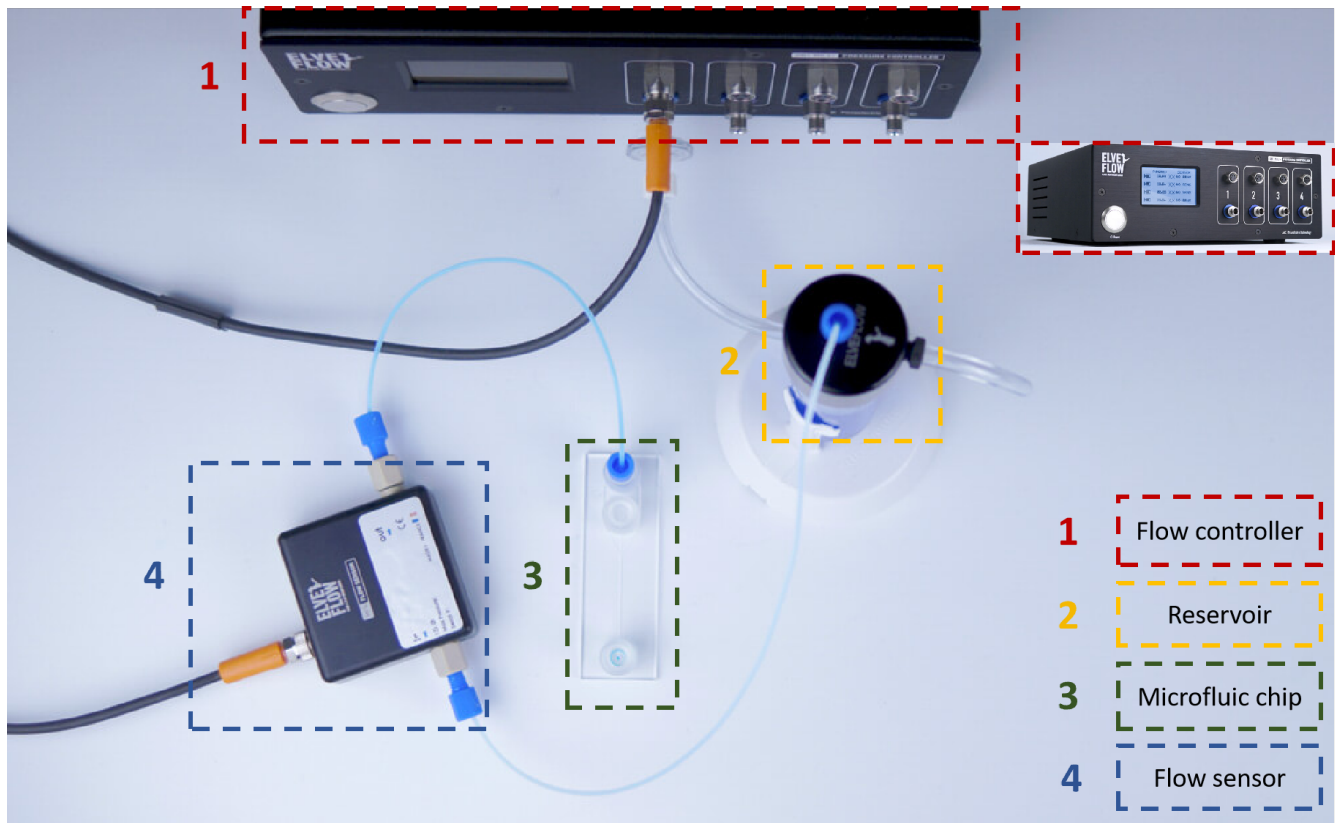


**Figure 1.3:** A typical but simplified microfluidic setup. No dispense reservoir is connected to the chip for the sake of clarity. The flow controller is connected to an external pressure source, and the flow sensor provides a feedback loop to adjust the pressure in order to keep a stable flow rate on the chip.

Edited from [14]

The flow velocity in such systems can be calculated from Equations 1.5 and 1.6. Consider a channel of infinite length ( $D \gg 2b$ ) as represented in Figure 1.4, but sufficiently wide such that the side walls do not affect the flow profile.

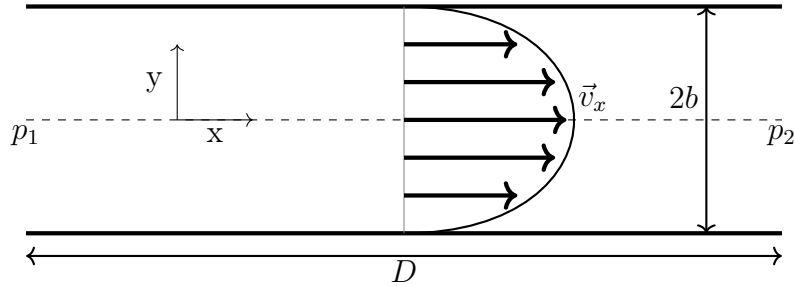


**Figure 1.4:** Schematic drawing of a 2D pressure driven flow in a microchannel.

Adopting the no-slip condition on both walls as well, the flow is essentially unidirectional, and  $\vec{v}_x$  is given by the Poiseuille law:

$$v_x(y) = -\frac{1}{2\eta} \frac{dp}{dx} (b^2 - y^2) \quad (1.7)$$

The average velocity is calculated by integrating with respect to  $y$ :

$$v_{avg} = -\frac{1}{2\eta} \frac{dp}{dx} \int_{-b}^b (b^2 - y^2) dy = -\frac{1}{2\eta} \frac{dp}{dx} \frac{2b^2}{3} \quad (1.8)$$

Equation 1.8 reveals the dependency of the average velocity on the square of the channel's height.

In this simplified 2D approach, if the channel's height is divided by 2, the pressure difference should be quadrupled to keep the flow constant. This is why this technique does not scale well with small channel dimension, and other techniques such as electrokinetic or optofluidic transport may seem more attractive at the nanoscale.

### 1.3 Integrated optical circuits

The propagation of light can be dimensionally restricted by trapping it in a region of high refractive index dielectric medium, thus limiting its propagation to particular set of paths. In geometrical optics theory this mechanism of confinement is explained by Total Internal Reflection (**TIR**). This way a one dimensional confinement creates planar waveguides, two dimensional confinement creates strip waveguide or optical fiber, finally a three dimensional one creates cavities as illustrated in Figure 1.5.

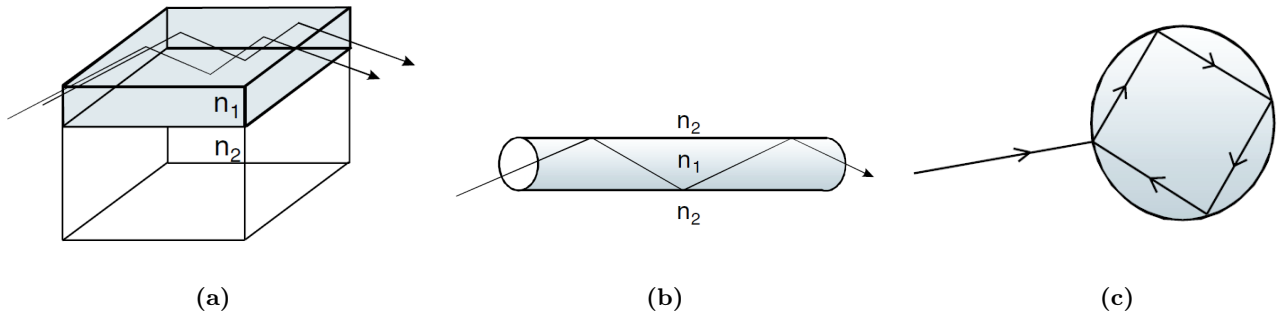


**Figure 1.5:** Light confinement in a high refractive index medium: (a) 1D confinement: planar waveguide, (b) 2D confinement: fiber or channel waveguide, (c) 3D confinement: cavity.

Integrated Optics (*IO*) are the third generation of miniaturised optics, they are mostly planar structures that deal with confined waves, in order to create microscale parallels for standard optical instruments (Table 1.1).

Technology	First generation: conventional optics	Second generation: micro optics	Third generation: integrated optics
Components	Gaz lasers Lenses Mirrors	LED, Diode lasers Multimode fibers Microlenses	Lasers Integrated optical circuits Single mode fibers
Alignment	Necessary	Necessary and hard to achieve	Unnecessary
Propagation	Beam ( $\sim 1\text{ cm}$ )	Multimode ( $\sim 1\text{ mm}$ )	Single mode ( $\sim \mu\text{m}$ )
Device fingerprint	$\sim 1\text{ m}^2$	$\sim 10\text{ cm}^2$	couple of $\text{cm}^2$

**Table 1.1:** From conventional optics to integrated optical circuits

When it comes to miniaturisation we can see great similarities between electronics, optics, and fluidics: the hope that small size will lead to better performance and lower consumption than bulk instruments. And of course, there is also the potential for integration, allowing increased portability and device complexity as illustrated in Figure 1.6.

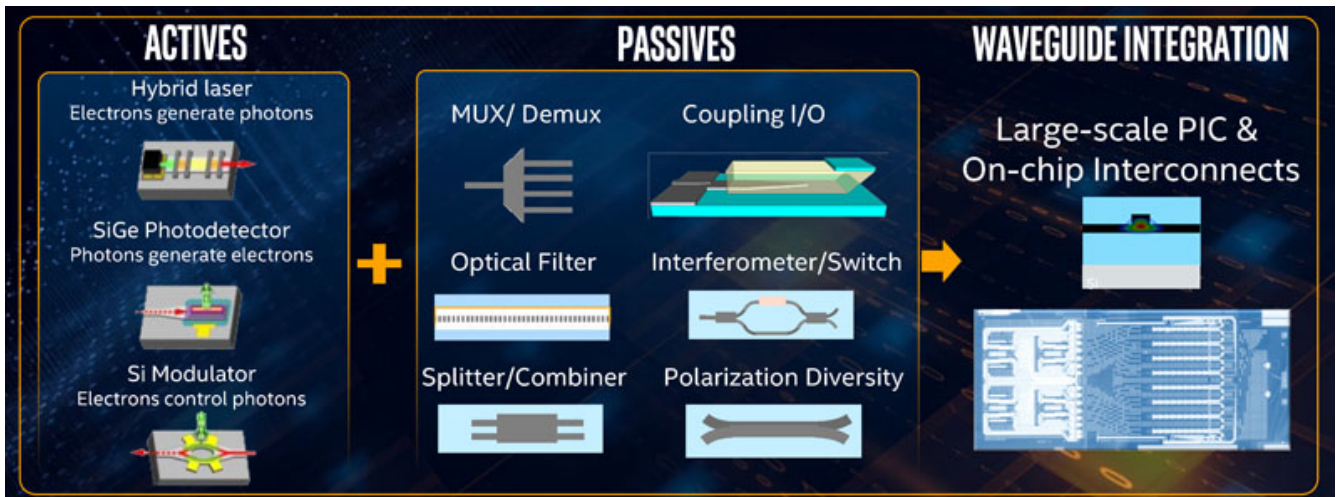


**Figure 1.6:** The level of integration allowed by photonic integrated circuits [15]

In the context of OMLoCs the use of different types of channel waveguides (Figure 1.7) is essential for sensing, control, and for signal transmission. Rectangular waveguides are the most commonly used for these applications.

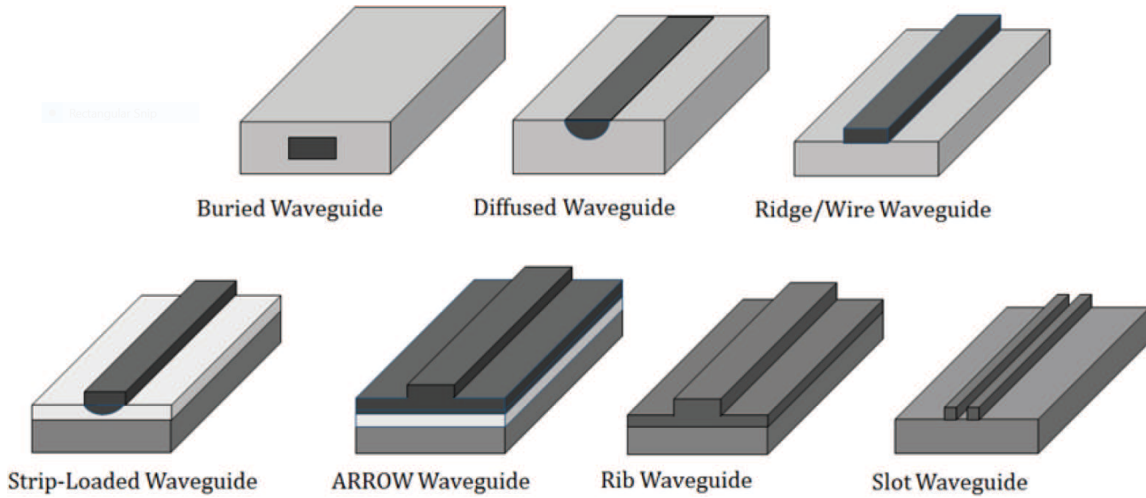


**Figure 1.7:** Schematic representation of various channel waveguides.

The integration of both optical and fluidic circuits in these devices, eliminates the need for precise alignment and results in a compact, robust and reliable device. Furthermore, other light guiding structures can be implemented, such as: periodic structures (photonic crystals of different orders), hollow core anti resonant reflecting waveguides (**ARROW**), metal-dielectric structure (such as Silicon on insulator waveguide) or using high surface reflectivity (mirror). All of which are beyond the scope of this manuscript, because our main focus is dielectric optical waveguides.

Due to technical considerations, we can either implement a ridge or a diffused waveguide as represented in Figure 1.8.

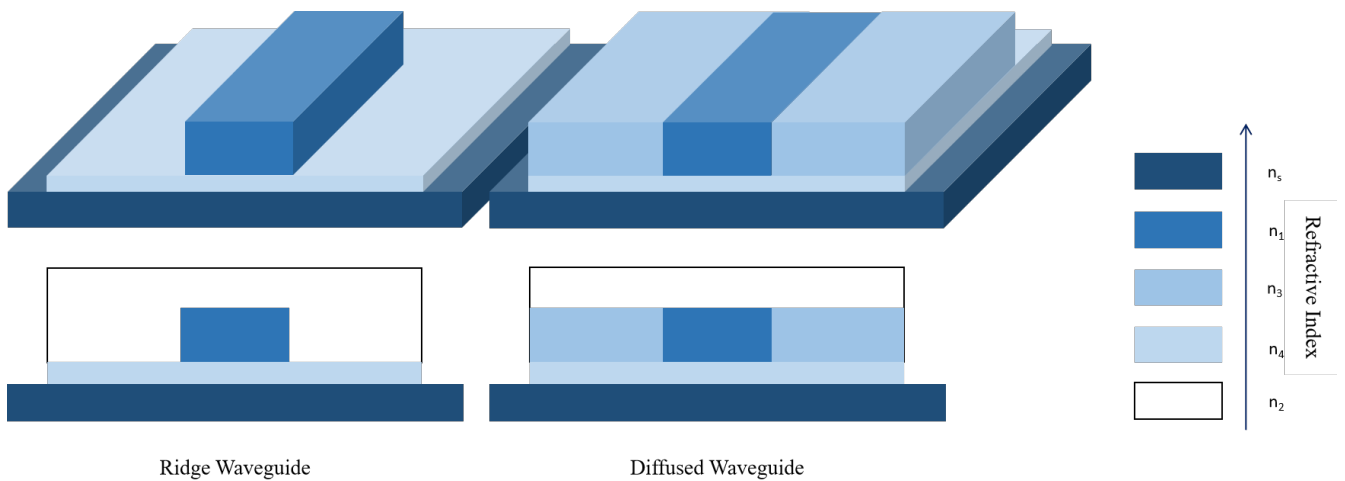


**Figure 1.8:** Schematic representation of the implemented waveguides

As such the indices around the waveguide might vary within the following possible cases:

- Either a waveguide of refractive index  $n_1$  on a buffer layer of refractive index  $n_4$  surrounded by a medium of refractive index  $n_2$ . This medium will most probably be water of refractive index 1.33<sup>2</sup> [16] in our case.
- Or a waveguide of refractive index  $n_1$  on a buffer layer of refractive index  $n_4$ , symmetric around the y axis with a medium of refractive index  $n_3$  and covered by a superstrate of refractive index  $n_2$  which once again will most probably be water.

### 1.3.1 Propagation in rectangular dielectric waveguides

During the late 60's and early 70's, with the advancement in the integrated circuit domain, it was expected that the building block for any of these circuits will consist of a rectangular dielectric core waveguide embedded in a medium of slightly lower refractive index. In anticipation for this development, many researchers have studied the propagation of EM waves in these structures.

We know that in the case of dielectric plate or a circular waveguide with axially symmetric fields, the fields distribution in the transverse plane depends only on one variable. In such case the solution can be found in terms of modes of transverse electric (**TE**) and transverse magnetic (**TM**) types. On the other hand, in the case of an open rectangular dielectric waveguide, this becomes impossible, and the propagating modes are referred to as hybrid modes. We will call the propagating mode  $E_{mn}^y$  if its electric field is polarized mainly along the y direction and  $E_{mn}^x$  if the strongest electrical field is polarised along the x direction. The  $m$  and  $n$  subscript are used to designate the number of maxima in the x and y directions, respectively.

Generally, it is impossible to get a closed-form analytical solution to the field problem in an arbitrary rectangular guide, thus an iterative computer analysis must be performed. In an attempt to theoretically investigate the propagation in such structures multiple approximate solutions appeared around the late 60's: Marcatili [17] presented his approximate analysis of the rectangular homogeneous dielectric structures and Goel [18] presented his circular-harmonics computer analysis. Knox and Toullos [19] presented the simple effective index method (**SEIM**) and later on Chiang [20] presented a more elaborate version of it, the dual effective index method (**DEIM**). In addition, numerical methods, such as the finite difference [21], the finite element [22, 23] and the beam propagation method [24] were also used in order to solve problems involving the Maxwell equations.

#### 1.3.1.1 Marcatili's analytical solution

Marcatili solved Maxwell's equations to find the approximate transmission properties of rectangular dielectric waveguide structures of width  $a$  and height  $b$  and whose profile is represented in Figure 1.9. This method was developed for low ratios between the core refractive index and that of the cladding region. In his analysis, fields with sinusoidal variation in the core of refractive index  $n_1$  are matched to exponentially decaying fields in the external media of refractive indices  $n_2, n_3, n_4$  and  $n_5$ .

---

<sup>2</sup>at 633 nm and at ambient temperature

The boundary conditions cannot be matched simultaneously in the x and y directions in the corner regions (grey regions in Figure 1.9), thus making the solution for the fields extremely complicated. In order to solve this issue, an assumption was made: most of the guided energy is confined within the dielectric core region for a wide range of parameters, and very little energy is guided in the corner regions of a rectangular dielectric waveguide so an approximate solution can be formulated by ignoring the field matching along the edges of the shaded areas in Figure 1.9.

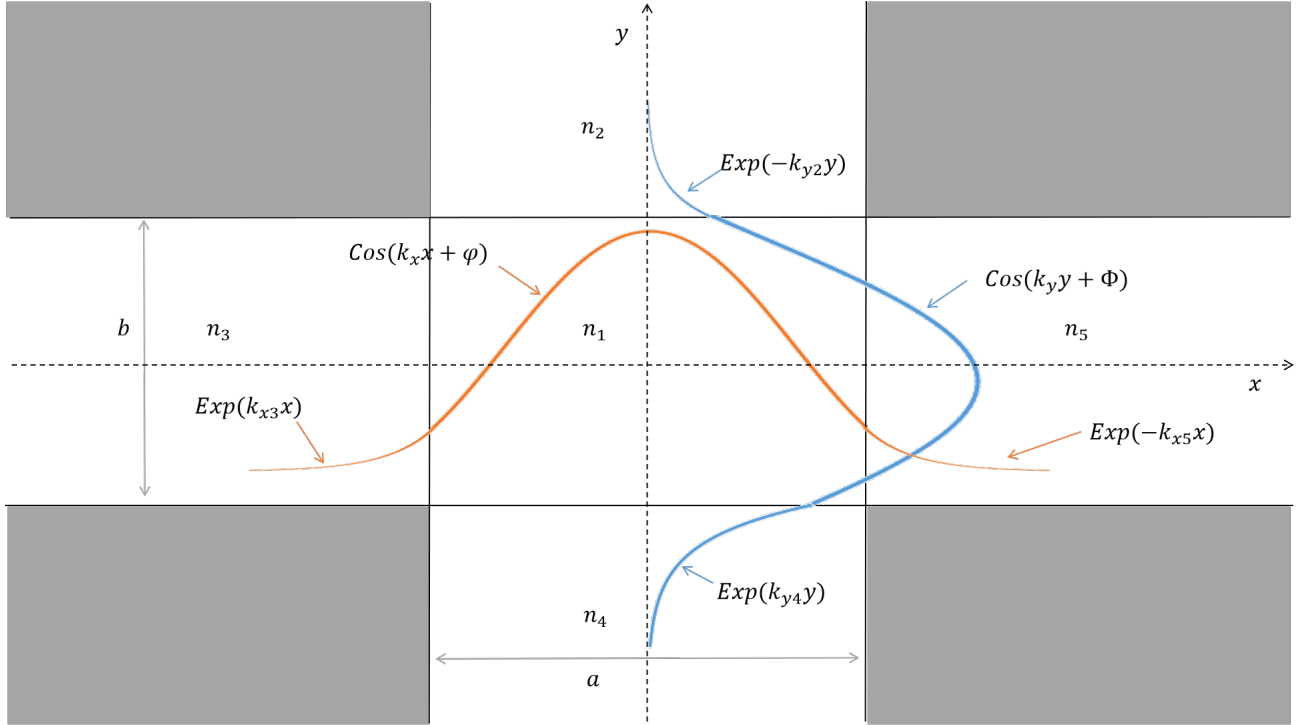


**Figure 1.9:** Geometry of the rectangular dielectric waveguide immersed in different dielectrics. Field distribution of the first order mode  $E_{11}^y$ , in blue  $H_x$  and in orange  $E_y$ .

By matching the tangential electric and magnetic fields only along the four sides of region 1, and assuming that the field components in region 1 vary sinusoidally in the x and y directions, those in 2 and 4 vary sinusoidally along x and exponentially along y, and those in regions 3 and 5 vary sinusoidally along y and exponentially along x, we may obtain a dispersion relation from which the propagation constants of various modes may be calculated.

For the  $E_{pq}^y$ , we express the field components, say,  $H_x$  as follows:

$$H_x^{(i)} = \exp\{-j(\omega t - k_z z)\} \begin{cases} M_1 \cos(k_x x + \phi) \cos(k_y y + \Phi) & \text{for } i=1 \\ M_2 \cos(k_x x + \phi) \exp\{-k_{y2} y\} & \text{for } i=2 \\ M_3 \cos(k_y y + \Phi) \exp\{-k_{x3} x\} & \text{for } i=3 \\ M_4 \cos(k_x x + \phi) \exp\{k_{y4} y\} & \text{for } i=4 \\ M_5 \cos(k_y y + \Phi) \exp\{-k_{x5} x\} & \text{for } i=5 \end{cases} \quad (1.9)$$

$E_y$  can be found from the Maxwell equations :

$$E_y^{(i)} = \frac{k_i^2 n_i^2 - k_{yi}^2}{\omega \epsilon n_i^2 k_z} H_x^{(i)} \text{ for } i=1,2,3,4,5 \quad (1.10)$$

The other field quantities  $E_x$ ,  $H_y$ ,  $E_z$  and  $H_z$  are small and don't need be considered. The superscript (i) represents the region of application.  $M_i$  are unknown amplitudes,  $k_x$  and  $k_y$  are the propagation constants in the guiding medium of refractive index  $n_1$  in the horizontal and vertical directions, respectively, and  $k_{y2}$ ,  $k_{y4}$ ,  $k_{x3}$ ,  $k_{x5}$  are the decay factors in the outer regions.  $\phi$  and  $\Phi$  are additional phase constants.

The free space wavenumber in the medium of refractive index  $n_i$  is expressed as:

$$k_i = \sqrt{k_{xi}^2 + k_{yi}^2 + k_z^2} = \omega n_i \quad (1.11)$$

Under the assumption that:

$$k_{x1} = k_{x2} = k_{x4} = k_x \quad (1.12)$$

$$k_{y1} = k_{y3} = k_{y5} = k_y \quad (1.13)$$

A first set of transcendental equations is derived, we will not include them here. In order to derive closed form solutions to these equations we assume that the waves impinge on the surfaces of the core at normal incidence ( $k_x$ , and  $k_y \ll k_z$ ).

This way, the solutions to  $k_x$ , and  $k_y$  are found in terms of the width  $a$  and height  $b$  of the rectangular dielectric waveguide cross section, and in terms of the difference between dielectric constants between the waveguide and its surrounding materials. For well guided modes the propagation constants can be put in closed forms as follows:

$$k_x = \frac{p\pi}{a} \left[ 1 + \frac{A_3 + A_5}{\pi a} \right]^{-1} = \frac{p\pi}{a} B_{3,5}^{-1} \quad (1.14)$$

$$k_y = \frac{q\pi}{b} \left[ 1 + \frac{n_2^2 A_2 + n_4^2 A_4}{\pi n_1^2 b} \right]^{-1} = \frac{q\pi}{b} B_{2,4}^{-1} \quad (1.15)$$

where  $a$  and  $b$  are the dielectric waveguide width and height,  $p$  and  $q$  are the mode numbers. The  $B_{3,5}$  and  $B_{2,4}$  were introduced to simplify the expressions. The  $A$ 's are given by:

$$A_i = \frac{\lambda_0}{2\sqrt{n_1^2 - n_i^2}} \quad \text{for } i=2,3,4,5 \quad (1.16)$$

where  $\lambda_0$  is the free space wavelength.

Although the transverse constants provide great insight, especially to quantify the distance that the fields penetrate outside the waveguide walls, the most useful quantity derived by this method is the longitudinal constant, here denoted by  $k_z$ . This can be found simply using Equation 1.11.

So  $k_z$  is expressed as follows

$$k_z^2 = k_1^2 - \left(\frac{p\pi}{a}\right)^2 \left[ 1 + \frac{A_3 + A_5}{\pi a} \right]^{-2} - \left(\frac{q\pi}{b}\right)^2 \left[ 1 + \frac{n_2^2 A_2 + n_4^2 A_4}{\pi n_1^2 b} \right]^{-2} = k_1^2 - \left(\frac{p\pi}{a}\right)^2 B_{3,5}^{-2} - \left(\frac{q\pi}{b}\right)^2 B_{2,4}^{-2} \quad (1.17)$$

The penetration depth of the evanescent field in the media 3 and 5 around the waveguide can be derived as well:

$$\frac{1}{k_{xi}} = \frac{A_i}{\pi} \left[ 1 - \left[ \frac{pA_i}{a} \frac{1}{B_{3,5}} \right]^2 \right]^{-1/2} \quad (1.18)$$

Same goes for the penetration depths in media 2 and 4:

$$\frac{1}{k_{yi}} = \frac{A_i}{\pi} \left[ 1 - \left[ \frac{qA_i}{b} \frac{1}{B_{2,4}} \right]^2 \right]^{-1/2} \quad (1.19)$$

For the  $E_{pq}^x$  the same reasoning is applied in order to deduce these quantities for which we are going to use the same nomenclature written in bold:

$$\mathbf{k}_z^2 = k_1^2 - \left( \frac{p\pi}{a} \right)^2 \left[ 1 + \frac{n_3^2 A_3 + n_5^2 A_5}{\pi n_1^2 a} \right]^{-2} - \left( \frac{q\pi}{b} \right)^2 \left[ 1 + \frac{A_2 + A_4}{\pi b} \right]^{-2} = k_1^2 - \left( \frac{p\pi}{a} \right)^2 \mathbf{B}_{3,5}^{-2} - \left( \frac{q\pi}{b} \right)^2 \mathbf{B}_{2,4}^{-2} \quad (1.20)$$

The penetration depth of the evanescent field in the media 3 and 5 around the waveguide can be derived as well:

$$\frac{1}{\mathbf{k}_{xi}} = \frac{A_i}{\pi} \left[ 1 - \left[ \frac{pA_i}{a} \frac{1}{\mathbf{B}_{3,5}} \right]^2 \right]^{-1/2} \quad (1.21)$$

Same goes for the penetration depths in media 2 and 4:

$$\frac{1}{\mathbf{k}_{yi}} = \frac{A_i}{\pi} \left[ 1 - \left[ \frac{qA_i}{b} \frac{1}{\mathbf{B}_{2,4}} \right]^2 \right]^{-1/2} \quad (1.22)$$

### 1.3.1.2 Goell's circular harmonic analysis

Goell used a circular harmonic analysis based on the expansion of the electromagnetic field ( $\mathbf{EM}$ ) into Bessel (in the core) and modified Bessel (outside) functions. Along with the adequate point matching at the boundaries this work yields a set of linear equations that are solved numerically in order to find the propagation constants and the intensity profiles of the modes allowed in a rectangular dielectric waveguide as illustrated in Figure 1.10 of refractive index  $n_1$  surrounded by an infinite medium having  $n_0$  as a refractive index.

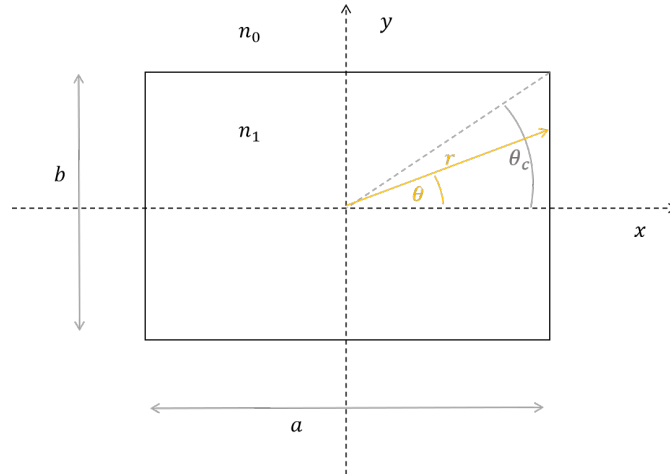


**Figure 1.10:** Dimension and coordinates system for Goell's method.

For Goel's Analysis we are only going to show the results and not the equations. For the fundamental mode for example, the maximum field intensity is concentrated in an oval section around

the centre of the rectangular cross-section with rapidly decreasing intensity outside that region, as seen in Figures 1.11a and 1.11b. Figures 1.11c and 1.11d show the energy profile distribution for the higher order mode  $E_{22}^y$ .

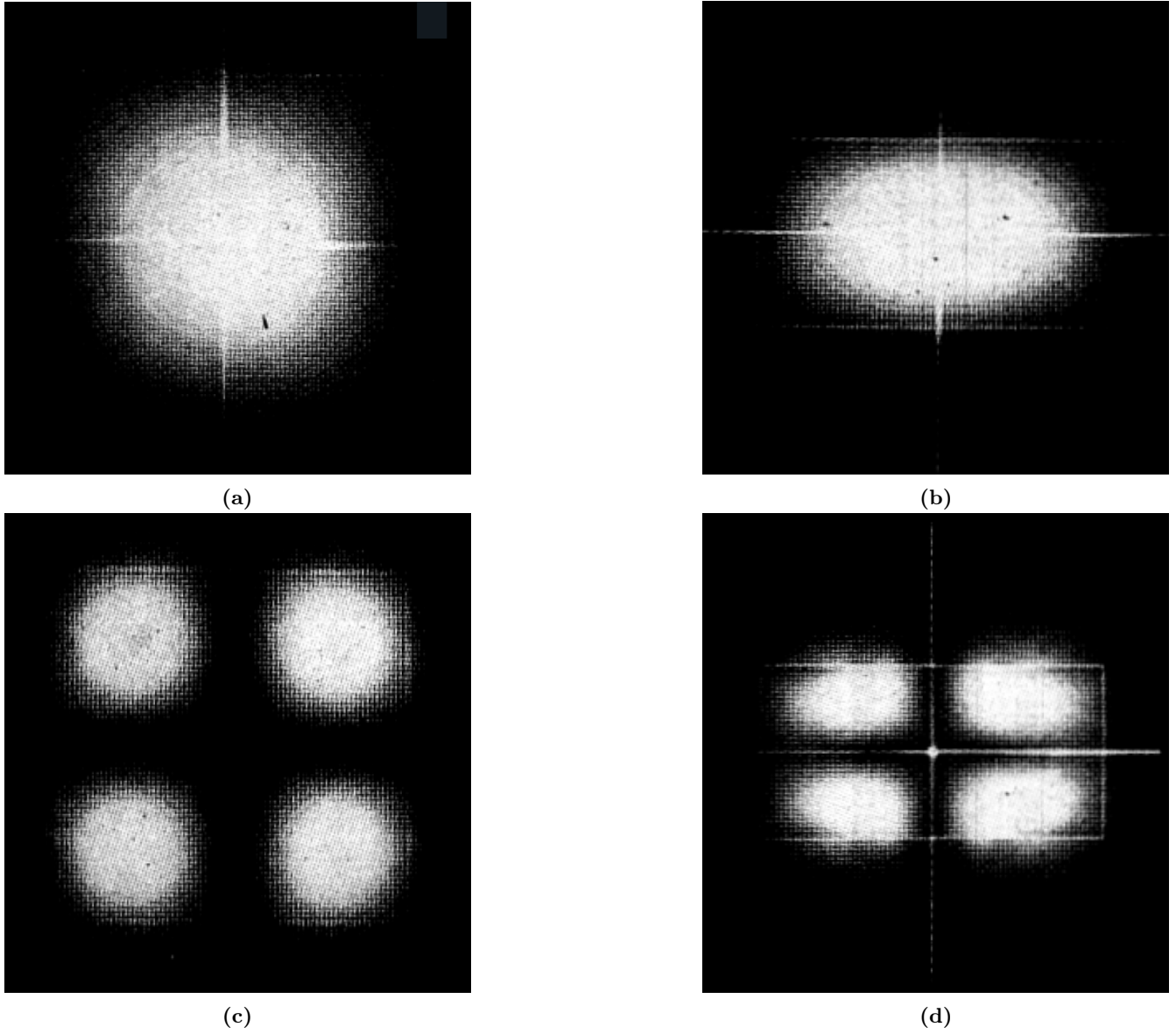


**Figure 1.11:** Intensity profiles of  $E_{11}^y$  (up) and  $E_{22}^y$  (bottom) for unity aspect ratio (left) and  $a = 2b$  waveguides (right),  $\Delta n = 0.01$  and  $\mathcal{B} = 3$  [18].

The propagation curves in Figure 1.12 are presented as a plot of the normalised propagation constant  $\mathcal{P}^2 = \frac{(k_z/k_1)^2 - n_1^2}{n_1^2 - n_0^2}$  against the normalized frequency  $\mathcal{B} = \frac{2b}{\lambda_0} \sqrt{\left(\frac{n_1^2}{n_0^2} - 1\right)}$  in for various modes and various  $a/b$  ratios. As presented in this work, they are refractive index independent as long as the difference between the refractive index of the core and the surrounding is small, which is exactly the case for integrated optics.

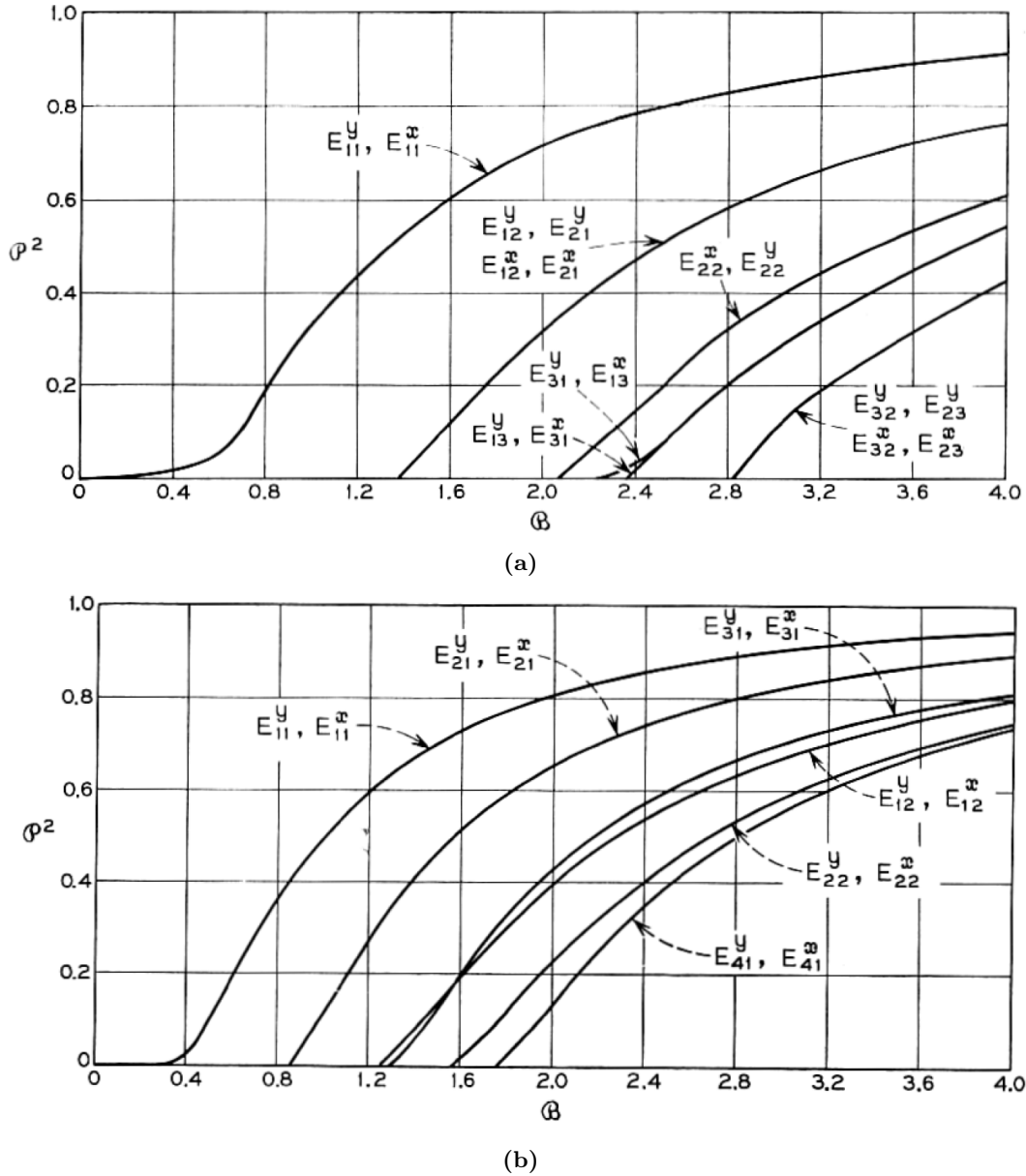


**Figure 1.12:** Propagation curves for the first modes in a waveguide of (a) unity aspect ratio, and (b) for  $a = b/2$ , when  $\Delta n \rightarrow 0$ .

### 1.3.1.3 The effective index method

Conventional effective index method is the most commonly used for analyzing the rectangular waveguides. However, as an approximate method, it produces accurate results only for far-from-cutoff-region. In fact, it is an adjusted version of the Marcatili's analysis where the corner regions are ignored by decomposing the problem into two slab waveguide problems as illustrated in Figure 1.13.

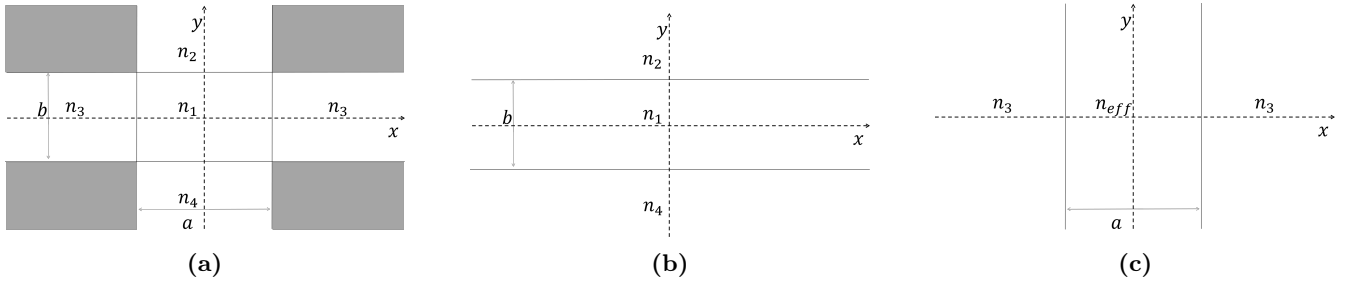


**Figure 1.13:** (a) Configuration of the rectangular dielectric waveguide. (b) A 1-D waveguide with equivalent confinement in the  $y$  direction. (c) An equivalent 1-D waveguide with confinement in the  $x$  direction.  $n_{eff}$  is the effective index of the mode in waveguide (b).

More precisely it consists in creating a first slab waveguide by letting the width  $a$  approach infinity. The propagation constant of this slab waveguide is then used to define an effective index  $n_{eff}$ . A second slab guide, having a core material of refractive index  $n_{eff}$ , is obtained by allowing the height  $b$  of the rectangular waveguide to approach infinity. This later waveguide is considered equivalent to the original rectangular waveguide.

A new effective-index method was introduced by Chiang [20], which has been named the **DEIM**, and showed improved capacity when compared to other approximate and iterative methods. as it will be shown in comparison with marcatili's method in the next section.

#### 1.3.1.4 Comparison of Marcatili's approximation with other methods

To be able to derive closed form solutions to the propagation constants, Marcatili has in fact done 2 major approximations:

- Ignoring the matching of the fields along the corner regions in order to derive a first set of transcendental equations.
- Consider that  $k_x$ , and  $k_y \ll k_z$  in order to transform the transcendental equations into the closed form equations presented in Section 1.3.1.1

Many references [20, 25] have evaluated the error introduced by the first approximation through comparing the results of Marcatili's transcendental equations with other approximate methods such as Goel's circular harmonic approximation, the **SEIM** and the **DEIM** as seen in Figure 1.14a and with the finite elements as well as presented in Figure 1.14b.

Ignoring the corner regions has resulted in an overestimation of the cutoff frequencies of all the modes. More specifically, this induced a relatively big disparity for the fundamental  $E_{11}$  mode cutoff frequency. For the degenerate  $E_{21}$  and  $E_{12}$  cutoff frequency, a 5% difference exists between Goel and Marcatili. In addition, for the values of the normalised waveconstant  $\mathcal{P}^2 > 0.5$  Marcatili's approximation aligns well with all of the other methods. Goel's approximation remains the most accurate when compared to experimental results [26]. The DEIM agrees perfectly with this later approximation and with the finite element method as seen in Figure 1.14.

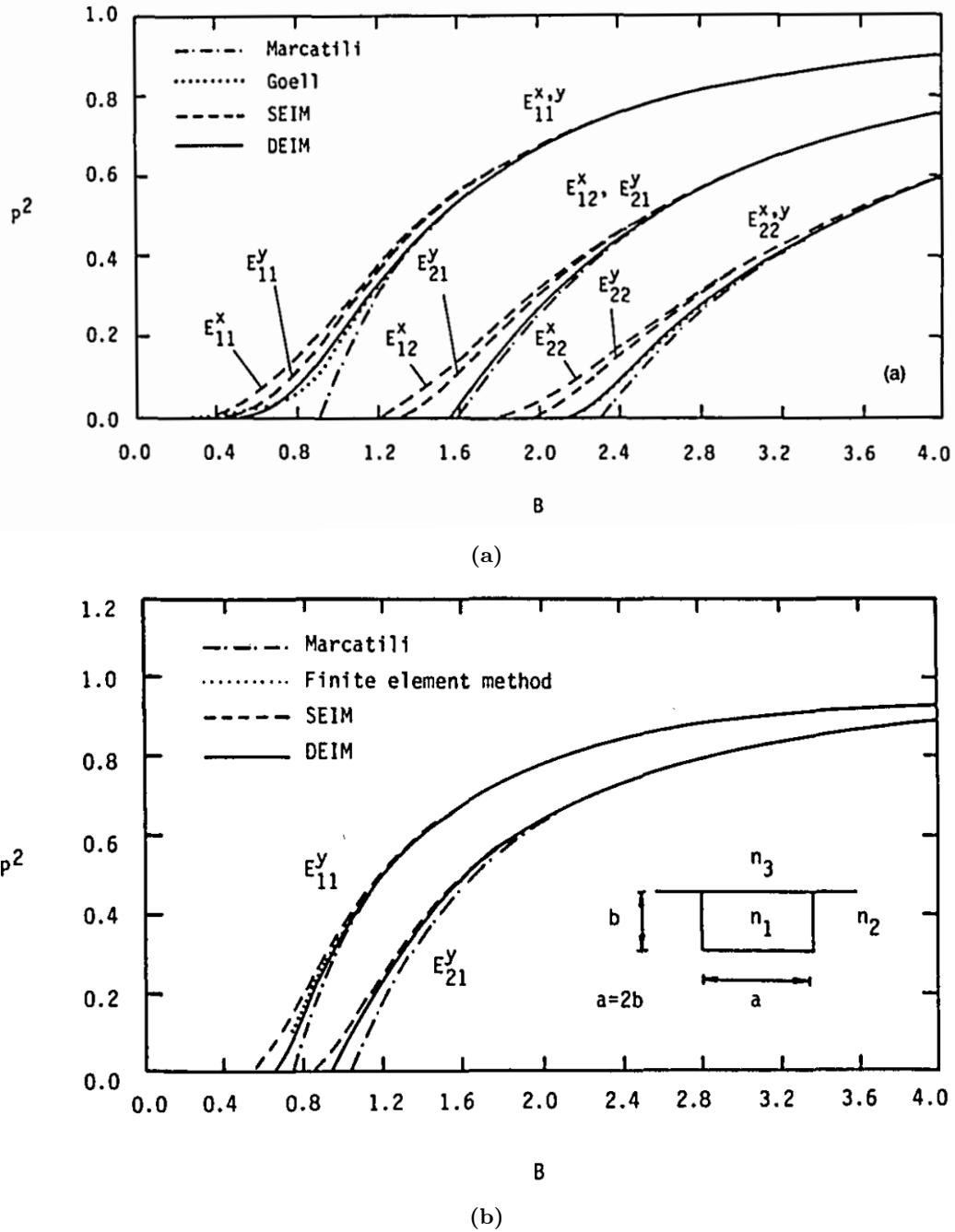
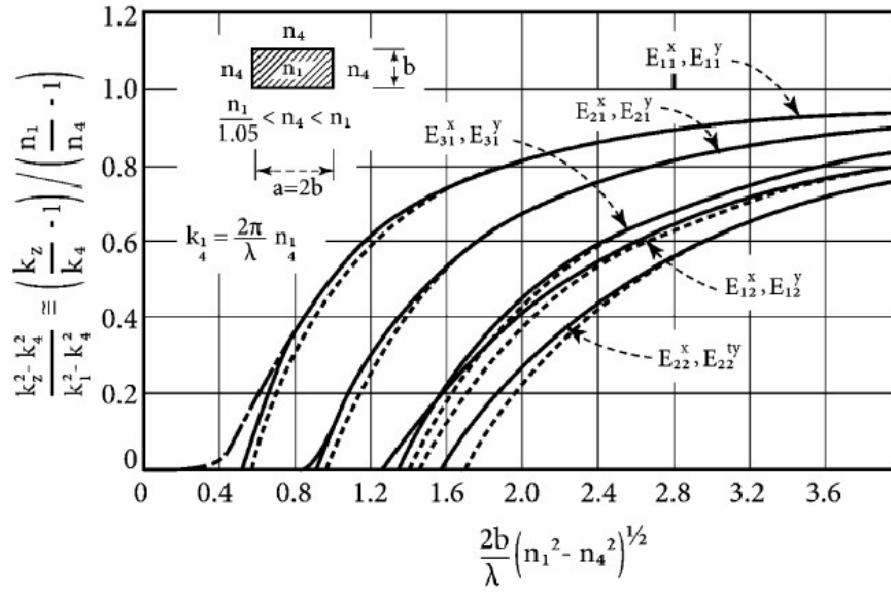
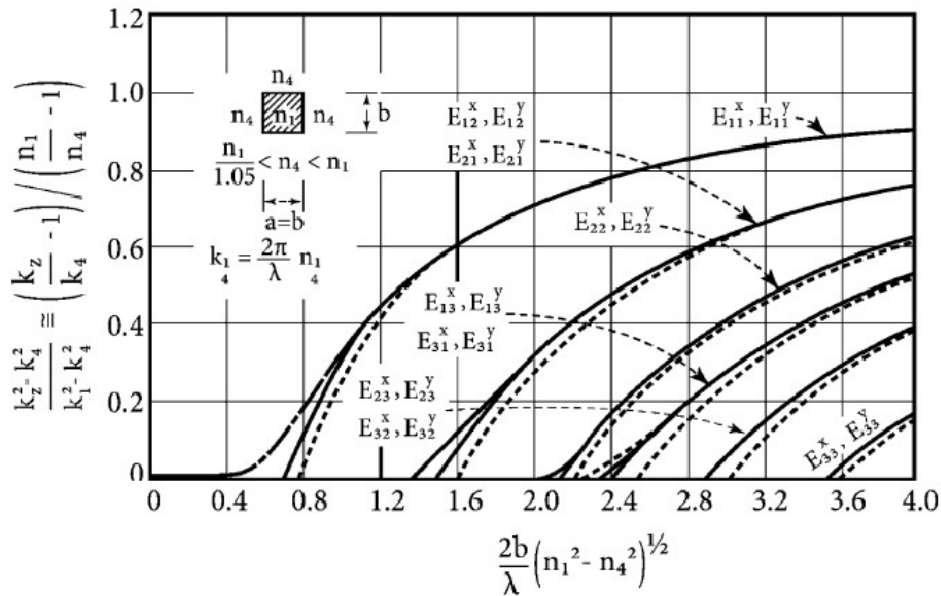


**Figure 1.14:** (a) Comparison between different approximations, of the dispersion curves for a square dielectric rod in air with  $n_1 = 1.5$  and (b) Comparison between Marcatili's approximation and other methods for a rectangular waveguide with  $a = 2b$  and surrounded by different media [20].

The second approximation taken into account, introduces a slight additional error when compared to the transcendental equation solutions as analysed by Marcatili himself, and as presented in Figure 1.15.



(a)



(b)

**Figure 1.15:** Propagation constant for different modes and waveguides geometry: (a)  $a = 2b$  and (b)  $a = b$ . Solid lines represent Marcatili's transcendental equation solutions. Dashed lines represent Marcatili's closed form solutions. The dot-dashed lines represent Goell's computer results.  $n_1^2/n_4^2 = 1.1$ . Edited from [17].

Nevertheless, the approximate dispersion relations derived by Marcatili are very useful especially for experimenting or preliminary studies. This is due to their simplicity and the fact that the dielectric media surrounding the four sides of the rectangular core may have different dielectric constants, which is not the case for Goell's method for example.

### 1.3.2 Losses in optical waveguides

Losses in integrated circuit waveguides can drastically limit the efficiency of the device. They result from multiple sources and can be divided into two types:

- Intrinsic losses that are directly related to the waveguide material and they are mainly propagation losses.
- Extrinsic losses that are leaks of light outside the waveguide caused by deformations or discontinuities, these include: coupling and bending losses.

#### 1.3.2.1 Propagation losses

In general, a wave propagating in a dielectric undergoes losses. This is a result of absorption and scattering phenomena in the core material, and it involves an attenuation  $\alpha$  expressed in dB per unit of length, such that the power  $P_L$  transmitted to a distance  $L$  is expressed with respect to the power  $P_0$  coupled into the waveguide as:

$$\frac{P_L}{P_0} = 10^{-\frac{\alpha L}{10}} \quad (1.23)$$

The attenuation  $\alpha$  can be attributed to multiple sources depending on the wavelength at which the waveguide operates:

- Absorption losses in the infrared region that might be attributed to molecular resonances, both in the dielectric bonds as well as in unwanted species, such as O-H bonds' peaks around  $1,39 \mu m$  for silica fibers as roughly illustrated in Figure 1.16.
- Rayleigh scattering losses in the visible, mainly due to non-homogenities of waveguide core and at the channel walls. It follows a  $\lambda^{-4}$  decrease which explains its dominance in the visible range, and it increases with the index step as explained in [27].

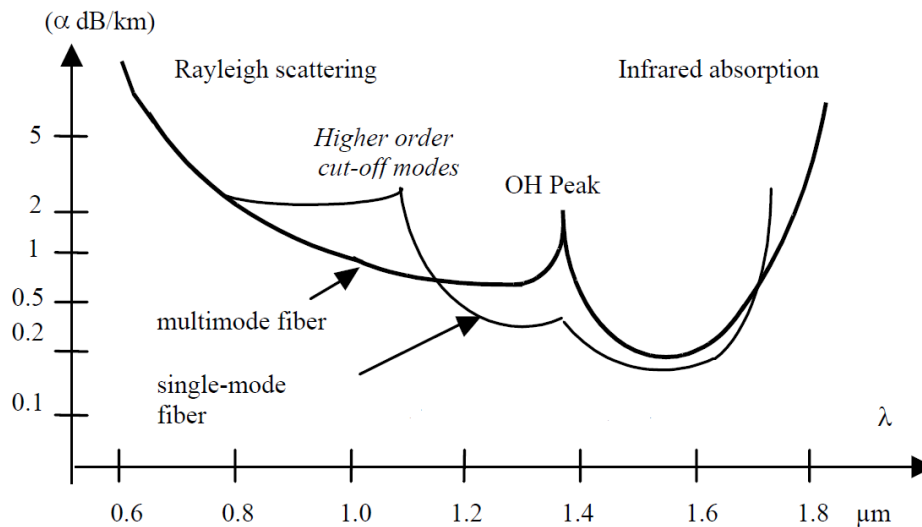


**Figure 1.16:** Intrinsic attenuation of silica optical fibers, edited from [27].

It is important to estimate the mode propagation losses in channel waveguides when using them in integrated optical circuits or devices. One of the most widely used to measure the total transmission loss in single mode waveguides, is the cut back method.

### 1.3.2.2 Coupling losses

Losses due to coupling occur whenever there is a need for interconnects between different components. For integrated optical circuits they are limited to the coupling in and out of the circuit, but they constitute a major part of losses involved in integrated optics. Losses at the connections are due to:

- Fresnel reflection at the air-core interfaces.
- Loss caused by parameters mismatch: modes, geometries, and numerical apertures of the waveguides .
- Loss caused by poor positioning of the fiber with respect to the waveguide.

When edge coupling light from an optical fiber to a waveguide and vice versa, the coupling can be enhanced in multiple ways:

- matching the refractive index of the fiber and the waveguide core materials
- using a waveguide coupler such as a tapered entry waveguide [28] as the one illustrated in Figure 1.17, of width equal or slightly larger than the fiber diameter. The same strategy can be undertaken at the exit facet of the circuit.

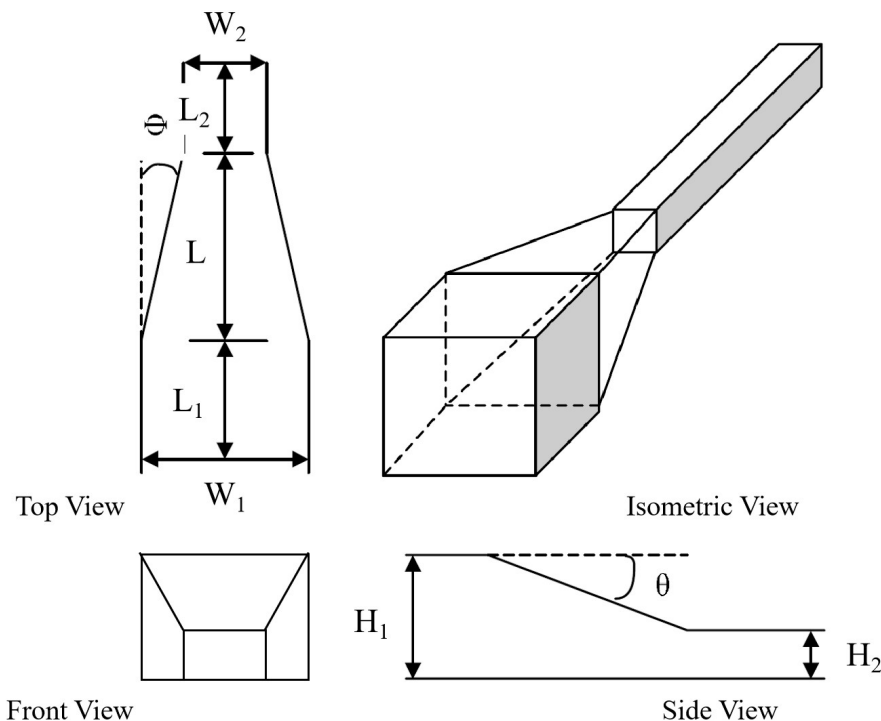


**Figure 1.17:** Geometry of a 3D linear waveguide taper. Edited from [29].

### 1.3.2.3 Bending losses

Since the dielectric waveguide is an open structure, radiative losses out of the waveguide may occur at angles and bendings. Most of the power will remain guided in the structure when the mode is well contained even if a gentle bend occurs.

Knowledge of bend losses is crucial for designing densely packed and complex optical circuits. An early contribution to the understanding of bending losses is a paper by Marcatili [30] on curved slab and rectangular waveguides, that appeared due to the need to implement complex optical circuitry elements. The attenuation of any dielectric waveguide of rectangular cross section as the one illustrated in Figure 1.18 is strongly dependent on the radius of curvature:

$$\alpha_c = M \exp\left\{\frac{-\lambda_z^2 R}{6\pi^2 |\eta_3|^3}\right\} \quad (1.24)$$

where  $M$  is independent of  $R$ ,  $\lambda_z = 2\pi/k_z$  is the guided wavelength along  $z$ , and  $\eta_3 = 1/k_{x3}$  is the length over which the field in medium 3 decays by  $1/e$  meaning the penetration depth.

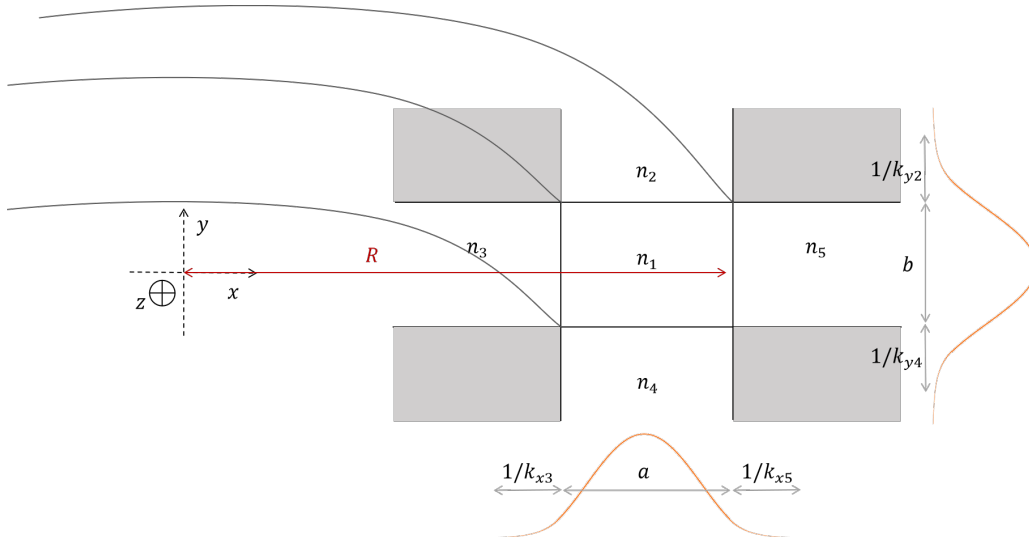


**Figure 1.18:** illustration of a curved dielectric guide.

This can be formulated as well in more experimental terms [31] as:

$$\alpha_c = K \exp\left\{-k_z \left(\frac{2\Delta n_{eff}}{n_{eff}}\right)^{3/2} R\right\} \quad (1.25)$$

Where  $\alpha_c$  is expressed in  $dB$  per unit length,  $K$  depends on the refractive indices of cladding and core and on waveguide thickness, and  $\Delta n_{eff}$  is the difference between the modal effective index  $n_{eff}$  and the cladding index.

Among many cases, Marcatili considered a waveguide with  $n_5 = n_3 \cong n_1$ , the height  $b = \infty$ , the width  $a$  is the maximum allowed for single mode propagation ( $\frac{2a}{\lambda}(n_1^2 - n_3^2)^{1/2} = 1$ ), and the attenuation per radian  $\alpha_c R = 0,087 dB$ . In this case, unless the index step is larger than 0.01, the radius of curvature  $R$  becomes uncomfortably large as seen in Table 1.2. If in addition  $b$  was not infinite, the values for  $R$  must be multiplied by an additional factor.

$\Delta$	$\frac{a}{\lambda}$	$\frac{R}{\lambda}$
0.1	0.745	30
0.01	2.36	1060
0.001	7.45	37000

**Table 1.2:** Dimensions for different values of  $\Delta$  assuming that the height  $b$  is infinite and  $n_3 = n_1(1 - \Delta)$ . Reproduced from [30]

Experimental losses in silica monomode waveguides at a wavelength of 1550 nm have shown that in order to have bend losses less than 0.1 dB it is necessary to keep a large radius bend [32]. For example, a refractive index difference of 0.25, 0.45 or 0.75, requires a bend radius of 25, 15 or 5 mm, respectively [33].

As a qualitative summary bending losses can be reduced most importantly by increasing  $\Delta$ . It can also be reduced in single mode waveguides by choosing the waveguides dimension that allow the best field confinement, meaning to increase them as much as possible while maintaining single mode operation.

### 1.3.3 Single mode propagation

Modes are orthogonal solutions of the wave equation. Depending on the normalised frequency of the waveguide at a certain wavelength, a waveguide is able to propagate one or more modes, and is subsequently named single or multi mode waveguide. So in contrast with multimode waveguides, single mode waveguides can only contain and propagate one mode, that is usually the fundamental mode. If the fiber-guide alignment is correct this wave travels straight down the middle without reflecting off the core cladding interface.

#### 1.3.3.1 The interest in single mode propagation

The interest in single mode propagation arises from multiple sources: first there are the many known conveniences of single mode propagation in the telecommunication that are also beneficial in the context of LoCs, and second there are some other aspects that are proper to LoCs for manipulation.

Each mode (or each group of degenerate modes) is characterised by its own propagation constant thus its own group velocity. As such in multimode waveguide, some modes may have a certain delay with respect to other, this phenomenon known as intermodal dispersion (or modal dispersion) results in the spreading of the pulse constituted of multiple modes. Intermodal dispersion is not present in single mode waveguides thus resulting in the transmission the signal without any temporal distortion.

In addition, the attenuation coefficient in glass waveguides depends on the scattering and absorptions that occur in the core as well as in the cladding materials. Since each mode has a different penetration depth into the cladding, and travels different effective distances in the guide, the attenuation becomes mode dependent. Thus the mode that travels the shorter distance is less prone to attenuation. As such, the fundamental mode have smaller attenuation than higher order modes [34].

More over, the total energy coupled into the waveguide is carried by the many modes that the waveguide hosts. Therefore, if only the fundamental mode propagates in the guide, all the power will be concentrated in this one mode. For optical manipulation, since the propelling force is proportional to the energy transported and coupled into the waveguide as we will see later on, the presence of a single mode that concentrates all the coupled power, is convenient for propelling a particle along a waveguide.

Finally, the presence of a single fundamental mode is indeed important, nevertheless the existence of few higher order modes can be beneficial for implementing optical mode beating traps [28]. What is important above all, is the ability to control the channels dimensions with accuracy in order to be able to control the number of modes that propagates in the waveguide and subsequently be able to master the particle propulsion or trapping along the guide.

### 1.3.3.2 Waveguide dimension requirements for single mode propagation

For any of the bound modes, the associated wave becomes unguided when the field extends to infinity outside of the guide. This occurs when the longitudinal propagation constant  $k_z$  of the waveguide equals the free-space propagation constant in the surrounding material. The frequency at which a wave becomes unguided is known as its cutoff frequency, or mode cutoff.

In order to set the dimension required to conceive a single mode waveguide channel which supports the propagation of the  $E_{11}$  modes, we need to examine the cutoff frequency of the higher order mode. As seen in Figure 1.15, a waveguide with  $a = 2b$  immersed in a dielectric having a refractive index contrast of around  $3.10^{-2}$  with the core material (contrast is defined as  $n_1^2 - n_4^2$ ) can operate as a single mode guide, for values of the normalised frequency less than 0.9 approximately. This will result in a  $5 \times 2.5 \mu m$  dimensions at around  $635 nm$ .

## 1.4 Optofluidics: the interaction between optics and fluidics

The earliest demonstrations of optofluidics were macroscale liquid-enabled optical devices. For example, as early as 1840's Giovanni Amici [35] introduced oil immersion microscope lens and a decade later water immersion objective [36], in order to minimise the optical aberration. This technique is still being used until these days and other sorts of fluid immersion microscope lenses [37] exist on the market because they are known to increase the resolution by increasing the numerical aperture of the objective. Liquid mirror telescope lenses [38] are popular as well because of their extremely reduced cost, smoother interface and configurability compared to their solid counterparts. Dye lasers [39] have the same advantages of telescope liquid mirrors and are an example of a system that can exist on both scales. Furthermore, liquid spectrophotometry, a classic example of optics-matter interaction falls in the realm of optofluidics as well.

For the sake of clarity, and since our aim is to address on OMLoCs we wish to tackle the subject of microscale interactions. A great interest was granted to miniaturised optofluidics in the early and mid 2000's with the efforts to fuse planar optics and microfluidics to produce tunable photonic crystals [40], Bragg grating feedback lasers [41], ring resonator dye lasers [42], ring resonators biosensors [43] and optofluidic transport in liquid core waveguides [44]. However this light fluid synergy has been subject to implementation since early 1970's, in the work of Ashkin for the

acceleration, trapping and deflection of particles using radiation pressure [45, 46].

This area of research appears to be a true manifold, but in fact, researchers were able to put a sense of order into it by arranging the possible outcomes of such integration into groups. In his famous review article on optofluidics [47], Psaltis has chosen to group the different applications based on the phases of the existing media in which the interaction happens, resulting in 3 different categories:

- Structured solid-liquid hybrids,
- Complete fluid based systems,
- Colloid based systems (solids in fluids).

However, to allow the reader to draw a global picture of the optofluidic applications' nature, a more appropriate categorization method was proposed in a review article by Monat et al. [48] and emphasized later on in Hawkins and Schmidt's Handbook of Optofluidics [13], in which fluid-light interaction can be exploited in two different ways as illustrated in the diagram 1.19.

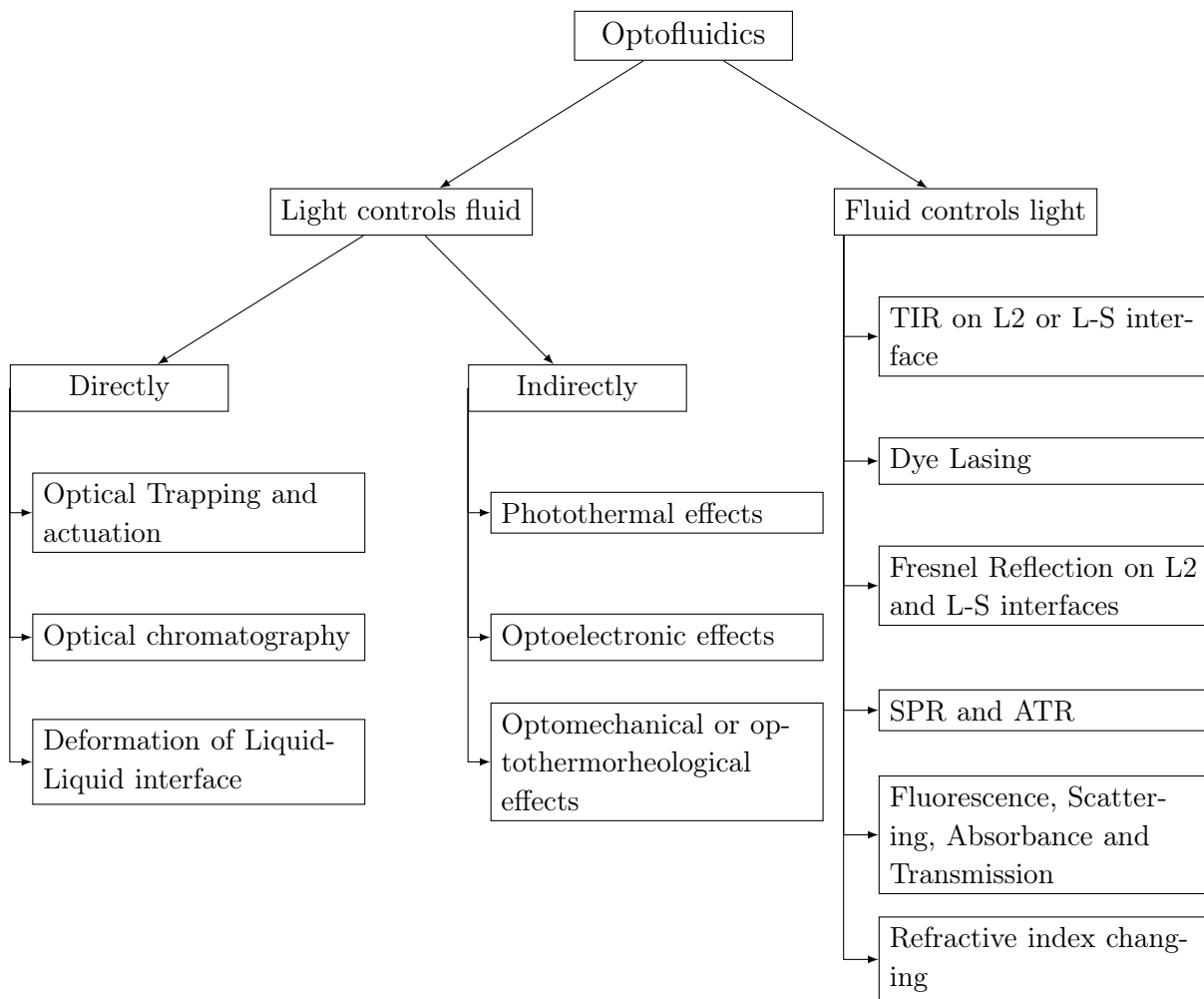


**Figure 1.19:** Roadmap to optofluidics. L2 is Liquid-Liquid, L-S is Liquid-Solid, SPR is Surface Plasmon Resonance and finally ATR is Attenuated Total Reflection.

- Either microfluidic transport phenomena could be exploited to control light propagation and emission in a reconfigurable manner or to change optical properties like refractive index, gain, and nonlinearity, on millimetric length scale,
- or conversely light can be used to actuate and analyze fluids, or trap and deform particles within a fluid.

This second aspect of the fluid-light interaction interest us the most, especially the optical manipulation of fluids and particles. This will be the subject discussed in the rest of this chapter.

### 1.4.1 Optics Enabled LoC Manipulation

Optofluidics has flourished and developed on the micro scale because it responded to LoC's essential need for integration: optical source integration through dye microlasers, signal amplification through microresonators, and on-chip optical detection and sensing. Bulk optical instrumentation (lenses, objectives, mirrors and even lasers) can be simply replaced through an integrated optical layer on chip. In this way, we get rid of the massive benchtop instruments, that eliminates many of the LoC advantages, which paves the way for increased device portability. Another reason for this success is the fact that certain aspects of this integration are more useful on the microscale, notably the use of optical forces for single molecule and mass manipulation.

Fluids and particles manipulation is an essential lab on chip function. Biology and biochemistry have both found a great interest in microfluidic based single and multiple particle manipulation, for both fundamental and applied research. Applications may include for example: isolating single particles such as DNA molecules [49] in order to analyse them, being able to manipulate single blood cells in order to study their elasticity [50], extracting the least abundant cells for diagnosis of diseases such as cancer [51], and HIV [52].

In a counterintuitive manner, fluids' behavior on this scale is marked by the interesting ability to exploit electrokinetic effects, optical, and acoustic nano forces. These later forces enable the implementation of on chip fluid actuators [45], mixers [53–55], traps [56], and cell sorters [57] for example.

High spatial resolution, and adjustable trap size along with low energy requirements, and the ease of on chip integration are the most important characteristic that influence the popularity of a manipulation technique. In order to respond to lab on chip needs, each one of the above cited techniques has its place in the art. Acoustic manipulation remains one of most nondestructive manipulation technique <sup>3</sup> [58]. Electrokinetic manipulation remains one of the easiest to implement on a chip through the integration of electrodes [59, 60]. Conventional optical tweezers (CTs) provide the highest degree of spatial resolution, but they suffer from high energy consumption and the bulkiness of their setup.

Direct optical control only became experimentally possible after the invention of lasers in the 60's. Traditional optical tweezers, or traps are created by using a high numerical aperture (NA)

---

<sup>3</sup>The order of magnitudes of powers ( $10^{-2} - 10 W/cm^2$ ) and frequencies (1 kHz to 500 MHz) that are employed are around those for ultrasonic imaging which are safely and widely used in diagnosis.

objective to tightly focus a laser beam, in order to create a region in space where a micro-metric particle will experience a force due to transfer of momentum from the scattering of photons. These CTs were first demonstrated to be useful for trapping particles, atoms, and molecules by Arthur Ashkin [45,46,61], who recently received the Nobel prize in 2018 for his work on this matter. Optical chromatography, appeared a couple of years later and exploited optical forces of loosely focused lasers for cell sorting applications [62–64]. Deformation of Liquid-Liquid ( $L_2$ ) interfaces was also reported, enabling droplet fabrication, menisci creation [65–67] and optically induced cavitation bubbles [68–70].

Optical trapping and actuation on both metal and dielectric particles can be implemented using electromagnetic forces. In order to do that an interplay between the gradient forces and the propelling forces is necessary. As seen in Figure 1.20 these traditional optical tweezers/actuators approach utilizes bulky, and delicate experimental setup, which is expensive and not adapted for full integration on a chip.

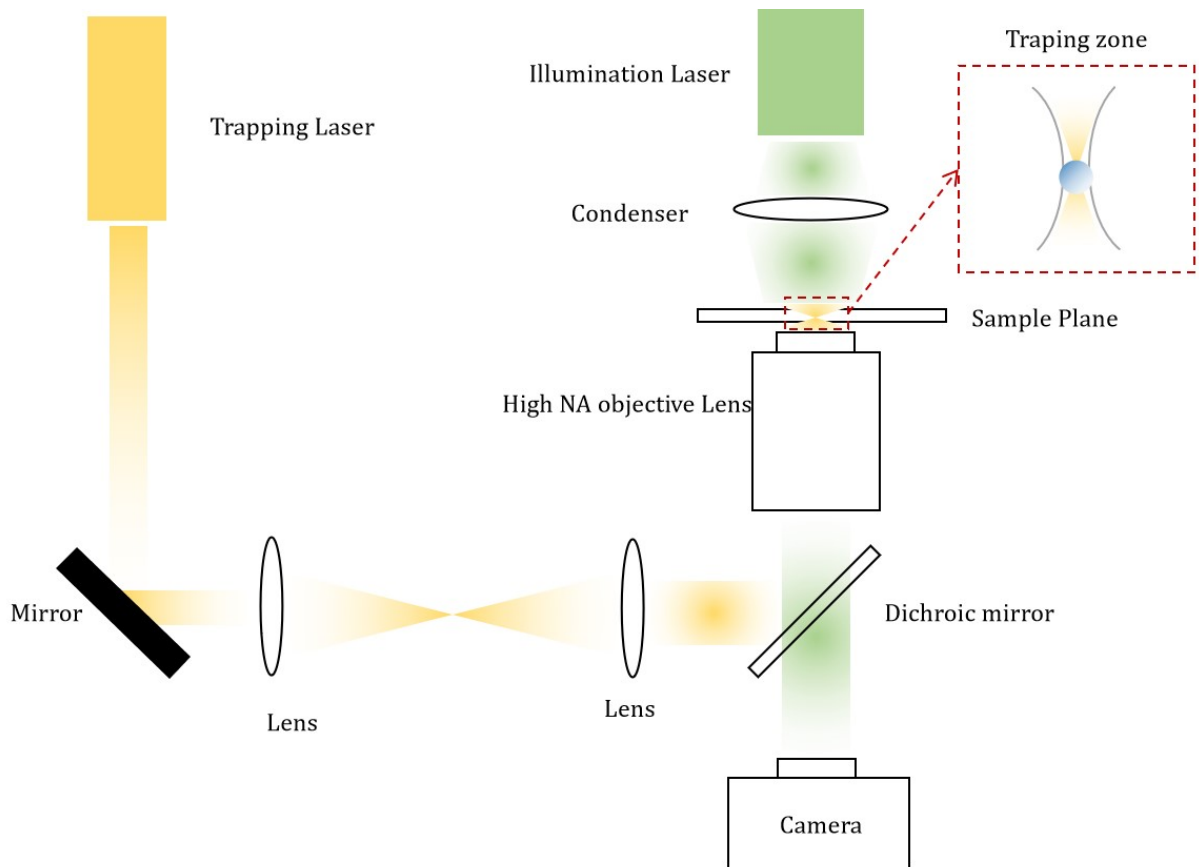


**Figure 1.20:** An example of an experimental setup of a traditional optical tweezer.

Also, these devices are only capable of implementing one trap at a time, which limits their throughput. Among the disadvantages of far field optical tweezers is the diffraction limit imposed by the  $NA$  of the objective and the wavelength<sup>4</sup>, resulting in an optically unresolved trap. As such, trapping nanometric samples becomes challenging. Needless to say that this setup very often

<sup>4</sup>The spatial resolution is usually taken to be  $0.61\lambda/NA$ , even for UV light, a lens is limited to the resolutions of around 200 nm [71]

requires high laser power, resulting in undesirable and irreversible thermal damage to biological samples. For applications dealing with biological samples, IR lasers should be used in order to offer a low damage manipulation of living cells and this will limit the resolution.

In order to solve the scaling problem as well as the high energy consumption and the full on chip operation, optical manipulation has lately found a solution in the evanescent field forces [28, 72], as schematically illustrated in Figure 1.21. This will be the main focus of the following sections.

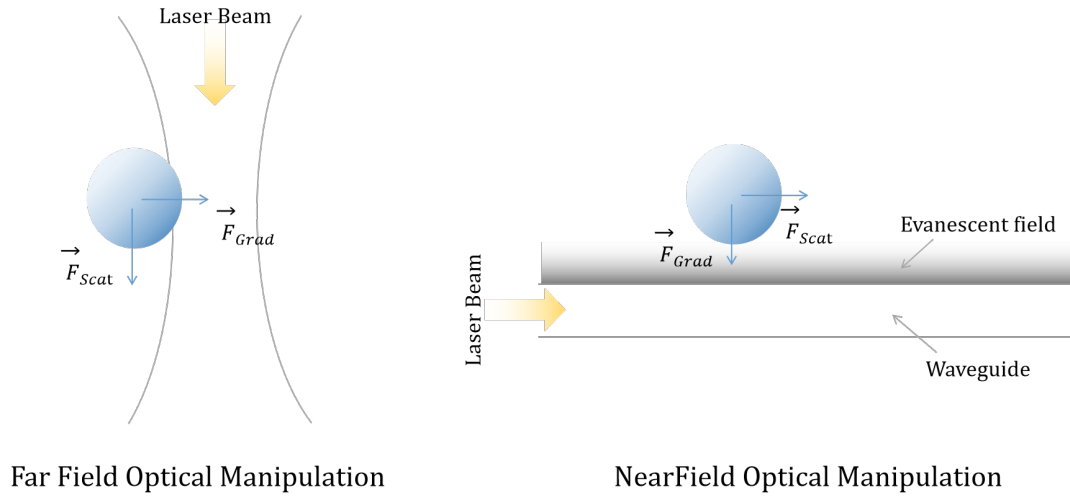


**Figure 1.21:** Schematic comparison between far field and near field optical manipulation.

## 1.4.2 Theory: Analytical Solutions and Numerical Simulations

Optical control applications might vary, however they basically rely on the same governing equations. Simply put, a light beam carrying momentum and energy can be used to directly move, trap, or waveguide a particle and is subsequently able to deform an L2 interface.

For a better understanding of the mechanisms by which optical forces act on an object, we will present the general equations that can describe a standard but simplified optical manipulation problem on a chip. We consider a spherical particle of radius  $a$  and refractive index  $n_3$  in the evanescent field of an electromagnetic wave created by total internal reflection on the interface between two medium of refractive indices  $n_1$  and  $n_2$  as seen in Figure 1.22.

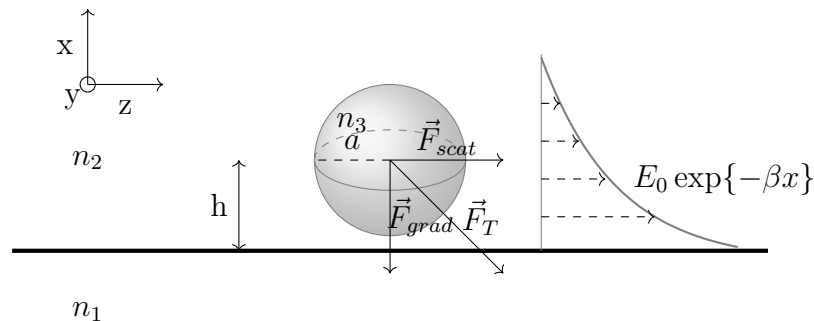


**Figure 1.22:** Schematic drawing of a sphere of radius  $a$  in the evanescent field of an optical waveguide.

To understand the underlying physical quantities, analytical equations are necessary along with the decomposition of the force into two components (Figure 1.22):

- (1) a scattering force  $\vec{F}_{scat}$ , in the direction of light propagation, thus in the  $z$  direction according to Figure 1.22.
- (2) a gradient force  $\vec{F}_{grad}$ , in the direction of the spatial light gradient, thus in the  $x$  direction according to the same Figure.

This results in a more direct relation between the force exerted and the experimental parameters such as the laser power and wavelength, the particles dimensions and refractive index as well as the medium's refractive index.

Let us first of all define the dimensionless size parameter  $\alpha = \frac{2\pi a}{\lambda_2}$ , representing the ratio of the particle radius  $a$  to the wavelength of the electromagnetic radiation  $\lambda_2$  in medium 2. Three regimes of interaction can be identified based on this ratio of particle dimension to the wavelength of manipulation:

- Rayleigh Regime: for ( $\alpha \ll 1$ ) hence for particles smaller than the wavelength. The theory for the evaluation of each one of them separately is based on electromagnetic model or what is also called the dipole approximation [73]
- Mie Regime: for ( $\alpha \gg 1$ )<sup>5</sup> hence particles larger than the wavelength, the calculation can be simplified by the use of ray optics [74, 75].
- Lorenz-Mie Regime: for ( $\alpha \sim 1$ ) when particle size is comparable to the wavelength of light, the generalised and more complex Lorenz-Mie theory must be applied.

#### 1.4.2.1 Rayleigh regime

For a spherical particle whose size is much smaller than the wavelength of light, the electric field induces an electric dipole moment in the object that is pulled toward the focus by intensity gradients of the electric field of light. Ng and coworkers have studied Rayleigh particle in the evanescent field of an optical waveguide [76, 77].

The time-averaged gradient force, arises from the interaction of the induced dipole with the inhomogeneous field:

$$\vec{F}_{grad} = \frac{2\pi\zeta}{cn_2^2} \vec{\nabla} I_0 \quad (1.26)$$

$$\zeta = n_2^2 a^3 \left( \frac{\left(\frac{n_3}{n_2}\right)^2 - 1}{\left(\frac{n_3}{n_2}\right)^2 + 2} \right) \quad (1.27)$$

where  $I_0$  is the intensity of the incident light,  $c$  is the speed of light in vacuum,  $\lambda$  is the wavelength of the trapping laser and  $\zeta$  is the polarizability of the sphere.

---

<sup>5</sup>Some researchers suggest that the applicability of the Mie Regime can extend to values of  $\alpha$  that are close to 1 [13]

This gradient force is proportional to the intensity gradient, and points either up the gradient when  $\frac{n_3}{n_2} > 1$  or down when  $\frac{n_3}{n_2} < 1$ .

On the other hand these propulsive forces take the form of:

$$\vec{F}_{scat} = \frac{I_0 \eta n_2}{c} \vec{z} \quad (1.28)$$

with

$$\eta = \frac{128\pi^5 a^6}{3\lambda^4} \left( \frac{(\frac{n_3}{n_2})^2 - 1}{(\frac{n_3}{n_2})^2 + 2} \right)^2 \quad (1.29)$$

$\eta$  is the scattering cross section of the sphere.

The scattering force is in the direction of propagation of the incident light and is proportional to the intensity. As we can see from equations (1.28) and (1.26) the scattering and the gradient forces respectively scale with  $a^6$  and  $a^3$ , for particle radius and with  $I_0$  and  $\vec{\nabla} I_0$ , for input power. Clearly, when the particle radius gets smaller more power and power gradient should be deployed.

### 1.4.2.2 Mie Regime

When the Mie scattering conditions are satisfied ( $\alpha > 100$  according to Roosen [78],  $\alpha > 80$  according to Almaas [79]), the problem can be solved by geometrical optics. Large objects act as lenses refracting the rays of light. Walz [80] has investigated the ray optics calculation of the radiation forces exerted on a dielectric sphere at a distance  $h$  of an evanescent field. While keeping in mind that rays in the evanescent field have imaginary refractive angles. When rays strike onto the sphere, a fraction of the beam is reflected and the other is coupled into the sphere where it is subject to multiple internal reflections in the sphere itself accompanied by a transmitted fraction at each encounter with the interface as seen in Figure 1.23.

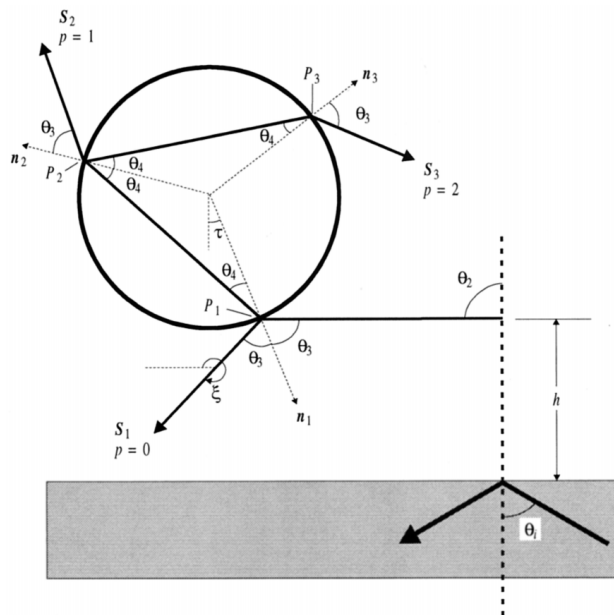


**Figure 1.23:** Schematic definition of the variables used in tracing the path of a ray through the dielectric sphere [80].

Complex angles and contact points must be calculated using Snell's law. After determining these quantities, and as a direct result of the momentum conservation, the total force  $\vec{F}$  is determined by the difference between the rate of momentum of the immersing and emerging rays.

$$\vec{F} = \vec{M}'_{in} - \vec{M}'_{out} \quad (1.30)$$

The rate of momentum contained in a propagating ray of light is related to the power of the ray P as:

$$\vec{M}' = \frac{Pn_2}{c} \vec{k} \quad (1.31)$$

$\vec{k}$  is the unit vector pointing in the direction of propagation of the ray. As a summary we can see that in the Mie regime the force exerted on a particle depends only on the power contained in the beam and the refractive index of the medium.

### 1.4.2.3 Lorentz-Mie Regime

For a particle whose size is comparable to the wavelength, no analytical expression of the force can be deduced and the general electromagnetic formalism should be applied in a simulation context.

Multiple software/programming languages were used in this context: Almaas and Brevik used Fortran for their simulation [79] while Helleso et al. used the RF-toolbox of Comsol [81] and Matlab [82] as well.

As ingeniously explained by Novotny [72] the optical force  $\vec{F}$  acting on the surface S of an object can be computed by integrating either the volume force density  $\vec{f}$  over the total volume or by integrating the Maxwell stress tensor (MST) over the surface of the sphere:

$$\vec{F} = \oint_V \vec{f} dV = \oint_S \mathcal{T}_{ij} d\vec{S} \quad (1.32)$$

Where  $\vec{f}$  is the volume force density, and  $\mathcal{T}_{ij}$  is the MST.  $dV$  is the elementary volume of the particle and  $d\vec{S}$  is the unit vector normal to the elementary surface  $dS$  and pointing outward with respect to the sphere as represented in Figure 1.24.

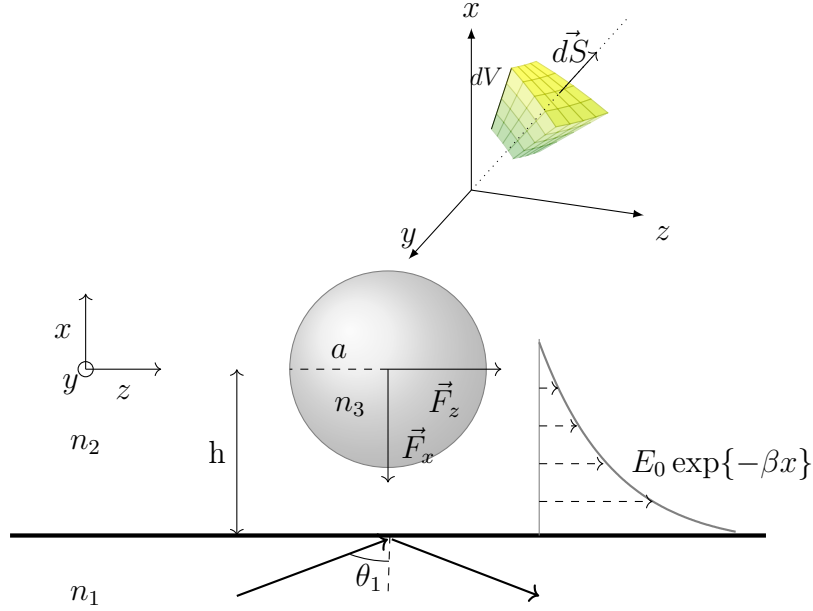


**Figure 1.24:** Schematic drawing of a sphere of radius  $a$  in the evanescent field of an optical waveguide.

$\vec{f}$  in a charge-free nonmagnetic medium, without electrostriction, can be found as the divergence of Maxwell's stress tensor and can be expressed as:

$$\vec{f} = -\frac{1}{2}E^2\vec{\nabla}\epsilon_2 \quad (1.33)$$

where  $\epsilon_2$  is the permittivity of the surrounding medium and  $E$  the electric field decaying exponentially with the penetration depth along the  $y$  axis:

$$E = E_0 \exp\left\{-\frac{2\pi}{\lambda_1} \sqrt{(\sin \theta_1)^2 - \frac{n_2^2}{n_1^2}} x\right\} = E_0 \exp\{-\beta x\} \quad (1.34)$$

With  $E_0$  being the amplitude of the electric field,  $\lambda_1$  and  $\theta_1$  being respectively the wavelength and the angle of incidence in the medium 1.

The MST  $[\mathcal{J}_{ij}]$  represents the density of momentum of the field. It can be written according to the definition proposed by Minkowski in the form:

$$[\mathcal{J}_{ij}] = [\epsilon_2 \vec{E}_i \vec{E}_j^* + \mu_2 \vec{H}_i \vec{H}_j^* - \frac{1}{2} \delta_{ij} (\epsilon_2 \vec{E}_k \vec{E}_k^* + \mu_2 \vec{H}_k \vec{H}_k^*)] \quad (1.35)$$

$\epsilon_2$  and  $\mu_2$  denotes the permittivity and the permeability of the surrounding environment (medium 2), and  $H$  the magnetic field. The notation \* designates the conjugate complex.

Almaas and Brevik [79] have applied this above explained method to the case of a micrometer sized spherical particle in the evanescent field of a waveguide. Their simulation considered a laser power of 150 mW and multiple combinations of refractive indices  $n_2$ ,  $n_3$  (while keeping  $n_1$  at 1.75) for both the parallel (p) and perpendicular (s) polarisation. Their results were presented as plots of nondimensional forms of  $F_z$  and  $F_x$  as a function of the size parameter  $\alpha$ . They all converged to the following explanation for all the combinations used:  $F_x$  being always negative meant an attractive force between the substrate and the sphere and  $F_z$  being always positive meant that the

sphere was being propagated along the positive  $z$  direction. As a rule of thumb the interaction between the sphere and the field is the strongest when the wavelength is of the same order of magnitude as the sphere diameter.

A more recent and elaborate work done by Hellesø [83] considered a dielectric sphere in the evanescent field of a waveguide (Figure 1.25).

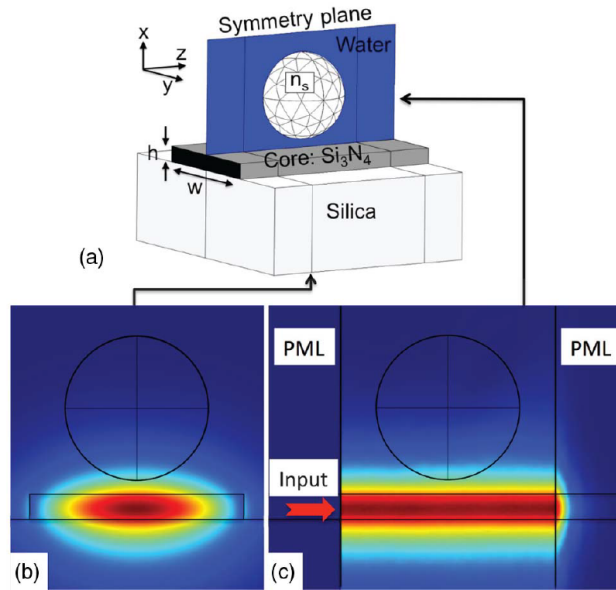


**Figure 1.25:** Outline of the model by Hellesø with (a) sphere 100 nm above strip waveguide and (b) the fundamental TE mode used to excite the waveguide with 1 mW power as shown in (c) as well.

Instead of integrating the Maxwell stress tensor on the surface of the sphere they expressed  $f$  as a function of a quantity called the Abraham-Minkowski surface pressure  $\sigma$ :

$$\sigma = -\frac{1}{4}\epsilon_0 \int_{-a}^a (|E_t|^2 + |E_r|^2) \frac{d\epsilon}{dr} dr \quad (1.36)$$

with  $E_t$  and  $E_r$  being the amplitudes of the tangential and radial components of  $\vec{E}$  with respect to the surface of the sphere. By integrating the local pressure on a particle, the optical force on the particle can be found, giving an alternative to using the MST.

Even though they are mathematically equivalent, the simulation results showed a better agreement with the Almaas and Brevik model (which they named the analytical model) especially for smaller index contrast between the medium and the sphere as seen in the comparison in Figure 1.26. The wavelength used for the simulation was 1070 nm, with a very low input power of 1 mW.

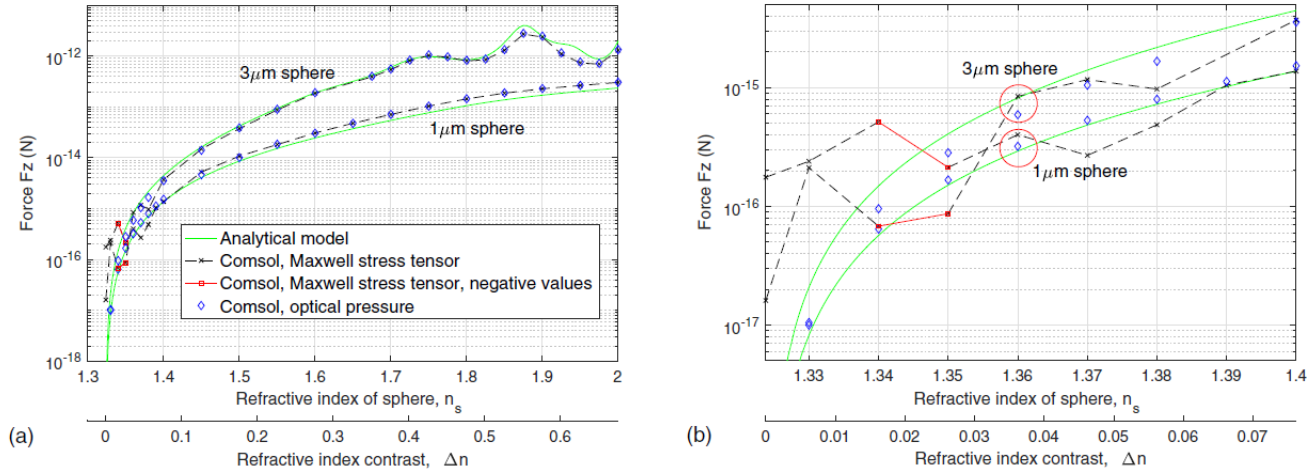


**Figure 1.26:** A comparison between MST and optical pressure for simulation [83]: Simulation results: Radiation force  $F_z$  on 1 and 3  $\mu\text{m}$  spheres for (a)  $n_{\text{water}} < n_s < 2$  and (b)  $n_s < 1.4$ , that is, zoom of (a).

### 1.4.3 2D Optical Manipulation: Actuators

Near field forces were first demonstrated in the early 90's as an alternative to far field optical control. A set of experiments by Kawata and coworkers [84], showed that an evanescent wave created under TIR over the surface of a high refractive index prism, can manipulate micrometer sized particles with the power of 150  $mW$  at 1.06  $\mu\text{m}$ . Later they demonstrated this using an optical waveguide, thus laterally trapping PS spheres with diameters of 1-27  $\mu\text{m}$ , and then longitudinally driving them along the direction of the waveguide channel using an effective power of 80  $mW$  at 1045  $\text{nm}$  [85].

In the 2000s, a series of papers by Ng et al [76, 77] demonstrated for the first time the propulsion of nano sized particles on the surface of a channel waveguide as seen in Figure 1.27a. Gold nanoparticles<sup>6</sup> of diameter ranging from 10  $\text{nm}$  to 23  $\text{nm}$  were used.

In an effort to further decrease the power used for such manipulation, only a 20  $mW$  power IR laser beam was used for the manipulation of cells and dielectric particles on the surface of silicon nitride waveguides [87]. This simple setup is schematically illustrated in Figure 1.27b.

<sup>6</sup>Some researchers may place this case in the realm of what they called direct plasmonic manipulation [86]

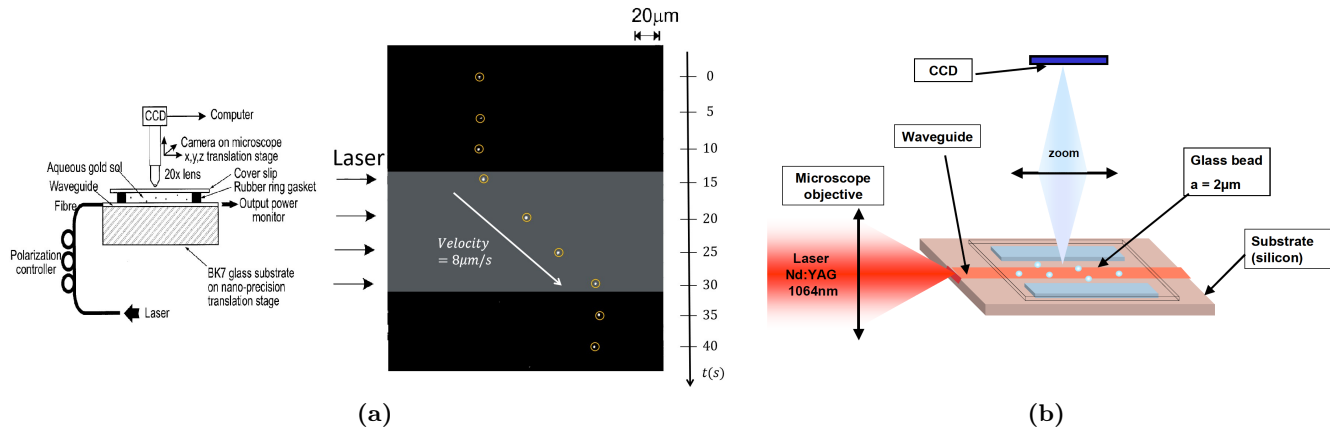


**Figure 1.27:** Examples of near field actuators: (a) The setup for Ng’s experiment (on the left) and a time lapse showing the propulsion of gold nanoparticles (on the right) [77] and (b) a setup for the manipulation of dielectric nanoparticles on the surface of a silicon nitride waveguide [87].

In order to compensate for the high energy requirements, especially when manipulating nanoparticle, slot waveguides<sup>7</sup> were found to be good candidates because they exhibit strong field confinement [88] as illustrated in Figure 1.28b. A standard single mode silicon waveguide with a sub-wavelength slot (usually between 50 nm and 120 nm wide) cut through the middle can concentrate the optical energy in the liquid core region of the waveguide [89] (Figure 1.28a). This setup was used to manipulate 75 nm diameter dielectric particles as well as DNA molecules with a input power of less than 300mW. And it could extend to even smaller particle sizes of around 10 to 20 nm as per their calculation [90].

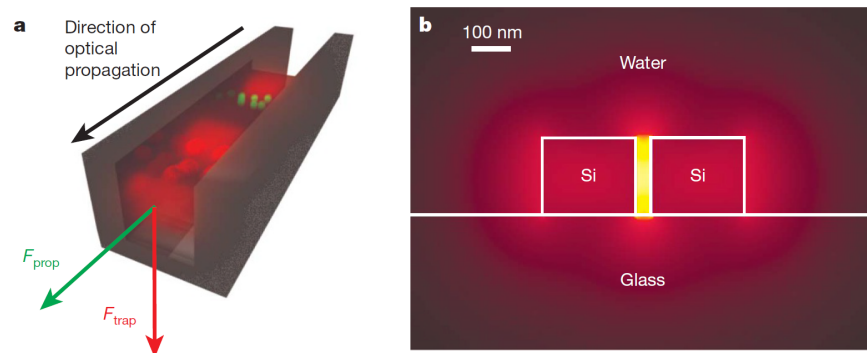


**Figure 1.28:** (a) Schematic illustrating the transport in a slot waveguide and (b) Mode profile for a SOI 40-nm slot waveguide [89]

For a low cost yet high-performing device, an actuation setup formed with an SU-8 epoxy-based photonic structures, combined with poly(dimethylsiloxane) (*PDMS*) microfluidics on a fused silica substrate was used by the pioneers Schmidt and Erickson [91]. This system however suffers from high guiding losses, preventing it from being used for complex devices fabrication such as those fabricated with silicon based platforms.

<sup>7</sup>The structure consists in a nanometer sized low refractive index slot between two region with high refractive index. The whole structure is surrounded by a cladding with low refractive index.

Also, PS microparticles were guided by the evanescent field of a more strongly illuminated, output of a Y branched waveguide produced by Cs<sup>+</sup> ion-exchange in glass [92]. An input laser power of 165mW was used in this experiment, as illustrated in Figure 1.29.

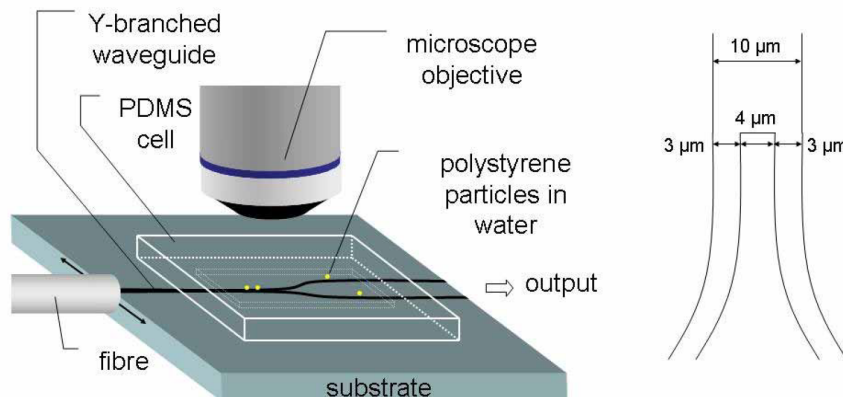


**Figure 1.29:** A schematic view of a Y branched sorter implemented by Grujic [92]. one of the two branches is directed towards the waste disposal and the other towards the sample outlet.

#### 1.4.4 3D Optical Traps/Tweezers

Due to the multiple inconvenient of traditional optical tweezers [93], the experiments of Kawata and coworkers [84, 85] paved the way for near field optical tweezers. Apart from conventional tweezers (*CT*) more sophisticated trapping platforms were later introduced, among which we cite: optical fiber and waveguide traps (*WGT*) [94], resonant cavity traps (*RCT*) [95] and surface plasmon-based optical tweezers (*POT*) [96,97]. These optical traps are of a great interest to LoC applications as they enable contact-less and non-invasive single particle manipulation along a wide range of particles size (Figure 1.30).

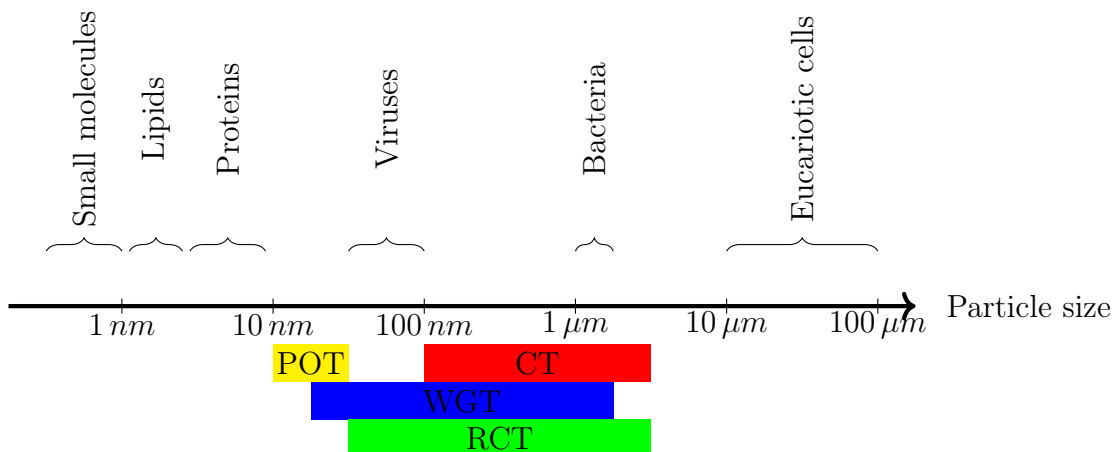


**Figure 1.30:** A scale roughly showing micro and nanometric organisms with the most convenient optical trapping techniques.

### 1.4.4.1 Waveguide traps (WGT)

Waveguide 3D trapping was successfully implemented using standing waves [98]. This device, illustrated in Figure 1.31a was fabricated using silicon waveguides on a silicon-on-insulator (*SOI*) platform, with a microfluidic layer formed by exposing the Si waveguide in the buried oxide. The position of the traps can be adjusted by exploiting the electro-optics effect in silicon waveguides, by the use of integrated microheaters. Recent work also demonstrated the flexibility of near field mode beating in trapping, actuating and positioning nanoparticles along a few mode waveguide [28] (Figure 1.31b). As such, the configuration in which particles can be trapped along the waveguide, depends on the hot spots created by the superposition of the evanescent fields of different modes propagating in the guide. More recently, with the emerging use of femto second laser processing, monolithic chips for manipulation were fabricated in glass [99]. A continuous wave ytterbium fiber laser, at 1070 nm, is used as light source. Trapping is achieved with an estimated optical power at each waveguide output of about 20 mW. This setup however consisted of two counter propagation beams and even though is not an evanescent field trap, it is worth mentioning.

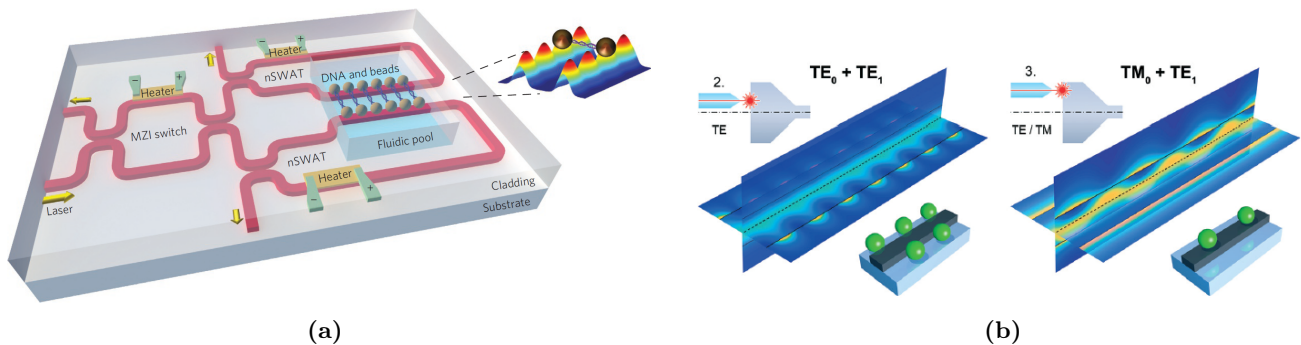


**Figure 1.31:** Different types of waveguide implemented traps: (a) standing wave trap [98], (c) mode beating optical trap [28]

### 1.4.4.2 Resonant cavity traps (RCT)

The strength of optical traps can be improved by exploiting the field amplification within an optical resonator. For example, the trapping of 48 nm and 62 nm dielectric nanoparticles is demonstrated by exploiting the stationary wave within a photonic crystal resonator [95] (Figure 1.32c). Arnold et al [100] demonstrated the trapping and circumnavigation of PS nanoparticles as small as 280 nm in diameter in a circular orbit around whispering gallery mode (WGM) resonators, with a power of around 10 to 50  $\mu W$  (Figure 1.32a). Silicon photonic crystal nanocavities can be used to trap 500 nm to 2  $\mu m$  beads as well as bacteria between the two main anti-nodes located in the central part of the cavity (Figure 1.32b) with a laser power of 31 mW [101]. Another setup consists of implementing an optical waveguide loop with a gap at the centre. The waveguide acts as an optical rail that delivers particles/cells towards the gap where they are trapped. Small gaps (2 – 10  $\mu m$ ) were found to be able to successfully trap single particles with a laser power of around 500 mW, while larger gaps (around 30  $\mu m$ ) enabled the trapping of multiple particles and the optical stacking of additional ones, upon saturation of the gap [102].

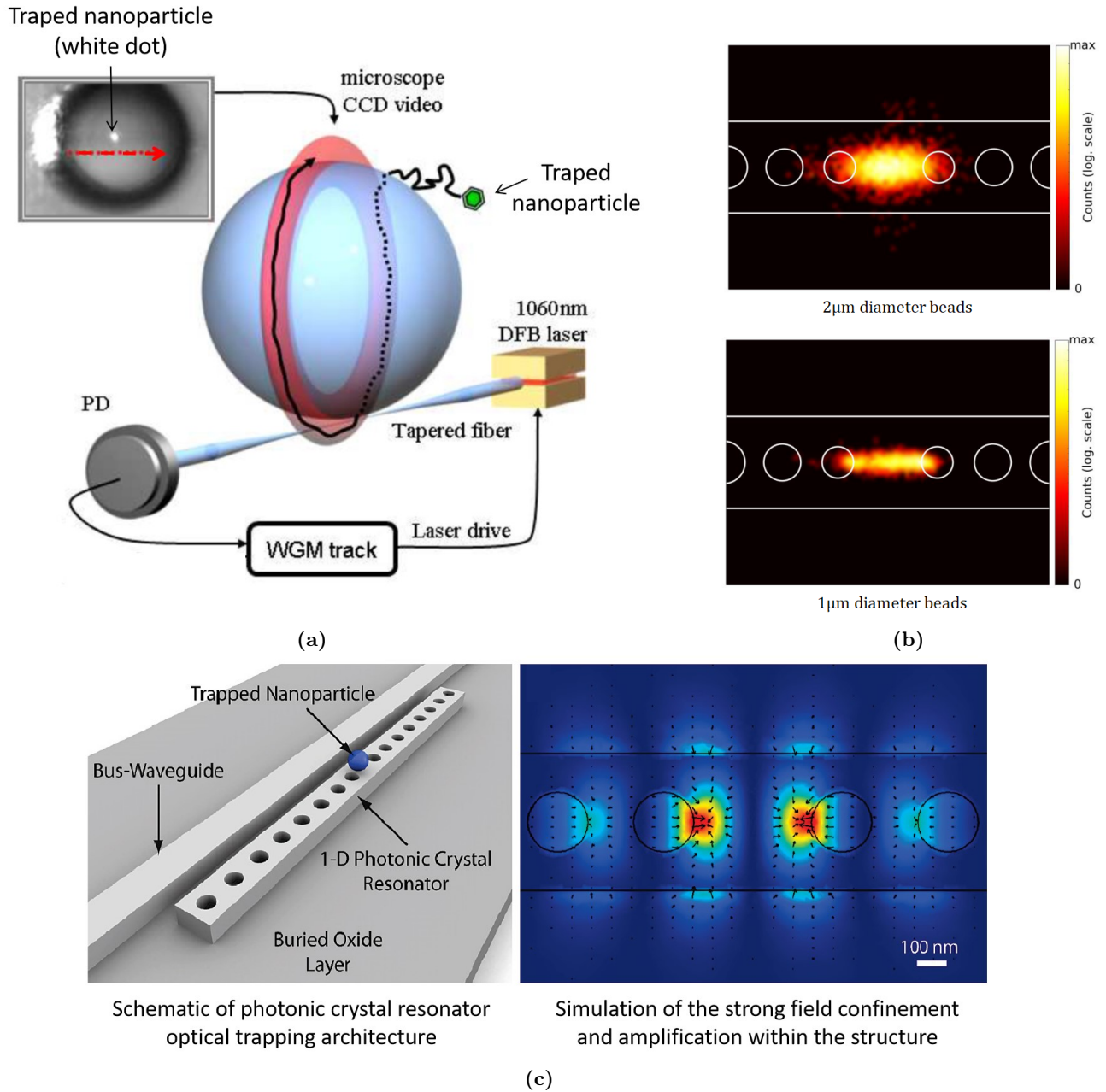


**Figure 1.32:** Examples of resonant cavity traps:(a) Nanoparticle navigating in the direction that light takes within the WGM. The red arrow represents the light path in the cavity [100] (b) a count of particles position in a photonic crystal resonator for different bead diameter [101] and (c) photonic crystal resonators architecture and field confinement [95]

#### 1.4.4.3 Plasmonic Optical Traps (POT)

Plasmonic traps use the unique optical properties of metallic nanostructures to enable the guidance and manipulation of light at the nanoscale using the collective oscillations of delocalized electrons of a metal, called plasmons. Surface plasmons are waves that propagate along the surface of such metal. These Plasmonic nanostructures (*PNS*) that can confine light into subwavelength volumes offer a promising alternative to traditional optical tweezers to overcome the diffraction limit and the high energy consumption.

The first plasmonic optical trap was proposed by Novotny with the intensity gradient generated by the strong evanescent field around a 5-nm radius metal tip [103].

Researchers have since experimentally demonstrated subwavelength optical trapping with various nanostructures such as isolated nanoparticles [104] nanogap antennas [105, 106] and nanostructured films [107] to trap particles using typically a couple of hundreds of mW, extremely lower power than conventional optical tweezers. Grigorenko et al [105] utilized the strongly enhanced and localized optical near-fields of closely spaced metallic nanostructures. Optical trapping of nanoparticles and proteins with resonant coaxial nanoaperture using 10 nm Gap was demonstrated with laser power of only 4.7mW [108]. PS nanoparticles in water were trapped using Au nano-antennas with a laser power of only 5.5mW [109]. These low power traps are shown in Figure 1.33. A concise review article on plasmonic optical trapping and actuation [110] can offer a good first insight into this particular case. In another review on nanoscale optical manipulation [86] a special attention was accorded to the plasmonic effects exploited for particle trapping.

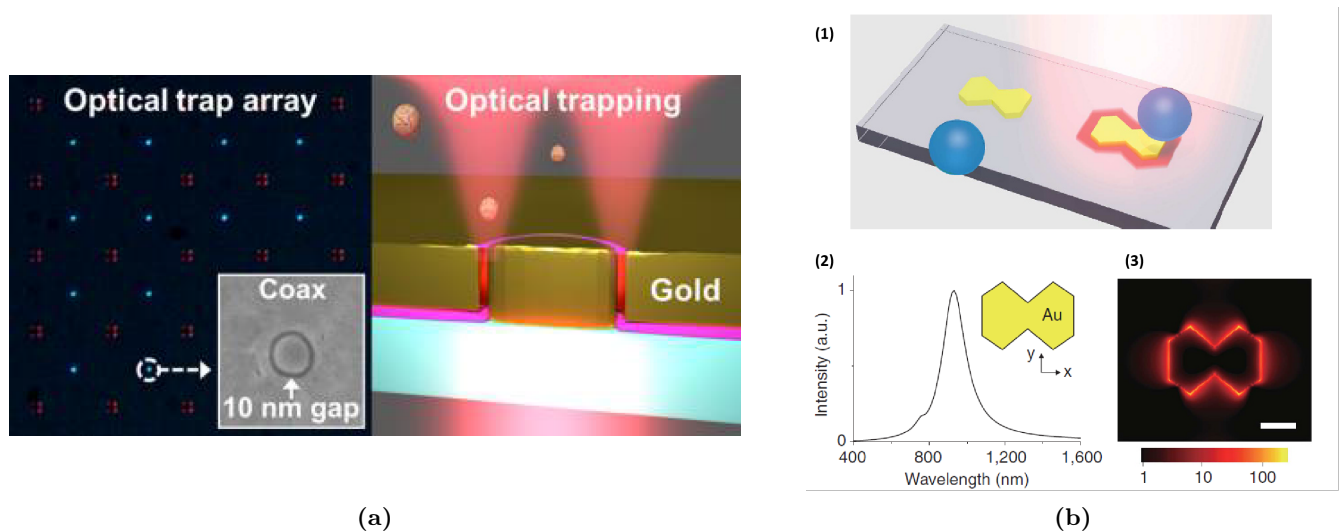


**Figure 1.33:** Low power plasmonic nano-traps examples: (a) View of the resonant coaxial nanoaperture traps, (b) Au nano-antennas traps: (1) is a schematic view of the trap [108], (2) is the calculated spectrum of the electric field intensity enhancement and (3) is the calculated electric field distribution around the structure exited at 980nm [109]

### 1.4.5 Deformation of Liquid-Liquid ( $L_2$ ) Interfaces and membranes

Throughout the literature, optical trapping and actuation have been the main focus of researchers. Deformation of soft interfaces remains out the spotlight in spite of many practical applications. On the fundamental level, optical bending of the meniscus of a phase-separated liquid mixture induced by the radiation pressure was observed and thoroughly studied by Casner and Delville [65–67]. On the practical level, since the primary method for disease (such as cancer) diagnosis remains morphological change in suspect tissue, deformability of cells can be used to locally probe mechanical properties of soft biological systems [111, 112]. Optical deformability is found to be a cell's fingerprint and can be useful as cell marker [113]. Since cellular mechanical properties may provide a direct route to detecting diseases, this method was used to study the elasticity of red blood cell (*RBC*) in a contactless manner [50, 114] as seen in Figure 1.34.

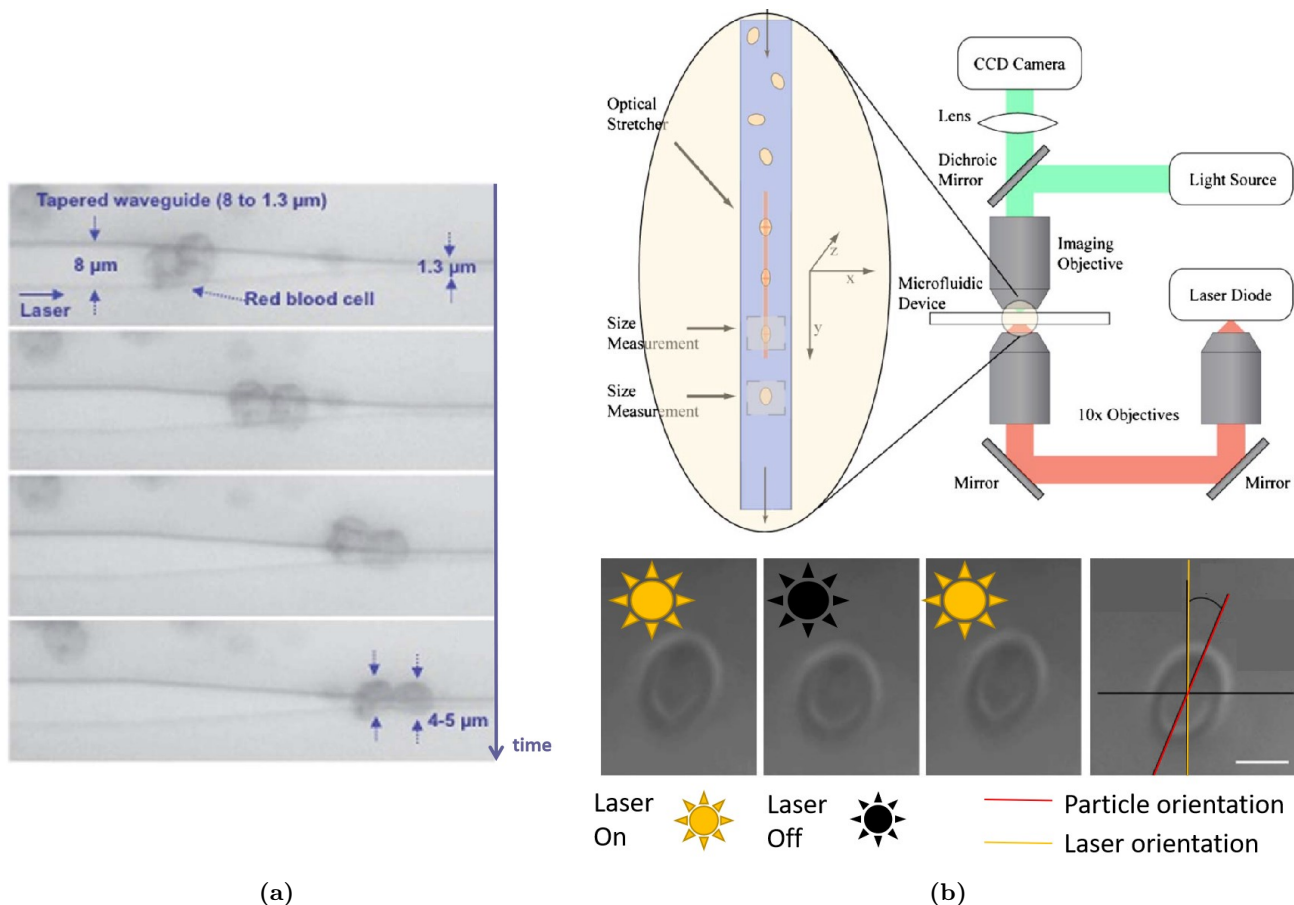


**Figure 1.34:** Near field optical forces applied to studies on the elasticity of RBC's: (a) Timelapse of RBC squeezed as they are propelled towards the waveguide taper. Edited from [50] and (b) Sequential images of an RBC repeatedly stretched with laser diode. Scale bar= $4\mu m$ . Edited from [114]

Traditional optical tweezers have demonstrated the ability to deform cells using silica beads attached to the membrane as local handles [115–117]. Another standard technique is based on the counter propagating beams' optical trap by Ashkin [45]. Light power as high as 800 mW in each beam can be used, which lead to surface forces up to hundreds of pico-Newton, while avoiding thermal heating. The stretching of the cells occur parallel to the beam propagation.

More recently [118] Martinez et al. used a monolithic optical stretcher fabricated in a commercial microfluidic chip (Translume) by direct implementation of optical waveguides through femtosecond laser writing. These waveguides are perpendicular to the flow of the RBC cells and they host two counter-propagating beams (25mW each) that will carry out the deformation when the laser power is increased to 1.2W for 5 seconds in order to stretch the cell. Other have implemented using the same principles a device to asses the mechanical properties of white blood cells as well [119].

In order to avoid cell damage and to attain a high throughput measurement, several near field approaches were used, nonetheless near field for interface deformation remain less present in the literature when compared to other implementations of optical manipulation. A diode-bar optical stretcher was used [114, 120] in order to trap and study the elasticity of RBC. As we can see in Figure 1.34b, the implementation of this system consist of casting the image of a diode bar onto

the lower surface of a glass slide on top of which a PDMS microfluidic pool was bonded. Due to the refractive index mismatch between the medium and the interior of the cell, an optical force is induced on the interface. This interaction deforms the cell until its elasticity balances applied optical forces which permits to calculate the elasticity.

Ahluwalia's work depicted in Figure 1.34a on RBC elasticity offers a better version of on chip manipulation [50, 121]. They demonstrated that the intensity gradient at the edge of narrow waveguides can be used to deform and squeeze cells. Their chip consisted of a tapered waveguide structure made of tantalum pentoxide ( $Ta_2O_5$ ) on oxidised silicon substrate on top of which a thin chamber made of PDMS contains the RBC and is covered with a coverslip.

## 1.5 Summary

Optical manipulation has proved to be irreplaceable by other forms of manipulation due to its versatility, resolution, its ability to manipulate a wide range of particles, and most importantly the ease of its complete integration on chip through the mounting of a microfluidic chip on a photonic circuit in order to exploit near field forces.

In this chapter we offered an insight into the physical principles that govern pressure driven flow on a chip, EM wave propagation and optical manipulation in order to conceive a chip that is able to perform particle manipulation on chip. In the following chapter the main focus will be the state of the art of the fabrication of these devices.



# Chapter 2

## Materials for OM-LoC

### 2.1 Introduction

During the past 50 years, there was a strategical trend for comprehensive miniaturization and larger levels of integration, all of which was enabled by state of the art fabrication technologies. Total analysis systems have found an interest in such miniaturisation [3], paving the way for what will be later baptised as microfluidics. The elaboration of these devices found a solution in the existing solid foundation of microelectronic fabrication: silicon processing [2]. This technology was later replaced by a wide spectrum of transparent materials, from glass to polymers supported by the emerging fabrication techniques. The integration of optical elements on a chip was also made possible using these same technologies, as long as a strategy to guide light in microfluidic chips can be implemented.

In Section 2.2 of this chapter, we are going to go through the materials' requirements for realising optofluidic lab on chips. Then in Section 2.3, we will tackle the state of the art of the fabrication of such devices, focusing mostly on the platforms used for evanescent field optical manipulation. In Section 2.4 we are going to introduce hybrid organic inorganic photoresists as potential candidates for the realisation of OM-LoCs. Afterwards in Section 2.5 we will briefly discuss the development of positive resists that are based on polyamic acids. Finally, Section 2.6 will be dedicated to the techniques that we use for processing these photoresists.

### 2.2 Materials requirement for OM-LoC

The material choice for microchannels depends enormously on the type of the application and fluids circulating inside the channels (biocompatibility, chemical and physical properties), the resolution, and the production scale. The cost in itself is not an independent parameter but a function of all the above. Prototyping material should be identical to the mass production one, otherwise extra effort, time and cost will be needed for redesign.

It is essential to acknowledge that OM-LoCs being descendants of the microfluidic LoCs, share major fabrication challenges. Additional constraints are imposed for photonic lab on chips. The design and the materials choice are closely related to the way we choose to guide the light on the chip. The design depends enormously on the type of interaction between the fluid and the light. Hence in order to conceive a photonic Lab on chip we either need:

- A double paths platform : one dedicated for optical guiding and the other for fluid guiding. For example applications that include near field interaction (sensing or control) cannot happen unless a dielectric boundary exists between the two systems which imposes the use of different routes for each one of them.
- Or a single path platform: where light and fluid take the same path. For example, an OM-LoC working in absorbance should have the longest possible optical-fluidic path, so as to enhance its sensitivity. Thus a setup where both liquid and light share the same trajectory would be ideal, in which case a configuration based on Hollow Core ARROW or Aerogel optofluidics should be put forward.

From a material's point of view, different approaches are proposed to create microfluidic and optical pathways on the same platform:

- A hybrid or heterogeneous approach like combining silicon based photonics and PDMS microfluidics [122, 123], or ARROW waveguides [124].
- A monolithic or homogeneous approach such as the use of femto second laser processing of fused silica, and Foturan glasses [125] to create both channels and waveguides, or the use of lithium niobate substrates to create waveguides by titanium local doping as well as microchannels by micromachining [126]. Moreover channels in low refractive index materials, such as aerogels can be micromachined and used to guide fluids and light at the same time due to total internal reflection (TIR) [127].

From a process point of view it is either:

- an additive process (such as metal and dielectric deposition), commonly used in the case of a hybrid integration
- or a subtractive process (e.g., micro machining, wet and dry etching), commonly used in the case of a monolithic chip.

The takeaway here is that there is no such thing as: the ultimate material/fabrication process for OM-LoCs fabrication. One should tailor one or multiple materials in order to create the perfect balance between:

- Compatibility with the fluid circulating in the channels
- Possibility to create a high refractive index region for waveguiding or to implement any other forms of light propagation.
- Design necessities imposed by the interaction one wishes to implement
- The production scale

## 2.3 Existing materials and associated fabrication techniques

Since much of the commercial success of the OM-LoC concept critically depends on the ability to successfully integrate optical and microfluidic elements in a simple, cheap and high throughput technique, we present in the following sub-sections the different materials and methods that are

used to realise this integration, in order to exploit the benefits of the evanescent field mostly for manipulation<sup>1</sup>. We are going to limit the discussion to the methods of implementing optical waveguides and microfluidic channels on the same chip, for each one of the commonly used materials, but we will not include the platforms that don't support evanescent field for manipulation or sensing, such as ARROW and ultra porous materials' based devices.

In the following subsections will differentiate optofluidic platforms based on the class of materials used for the waveguides fabrication. Then in each of these subsections, we will also introduce the materials that are used for the mounting of the microfluidic layer. The purpose being to treat the fabrication of optofluidic platforms as whole entity, instead of treating both waveguides and channels fabrication separately.

Before starting it is important to note that the waveguide materials used for manipulation platforms can be classified according to the RI step that exists between the core and the cladding:

- very high RI step (around 2) for silicon on insulator waveguides
- high RI step (around 0.5) for silicon nitride and tantalum pentoxide waveguides
- medium RI step (around 0.1) for SU-8 and other polymer waveguides
- low RI step (around 0.04) for Cesium or Potassium ion-exchanged waveguides

It was also demonstrated that the higher the refractive index of the core, the more intense the near field forces are [87], even if the field decay is faster. The use of high refractive index waveguides can drastically reduce the power engaged to trap or move particles. An extensively detailed table about the materials, and techniques used for the fabrication of waveguides for OM-LoCs, as well as the key characteristics of each one of them will be provided in Appendix A.

### 2.3.1 Silicon based platforms

Silicon is the most widely used substrate for the integration of optical components, since it is accessible, cheap, robust and its fabrication methods are well established based on the complementary-metal-oxide-semiconductor (**CMOS**) technology. It has also a wide spectrum of transparency depending on the dopants that are introduced. In the following paragraphs we are going to present and compare the CMOS compatible materials used in OM-LoC fabrication. All of them are deposited on silicon substrates, this is why we named them "silicon based platforms". They are usually combined with polymeric materials for the constitution of the microfluidic layer due to the ease of their fabrication and integration with the optical layer.

#### Waveguides fabrication

Silicon (Si), silicon nitride ( $Si_3N_4$ ), silicon oxynitride ( $SiON$ ) and silicon dioxide ( $SiO_2$ ) are widely used in the context of OM-LoCs for manipulation. While the first 3 are used as core materials,  $SiO_2$  is reserved for the cladding layer as it has the lowest refractive index among all of them.

---

<sup>1</sup>We may include some techniques that weren't used in the realisation of OM-LoCs for manipulation, but that can potentially be implemented in such context.

Si is optically transparent in the wavelength range above  $1200\text{ nm}$ .  $\text{Si}_3\text{N}_4$  broadens the transparency range into the visible.  $\text{SiON}$  being an intermediate phase between  $\text{SiO}_2$  and  $\text{Si}_3\text{N}_4$ <sup>2</sup>, it can extend the transparency down to the UV range<sup>3</sup>. These materials can easily cover the range of operation of the lasers used in optical manipulation (visible to mid-IR) as well as in fluorescence sensing (UV).

Waveguides having an Si core are extremely interesting especially for manipulation of particles in the infrared region. Silicon has a refractive index of around 3.5 in the near IR [129]. As such, its extremely high RI as well as the RI difference that exists with its surrounding<sup>4</sup>, allows a good light confinement, small bending radii, and reduction of the device footprint. Nevertheless it imposes nanometric dimensions of the waveguides for single mode propagation, which creates a dimension mismatch with microfluidics as well as with fiber optics. This makes the coupling with an optical fiber of micrometric dimensions challenging because of both the core size and the RI mismatch<sup>5</sup>. Si also offers the possibility to exploit thermo-optic effects as it has a large thermo-optic coefficient ( $1.86 \times 10^{-4}\text{K}^{-1}$ ) [131]. Silicon core waveguides can be realised in a silicon-on-insulator (SOI) wafer. The patterning of the silicon waveguides is done using electron beam lithography (*E-Beam*), and the etching can either be done using plasma [98, 131] or reactive ion etching (*RIE*) [28], both dry etching techniques. These fabrication steps are depicted in Figure 2.1a. Figure 2.1b is a scanning electron micrograph of the trapping region of the nSWAT waveguides fabricated by Soltani et al. [98].

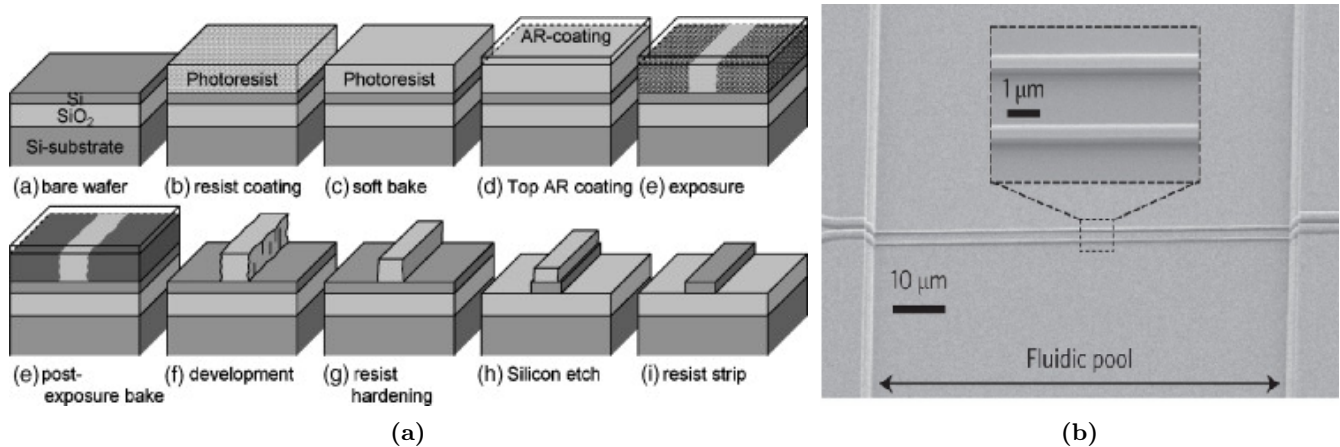


**Figure 2.1:** (a) Steps of silicon waveguide fabrication in a SOI wafer [132], (b) nSWAT waveguides fabricated in SOI wafers [98]

Silicon nitride has a RI of around 2.07 at  $1565\text{ nm}$ . When deposited on a silica cladding it yields a RI step in the range of 0.5 – 0.6. The use of silicon nitride waveguides for manipulation was found to increase the optical forces by a hundredfold when compared to lower index difference

<sup>2</sup> Thus its optical properties can be customized depending on the ratio of nitrogen to oxygen introduced during the deposition.

<sup>3</sup>This is not always the case for doped fused silica; for example Germanium doped silica exhibit losses below 500 nm due to UV absorbing centers, while nitride doped silica shows a very good performance [128]

<sup>4</sup>Either the cladding or the surrounding environment such as the microfluidic sample in the case of optofluidics

<sup>5</sup>Coupling strategies such as waveguide tapers [28] or bragg grating couplers [130], were put in place to decrease the coupling losses

waveguides such as ion exchange waveguides [87]. These optical waveguides can be produced with Low Pressure Chemical Vapor Deposition (*LPCVD*) of  $Si_3N_4$ , on a silica thin film, thermally grown on Si substrate. The patterning is done using a photolithography followed by dry etching such as RIE as illustrated in Figure 2.2a [87, 133].

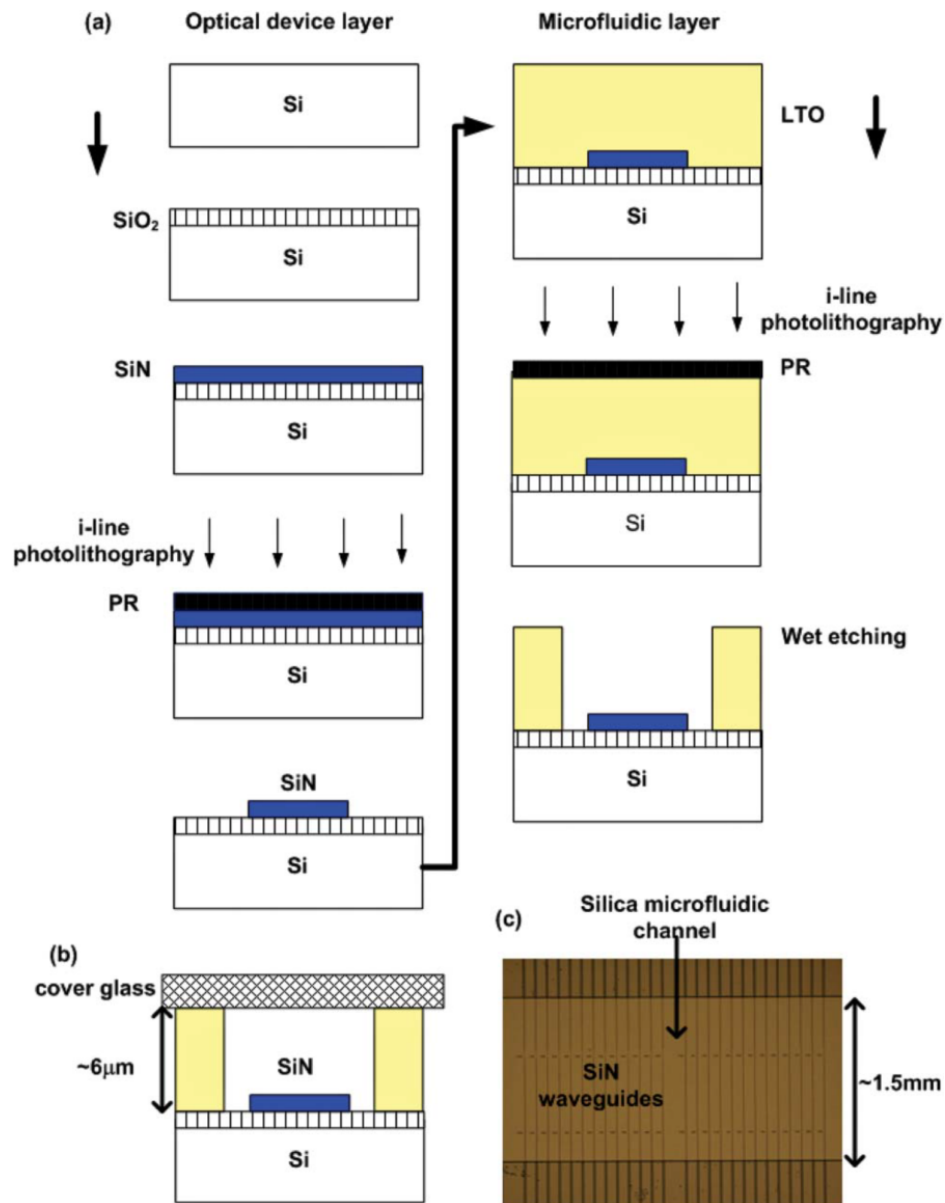


**Figure 2.2:** (a) CMOS-compatible fabrication process of an optofluidic chip. (b) Schematic of the optofluidic chip cross-section. (c) Optical micrograph of the fabricated optofluidic chip with air-cladding. PR: photoresist, RIE: reactive ion etching, LTO: low-temperature oxide [133].

A high refractive index core can also be achieved in silicon dioxide, by the addition of dopants during the deposition phase of the core layer. These dopants generally are phosphorus, germanium and nitrogen. As such patterned silicon oxynitride (SiON), sandwiched between 2 layers of silica ( $SiO_2$ ) cladding can be used to guide light on the chip, with a RI step of 0.013 [128, 134, 135]. However, this seemingly simple setup takes around 20 days at 1000° C to thermally grow the lower cladding of  $SiO_2$  on a silicon substrate. The core of the planar waveguide circuit formed of SiON

is deposited using plasma-enhanced chemical vapor deposition (*PECVD*) and patterned by RIE. The upper Silica cladding is done using PECVD as well, before the final step of the microfluidic channel fabrication takes place. A final annealing at  $1000^{\circ}C$  for around six hours is necessary to stabilise and densify the glass.

Other waveguide materials compatible with the CMOS technology were used for the fabrication of optofluidic manipulation chip, this is the case of Tantalum Pentoxide ( $Ta_2O_5$ ). The refractive index of  $Ta_2O_5$  is 2.15 at  $1070\text{ nm}$ .  $Ta_2O_5$  waveguides were fabricated on oxidised silicon substrates by magnetron sputtering, thus yielding a very high refractive index step of 0.65 between the buffer and the guiding layer [50, 102, 136].

### Channels fabrication

As a rule of thumb, microfluidic channels are replaced by microfluidic chambers or pools, since optical forces are used to guide the movement of the particles, as if they are moving on a conveyor belt. The fluidic layer can be formed using a photosensitive resist, that is compatible with the CMOS fabrication process, or with PDMS that can be easily bonded to Si and  $SiO_2$  through surface plasma activation. Another method consists of directly etching the cladding layer.

As such, a microfluidic chamber can be fabricated with the use of a spacer either made of manually cut PDMS [28], or simply with a double sided adhesive tape [87, 92, 137]. The chamber is usually sealed with a glass plate after sample introduction.

The fluidic pool can also be selectively revealed in the oxide cladding of the waveguides after standard photolithography followed by plasma etching [98, 131, 133–135]. A metal layer needs to be deposited and patterned prior to the etching in order to protect the  $SiO_2$  where no subtraction is required. A borosilicate lid with pre-perforated holes can be anodically bonded to the  $SiO_2$  substrate, for the sealing of the fluidic layer [135, 138].

## 2.3.2 Glass Platforms

A wide variety of glass<sup>6</sup> could be considered as an adequate choice for microfluidic chips fabrication due to its well known benefits: it is chemically inert, robust, stable in time, hydrophilic, nonporous, and optically clear. The use of fused silica in particular, is very advantageous because of its high optical transparency, down to the UV range, and its low background fluorescence. In addition, glass remained adequate for optofluidics, because waveguides can be implemented in bulk glass. The local increase of the glass refractive index is usually done by ion exchange and more recently by high power laser.

### Waveguides fabrication

The fabrication of the optical waveguide in soda-lime, or crown (BK7) glass is often realized by the potassium  $K^+$  or Cesium  $Cs^+$  ion exchange method (Figure 2.3). It results in the local increase of the refractive index of glass: a time consuming process that could extend from 4 [77]

---

<sup>6</sup>Forturan Glass, Silica Glass, Lime Glass

to 192 hours [139], performed at high temperature ranging from 380 to 450° C, in an environment of the molten salt of  $KNO_3$  or  $CsNO_3$  depending on the ions to be exchanged [92, 137, 139].

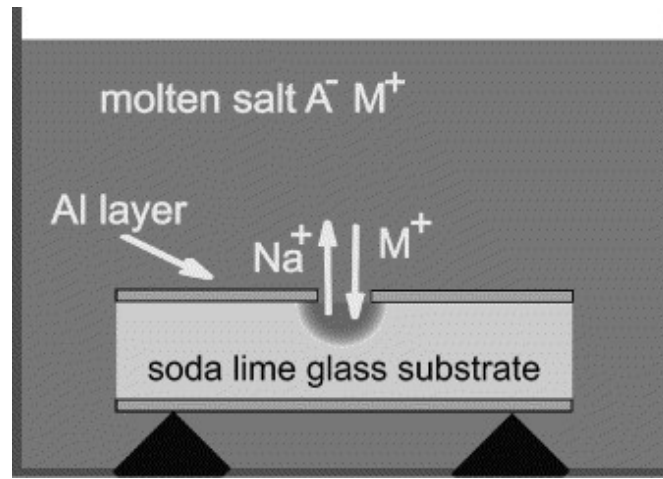


**Figure 2.3:** Ion exchange for the fabrication of channel waveguides.

Ion exchange in glass requires a nanometric aluminum mask deposition, followed by patterning and etching, to the width of the waveguide, before the process of ion exchange can be performed in a localised manner. After which the aluminum mask should be completely removed because the channels fabrication is carried afterwards. This technique yields a low RI change of around 0.005 for  $K^+$  up to 0.03 for  $Cs^+$ .

By focusing the laser beam through a microscope objective, researchers have successfully written a step index waveguide in high-silica, borate, soda lime silicate, and fluorozirconate bulk glasses<sup>7</sup> with 0.01 to 0.035 refractive-index increase depending on the dose [141]. The physical mechanisms responsible for this refractive index change in glasses are not yet fully understood. Several hypothesis were proposed but none of them can be generalized to all glass types. The RI variation can be attributed to a combination of three mechanisms. First, there is the thermally induced material densification. Second, there is the unequal cooling of the irradiated glass as we move farther away from the focal point of the laser. This puts the material that is the closest to the focal point of the laser under pressure and subsequently changes its RI. Finally, there is the direct structural change induced by the laser pulses, meaning the rearrangement of the network of chemical bonds in the glass matrix leading to a density increase.

The fabrication of optical waveguides written by a focused ultra-short pulse laser is recent compared to other methods. Nevertheless, it presents a couple of advantages over other techniques applied to glass: such as the capacity to create 3D waveguides in the bulk materials, a more rapid process than other glass processes as it is a direct maskless fabrication technique, and its applicability to various types of glass. The only disadvantages is its high energy consumption. A single pulse has a peak power ranges between  $10^9 W/cm^2$  [140] and  $10^{13} W/cm^2$ , a much larger power than that needed for stereo-lithography for example.

<sup>7</sup>The repertoire includes as well: synthetic silica, Ge-doped silica, borosilicate, phosphate, Fluorophosphate, Fluoride, and chalcogenide glasses [140]

## Channels fabrication

For channels fabrication, a well established processes based on silicon fabrication developed for the microelectronics industry such as photolithography and wet/dry etching can be applied on glass as well. Even if these processes are well established, they are still hideous and harsh ones.

A wet etching process, illustrated in Figure 2.4a, includes at least 4 different interventions of complex nature: **i)** the deposition of a nanometric chromium layer on both sides of the substrate by magnetron sputtering (step 2). **ii)** Then, the photo-lithography process (deposition, insulation and photoresist revelation) used to pattern the chromium layer (step 3). **iii)** A first cycle of wet etching (chromium etchant) used to open windows in the chromium layer (step 4). **iv)** Subsequent numerous wet etching cycles should be used to fabricate the microfluidic channels with the use of the mixtures of buffered oxide etchant, and hydrochloric acid (step 5) [139]. The final product of this process is illustrated in Figure 2.4b.

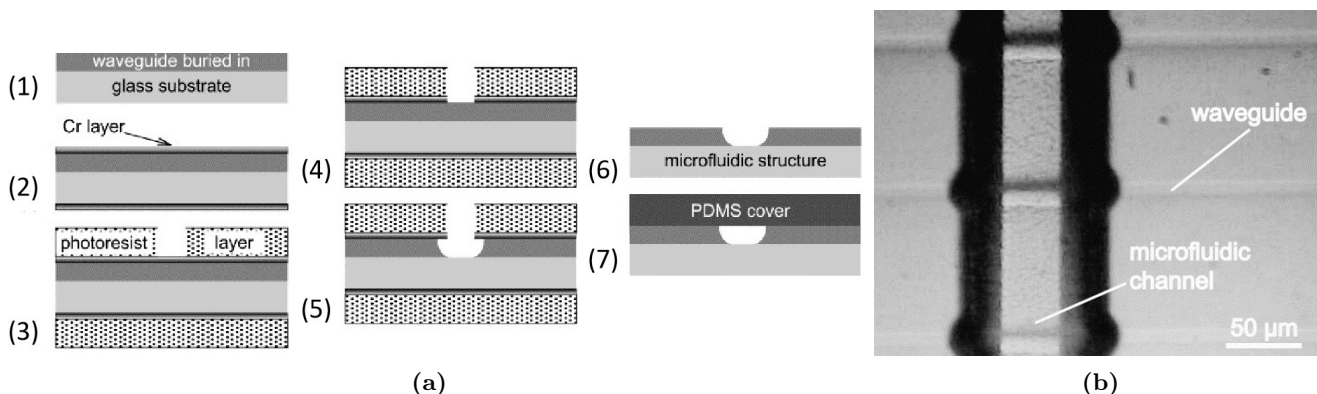


**Figure 2.4:** (a) The steps for the fabrication of a microfluidic channel in a soda lime glass substrate with an integrated waveguide. (b) The final product, channel and waveguides of this process [139].

Femto second laser writing in glass, leads to cracking due to thermal shock that occurs when the pulse is focused near surface of the glass samples. These generated defects increase the etching rate by up to two orders of magnitude, thus enabling the realization of high aspect ratio channels<sup>8</sup>. This technique enables the creation of microfluidic channels while at the same time writing the waveguides [143, 144]: a single step process known as Femtosecond Laser Irradiation followed by Chemical Etching (**FLICE**). As the name suggests, this laser irradiation requires etching of the laser modified zone by a hydrofluoric acid *HF* solution in water. FLICE was only used with fused silica and Foturan glass until now. This method of glass processing has the ability to produce monolithic devices, with 3D channels and waveguides as illustrated in Figure 2.5. These images are adapted from multiple works of Bellini and Osellame using similar device formation: those marked with a red dot are from reference [143] and those marked with a blue dot are from another work of the same group [144].

<sup>8</sup>High-intensity femtosecond laser irradiation in fused silica creates self-ordered nanocracks, orthogonally aligned to the laser polarization [142].

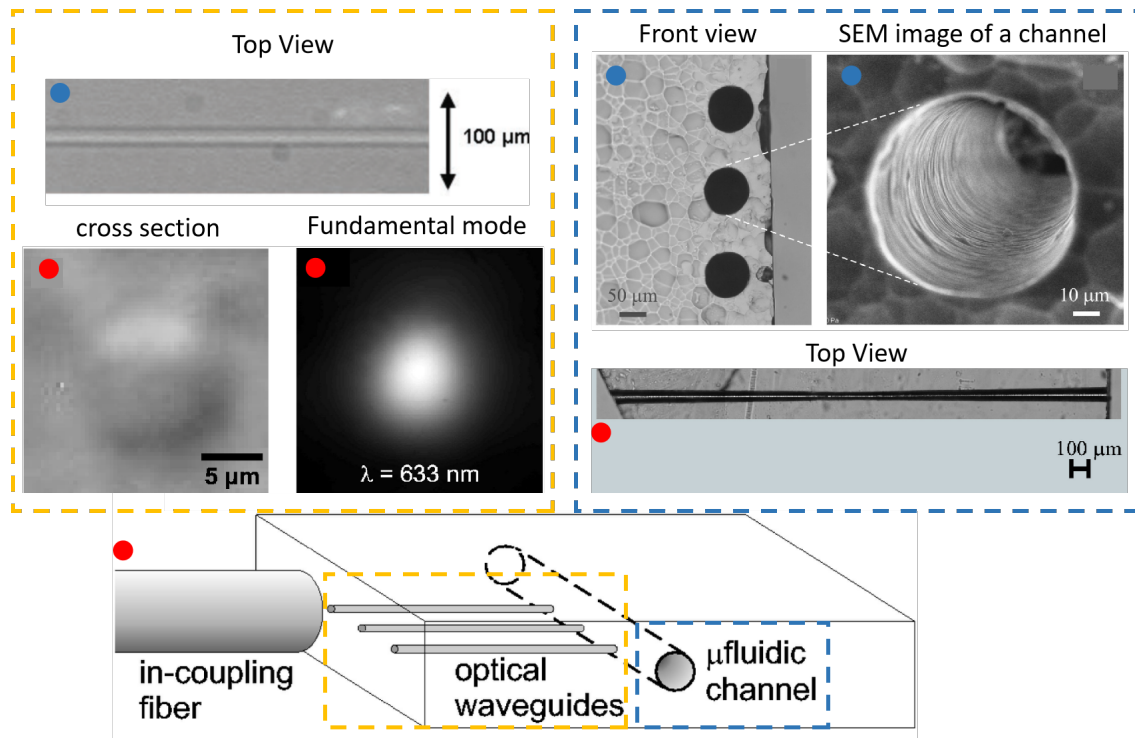


**Figure 2.5:** Femto second fabricated optofluidic platform for parallel multiple sensing at different positions in the micro channel. Adapted from [143] and [144], with the permission of AIP Publishing.

### 2.3.3 Organic polymer Platforms

As soon as soft lithography techniques (such as micro-contact printing, micro-molding in capillary, and replica molding) emerged in the late 80's [145], polymers soon took their place in the fabrication of microfluidic system. Mainly because they have some key advantages over their silicon and glass based counterparts. That is, their low cost and energy efficient fabrication on one hand, and the rapidity of their realisation on the other hand, making them more suitable for prototype evaluation. In addition the wide spectrum of polymer specifications and characteristics makes them an attractive material for the industry. They remained adequate for optofluidics, because of their wide range of transparency in the optical domain, and the ability to successfully implement waveguides in these materials, as we will see in the following subsections.

Polymers are usually classified according to their response to heat treatment or to their mechanical properties. In this section we are going to choose among them, the most widely used for the fabrication of optofluidic systems, and we are going to classify them based on their photosensitivity: non photosensitive, and photosensitive polymers.

#### 2.3.3.1 Non photosensitive polymers

Even though many non photosensitive organic polymers are utilised for the microfluidic channels elaboration, only polymethyl methacrylate (*PMMA*) is used material for optofluidic systems fabrication.

## Waveguides fabrication

PMMA has a transparency window that ranges from 300 to 1330  $nm$  [146], thus covering a part of the UV-vis wavelengths used for fluorescence sensing application, as well as a good part of the wavelengths used for manipulation, that is the upper visible to the near IR range (even though it was never used for manipulation applications). As such, it is considered as a good candidate for waveguides fabrication in optofluidic systems.

Waveguides can be implemented in PMMA with an undercladding of poly-fluoroalkyl methacrylate (*PFMA*). This is done using selective RIE [147] of a PMMA layer on PFMA, through a protective aluminum mask. In addition, exposure to deep UV radiation causes breaking of the molecular chains in PMMA and increases its refractive index locally. As such, fabrication of optical waveguides can be accomplished by DUV exposure through a photomask [148]. These PMMA waveguides presents a low refractive index step of around 0.007 in the visible, and they are graded index waveguides. This is what makes them suitable for sensing applications, but less adapted for optical manipulation.

## Channel fabrication

Femtosecond laser ablation of polymeric substrates such as PMMA can also be used for the fabrication of microfluidic channels [149]. The width and depth of the channels are defined by the polymer type, the geometrical characteristics of the focused laser beam<sup>9</sup>, the average laser power, and the structuring speed<sup>10</sup>. The drawback of this method is the high surface roughness induced in the polymer.

Hot embossing of PMMA is the most popular method for the channels fabrication, since it is very adapted for mass production. It can either be done as a first step before the fabrication of the waveguides [148], or to simultaneously define microchannels as well as the waveguides' void [150]. These structures are visible in Figure 2.6. In the case of plastics such as PMMA, the channels can be sealed with a lid bonded using a combination of high temperature and high pressure [148].

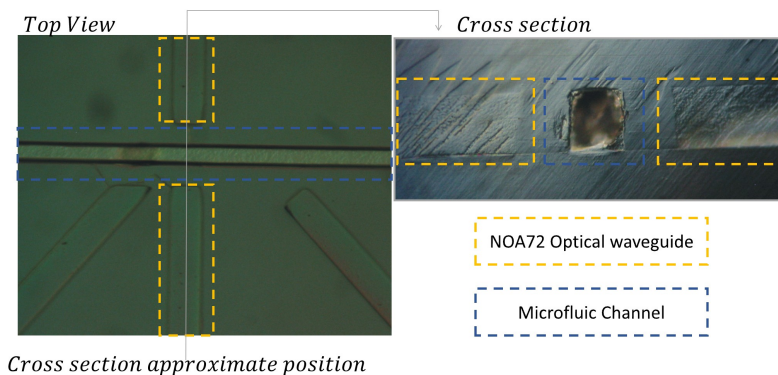


**Figure 2.6:** The microfluidic channels and the waveguides fabricated by hot embossing in PMMA [150].

<sup>9</sup>especially the beam diameter, which was found to be approximately equal to the width of a the channel created by a single passage for a laser power that is equal the ablation threshold

<sup>10</sup>the laser speed and power define the material removal rate.

### 2.3.3.2 Photosensitive polymers

The use of photosensitive polymers for the realisation of either the channels or the waveguides has the advantage of reducing the processing time and the task complexity. A typical process would only consist of three simple steps: deposition, insulation and development, each one of them is usually followed by a baking step. Photosensitive polymers can be classified depending on their reaction with respect to insulation as illustrated in Figure 2.7.

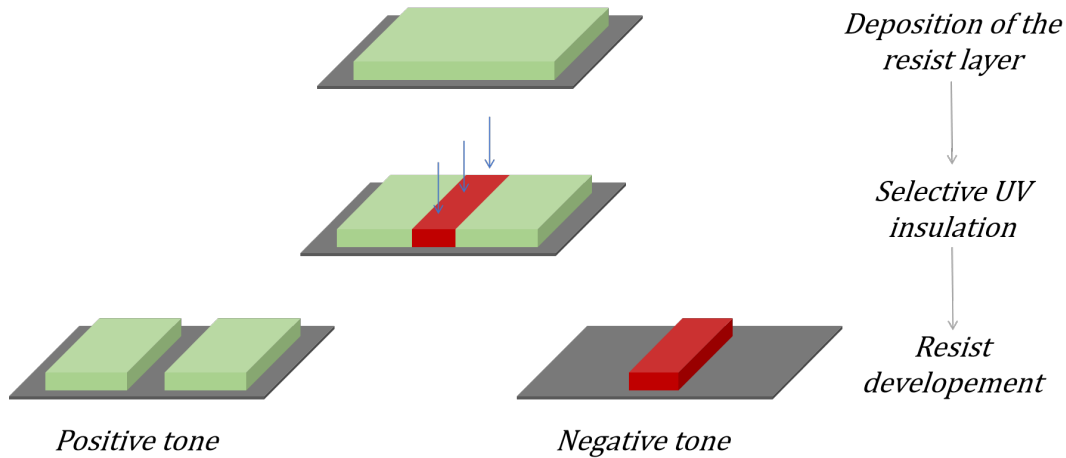


**Figure 2.7:** Positive and negative photoresist response to selective UV treatment.

- A negative resist, where the insulated image hardens, and remains after immersing the sample in the developer. It is composed of a monomer, and a photoactive compound. Upon UV exposure, the photoactive species is able to induce a polymerisation, that renders the film insoluble in the developer solvent.
- A positive resist, where the insulated image decomposes and is wiped out by the developer. It is composed of a polymer, a dissolution inhibitor (DI), and a photoactive compound. Initially the polymer is soluble in the developer. Upon thermal treatment it reacts with the DI and create a co-compound. Upon irradiation, the photoactive species generate acids <sup>11</sup>, that depolymerise the co-compound already formed by the polymer and the DI. This is what makes the photoresist soluble once again in the developer.

Some resists exhibit either a negative or a positive behavior depending on the process conditions, more precisely on the baking and exposure steps. This type is called an image reversal photoresist and will not be considered here.

### Waveguides fabrication

For waveguides fabrication, the use of negative tone resists is the most common. These resists harden upon insulation, and they also exhibit a RI change. This can be explained by the fact that the RI of a dielectric is linked to its molecular structure (given in terms of molar refraction  $R$  expressed in  $[cm^3.mol^{-1}]$ ) and its volumetric mass  $\rho$  expressed in  $[g.cm^{-3}]$ .

<sup>11</sup>in the case of a chemically amplified positive photoresist.

One of the expressions to formulate this dependency is given by the empirical Lorentz-Lorenz model [151], linking  $R$  to  $\rho$ , the refractive index  $n$ , and the molar mass  $M$  expressed in [ $g.mol^{-1}$ ]. This expression is written as follows:

$$R = \frac{n^2 - 1}{n^2 + 2} \frac{M}{\rho} \quad (2.1)$$

With  $R = \sum R_i$ , where  $i$  refers to the different group of atoms in the molecule.

As such the refractive index squared can be expressed as:

$$n^2 = \frac{2R\rho + M}{M - R\rho} \quad (2.2)$$

The change in this quantity can be written as follows:

$$d(n^2) = \frac{3M}{(M - R\rho)^2} (Rd\rho + \rho dR) \quad (2.3)$$

Equation 2.3 shows that, the refractive index change can be either positive or negative depending on the quantity  $(Rd\rho + \rho dR)$ .

Usually during insulation, two opposed phenomena take place:

- a decrease in the molar refraction due to polymerisation,
- and an increase in the volumetric mass, thus an increase in the density.

For example the polymerisation of acrylates consists of a transformation of  $\text{CH}_2=\text{C}$  double

bonds into  $\text{—CH}_2\text{—C—}$  single bonds. The molar refractivities of these two groups can be calculated based on data from Table 2.1.

Chemical Bond	R [ $cm^3/mol$ ]
C-H	1.69
C-C	1.25
C=C	4.16

**Table 2.1:** Bonds refractions at 587.56 nm, based on data given in Landolt-Bornstein, as they appeared in reference [152].

This gives  $9.23 cm^3/mol$  for the first monomeric group and  $7.13 cm^3/mol$  for the second polymeric group. Thus no refractive index increase can be seen, unless this decrease in  $R$  could be compensated by an increase in  $\rho$  according to equation 2.3. So in order to create a region of higher refractive index in a photosensitive material we can proceed in two different ways:

- If the density increase compensates the molar refraction decrease, selective UV insulation can be solely used to create waveguides. The other option is revealing the guiding structures and covering them with a lower refractive index cladding.

- If the molar refraction decrease has the dominant effect, the UV insulation must be followed by a structure development and the use of a lower refractive index cladding.

Among polymer photoresist, a commercial epoxy based negative photoresist under the name of SU-8, takes the biggest share of the waveguides fabrication for optofluidic chips [153–156]. It is compatible with the CMOS fabrication, thus complex structures can be accomplished, as seen in Figure 2.8.

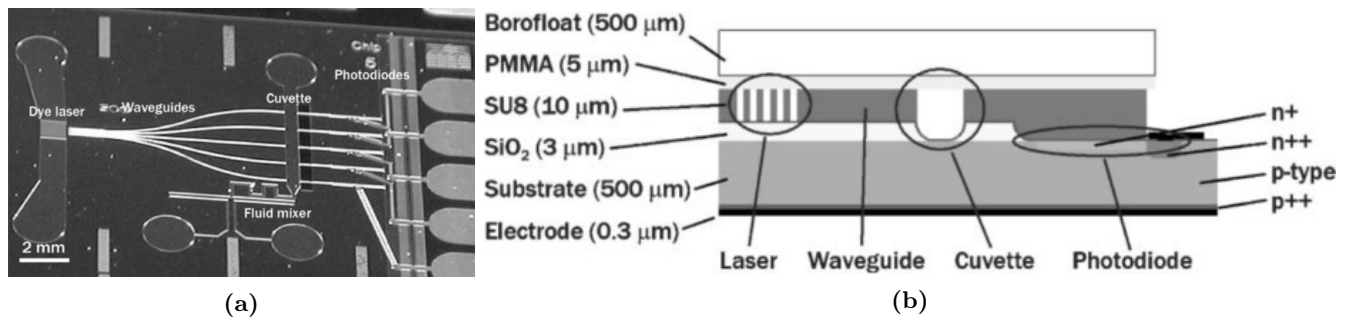


**Figure 2.8:** (a) Photograph of the lab-on-chip before sealing: with integrated microfluidic dye laser, optical waveguides in SU-8, microfluidic network and photodiodes. (b) a cross section of the fabricated device showing the same components. [156]

Its optical transparency in the near IR ( $850 - 1100 \text{ nm}$ ) makes it suitable for particle manipulation [91]. SU-8, deposited on  $\text{SiO}_2$  thin layer<sup>12</sup> or borofloat, presents a sufficiently high refractive index difference of 0.1, capable of successfully creating optical manipulation functionalities as demonstrated in the work of Schmidt et al. [91]. However, it suffers from high losses in the IR region ( $1.3 - 2.5 \text{ dB/cm}$ ) [91, 156] and from being thermally unstable<sup>13</sup> [154].

## Channels fabrication

The channel walls can also be defined by a void created by the SU-8 bonding region as seen in Figure 2.9 [154]. The cuvette previously seen in Figure 2.8 is also defined in the SU-8 optical layer by etching down until the oxide buffer layer [156].

<sup>12</sup>Thermally grown on a silicon substrate

<sup>13</sup>Indeed, the thermal stability is not a problem for the application type, but it can be a problem if the process includes steps that are performed at high temperatures.

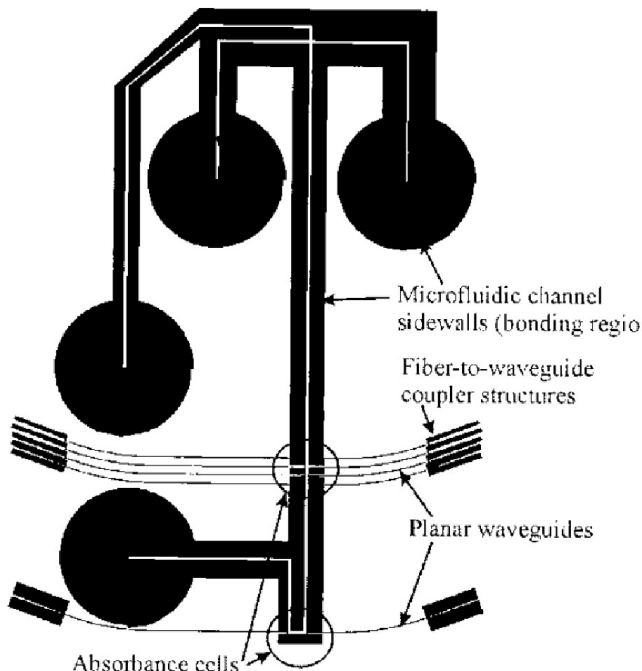


**Figure 2.9:** Mask design of the device in [154]. All optical structures as well as the channel walls and defined in the same layer. The dark regions correspond to the remaining SU-8 layer after structuring which will be used for channel sealing.

The fluidic layer can be sealed by lamination of an aluminum foil, or through adhesive bonding when working with polymeric resists [154]. A non adhesive intermediate layer can also be used for bonding. As such, a  $5\ \mu\text{m}$  polymethyl methacrylate (PMMA) layer is used as an intermediate, in order to bond the  $500\ \mu\text{m}$  borofloat glass lid with the SU-8 layer [156].

### 2.3.4 Hybrid organic-inorganic platforms

Hybrid organic-inorganic polymers refer to a class of crosslinked materials that are constituted of both organic, and inorganic parts. They will be thoroughly discussed later in this chapter. An important family of hybrid materials is polysiloxanes, commonly known as silicones. This is the family to which Polydimethylsiloxane (*PDMS*) belongs. Polysiloxanes are molecules with

an oxygen-silicon backbone  $\text{---Si---O---Si---}$ , with the possibility of having side chains at-

tached to the silicon atoms. These side chains determine the mechanical and reactive properties of polysiloxanes. In fact siloxane monomers  $R_n\text{SiO}_{4-n}$  can either be, monofunctional, difunctional, trifunctional or tetrafunctional depending on the number  $n$  (for  $n=3,2,1,0$  respectively) of organic groups  $R$  attached to the Si;  $R$  groups are organic radicals possibly bearing functional groups, that may or may not be photopolymerisable.

### 2.3.4.1 Non photosensitive hybrids

PDMS originally utilised for microfluidic fabrication, remained adequate for optofluidic chips fabrication, because it is optically transparent from 240 to 1100 nm [157], and waveguides can be successfully implemented in it.

#### Waveguides fabrication

The need for optical integration into LoC devices, led to waveguides realisation in very innovative ways in non photosensitive materials especially in PDMS. This can be done in three different ways:

1) First, through doping the polymer with a photopolymerisable monomer. The monomer can either be an intrinsically photosensitive polymer such as phenylacetylene [158] or a combination of a photoinitiator and photopolymerisable monomer such as oxime ester photoinitiator Irgacure OXE02 and divinylbenzene [159]. This fabrication is described as a four steps process, and is illustrated in Figure 2.10:

- a) the preparation of the cured PDMS slab
- b) immersing the PDMS slab in the liquid monomer formulation, until the PDMS is saturated with the monomer<sup>14</sup>
- c) the exposure of the monomer-permeated PDMS slab to a focused ultrashort laser irradiation, in order to form waveguide structures by induced polymerization of the monomer
- d) finally, an ethanol washing followed by a heating routine at 100 – 130° C for two hours, to remove unreacted monomer from the PDMS matrix

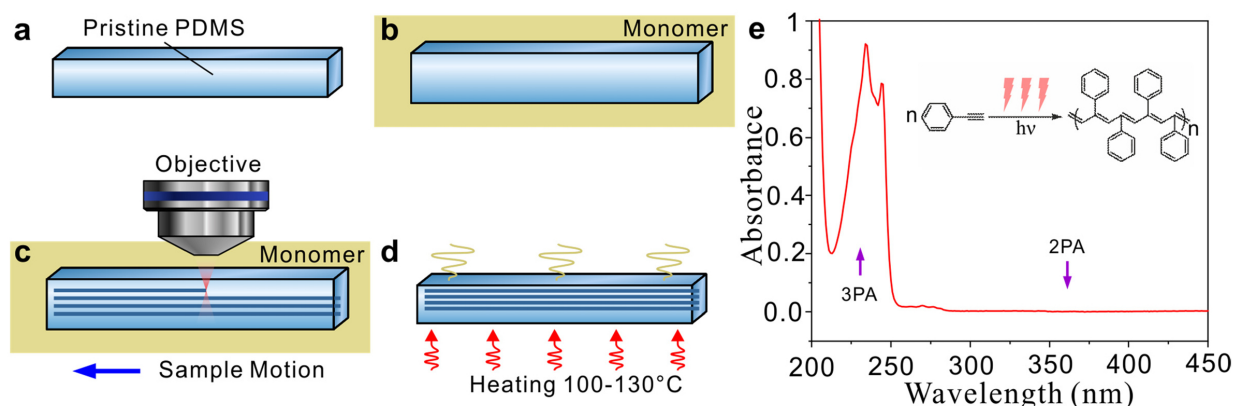


**Figure 2.10:** Principle of waveguides fabrication in PDMS by multiphoton polymerization: (a, b, c and d) in their respective order illustrate the four steps of fabrication. (e) Absorption spectrum of 0.01 mM phenylacetylene in acetonitrile. Violet arrows indicate energies of two-photon absorption (2PA) and three-photon absorption (3PA). Inset illustrates the reaction of multiphoton polymerization of phenylacetylene [158].

2) Second, a simple yet novel and innovative way to implement waveguides in PDMS was proposed by Cai [160]. It is based on the fact that PDMS of different mixing ratio of base to curing agent, have different refractive indices as shown in Figure 2.11.

<sup>14</sup>the immersion time depends on the monomer and photoinitiator size, it can range from 48 to 144 hours.

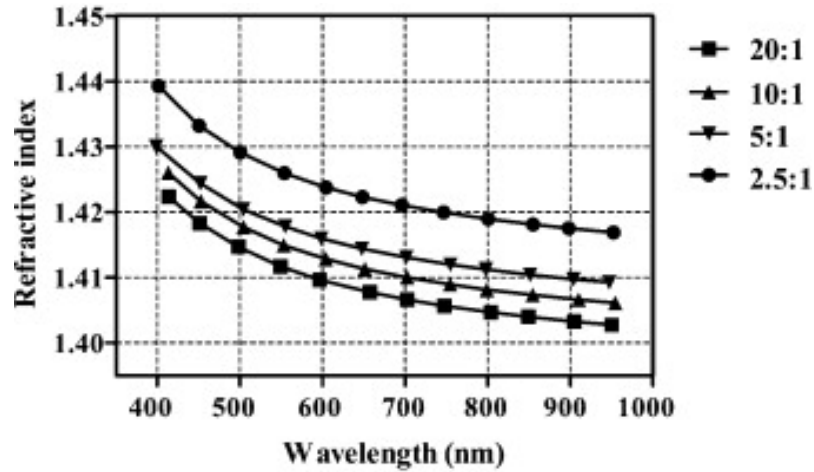


**Figure 2.11:** The measured values of refractive index for PDMS in different mixing ratios of the base to curing agent

This process can be accomplished using soft lithography techniques, and with commercial PDMS. The steps are illustrated in details in Figure 2.12. The waveguides fabrication is depicted in the steps (11) to (13), and is carried out by injecting uncured PDMS of higher refractive index (5:1 mixing ratio for example) in the channels, This is done by placing drops above the holes then expelling the air in the channel using vacuum. Due to the permeability of PDMS, this step expels the air through the materials matrix and fills the channel with uncured PDMS.

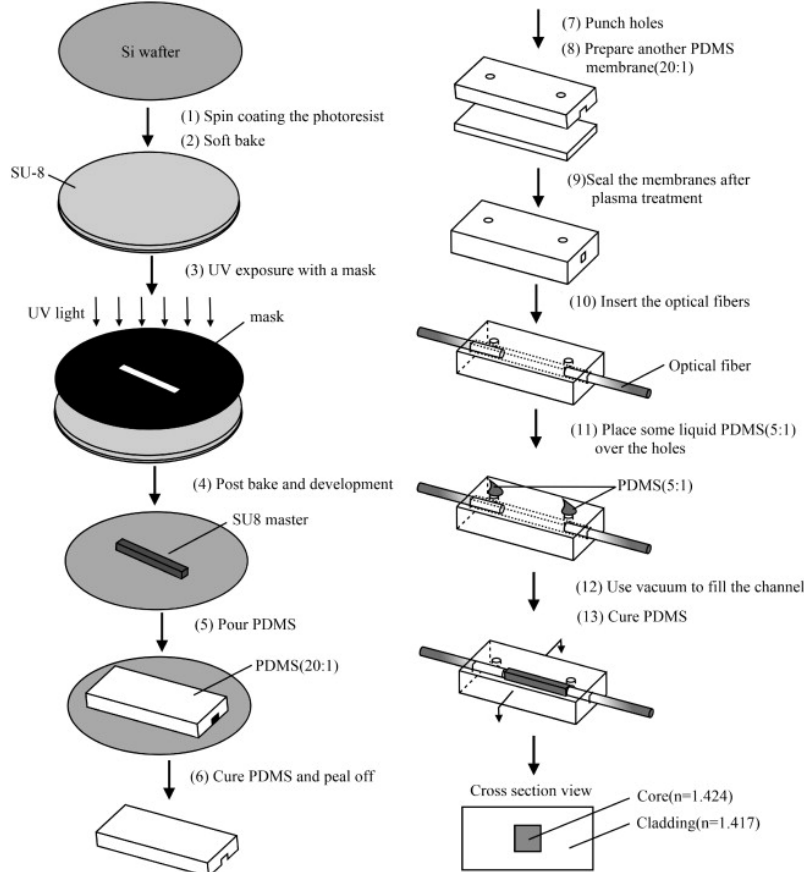


**Figure 2.12:** Schematic procedures to fabricate the PDMS waveguide [160].

3) The third way is to tune the PDMS refractive index in each component of the waveguide, by employing different curing processes for the core and the cladding [161].

Single mode waveguides fabrication is challenging using molding techniques. On the contrary direct laser writing cannot produce core sizes higher than a couple of microns [158]. As for the maximum refractive index step, the increase induced by the permeation technique ( $\geq 0.06$ ) is higher than that of soft lithography techniques (around 0.02). Direct writing permits the fabrication of submicrometric waveguides, which leads to high losses ( $13 \text{ dB/cm}$ ) for single waveguide. Thus a multi-track approach should be implemented in order to decrease the losses down to  $0.1 \text{ dB/cm}$  in the visible region. The lowest propagation loss for PDMS waveguides was measured by Panusa and coworkers [158] as  $0.03 \text{ dB/cm}$  with the use of an intrinsically photosensitive monomer.

## Channels fabrication

Channels are most commonly produced in PDMS [91, 155, 162], regardless of the material used for the waveguides. This is due to the ease of channels fabrication by molding, the perforation of the inlets and outlets, and finally the bonding with the optical layer either by plasma or by the use of an adhesive. Moreover the use of a PDMS layer, eliminates the need to seal the channels.

### 2.3.4.2 Photosensitive hybrids

Organic-inorganic photosensitive materials can be patterned using standard photolithographic techniques due to the ability to photosensitize their reactive organic part. They are also able to form a mineral network due to their inorganic content, by a process called sol-gel. These materials were separately used for the fabrication of optical circuits using negative tone resists [163–165], as well as microfluidic channels using both negative [166] and positive tone resists [167].

To our knowledge, there is no literature on the use of photosensitive hybrids in the fabrication of optofluidic systems for manipulation applications. Their use in the optofluidic context remains limited to sensing applications. The elaboration of a high refractive index layer ( $n = 1.764$  at  $635 \text{ nm}$ ) for the improvement of evanescent field optical sensing, was possible using a hybrid formulation containing high molar content of zirconium propoxide ( $Zr(OPr)_4$ ) [168]. A photosensitive organically modified precursors containing 3-(Trimethoxysilyl)propyl methacrylate (MAPTMS) and  $Zr(OPr)_4$ , was used to create waveguides and vertically integrated sensing windows. A tantalum-based material having high refractive index of 1.87 was also synthesized and used as a thin layer deposited on top of the waveguide, in order to enhance the evanescent field penetration depth [169, 170]. These materials allow the fabrication of relatively complex structures such as Y splitters, couplers, and Mach-Zender interferometers.

We will not go into the details of using these materials for optofluidic chips here. The following section, we will discuss in details the chemistry, and the properties of these photosensitive hybrids, as well as their potential to be a part of the materials used for optofluidic chips fabrication, especially for evanescent field control and sensing applications.

## 2.4 Hybrid organic-inorganic materials for optofluidics

In general a hybrid material is a system in which both organic and inorganic moieties coexist. These organic and inorganic parts can be molecules as well as interconnected networks. Certain hybrids are jointly formed by a mineral network and a polymeric network each granting the material specific properties that are proper to each one of these networks. Thus one way to tune the properties of the material is by tailoring the ratio of organic to inorganic. Simply put, these materials exhibit at the same time glass like and polymer like behaviours.

As we have already seen, glass has been an attractive material for photonics as well as for optofluidics, due to its many advantages, among which its transparency in the spectral range of interest, and its inertness. The classical methods of bulk glass processing and patterning are however costly, complicated, time and energy consuming. An alternative method is proposed by a technique of soft chemistry called sol-gel. Using this technique it is possible to fabricate a three dimensional mineral network at low temperature: starting from the preparation of a colloidal solution that evolves into a sol, then transforms into a gel. Once the solvent is finally evaporated a solid oxide matrix is formed. These sol-gel techniques for glass fabrication, had found great success in thin film elaboration.

In addition to the formation of an oxide matrix by sol-gel, organic-inorganic hybrid molecules, offer the possibility to photo-sensitise the organic moieties. As such, these materials present as well, the attractiveness of photosensitive polymers such as SU-8 resist. This makes the vertical integration and the alignment of a device's layer easier than with other non photosensitive materials. In addition it offers, to a certain degree, a compatibility with the CMOS fabrication techniques and can potentially be combined along with other materials on a silicon platform. Moreover the formation of an organic matrix permits to attain thick layers deposition while preventing the collapse of the mineral network. Thus it can also be adapted for the fabrication of microfluidic systems, which usually requires high channel walls.

For the reasons briefly mentioned above, we suspect that these materials can be good candidates for the fabrication of optofluidic systems. We will develop these points in the remaining part of this chapter.

### 2.4.1 Definition of hybrid materials

Hybrid materials are composed of organic and inorganic interacting systems. The degree of interaction between these two systems depends on the type of bonds/forces that exist between them as illustrated in Figure 2.13.

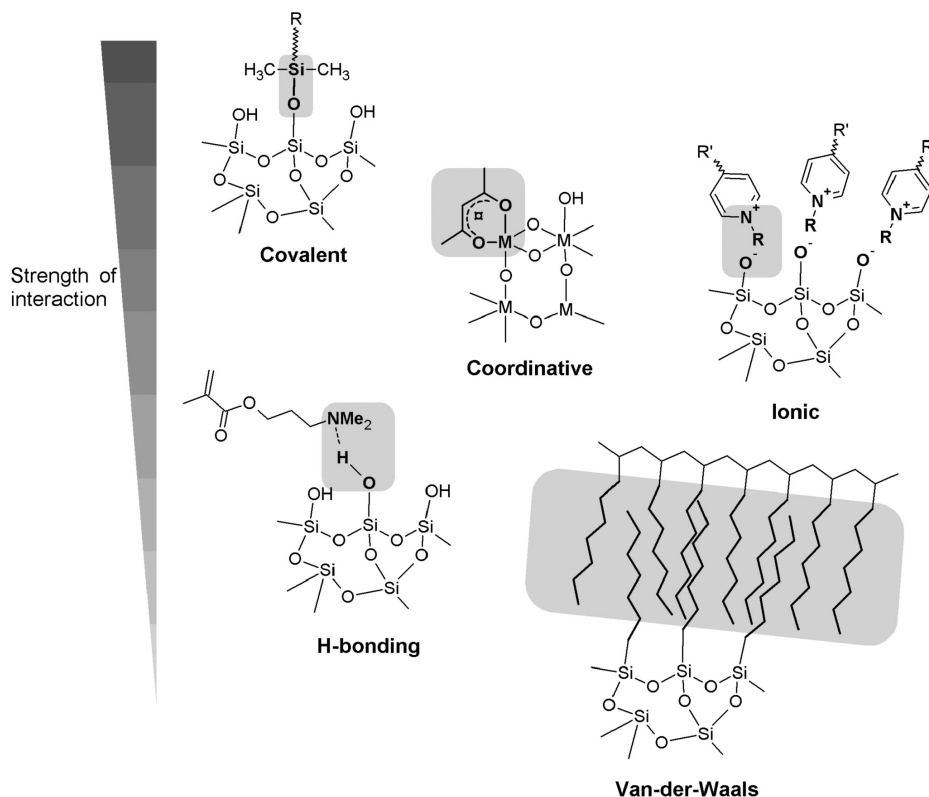


**Figure 2.13:** Typical interactions in hybrid materials and their relative strength [171]

Accordingly, they can be classified into two classes:

- Class I hybrids show weak interactions between the two phases, such as Van der Waals, hydrogen bonding or weak electrostatic interactions. This is the case of discrete inorganic moieties entrapped in an inorganic network (Figure 2.14a), or interpenetrating organic and inorganic networks (Figure 2.14b).
- Class II hybrids show strong chemical interactions between the components, such as covalent, strong coordinative, or ionic bonding. This is the case of discrete inorganic building blocks, covalently bonded to the organic polymer (Figure 2.14c), or covalently connected inorganic and organic matrices (Figure 2.14d).

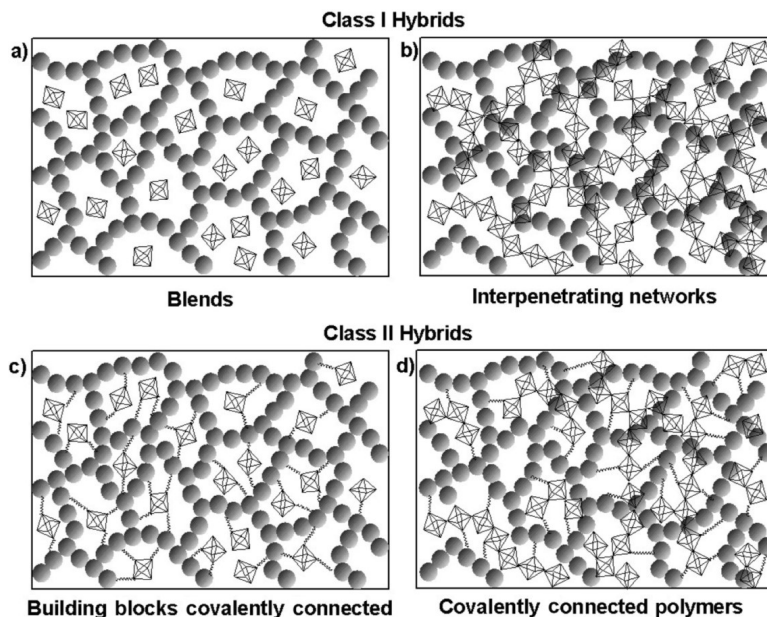


**Figure 2.14:** The two classes of hybrid materials, and their respective network formations. Connected filled in circles are polymeric chains, and empty octahedrons are inorganic entities [171].

A type of commonly used precursors for organic-inorganic networks is called ORganically MODified CERamics (ORMORCERs), where the mineral element can be any metal (silicon, zirconium, titanium, aluminum...). Their general formula is  $R'_n M(OR)_{4-n}$ . ORganically MODified SILoxanes (ORMOSILs) are one type of ORMORCERs, where the metal is a silicon atom. The general formula for ORMOSILs is  $R'_n Si(OR)_{4-n}$ .

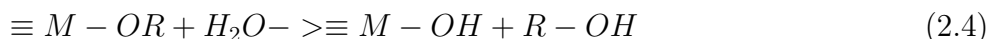
- $OR$  is an alkoxide group that grants the compound its ability to form the mineral network by a series of hydrolysis and polycondensation (that is called the sol-gel process). The number of  $OR$  groups determines the stiffness of the inorganic network.
- $R'$  is the organic group that can act in multiple ways:
  - It can be inert and when introduced to a mineral network, the precursor acts as a network modifier as in the case of methyl or phenyl groups.
  - It can be reactive in three different manners :
    - \* by acting as a network functionalizer, as in the case of amine groups that are able to form amino functionalized silica when introduced to  $Si(OR)_4$
    - \* by being a radically or a cationically polymerisable group. These radicals/cations can be photo-generated, which results in what we call organic-inorganic negative tone photoresists. This is the case of, epoxy, vinyl ether (VE) or methacrylate terminated radicals
    - \* and finally by being thermally polymerisable, as it can be the case for methacrylate terminated groups. If the occurrence of an acidolitic decrosslinked of this polymer is possible, and if the acids are photogenerated, this will result in what we call an organic-inorganic positive tone photoresist.

In order to show the potential of hybrid materials, we are going to explain the sol-gel process which leads to the mineral network formation. Then we are going to get into the role of the organic moieties that gives organic-inorganic materials their versatility.

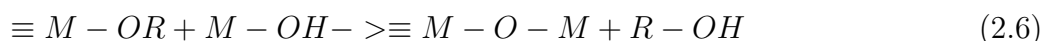
### 2.4.2 The sol-gel process: formation of the inorganic network

The inorganic network can be formed by a process called sol-gel. This process denotes the formation of the mineral network by hydrolysis and condensation of alkoxy groups  $OR$ . This is what causes the transition from a metal alkoxide solution, to a stable suspension of colloidal particles in a liquid called a sol, then to a continuous solid network bathing in a liquid phase called a gel.

The process starts with the formation of metal hydroxide  $M - OH$  groups as a result of the hydrolysis of alkoxides  $M - OR$ .



As soon as the first metal hydroxides  $M - OH$  are formed by reaction 2.4 the condensation begins. This results in the formation of  $M - O - M$  bonds, and by elimination of either alcohol, or more often water. As such the reaction of two  $M - OH$  groups will give water as by-product (reaction 2.5), whereas the reaction of  $M - OH$  with  $M - OR$  will release an alcohol molecule (reaction 2.6).



Both hydrolysis, and condensation can happen in two different pathways depending on the catalysis conditions. These two different pathways are briefly explained in the following two sections.

#### Acid catalysis

In an acid catalysis, the most negatively charged atom will be the target of the protons  $H^+$ . It is the oxygen in the  $OR$  or  $OH$ , that attracts a proton  $H^+$ : this is called the protonation and is an extremely fast reaction. This shifts the electronic cloud from the metal to the oxygen, which will increase the positive charge of the metal atom. As a result the metal becomes more electrophilic and more likely to be attacked by:

- $H_2O$  in the hydrolysis (This is indeed for  $OR$  groups only)
- $M - OH$  in the condensation

The higher the electrophilicity of the metal the more it is reactive. This can be due to the nature of the metal, or it can also be induced by the protonation reaction. This explains why certain metal alkoxides  $M - (OR)_4$ <sup>15</sup> are extremely reactive vis-a-vis the hydrolysis, which results in the precipitation of their corresponding metal oxides<sup>16</sup>. It also explains why unreacted metal alkoxide  $M - (OR)_4$  hydrolyzes faster than the partially hydrolyzed  $M(OR)_{4-x}(OH)_x$ .

Let us examine the case of Zirconium propoxide  $Zr(OC_3H_5)_4$  also known as  $Zr(OPr)_4$  and the trialkoxysilane, 3-(Trimethoxysilyl)propyl methacrylate,  $H_2C = C(CH_3)CO_2(CH_2)_3Si(OCH_3)_3$  also known as *MAPTMS*. On one hand,  $Zr$  is more positively charged than  $Si$  in an  $M - OR$

<sup>15</sup>M being Al, Ti, or Zr

<sup>16</sup>such as  $Al_2O_3$ ,  $TiO_2$ , or  $ZrO_2$

group, because on a Pauling scale the difference in the electronegativity of  $O$  and  $Zr$  is more than that of  $O$  and  $Si$ . So it is obvious that  $Zr$  in  $Zr(OC_3H_5)_4$  is more electrophilic than  $Si$  in  $Si(OCH_3)_4$  which in its turn is more electrophilic than the  $Si$  in  $H_2C = C(CH_3)CO_2(CH_2)_3 - Si(OH)_3$ <sup>17</sup>. On the other hand a mono substituted  $-Zr(OR)_3$  is less reactive than  $Zr(OR)_4$ . Thus by chelating  $Zr(OR)_4$  we can decrease its reactivity by reducing the number of alkoxide groups. So if a heterogeneous sol of MAPTMS and  $Zr(OR)_4$  is to be elaborated, a prehydrolysis of the MAPTMS and a chelation of the  $Zr(OR)_4$  should be performed separately before the mixing of the two solutions together.

### Base catalysis

The same reasoning is applicable for base catalysis, with the slight difference that, it is the most positively charged atom that is subject to the attack of deprotonated groups. The metal in the alkoxide, is the atom which is carrying the highest positive charge. Therefore it becomes the target of the nucleophilic attack from deprotonated hydroxyls  $OH^-$  or deprotonated  $M - O^-$ . These species will replace  $OR$  (hydrolysis and condensation) or  $-OH$  and  $-OR$  (condensation), respectively.

### 2.4.3 The formation of the organic network

We introduced the general framework of sol-gel chemistry for metal alkoxides. For hybrid materials, the organic groups are also an important component. In fact, they determine the usage of the material as a negative, or a positive tone resists. For a negative type resist, the polymerisation of the organic entities is triggered by UV insulation. Whereas for positive tone resists, the polymerisation is thermally provoked and the depolymerisation is UV induced.

In order to understand how these two types of resists can be elaborated we are going to address 4 different points:

- the role of the photoinitiator
- the photopolymerisation of methacrylates to form polymethacrylates,
- the thermal polymerisation of VEs, and carboxylic acids to form hemiacetals,
- and finally the photo-induced acid depolymerisation of hemiacetals.

#### 2.4.3.1 Photoinitiators

Photoinitiators are photosensitive compounds, that are able to absorb a certain energy of light and undergo a structural change that will result in the creation of either free radical  $I^\bullet$ , or free ion  $I^\pm$ . These photogenerated compounds are responsible of triggering either the polymerisation or the depolymerisation reactions of the organic entities.

The choice of the photoactive compound depends on three criteria:

- its ability to initiate the polymerisation/ depolymerisation of the organic entities of the ORMOCERs/ copolymers

---

<sup>17</sup>Given that C is less electronegative than O

- its sensitivity to the wavelength of irradiation
- its solubility in the sol.

Accordingly we distinguish two types of photoinitiators with respect to the polymerisation type they are able to initiate:

- radical photoinitiators able to crosslink acrylates, methacrylates, polyurethane, unsaturated polyesters-styrene and thiol-polyenes, through the generation of free radicals that can initiate such reaction.
- ionic photoinitiators that are able to crosslink VEs or epoxy groups, through the generation of either cations or anions to initiate the polymerisation. They are also able to decrosslink acetal groups. Among this type of photoinitiators there are photoacid generators (PAGs) and photobase generators(PBGs).

We also distinguish different types of photoinitiators with respect to their light sensitivity:

- g-line (435 nm) and h-line (405 nm) sensitive that can be excited in the visible range (400 – 450 nm).
- The i-line (365 nm) sensitive that can be excited in the long wave UV (315 – 400 nm), also called the UV-A.
- The mid wave UV (280 – 315 nm) also called UV-B sensitive.
- 247 nm and 193 nm sensitive, that can be excited in the short wave UV also called UV-C or more commonly deep UV.

The absorption of a photon by the photoinitiator creates a cascade of energetic states. Initially a high-energy singlet state is produced, then it is converted to a more stable, but less energetic, triplet state by intersystem crossing. This triplet state may decay by various mechanisms: phosphorescence, quenching by monomers or oxygen, or finally by producing free radicals or ions as seen in Figure 2.15.

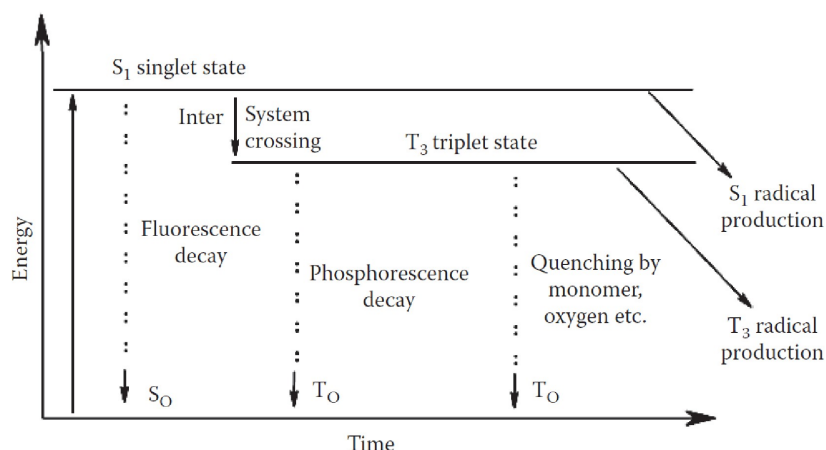


**Figure 2.15:** Jablonsky diagram, energy levels vs. time [172]

The rate of initiation  $r_i$  is directly related to the incident light intensity  $I_0$ , the sample thickness  $l$ , the absorptivity  $\epsilon$ , the concentration of the photoinitiator  $[PI]$ , and the quantum yield of initiation  $\Phi_i$  (number of initiating species produced per photon absorbed):

$$r_i = \Phi_i I_0 [1 - \exp\{-\epsilon l [PI]\}] \quad (2.7)$$

Thus when choosing a photoinitiator its quantum yield  $\Phi_i$  and its absorptivity  $\epsilon$  are the parameters that determine the conversion rate of the polymerisation reaction. If the absorptivity peak of a photoinitiator is not centered around the wavelength of insulation an increase in the concentration of the photoinitiator can compensate for the low value of  $\epsilon$ . This increase in the concentration of the photoinitiator should not surpass a rough 5%, because it results in low molecular mass of the polymer (this will be addressed in details after the photopolymerisation reaction is explained).

### 2.4.3.2 The radical photopolymerisation of methacrylates

A hybrid precursor containing methacrylates as its organic part, can be used to fabricate a negative tone photoresist. This negative working aspect is a result of the photopolymerisation of methacrylates. They are radically polymerisable entities. Since they are not photosensitive to the commonly used UV sources for photolithography, a photoinitiator is essential to generate these radicals.

In order to illustrate how this polymerisation proceeds, let us consider the methacrylates as a monomer  $M$ . Upon irradiation of a suitable photoinitiator, followed by radical generation  $I^\bullet$ , the polymerisation is initiated:



Then in the same manner  $IM^\bullet$  successively reacts with other monomers until formation of an oligomeric chain  $IM_n^\bullet$ , this reaction is called the propagation reaction:



When it meets another oligomer  $IM_m^\bullet$ , it terminates by forming a polymer  $IM_{n+m}I$ :



At any stage of this chain reaction, an oxygen<sup>18</sup> can interact with the system, and is able to form an  $I(M)_iO_2$  thus blocking the chain propagation. This oxygen inhibition, especially at the air-film interface, is the main inconvenience of radically polymerisable systems [173]. The most efficient method to overcome oxygen inhibition is the use high light irradiance, that can provoke high initiation rate [174]. In a UV cured polyurethane-acrylate for example the degree of conversion reaches nearly 100% at  $600 \text{ mW/cm}^2$  [175]. Other methods include the use of a physical or chemical barrier [176] that limit the oxygen presence to that dissolved in the photoresist formulation.

If the concentration of the photoinitiator in the sol is high, many radical will be generated. This will initiate the formation of many  $IM^\bullet$ . Due to their high concentration in the sol, the reaction will not have the time to propagate and the oligomers will recombine rapidly. This will lead to the formation of smaller polymeric chains.

---

<sup>18</sup>Either dissolved in the photoresist formulation or introduced by the photoresist surrounding at the surface and down to a certain diffusion depth.

### 2.4.3.3 The thermal crosslinking of VEs and carboxylic acids

A polymer containing a carboxylic acid is soluble in an aqueous solvent. In order to reduce its solubility the COOH groups need to be protected with the use of a reactive compound such as VEs. These groups can thermally copolymerize with carboxylic acids under very strict conditions to form cross-linked networks with an acetal structure [177, 178] as illustrated in Figure 2.16.

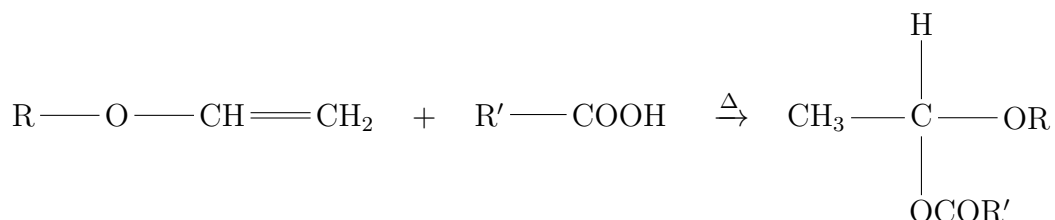


**Figure 2.16:** The thermal polymerisation reaction of VE and carboxylic acid to form hemiacetal groups,

The mechanism of this reaction is not well explained in the associated literature. One might suspect that the hydrogen from the carboxylic acid is capable after a sufficient thermal energy flow to dissociate and cleave the VE's double bond. The reaction rates increase as acidity of carboxylic acid increases [177, 179]. By comparing meta and para benzoic acids reaction rate, Mukaiyama and coworkers concluded that, there is also an effect of steric hindrance in benzoic acids<sup>19</sup>.

Also, the same reaction is known to happen in high yields in the presence of a catalytic amount of a strong acids, such as hydrochloric acid, sulfuric acid and phosphoric acid [179] as illustrated in Figure 2.17. This is because the acid is capable of cleaving the VE's double bond.

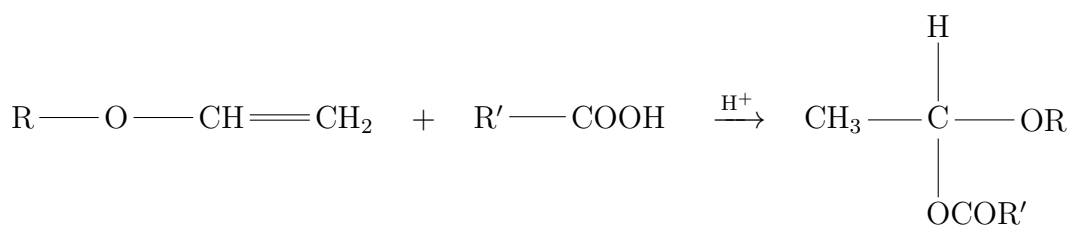


**Figure 2.17:** Acid catalysed addition reaction of VEs and carboxylic acid to form hemiacetal groups.

In addition, the solvent used has a remarkable effect on the reactivity. The possible formation of complex from carboxylic acid and solvent containing ether linkage such as dioxane, competes with the formation of the complex from VE and carboxylic acid.

### 2.4.3.4 The photoinduced decrosslinking of hemiacetals

After UV insulation, the PAG present in the film of the resist, generates strong acids. The hemiacetals crosslinks can be cleaved acid-catalytically via protonation by these photogenerated acids and subsequent hydrolysis to give alcohol and aldehyde, as seen in Figure 2.18. This reaction deprotects the COOH groups, making them soluble in the developer.

<sup>19</sup>Rates are lower than expected for their acidity

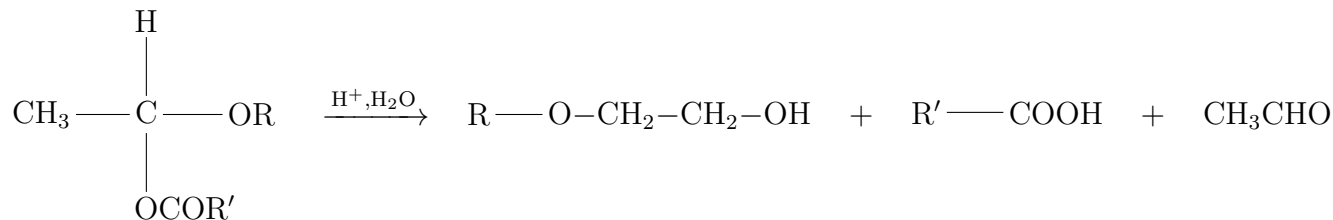


**Figure 2.18:** The acidolitic de-crosslinking of hemiacetal groups

It is important to note that, in the presence of an acid, VE groups can also undergo a competing reactions of cationic polymerization [180,181], and an acidolysis by photogenerated acids depending on the process conditions [182] such as the soft baking temperature and the exposure (see Appendix B for details). It was also demonstrated that unless acid groups of the polymer are 20 times the number of VEs of the crosslinker monomer the cationic polymerisation of VE is more probable than the copolymerisation with a COOH [177].

#### 2.4.4 Applications

In the following sub-sections we are going to introduce how the reactions explained above can be put in practice to create:

- a negative photoresist based on MAPTMS and  $Zr(OPr)_4$  that can be used to fabricate optical circuits
- and a positive photoresist based on a polyamic acid (**PAA**), poly(pyromellitic dianhydride-co-4,4'-oxydianiline) (**PMDA-ODA**), 4-vinyl ether-phenyltriethoxysilane (**VEPTES**) and 1,3,5-tris[(2-vinyloxy)ethoxy]benzene (**TVEB**) that is adapted for rapid prototyping of microfluidic channels by laser writing.

The aim being, to use them for the fabrication of optofluidics platforms for evanescent field manipulation and sensing applications. The perspective of using hybrid materials for the fabrication of sensing platforms has begun to develop, especially for evanescent field sensing applications [168]: it enabled the fabrication of high refractive index layer to be deposited on a slot waveguide to increase the penetration depth of the evanescent field, as we already said in section 2.3.4.2.

##### 2.4.4.1 Negative working photoresist for integrated optics

Since 1992 works of different groups have shown the effectiveness of different compositions based on a mixture of MAPTMS and  $Zr(OPr)_4$  chelated with MAA [183–185], for the fabrication of optical waveguides. In this material the silicon introduced by the MAPTMS and the zirconate introduced by the  $Zr(OPr)_4$  will jointly form the mineral network. The compositions studied had different ratios of MAPTMS to  $Zr(OPr)_4$  and MAA. The following configuration MAPTMS: $Zr(OPr)_4$ :MAA will be used to identify the different compositions. As such 10:X:X represents a formulation where the ratio of MAPTMS to  $Zr(OPr)_4$  is 10 to X.

The composition and the process is optimized for the use in the near infrared region more specifically at 1300 nm by reducing the residual OH groups in the sol. The addition of  $Zr(OPr)_4$  to the polymethylmethacrylate network is used to adjust its optical properties, notably to increase the refractive index [183,184]. The zirconate content increases linearly and rapidly the refractive

index as seen in Figure 2.19 due to its high atomic size and strong polarizability which provoke a more important molar refraction. It also enhances the quality of the waveguide profile after revelation since it leads to a well-polymerized and hydrophilic surface under UV-illumination [185].

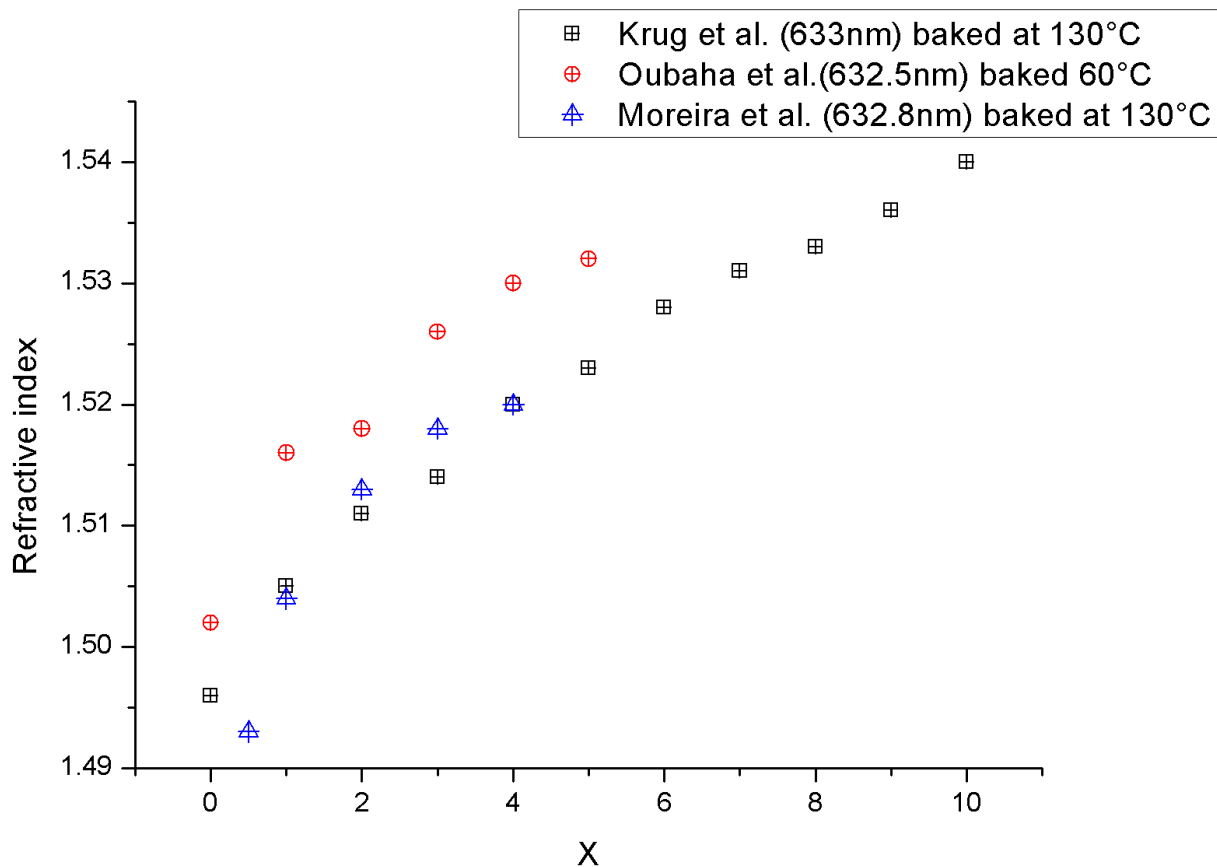


**Figure 2.19:** The refractive index increase as a function of the  $Zr(OPr)_4$  molar loading as per multiple references [164, 183, 184].

This can yield a maximum index difference of 0.04 between a composition having no  $Zr(OPr)_4$  content and a composition having equal molar ratio of both precursors. As such two different compositions of this photoresist can be used for the elaboration of the buffer layer and the guiding layer, while keeping the refractive index as close as possible to that of optical fibers in order to reduce the coupling losses.

We can as well note that the samples baked at higher temperature, exhibit a lower refractive index. As per Oubaha [165], this is due to the increase in the network connectivity. This leads to a decrease in the molar refraction that is reflected as a decrease in the refractive index as well. As a summary this MAPTMS- $Zr(OPr)_4$  system can be used to constitute the multiple layers of an integrated optical circuit by tailoring the  $Zr(OPr)_4$  content.

A special attention to the UV induced refractive index step was drawn by Coudray et al. [163]. A step of 0.013 can be attained by using the adequate photoinitiator (Irgacure 1800), and lower

soft baking temperature, or no soft baking at all. While the overall refractive index was found to increase with increased prebake temperature. This is because higher soft bake temperatures affects most of all the reticulation of the mineral network. This leads to a rigid network limiting the mobility, hence the reactivity of the organic moieties upon insulation.

This photoresist however present some disadvantages such as poor mechanical properties and adhesion to Si and glass, as well as the inhibition by oxygen of the radical polymerization leading to the waveguide formation. Even though it cannot compete with the index difference offered by silicon, and silicon nitride waveguides it can offer an acceptable trade off between a good light confinement and low coupling losses.

#### 2.4.4.2 Positive working photoresist for microfluidics

Generally speaking, a positive photoresist is adapted for rapid prototyping of microfluidic chips using direct laser writing, as it decreases laser writing time. The use of such a photoresist in research and development is essential. This is why a positive photoresist based on PMDA-ODA protected by the addition of TVEB and VEPTES was synthesised and studied in our labs [167,186].

We have explained in section 2.4.3.3 and 2.4.3.4, the reactions of crosslinking of VE and COOH and the decrosslinking of hemiacetals. Many research groups have exploited these reactions in order to fabricate positive working resists [177,178,187]. Thus a photosensitive composition can be formed with:

- a co-polymer that is insoluble an aqueous solvent and composed of:
  - a polymer having carboxyl groups<sup>20</sup>, that is soluble in an aqueous solvent
  - a VE monomer as a crosslinker or dissolution inhibitor for the polymer.
- and a photosensitive compound: a PAG

The main purpose being to tune the solubility of the material in an aqueous solvent. The steps of this protection/ de-protection are illustrated in Figure 2.20.

---

<sup>20</sup>Mostly located in the side chains and not in the polymer body, to limit steric effects [177,188]

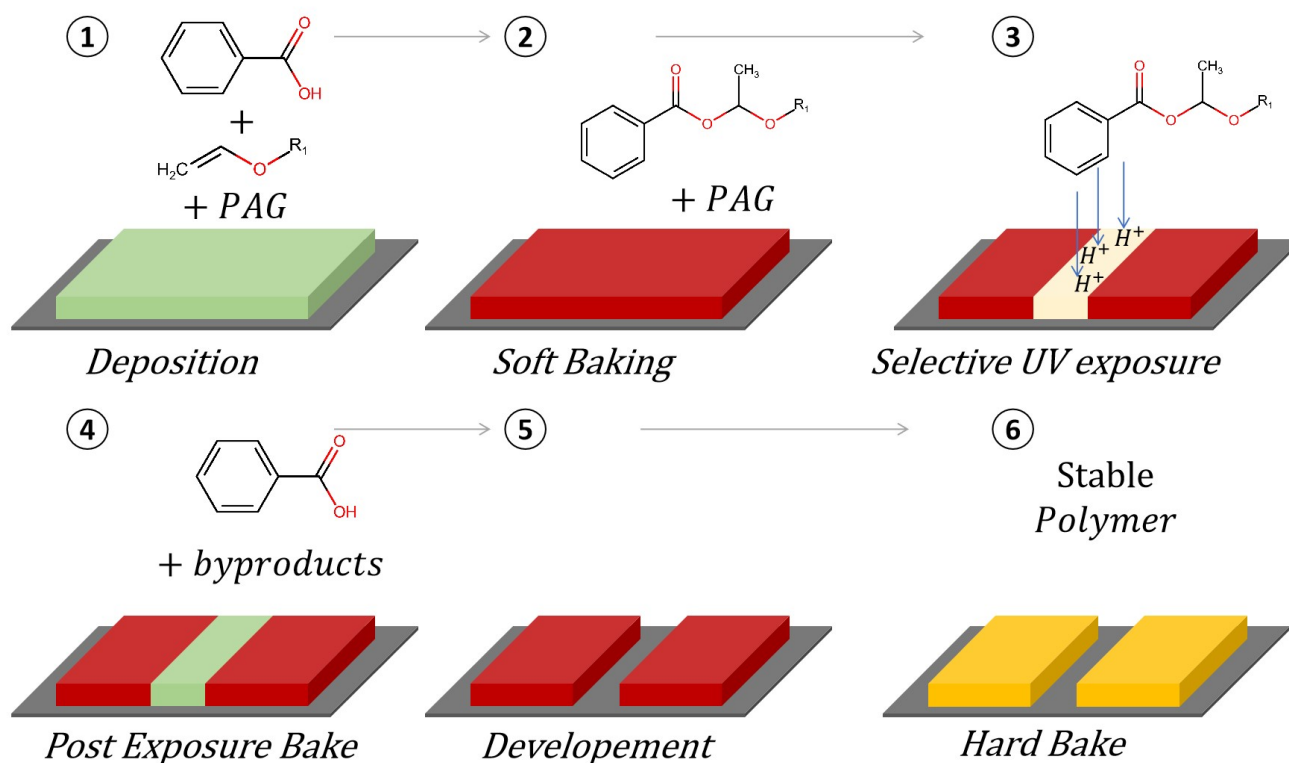


**Figure 2.20:** The steps for processing the positive photoresist based on PMDA-ODA and a VE crosslinker. The changes in the material chemistry are highlighted at each step. The green coded material is the only one soluble in an aqueous solvent.

The protection of the  $\text{COOH}$  groups of the polymer, happens during the soft bake (**SB**) (step 2), then the deprotection takes place after the localised UV exposure (step 3) and during the post exposure bake (**PEB**) (step 4), in order to create a contrast between the two regions. This action is only enabled by the presence of an adequate PAG, that generates strong acids upon irradiation. This allows the development of a positive image in the material (step 5). Once the surface is patterned the sample should be hard baked at high temperature to transform the complexed compounds into a stable polymer (step 6).

As we already said in section 2.4.3.3, the reaction of VEs and carboxylic acids gives hemiacetal esters in the presence of strong acids, such as hydrochloric acid, sulfuric acid and phosphoric acid [179]. Nevertheless in the papers tackling the fabrication of this type of photoresist, VE is said to react with carboxylic groups upon thermal treatment [177, 178, 187]. This reaction is responsible for the protection of  $\text{COOH}$  groups by VE groups and is schematically represented in Figure 2.21. The deprotection of the previously formed acetals is also represented, and is enabled by the catalytic effect of the  $\text{H}^+$ . Thus the acids generated during the exposure are never consumed. They are regenerated after each deprotection, and this is what gives these resists their chemically amplified character. As such only small amounts or catalytic amounts of acids are needed.

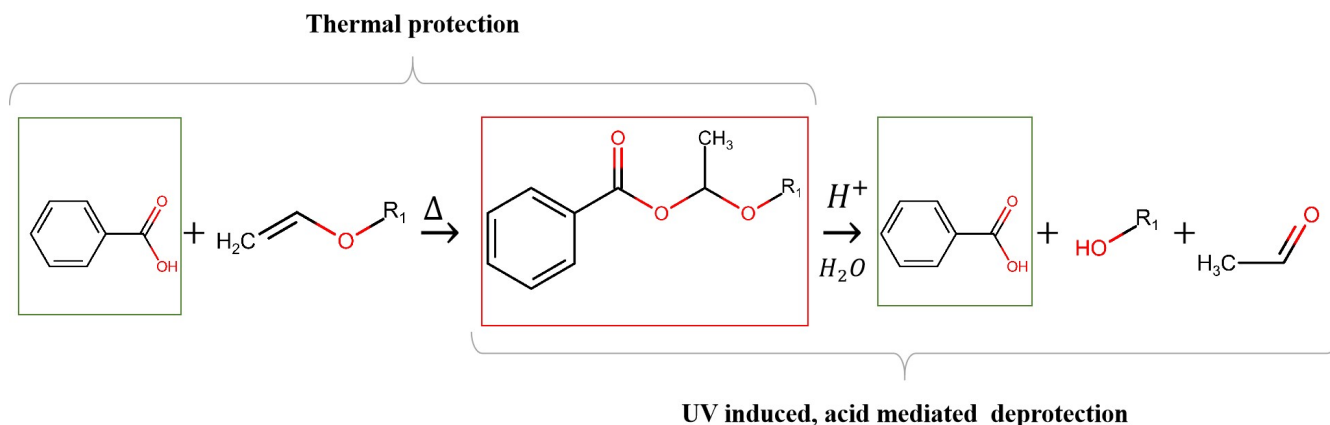


**Figure 2.21:** The protection and deprotection of  $COOH$  groups with VE groups. The green and red squares around the different groups indicate that they are either soluble or insoluble in an aqueous solvent.

The positive photoresist that we are going to work with is based on a polymer, and 2 DIs: a polyamic acid PMDA-ODA, VEPTES, and TVEB respectively. The reactive groups are carboxylic acids  $COOH$  introduced by the PMDA-ODA and the VEs  $O-CH=CH_2$  introduced by the TVEB and the VEPTES. Among these compounds only the VEPTES is a hybrid precursor. This composition based on organic and hybrid compounds<sup>21</sup> was formulated in our labs [167, 186], and is constituted of:

- PMDA-ODA, a polyamic acid (**PAA**) as a backbone
- TVEB for the crosslinking of the different PMDA-ODA linear chains and for the protection of the  $COOH$  groups of the PMDA-ODA
- VEPTES for the formation of the inorganic network as well as for the inorganic network, in addition of being a dissolution inhibitor like the TVEB

The precursors are illustrated in Figure 2.22

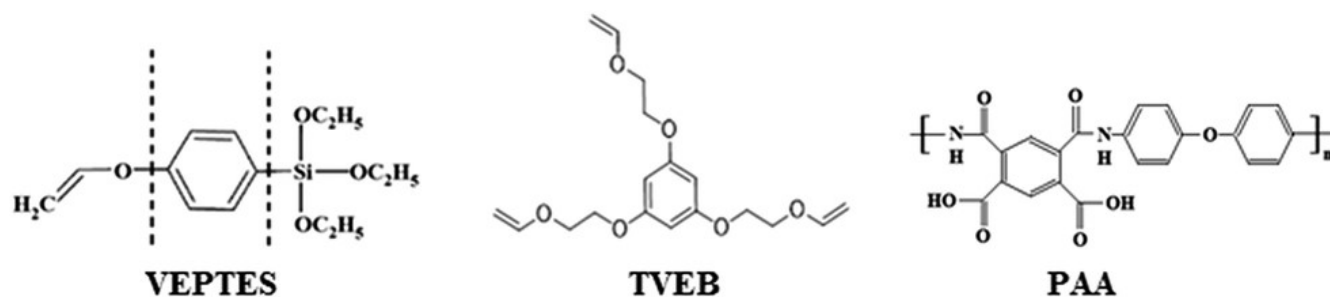


**Figure 2.22:** The precursors used for the elaboration of the co-polymer, used in the positive photoresist composition.

The PAG used is (5-propylsulfonyloxyimino-5H-thiophen-2-ylidene)-2-(methylphenyl)acetonitril (PTMA)<sup>22</sup>, formerly commercialized under the name Irgacure PAG 103 by BASF. It is able to

<sup>21</sup>Both VE containing molecules were synthesized at Institute Charles Gerhardt Montpellier by the "Chimie Moleculaire et Organisation du Solide" (**CMOS**) group.

<sup>22</sup>It is a non ionic oxime sulfonate PAG.

generate n-propane sulfonic acid by N-O bond cleavage upon irradiation. A mechanism for the cleavage is proposed in [189].

The VEs from the TVEB and the VEPTES, ensure the thermal crosslinking with the *COOH* groups of the PMDA-ODA chains. These precursors play the role of dissolution inhibitors, through the protection of *COOH* groups. The de-protection of these groups, leading to the positive working aspect of this resist, is mediated by the generated acids upon insulation in the UV. These crosslinking and decrosslinking reactions are presented in Figure 2.23.

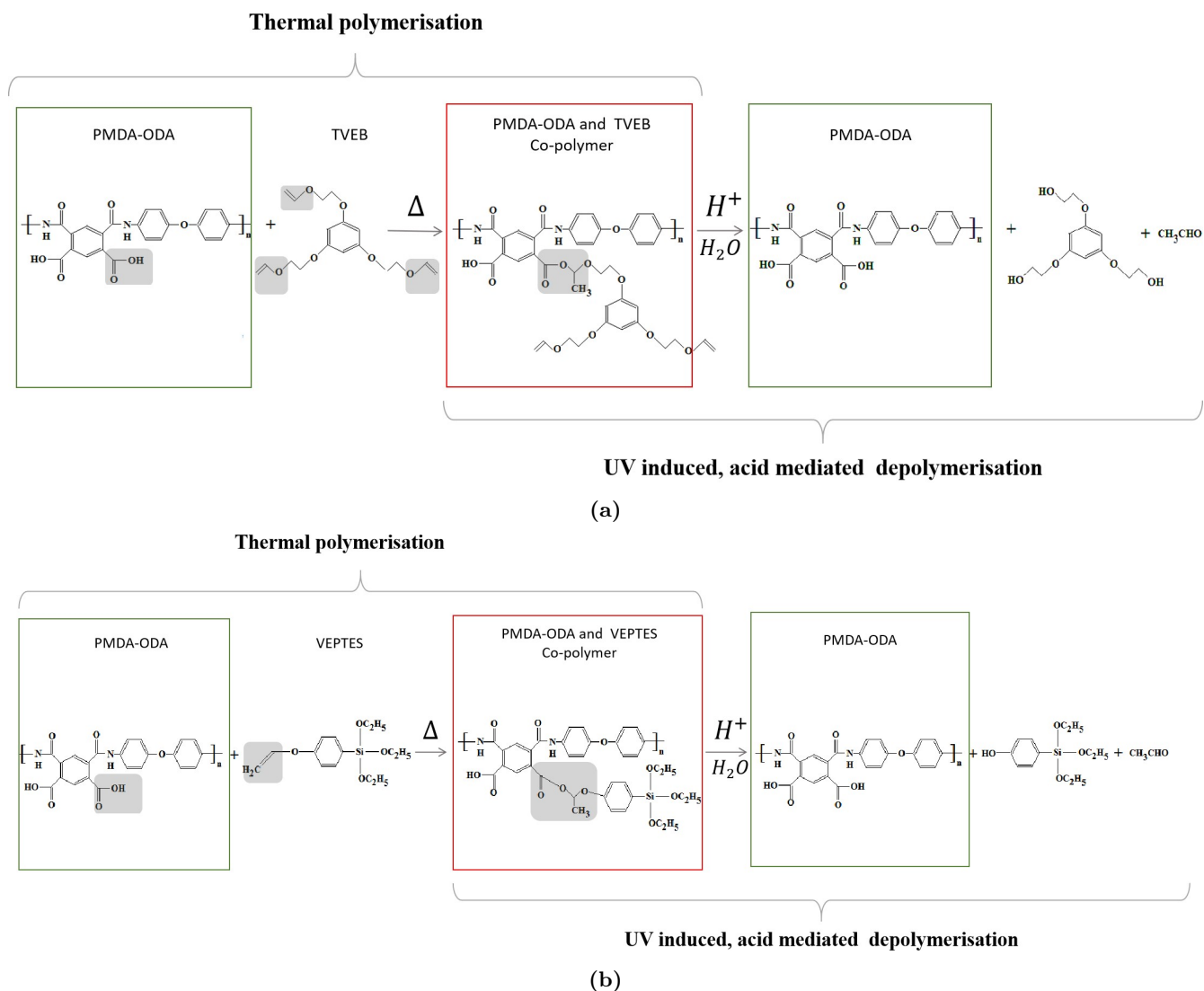


**Figure 2.23:** Polymerisation of PMDA-ODA and (a)TVEB, (b)VEPTES, via VE and *COOH* functions, resulting in an insoluble copolymer. This is followed by the UV depolymerisation of the resulting copolymers, leading to deprotection of the *COOH* groups of the PMDA-ODA. The green and red squares around the different compounds indicate that they are either soluble or insoluble in an aqueous solvent.

The functional groups are highlighted in grey.

It was deduced by Fourier Transformed IR (**FTIR**) spectroscopy that a composition of molar ratio 10:3:3 (PMDA-ODA:TVEB:PTMA)<sup>23</sup> diluted in NMP, has showed a  $43 \pm 2\%$  conversion rate of amide C=O groups after 15 minutes thermal bake at  $110^\circ C$ . These results were confirmed by a contact angle measurements that showed an increased hydrophobicity of this composition when compared to PMDA-ODA film, with a contact angle increasing from  $50 \pm 2^\circ$  to  $90 \pm 2^\circ$  which can be an indicator of the reduction of *OH* groups. In addition the essential parameter, that is the reduced solubility in aqueous solvent (2.38% wt of Tetramethylammonium hydroxide (TMAH)), was also confirmed by conducting a dissolution of PMDA-ODA film as well as PMDA-ODA complexed with TVEB film: indeed the later was insoluble, in contrast with the former. It is important to note here that at lower baking temperatures no change in the solubility was found even for prolonged baking times.

On the other hand a composition of PMDA-ODA:VEPTES:PTMA with a molar ratio of 10:5:3, that was subject to the exact same treatment and characterisation showed lower reactivity with a conversion rate of  $14 \pm 2\%$  only. Finally an optimised composition having a molar ratio PMDA-ODA: TVEB: VEPTES: PTMA, of 10:3:5:3 was prepared as per the process flow in Figure 2.24.

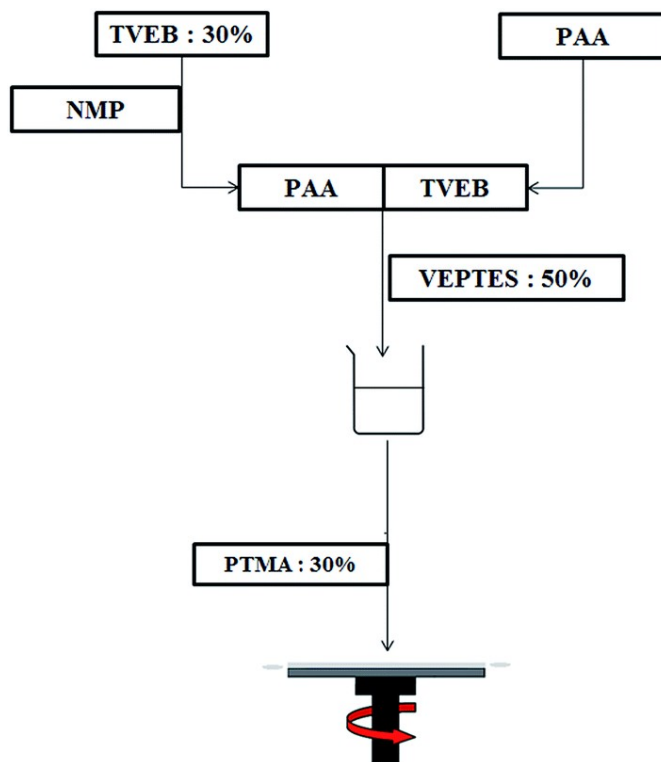


**Figure 2.24:** The process flow for the photosensitive resist elaboration.

This formulation was used to fabricate  $110 \mu m$  wide and  $3 \mu m$  thick channels. However a  $3 \mu m$  thick layer is not adapted for microfluidic applications where higher channel walls are necessary. Thus it is essential to investigate the potential of this photoresist to be utilised for such application. This subject will be the main focus of Chapter 4.

<sup>23</sup>the 10 molar units of PAA indicate the number of PAA repetitive units, having each a molecular weight of  $418 g/mol$ .

## 2.5 Polyamic acid positive resists

Since the polymer we are using is a PAA that will later transform during the hard bake into its stable form a Polyimide, we find it necessary to briefly introduce the resists that were fabricated using this polymer. This paragraph is also destined to show how the choice of the composition of PAA and a VE crosslinker was made. Polyimides are widely known for their use in microelectronics fabrication and packaging due to their outstanding mechanical and thermal properties and low dielectric constant. Their use for microfluidic applications is not as common. Nevertheless, they are used for encapsulating biomedical implants, which asserts on their biocompatibility and long-term inertia in vivo [190]. In order to facilitate their patterning many attempts were made in order to fabricate a positive working photoresist based on PAA.

To our knowledge the earliest attempt to make a positive working polyamic acid photoresist was disclosed in U.S. Pat. No. 4,093,461 [191]. This was done by simple admixture of a PMDA-ODA with a photosensitizer: a diazide. They are known to be water-insoluble, hydrophobic, and organic solvent soluble. Once exposed to light, they are converted into water soluble derivatives. Regardless of the PMDA-ODA solubility in the alkaline developer, it was claimed that it is the diazide and its derivative (upon photolysis) that grant the photoresist its positive working character. After development, the patterns essentially constituted of PAA are converted by heat to a thermally and chemically stable polyimide.

This attempt and others to follow had limited success because PAA exhibit such a high dissolution rate in alkaline solutions even with the addition of diazide sensitizers. This high dissolution rate in aqueous solution is directly linked to the presence of *COOH* groups in PMDA-ODA. This is why most of the following studies on a PMDA-ODA based photoresist tried to protect the *COOH* groups by the means of the addition of a dissolution inhibitor that reacts with these functional groups.

For example in the U.S. Pat. No. 4,093,461 [192] they attempted to regulate the PAA solubility by thermally converting some of the carboxylic acid groups to imides, which are not base-soluble. In the case of PMDA-ODA a temperature of 160-170 degrees is required to achieve an acceptable contrast, while the diazide sensitizer doesn't support such high temperature. Another attempt consisted of protecting these carboxylic acid groups by the means of a partial esterification reaction [193]. Others [178,194–196], have used the crosslinking of a vinyl ether (*VE*) and a carboxylic acid in order to protect the later groups. This method constituted the starting point for the work of Mechref et al. [167,186], with the slight variation that a fraction of the used crosslinker was replaced with the hybrid precursor VEPTES, in order to tune the mechanical and thermal properties of the material.

## 2.6 Processing methods of photoresists

In order to utilise these photoresists for the fabrication of waveguides and microfluidic channels, we must utilise a deposition method such as spin coating along with a photoinscription method such as laser writing. The theory of these processes is highlighted in the following subsections.

### 2.6.1 Deposition by spin coating

Among other deposition techniques, spin coating is the most used for thin film deposition on the industrial scale. Mainly because it gives films of reproducible thickness, as well as the fact that it permits the coating of one surface as opposed to dip coating for example, which could be very resource wasteful on the manufacturing level. Spin coating has also the advantage to be a very rapid deposition technique.

During spin coating, an interplay between the centrifugal forces and the viscous forces will cause the resist to spread and set to its final film thickness. This later will depend not only on the parameters chosen for the spin process but also on the nature of the resin, this means its viscosity, drying rate, percent solids, and surface tension. As illustrated in figure 2.25, four stages can define a typical spinning process.

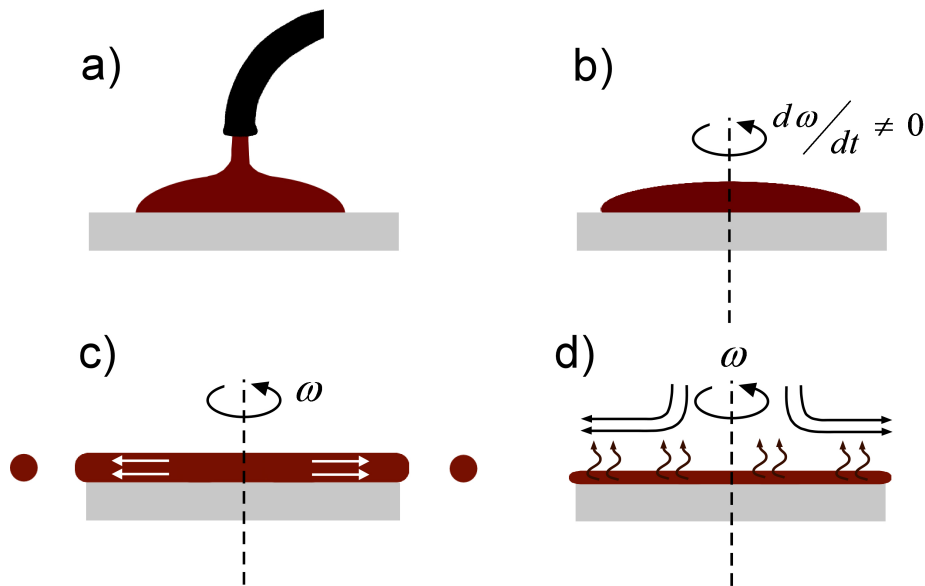


**Figure 2.25:** The four stages of the spin coating process: (a) dispense, (b) ramping up, (c) spinning at constant rate, (d) solvent evaporation [197]

- The dispense stage: during this step the fluid is deposited onto the substrate. The two most common methods of dispense are static dispense, and dynamic dispense. Static dispense is simply depositing a small puddle of fluid in the center of the substrate. Dynamic dispense is the process of dispensing while the substrate is turning at low speed (typically around  $500\text{ RPM}$ ). During this step the film thickness is considered to be  $h_0$ .
- Ramping up: in order to reach the final spin speed  $\omega$ , an acceleration phase is essential. During this step excess fluid is drawn off the substrate. Ultimately, the wafer reaches its desired speed and the fluid is thin enough that the viscous shear drag exactly balances the rotational acceleration.
- Spinning at constant speed: this step is characterized by gradual fluid thinning due to the centrifugal force. Fluid thinning is generally quite uniform, though with solutions containing volatile solvents, it is often possible to see interference colours.

- Solvent evaporation: in order for a solid film to be produced the majority of the solvent must evaporate. Even though solvent evaporation is present from the start of the process, during this step the evaporation of any volatile solvent species will become the dominant process. Any further thinning during this step is attributed to solvent evaporation.

Until now the most widely used model and the most complete explanation of the spin coating process, remains the one introduced by Meyerhofer [198] for Newtonian fluids having a viscosity  $\eta$ , and a volumetric mass  $\rho$ , cast on a disk rotating at a speed  $\omega$ .

$$h_f = x \left[ \frac{e}{2(1-x)K} \right]^{(1/3)} \quad (2.11)$$

where:

- $x$  is the solid content
- $e$  is the evaporation rate expressed as  $e = C\sqrt{\omega}$ ,  $C$  is a proportionality constant that depends on whether airflow above the surface is laminar or turbulent, and on the diffusivity of solvent molecules in air
- $K$  is the flow constant expressed as  $K = \frac{\rho\omega^2}{3\eta}$ .

This results in a relation between  $h_f$  and  $\omega$  as follows:

$$h_f = x \left[ \frac{3\eta C}{2(1-x)\rho} \right]^{(1/3)} \omega^{-1/2} \quad (2.12)$$

The evaporation rate  $e$  depends very strongly on how fast the vapor phase above the liquid is removed. If it is assumed to vary as the square root of the spin speed, a good agreement is found between the model and the experimental results<sup>24</sup> [198]. This is not always the case, because even in Meyerhofer's work, very dilute solutions didn't follow this  $\omega^{-1/2}$  dependency.

### 2.6.2 The Laser writing model for photoresists

This section is dedicated to a brief emphasis on existing models that describe the laser writing process in photoresists. Many models were proposed in order to describe the feature size produced by direct laser writing upon a photoresist relative to various experimental parameters [199–201].

Since the cured line is the building block for any pattern, it is important to build a correlation between linewidth and the laser parameters for each photoresist. With each passage of the laser on photoresist a cured line is created. The maximum width of a cured strand is called the 'cured line width'  $L$ . A couple of key parameters have a direct effect on the geometrical and dimensional accuracy of the laser written microstructures, more specifically on  $L$  and the cross sectional shape of a cured line. These parameters are:

- the laser technical parameters such as: laser power  $P$ , and laser scanning velocity  $v$  which associate to define  $\Omega = P/v$  expressed in  $[\frac{mJ}{mm}]$ . These variable affects the dynamic dose that can be expressed by multiplying the irradiance  $I$  by exposure time  $dt$ :

$$D = \int_{-\infty}^{+\infty} [I \cdot dt] \quad (2.13)$$

---

<sup>24</sup> The predictions of the spinning model were tested on commercial positive-working photoresists: Shipley AZ-1350 and Mark II'

- and the properties that are intrinsic to the photoresist, such as penetration depth and the critical energy dose.

Let us consider the case of a laser moving in the  $\eta$  direction at a scanning speed  $v$ , as illustrated in Figure 2.26. According to the reference system illustrated we may define a radial variable  $\rho$  such that  $\rho^2 = \eta^2 + \zeta^2$ .

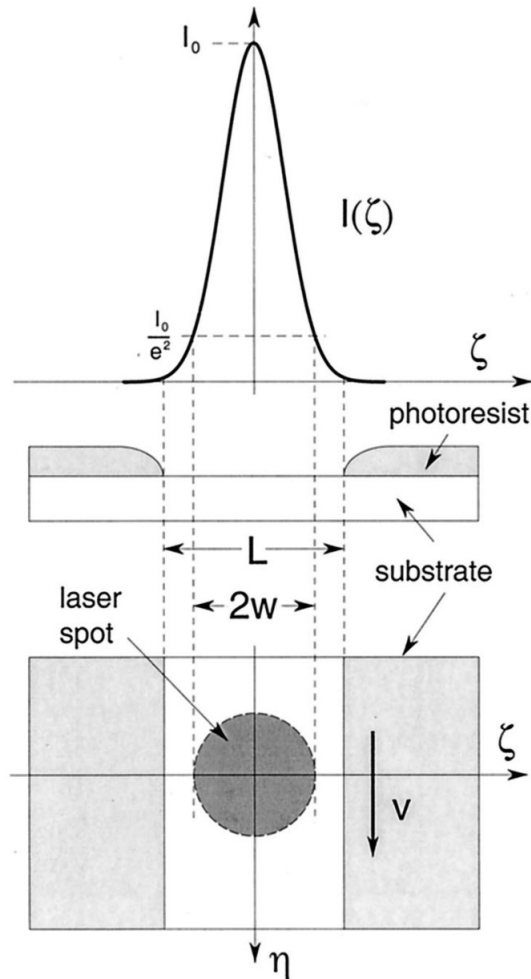


**Figure 2.26:** Schematic of the laser spot profile (Gaussian profile) and the line drawn on the photoresist film, together with the reference system used [199].

We can differentiate two major regimes depending on the laser irradiance distribution after being focused by an objective of focal length  $f$ , and numerical aperture  $NA$ . Assuming that the objective is diffraction limited, the spot size and its profile will depend on how much the objective changes the intensity distribution of the originally gaussian beam. For that we need first to define the truncation relation  $\gamma = w/fNA$ .  $\gamma$  indicates the extent to which the laser beam is limited by the aperture of the objective.

- For  $\gamma \ll 1$ , it is the case of a non-truncated beam. Which is a Gaussian beam that is not affected by the objective.

- For large truncation  $\gamma \gg 1$ , that is where the smallest focal spot is obtained. Secondary diffraction rings appear as an Airy disks, and an important fraction of the beam power is wasted, because the spot diminishes exponentially with the truncation relation.

The transition between these two regimes can be seen in Figure 2.27

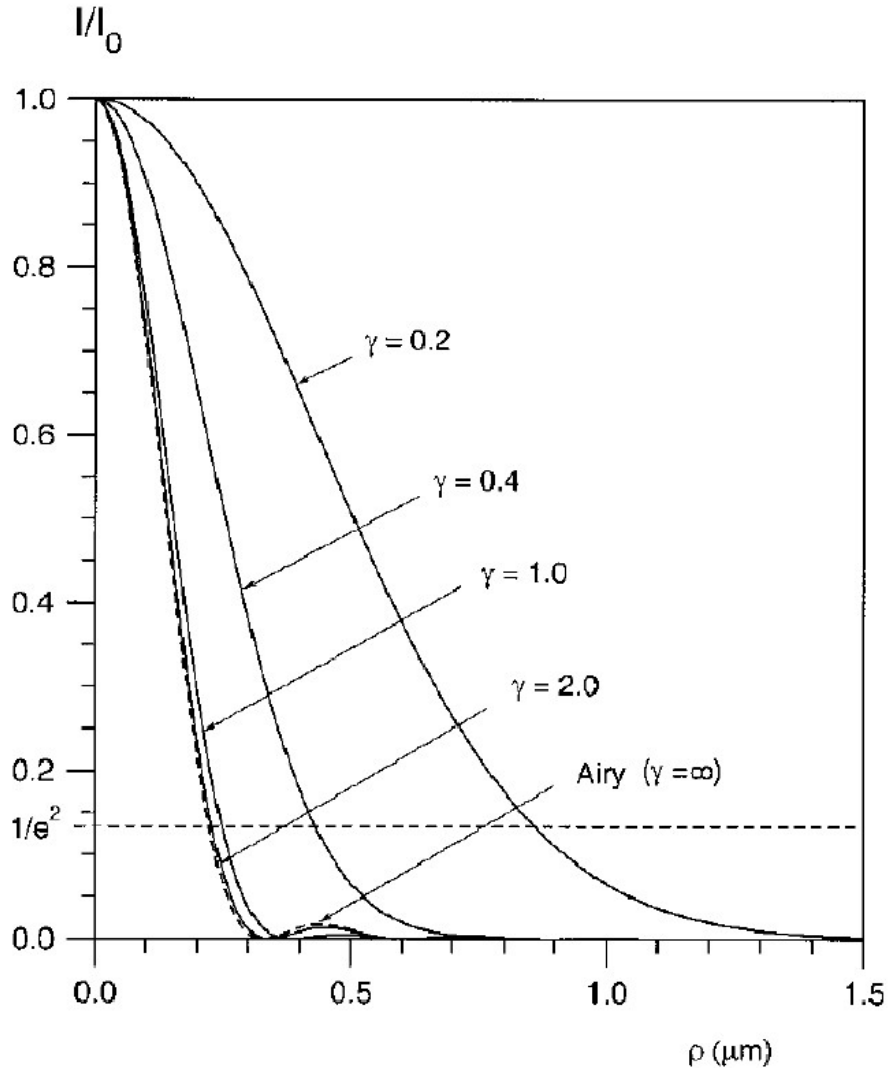


**Figure 2.27:** Experimental results showing, irradiance distribution of the focal spot for several values of  $\gamma$ . [199].

### 2.6.2.1 Small truncation: Gaussian beam

For the case of a Gaussian beam having a waist  $w_g$ , and an irradiance profile:

$$I_g(\rho) = \frac{2P}{\pi w_g^2} \exp\left\{-\frac{2\rho^2}{w_g^2}\right\} \quad (2.14)$$

- where the  $g$  subscript means that this is the expression for a Gaussian beam
- and  $2w_g = \frac{4\lambda f}{\pi(2w)}$ , where  $w$  is the waist before the laser beam focusing by an objective of focal length  $f$

In that case, the same expression for  $L_g$  that is proposed by Jacobs [200,201] is also confirmed by Salgueiro [199]. So the linewidth can be expressed as a function of ratio of the laser power  $P$  over the scanning speed  $v$ :

$$L_g = w_g \left[ 2 \log \left( \sqrt{2/\pi} \left( \frac{P}{w_g v E_c} \right) \right) \right]^{1/2} = w_g [2 \log(k_g \Omega)]^{1/2} \quad (2.15)$$

Where  $k_g = (\sqrt{2/\pi} / (w_g E_c))$  accounts for all the fixed parameters and  $\Omega = \frac{P}{v}$  accounts for the variable ones.

$E_c$  is the critical exposure, below which the photoresist remains liquid and no line can be traced. If  $E = E_c$  the photoresist is at the so-called gel point corresponding to the transition from the liquid to the solid phase.

### 2.6.2.2 Large truncation: uniform irradiance

In the case of uniform illumination, achieved when the laser beam is highly truncated by the objective aperture ( $\gamma \gg 1$ ), we have an Airy diffraction pattern with an irradiance distribution:

$$I_a(\rho) = \frac{P' \alpha^2}{4\pi} \frac{2J_1(\alpha\rho)}{\alpha\rho} \quad (2.16)$$

The power is denoted  $P'$  to account for the fraction lost by the aperture truncation as cited above, such that  $P' = P(1 - \exp\{-2/\gamma^2\})$ . The subscript a indicates that the magnitudes correspond to the Airy irradiance profile.

$L$  can be expressed as:

$$L_a = \frac{1}{\alpha} \Phi^{-1} \left( \frac{1}{k_a \Omega} \right) \quad (2.17)$$

- $\alpha = \frac{2\pi NA}{\lambda}$  where  $\lambda$  is the operating wavelength of the laser.
- $\Phi(2\alpha\zeta) = \frac{H_1(2\alpha\zeta)}{(2\alpha\zeta)^2}$ ,  $H_1$  is the first order Struve function
- $\Phi^{-1}$  is the inverse function of  $\Phi$
- $k_a = \frac{4\alpha}{\pi E_c} (1 - \exp\{-2/\gamma^2\})$

So  $L_a$  varies as the inverse function of  $\Phi$ . A plot of this function is illustrated in Figure 2.28. This function presents a principal maximum and secondary maxima produced because of the diffraction rings in the Airy pattern. We can note that, for high values of  $\Omega$ ,  $\Phi$  is not monotone, thus  $\Phi^{-1}$  will be an application that gives different values of  $L$  for the same parameter  $\Omega$ .

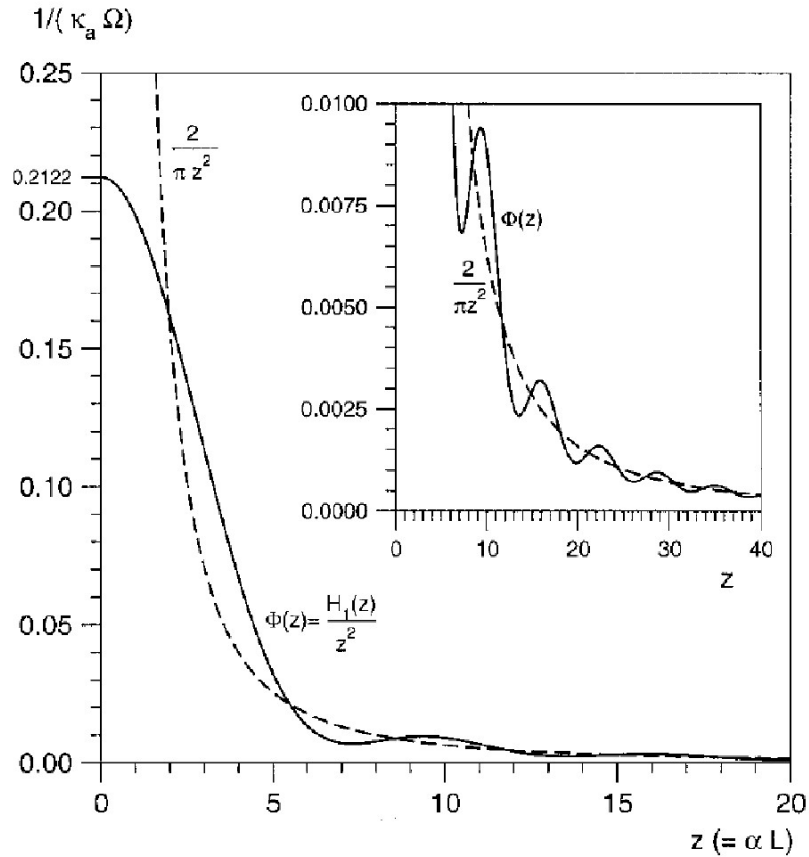


**Figure 2.28:** Plot of the first order Struve function (continuous curve) together with that which describes its asymptotic behavior,  $\frac{2}{\pi z^2}$  (dashed curve). Inset, the region containing the secondary maxima plotted on a different scale for clarity. [199]

Thus two different sub regimes exist, depending on the values of  $\Omega$ :

- For low  $\Omega$ , the linewidth is comparable with spot size.
- For high values of  $\Omega$ , the line width slightly oscillates giving different values for the same parameters. By setting  $\Omega$  high enough it is also possible to draw much broader lines than the spot size.

Since  $\Phi$  oscillates at high values of  $\Omega$ , it will be hard to have a description for the linewidth. Thus a monotone function with the same average behavior as  $\Phi$  should be used for high values of  $\Omega$ . To do so we can consider an asymptotic expansion that gives the function illustrated in dashed curve in Figure 2.28, and expressed as:

$$\Phi(z) = \frac{2}{\pi z^2} \quad (2.18)$$

In that case  $L$  can be expressed as:

$$L_b = k_b \sqrt{\Omega} \quad (2.19)$$

with  $k_b = \sqrt{\frac{2k_a}{\pi\alpha^2}}$ .

On the other hand their experimental study (Figure 2.29) showed that, for a Gaussian beam the linewidth fits very well with the square root of  $\log(\Omega)$  as expected from Equation 2.15:

$$L_g = a_0 + a_1[\log(a_2\Omega)]^{1/2} \quad (2.20)$$

For truncated beams it fits with the square root of  $\Omega$  as approximated for high values of  $\Omega$  thus giving:

$$L_b = a_0 + a_1\Omega^{1/2} \quad (2.21)$$

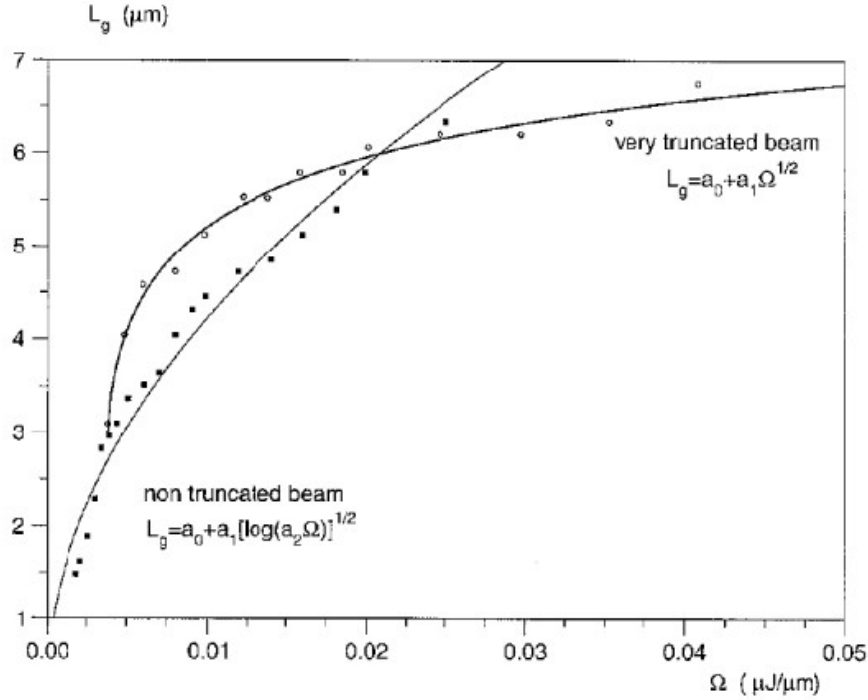


**Figure 2.29:** Linewidth versus  $\Omega$  for the two limiting cases of a nontruncated laser beam (Gaussian spot profile) and a strongly truncated beam (uniform illumination), together with the respective fits to the corresponding theoretical functions. A  $20\times$  microscope objective was used, with  $f = 8.3\text{mm}$  and  $NA = 0.40$ . The line  $\lambda = 475.9\text{nm}$  from an  $\text{Ar}^+$  laser is used as the light source.

In both cases an additional parameter,  $a_0$ , was introduced to improve the fit, and to account for the parameters that were not taken into consideration, such as scattering of light inside the photoresist film, reflection on the substrate, process bias and other parameters...

## 2.7 Conclusion

This chapter was fully dedicated to the materials and methods used for optofluidic applications. We first presented the state of the art of optofluidic chips fabrication, while putting an emphasis on those used for manipulation applications. We tried as much as possible to treat the fabrication of optofluidic systems as a whole system, and not as two separated chips: a microfluidic one and an optical one. We also proposed a new set of materials, called hybrid organic-inorganic resists, that can be a potential candidate for the fabrication of optofluidic chips. We also introduced the processing methods that we will use in order to cast and pattern these photoresists.

## Part II

# Experimental study



# Introduction

The aim of this work is to fabricate an optofluidic platform integrating vertically, **i)** an optical layer, and **ii)** a microfluidic layer, using photosensitive organic-inorganic photoresists. The device we choose to fabricate will be destined for optofluidic manipulation on a chip. We propose to implement a basic functionality of manipulation on a chip: a cell sorter, in the same spirit of the work already presented in Chapter 1 [87, 92]. The 3D design of a first prototype of the device is illustrated in Figure 2.30.

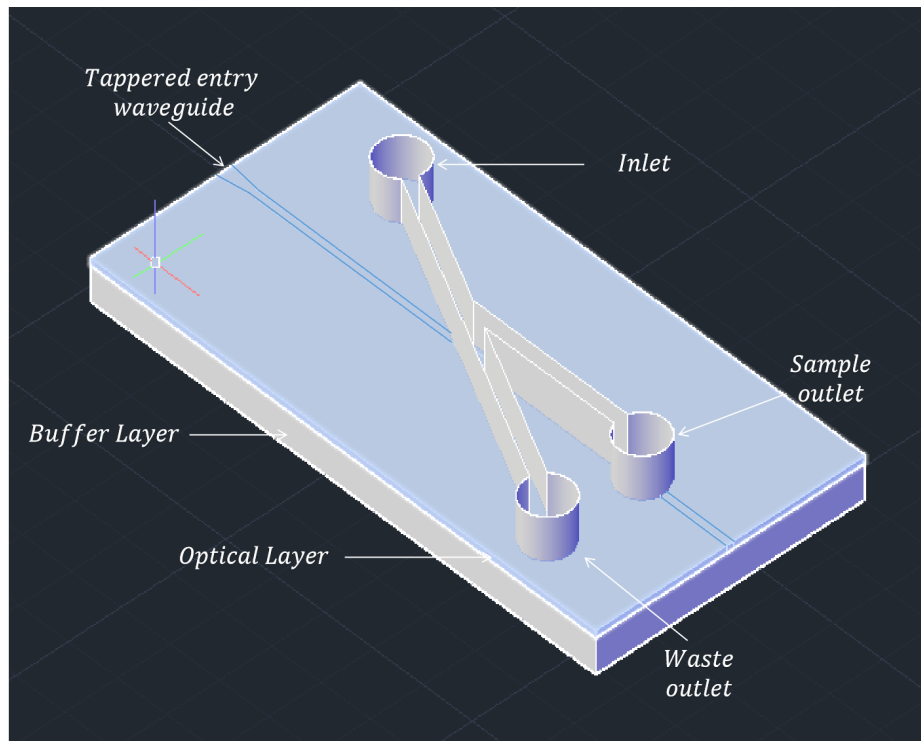


**Figure 2.30:** The 3D design of the cell sorter. The substrate is not illustrated and the drawing is not to scale.

The device consists of a tapered entry waveguide for the optical layer. On top of it, there is one microfluidic channel that bifurcates into waste and sample outlets. The inlet is connected to a microfluidic pump, the two outlets are connected to respective containers. If no light is coupled into the waveguide, we can expect the particles<sup>25</sup> to flow under the pressure of the pump at the velocity of the fluid in the channels. Once the waveguide is excited, the particles will perceive in

<sup>25</sup>Such as PS microspheres or living organisms.

addition to the hydrodynamic forces, the effect of an optical force that deviates them towards the sample outlet as this is the direction of propagation of light in the waveguide.

The fabrication process is a standard photolithographic approach as illustrated in Figure 2.31. It starts with the fabrication of the waveguides by deposition of the photoresist (step 1) and UV laser writing (step 2). As we can see two options exist for fabricating the waveguides, either by UV induced refractive index increase, or by developing the negative photoresist like any photoresist (step 3). The fabrication of the microfluidic channels is carried out afterwards (steps 4-6). It starts with the deposition of the positive tone photoresist (step 4), followed by the UV exposure using laser writing (step 5) and photoresist development to reveal the written channels (step 6). The final step is the sealing of these channels (step 7).

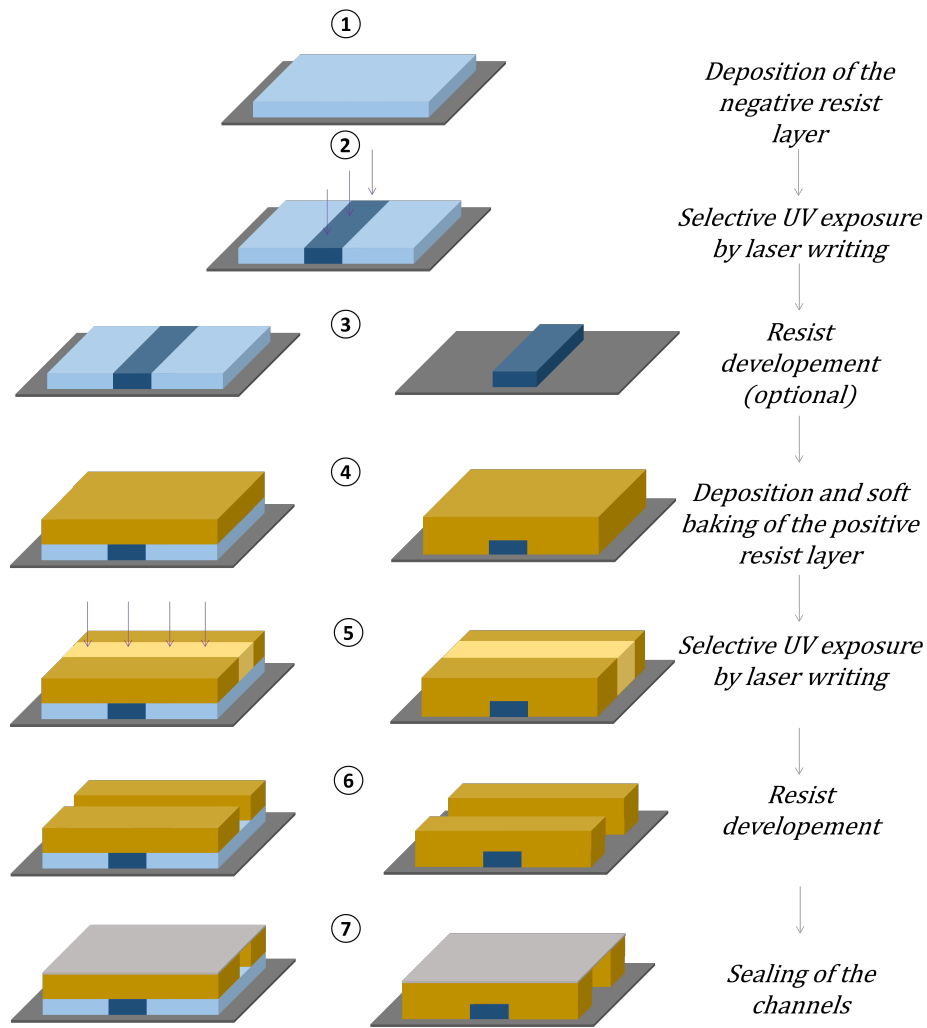


**Figure 2.31:** The process for the vertical integration of an optical layer and a microfluidic layer using photolithography of hybrid materials. The baking steps are not illustrated.

The dielectric material that we use for the fabrication of the optical waveguide, has a refractive index that can vary between 1.49 for a composition made only of MAPTMS [165], and 1.7 for a composition containing a 1:10 ratio of MAPTMS to  $Zr(PrO_4)$  [170]. As such, depending on the molar ratios of these two precursors, we can expect a refractive index difference in the range

0.2 – 0.4, with the surrounding environment<sup>26</sup>, for revealed waveguides. Which puts them in the categories of medium to high refractive index step waveguides<sup>27</sup>, that are particularly adapted for optical manipulation. For UV induced waveguides we expect a refractive index change of around 0.01 [163], thus putting these waveguides in the category of those having a low refractive index contrast with their surrounding<sup>28</sup>. In this case the interaction between the light and the particles will be only limited to the top region of the waveguides as it is the case in ion exchange waveguides, and the field will be less confined in the structure. The actuation of particles can still be possible using these waveguides. Nevertheless we will not privilege their use unless they show less propagation losses than revealed waveguides. In the first chapter of the experimental part (Chapter 3), we will address the fabrication of the optical circuit using the negative tone photoresist based on *MAPTMS* and *Zr(OPr)<sub>4</sub>*. We will also assess the propagation losses due to scattering in revealed and unrevealed waveguides.

For the fabrication of the microfluidic layer, it is essential for us, to use a positive photoresist for rapid processing by laser writing. We plan on using a hybrid positive photoresist elaborated in our labs [167, 186], as a starting point to fabricate the microfluidic layer. The second chapter of the experimental work will be fully dedicated to adapt this photoresist in order to fabricate high channel walls for microfluidics. The use of this photoresist will demonstrate to be complicated for creating microfluidic channels as we will explain in chapter 4. As such the aim of chapter 5 will be to replace this photoresist with PDMS for the fabrication of the microfluidic layer.

---

<sup>26</sup>Being water

<sup>27</sup>As we categorised them in the beginning of chapter 2

<sup>28</sup>Being considered here as the cladding of slightly lower refractive index



# Chapter 3

## Fabrication and characterisation of waveguides using an established hybrid photoresist

### 3.1 Introduction

This chapter is dedicated to the fabrication and characterisation of optical waveguides of the optofluidic chip using an established formulation of a hybrid organic inorganic photoresist. Our main goal is producing a single mode, or few modes waveguides using a fast prototyping technique that is laser writing. This can be done in two different ways in our case:

- either by creating a region of slightly higher refractive index, induced solely by a change in molar refractivity due to the polymerisation that occurs upon insulation.
- or by dissolving the unpolymerised photoresist in order to reveal a waveguide identical to the written polymerised pattern, in a similar way to any negative photoresist.

In addition to producing the waveguides using these two strategies, we need to compare them by assessing the propagation losses in each one of them. Thus, the purpose of this chapter is to present the different steps needed to fabricate and characterise optical waveguide. In the first Section 3.2, we will tackle the photoresist preparation. This will be followed by presenting the spin coating working curve, for different photoresist formulation in Section 3.3. Since the refractive index is an essential parameter in the conception of optical waveguides, its measurements will be presented in Section 3.4. After addressing the sol elaboration, the film deposition and characterisation we will go through the machinery used for laser writing, in Section 3.5. In the end, the characterisation of the waveguides will be presented: this includes the dimension and geometry (Section 3.6) and the light propagation in these structures (Section 3.7).

### 3.2 Photosensitive resist development

Our sol-gel photosensitive resist fabricated from hybrid ORMOCERs is elaborated in two steps:

- The fabrication of the mineral network by hydrolysis and condensation in the sol. The resulting sol should be transparent to the UV curing wavelength.

- The addition of a suitable photoactive compound that is able to initiate a polymerisation of the organic entities upon irradiation at this same wavelength.

In this section we are going to tackle in details these steps for the elaborated photoresist based on MAPTMS and  $Zr(OPr)_4$ . The MAPTMS,  $Zr(OPr)_4$  solution (70% in 1-propanol) and MAA were purchased from Sigma-Aldrich. The HCl(0.1N) were purchased from Honeyell, Fluka. The water is distilled in our labs. The photoinitiator compounds used were also purchased from Sigma-Aldrich, and we will present them later in details.

### 3.2.1 Precursors and process

This sol-gel synthesis uses two hybrid precursors as illustrated in Figure 3.1: MAPTMS, and ( $Zr(OPr)_4$ ) chelated with MAA.

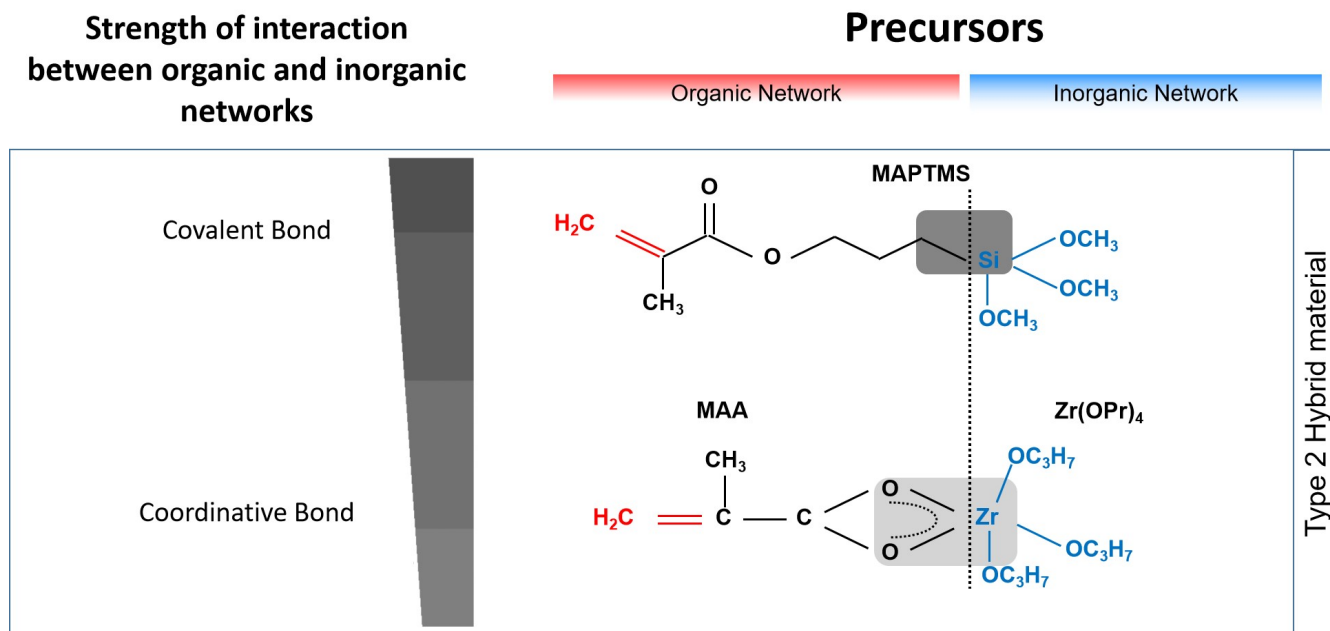


**Figure 3.1:** Schematic illustration of the precursors used for the sol.  $Zr(OPr)_4$  is illustrated as complexed to MAA in a 1:1 ratio.

In separate solutions, each of these precursors is able to form by hydrolysis and polycondensation,

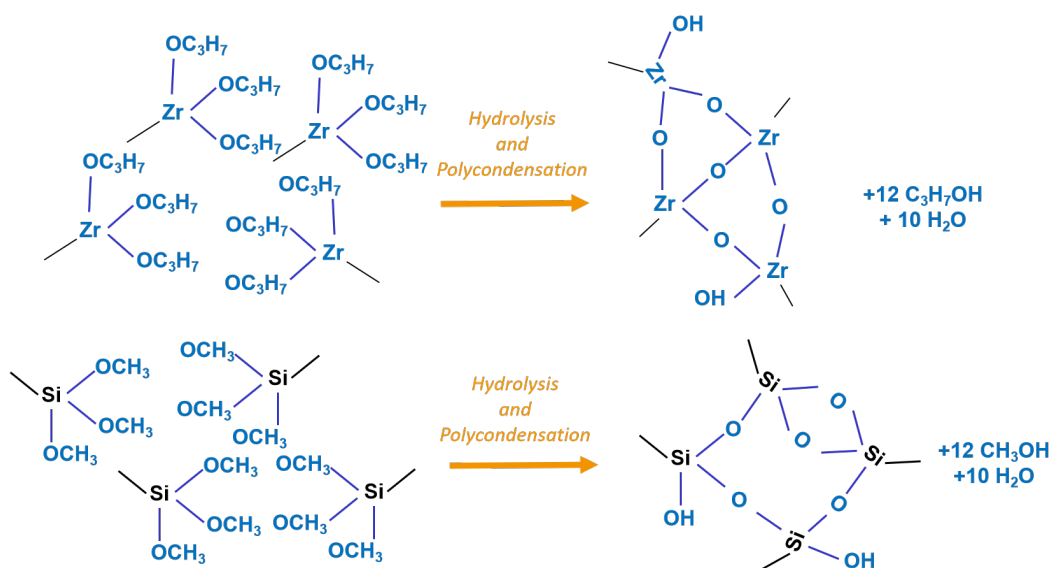
a tridimensional inorganic network  $\begin{array}{c} \text{O} \\ | \\ \text{---M---O---M---} \\ | \qquad \quad | \\ \text{O} \qquad \quad \text{O} \end{array}$  initiated by the  $\text{M---(OR)}_x$  entities,

where M, R and x respectively are:

- Si,  $\text{---CH}_3$ , and 3 for MAPTMS,
- Zr,  $\text{---C}_3\text{H}_7$ , and 4 for  $Zr(OPr)_4$ .

Even though the  $Zr(OPr)_4$  has in fact four reactive groups, the complexation of the MAA limits the reactivity of some of these groups as illustrated in Figure 3.2. The ratio of MAA to  $Zr(OPr)_4$

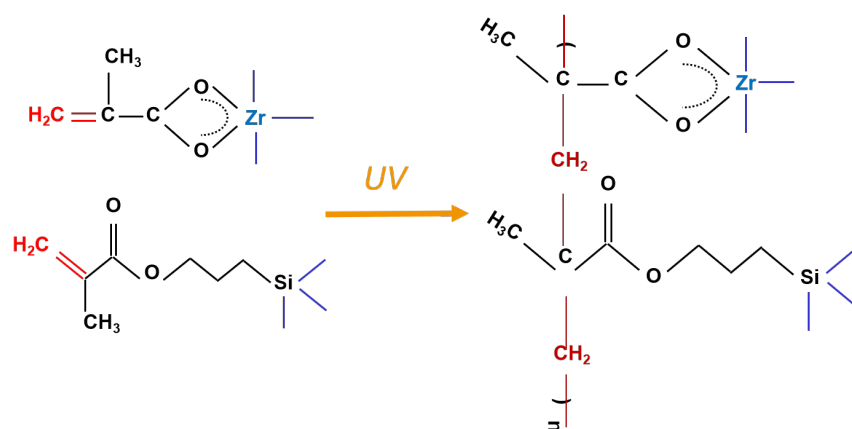
should be kept between 0.7:1 and 1.8:1. In order to avoid the precipitation of  $Zr(OPr)_4$  with excess water for values lower than 0.7, and the presence of free acids in the sol for values higher than 1.8 [202].



**Figure 3.2:** Schematic representation of the hydrolysis and polycondensation of both precursors. The  $Zr(OPr)_4$  is illustrated as complexed to MAA in 1:1 ratio.

Once the two solutions are mixed the residual  $Si-OH$  and  $Zr-OH$  will form an inorganic heterometal bond  $Zr-O-Si$ . The formation of these heterometal bonds is regulated by limiting the mixing time of each solution separately to around 45 min [165]. These hydrolysis and polycondensations will produce methanol, propanol and water as by-products. In addition, they will be able to jointly constitute a polymethylmethacrylate network  $\left( \begin{array}{c} \text{---C---CH}_2\text{---} \\ | \\ \text{CH}_3 \end{array} \right)_n$ .

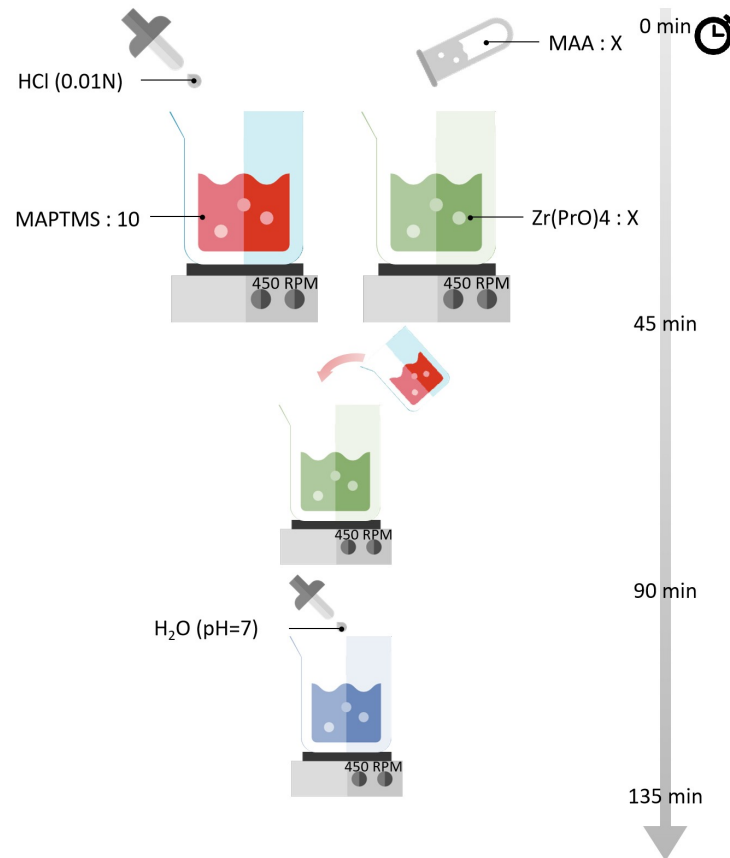
later reaction is a radical polymerisation that is initiated by the excitation of an adequate UV sensitive photoinitiator, as illustrated in Figure 3.3 and usually happens once the sol is cast as a film.



**Figure 3.3:** Schematic representation of the photopolymerisation reaction of both precursors.

In the light of these studies the sol elaboration process is illustrated in Figure 3.4, and summarised as follows:

- For 10 molar units of MAPTMS we add a quarter of the stoichiometric amount of aqueous hydrochloric acid ( $HCl$ ) (0.01N) dropwise, while we maintain the stirring.
- Simultaneously in another beaker, for X molar units of  $Zr(OPr)_4$  we add the MAA in a molar ratio of 1 to 1 while agitating.
- After 45 min, MAPTMS is added slowly to the  $Zr(OPr)_4$  solution to avoid precipitation.
- Following another 45 min, the additional amount of water needed for the hydrolysis is added dropwise.

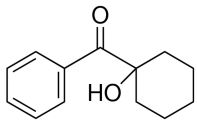
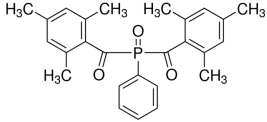


**Figure 3.4:** Process flow chart for the MZ10-X photoresists

All the compositions prepared were named according to the following coding method MZ10-X, X being the aforementioned molar ratio. This process will form the Silica/Zirconate compound to which is added the photoactive compound, for an overnight mixing at room temperature. The final photosensitive sol is filtered using a  $0.2 \mu m$  filter, prior to use.

### 3.2.2 The addition of the photoactive compound

In order to choose a suitable photoinitiator, some criteria must be fulfilled: we need an i-line sensitive, radical photoinitiator that is soluble in a mixture of methanol and propanol. Many photoinitiators that can accomplish this task were formerly commercialised by Ciba/ BASF. Unfortunately, they are not available on the european market through BASF anymore. As an alternative, 1-Hydroxycyclohexyl phenyl ketone (99%*Assay*) was purchased from Sigma Aldrich. This photoinitiator was previously commercialised under the name of Irgacure 184. It is a non yellowing radical photoinitiator that is the most widely used for MAPTMS/ $Zr(OPr)_4$  systems. On the other hand, no alternative could be found for the Bis Acyl Phosphine Oxide (**BAPO**) used in the formulation of the Irgacure 1800 <sup>1</sup> that showed the highest index step in Coudray's work [163]. For this reason Another BAPO was used: Phenylbis(2,4,6-trimethylbenzoyl)phosphine oxide (99%*Assay*), because it has a sharp absorption peak at 365 nm. The key properties of these compounds are summarized in Table 3.1.

Name	1-Hydroxycyclohexyl phenyl ketone	Phenylbis(2,4,6-trimethylbenzoyl)phosphine oxide
Commercial Name (BASF)	Irgacure 184	Irgacure 189
Cas Number	947-19-3	162881-26-7
Molecular weight (g/mol)	204.3	418.46
Key properties	non yellowing	low odor, low volatility
Class	$\alpha$ -hydroxyketone	BAPO
UV absorption peaks (nm)	246, 280, 333	360, 365, 405
Solubility	good	low
Molecular structure		

**Table 3.1:** A summary of the photoinitiators characteristics

As we have seen in Chapter 2, increasing the photoinitiator concentration in the sol can lead to a better initiation rate. The concentration of the photoinitiator shouldn't exceed a rough 5% of the precursor's weight, because the concentration of initiated radicals will be high, and the termination of the polymerisation occurs prematurely. This will result in short molecular chains, hence a low molar mass of the polymer. Moreover, for values less than 1% the initiated radicals will not be able to terminate due to the limited mobility in the film. This will also lead to the formation of a polymer having a low molecular mass. In fact, a decrease in the molar mass of a polymer, is reflected as a higher dissolution rate of the polymerised structures in the solvents, and poorer mechanical properties, which are both not desired in negative photoresists. Therefore, the

<sup>1</sup> bis(2,6-dimethoxybenzoyl)(2,4,4-trimethylpentyl)-Phosphine oxide, CAS Number:145052-34-2

quantity of the photoinitiator to be added should range between 1 and 5% of the precursors mass, in order to maintain an equilibrium between a good initiation rate, and an ideal polymeric chain length. Based on existing studies [163,203], we used a 4% mass of both Irgacure 184 and 189.

### 3.2.3 The solid content

Along with the viscosity, the solid content is an important parameter in section 2.6.1 of Chapter 2 when elaborating a photoresist, since it has an effect on the range of thicknesses that can be achieved with a certain formulation, as seen in in section 2.6.1 of Chapter 2 section 2.6.1 of Chapter 2. Evaluating it is a simple task that consists of weighting a in section 2.6.1 of Chapter 2 small sample of the sol, before and after baking it on a hot plate until all the solvents evaporate. The solid content is evaluated as the ratio of these two quantities and can be expressed as a percentage according to the below equation:

$$\text{Solid content} = \frac{\text{sample weight}_{\text{after}}}{\text{sample weight}_{\text{before}}} \times 100 \quad (3.1)$$

Thus after elaborating the sol, the solid content is measured. It is  $49 \pm 3\%$  for MZ10-2.5 and  $58 \pm 1\%$  for MZ10-1. This difference is due to the higher content of  $Zr(OPr)_4$  in the MZ10-2.5, which introduces addition solvent to the composition. The MZ10-2.5 will be used for the core layer, thus its solid content is in the appropriate range for in section 2.6.1 of Chapter 2 deposition of thin layers. MZ10-1 will serve for the deposition of the buffer layer which is a thick layer, thus a higher solid content is needed. For that we proceed into a concentration by evaporation using a rotary evaporator (*rotavap*). The rotavap is able to extract the solvents by evaporation and condensation in section 2.6.1 of Chapter 2 into a waste container. The pressure of the pump is kept at 80 bars and the temperature at  $40^\circ C$ . The rotation is set at 2 rounds per seconds and the concentration is carried out for 15min after the pump reaches 80 bars. the solid content of MZ10-1 after evaporation is  $79 \pm 2\%$ .

## 3.3 Deposition of the photoresist

The deposition of the films was performed using the spin coating process already presented in section 2.6.1 of Chapter 2. The MZ photoresists, especially the MZ10-X at around 50% solid content, exhibit a high evaporation rate due to their methanol content. For this reason, a special care should be taken while casting the film. In fact, multiple trials have lead to the conclusion that ramping time should be kept minimal, otherwise the solvent totally evaporates before the final speed is attained and the film thickness may set into its final value during the ramp up. This was numerically and experimentally confirmed [204]. The fast evaporation of solvent causes also the formation of defects called striations as observed in Figure 3.5. They are mainly a result of a delicate balance between evaporation and surface tension effects [205]. Increasing solvent partial pressure in the chamber is expected to reduce solvent evaporation and limits the presence of these waves in the film-thickness profile. An ethanol saturation of the spinner chamber is done in order to limit the evaporation and to produce more uniform films.

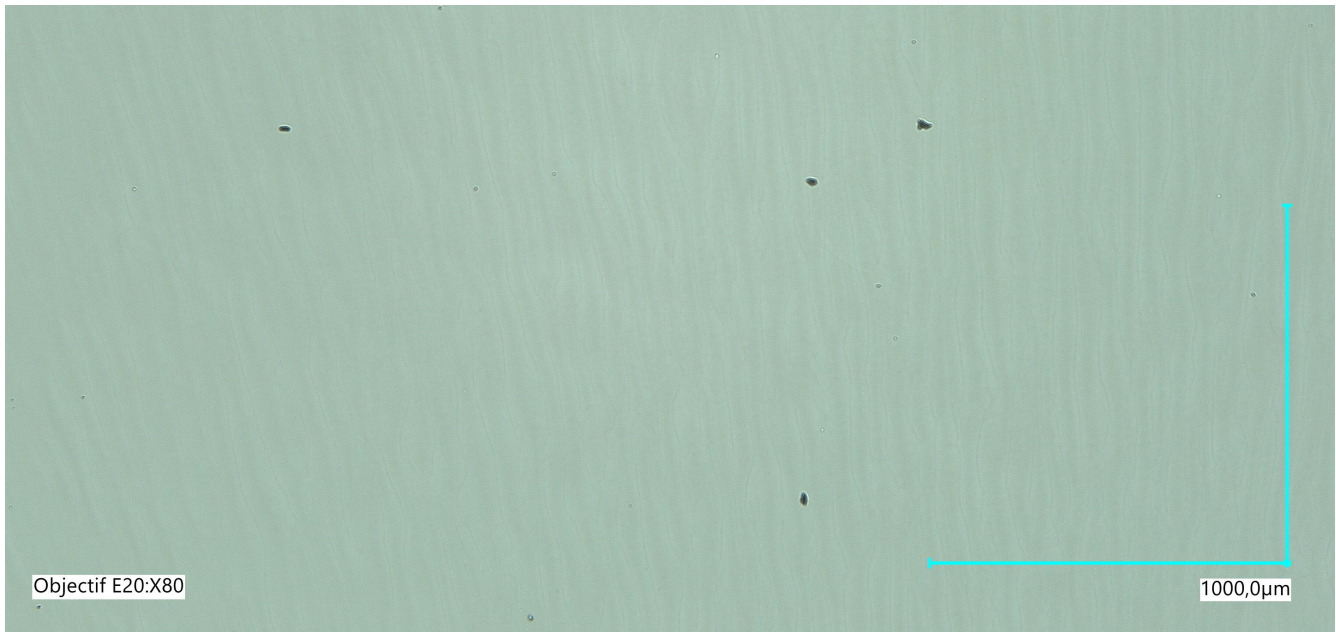
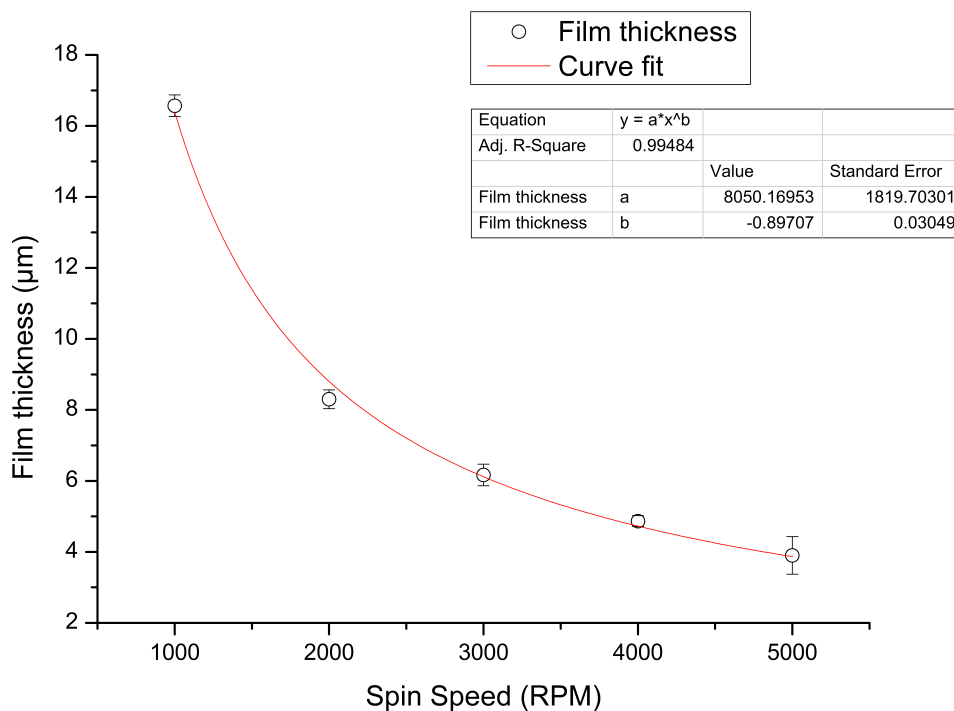


**Figure 3.5:** Striation effects on the surface of an MZ10-2.5 layer

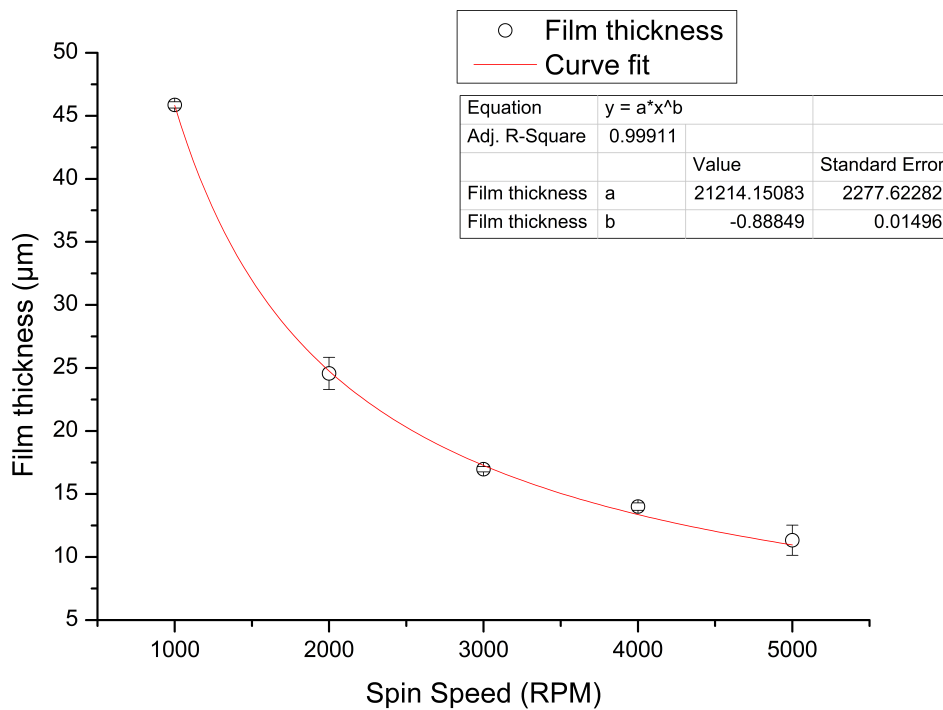
In order to establish a working curve for the thickness as a function of the spin speed we proceed for each of the two photoresists as follows:

- For the MZ10-1 (after concentration) at 80% solid content: we cast a layer of the photoresist on a clean silicon substrate at different speeds between 1000 and 5000 RPM for a duration of 10s while keeping the ramping time at 1 second.
- For the MZ10-2.5 at 50% solid content: In order to account for the adhesion between this layer and the buffer layer beneath it, we cast the photoresist on a silicon substrate covered with the buffer layer. The duration of the spin coating is 2s, for a spin speed that vary between 1000 and 5000 RPM. The ramping time is kept at 1 second as well.

Afterwards, we bake all the samples at  $110^{\circ}C$  for 1h30min. In order to measure the thickness of the layer, we cleave the sample and observe the cleaved profile under a microscope. The results are presented in Figure 3.6 as a scatter plot of the film thickness in  $\mu m$  as a function of the spin speed in RPM, along with their corresponding fit.



(a)



(b)

**Figure 3.6:** Film thickness as a function of spin speed for MZ10-X photoresists with different solid content: (a) the MZ10-2.5 with 50% solid content and (b) the MZ10-1 with 80% solid content, and their corresponding fits.

As we can see in Figure 3.6, the thickness is a function of  $\omega^{-0.9}$ , for both compositions of the MZ10-X. This clearly deviates from the Meyerhofer prediction:

$$h_f = A\omega^{-1/2} \quad (3.2)$$

where  $A = x[\frac{3\eta C}{2(1-x)\rho}]^{(1/3)}$  as already seen in chapter 2.

If we recall the equation of  $h_f$  before explicitly expressing it as a function of  $\omega$ :

$$h_f = x[\frac{e}{2(1-x)K}]^{(1/3)} \quad (3.3)$$

The only two quantities dependant on the spin speed in this equation are the evaporation rate  $e = C\omega^{1/2}$ , and the flow constant  $K = \frac{\rho\omega^2}{3\eta}$ . The relation between  $K$  and  $\omega$  results from the drag force expression. For  $e$  no measurement could be done to find out its relation with the spin speed. Thus, the simplest relation was assumed, that is the proportionality with  $\omega^{1/2}$ . As a result, one of these expressions does not apply to the studied case. We suspect that the sol does not behave as a Newtonian fluid since it is close to its gel point. Thus, the first assumption of the model described by Meyerhofer will not stand, and the flow constant  $K$  does not scale with  $\omega^2$ .

### 3.4 Refractive index measurement

After we establish the film thickness of the different layers in order to control the vertical dimension of the buffer and the guiding layer of the waveguide, we need to investigate the refractive indices of the material. In order to determine the refractive indices of the different MZ10-X compositions, refractometric measurements were done at 4 different wavelengths 450, 546, 598 and 680 nm. An ATAGO's Multi-Wavelength Abbe Refractometer DR-M2, having an instrumental error of  $\pm 5 \times 10^{-5}$ , was used. An Abbe Refractometer exploits the TIR of light to measure the critical angle and deduce the refractive index of a material. It consists of a prism of known refractive index  $n_p$  on which a sample of unknown refractive index  $n_s$  can be placed. Indeed, the refractive index of the prism is higher than that of the sample. A contact liquid having a refractive index in between the two is necessary to ensure proper contact as well as the occurrence of TIR on the different interfaces. The principle is simple and illustrated in Figure 3.7.

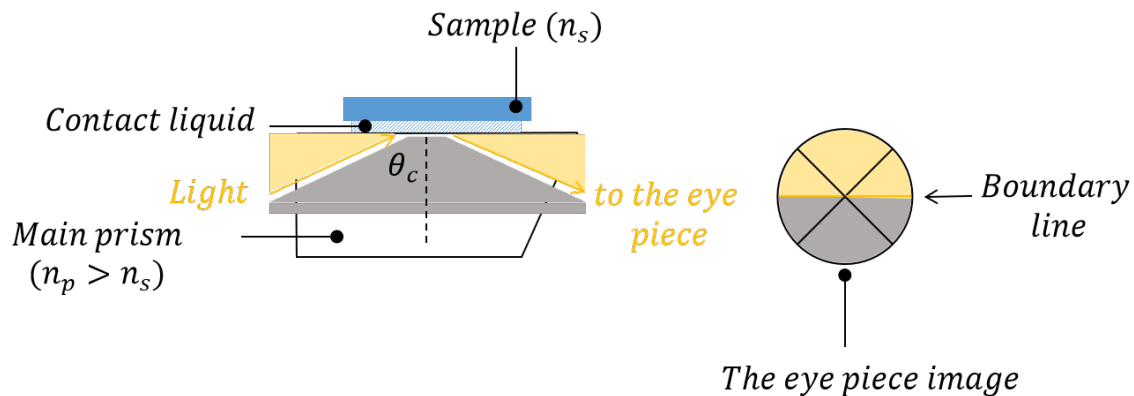


**Figure 3.7:** The working principle of an Abbe refractometer, illustrated here in the case where the sample is a thin film deposited on a substrate.

A polychromatic light source equipped with different monochromatic filters illuminates the sample through a prism. Only the rays that corresponds to incidence angles higher than the critical angle  $\theta_c$  are reflected. Through an eye piece, the user is able to locate the boundary line that corresponds to the ray at  $\theta_c$ . By placing it in the center of the eye piece marked by the intersection points of the cross hairs, the machine is able to detect  $\theta_c$  and return the refractive index of the sample  $n_s = n_p \sin(\theta_c)$ . We performed these measurements for different formulations of the MZ10-X photoresist, which we will present in the following sections.

### 3.4.1 MZ10-2.5 with Irgacure 184

We prepared different samples of this MZ10-2.5, with Irg184, which we called MZ10-2.5+. We measured the refractive indices of 2 sets of 12 samples each, all coated on a silicon wafer:

- MZ10-2.5+ UV cured and baked at  $110^\circ C$  for 2h.
- MZ10-2.5+ uncured and baked at  $110^\circ C$  for 2h

The curing of these samples was done using a UV-LED masking system: UV-KUB 2, fabricated by Kloe-France. Its insulation wavelength is  $365 \pm 5 nm$  and the power density it delivers is  $25 mW/cm^2 \pm 10\%$ . The curing time was  $5 min$  which delivers a dose of  $7500 mJ/cm^2$ . The aim is to measure the refractive index change due to curing, by comparing cured and uncured samples of MZ10-2.5+. The raw measurements performed on all the cured and uncured samples of MZ10-2.5+ are presented in Figures 3.8 and 3.9.

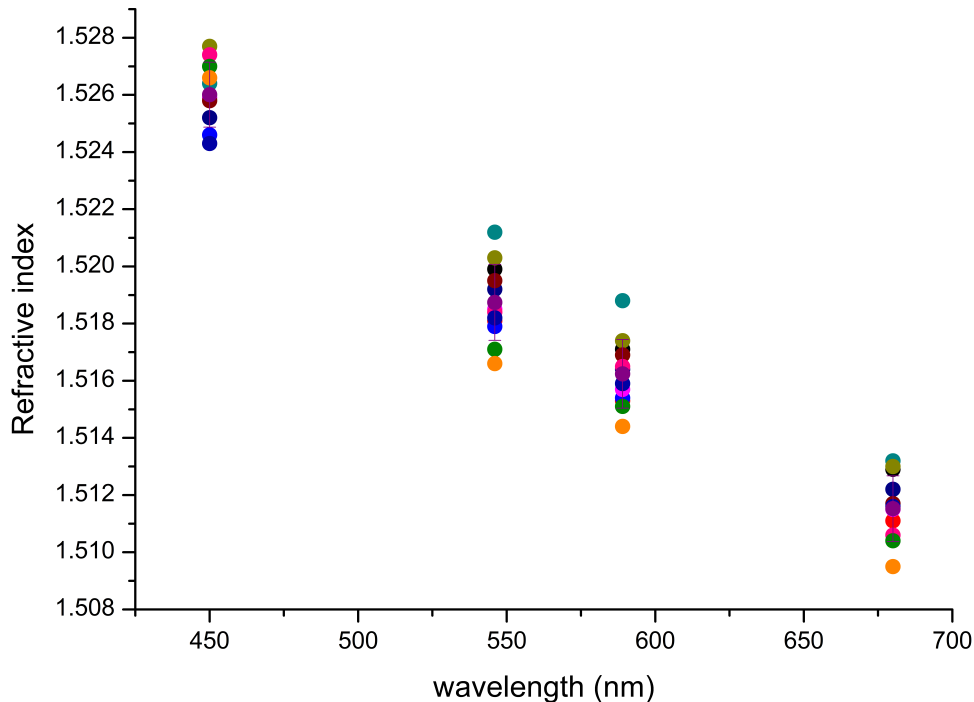


**Figure 3.8:** The refractive indices of uncured samples of  $MZ10 - 2.5+$ . All samples are hard baked at  $110^\circ C$  for 2h.

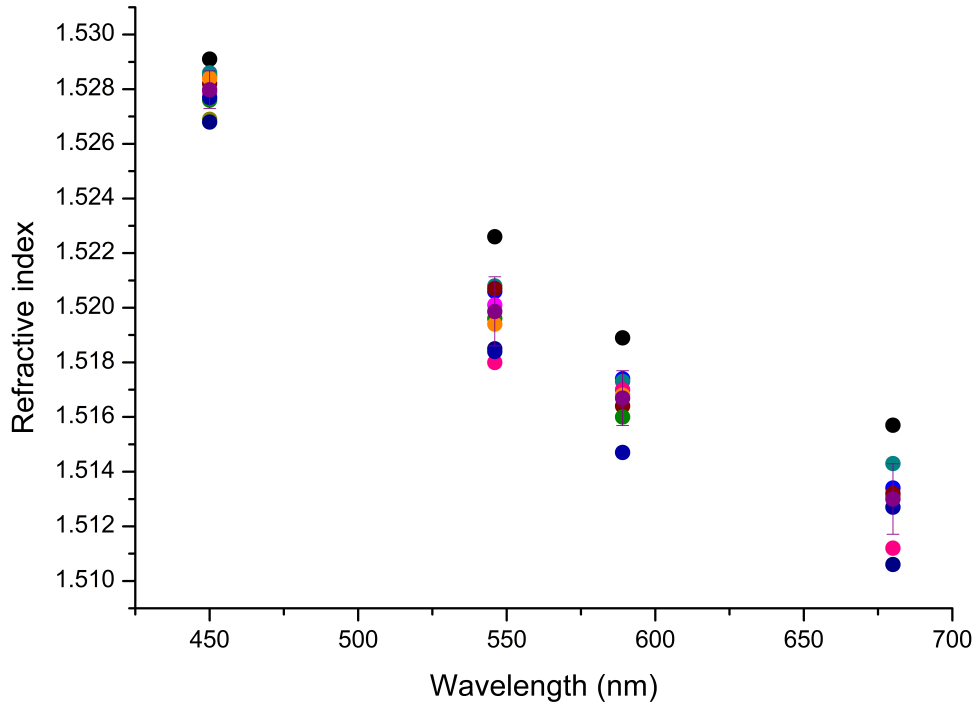


**Figure 3.9:** The refractive indices of UV cured samples of  $MZ10 - 2.5+$ . All samples are hard baked at  $110^{\circ}C$  for 2h.

The mean value of the RI, as well as the RI step induced can be seen in Figure 3.10. We can note that,  $MZ10-2.5$  showed an index increase of around 0.002 in the visible after UV curing. Even with a RI step as low as 0.002 and a standard deviation around the same order, we were able to confirm that the waveguides were operational in single mode. This means that the refractive index step we measured is real and that the standard deviation we calculate is overvalued. An optimisation of these measurements is indeed necessary.

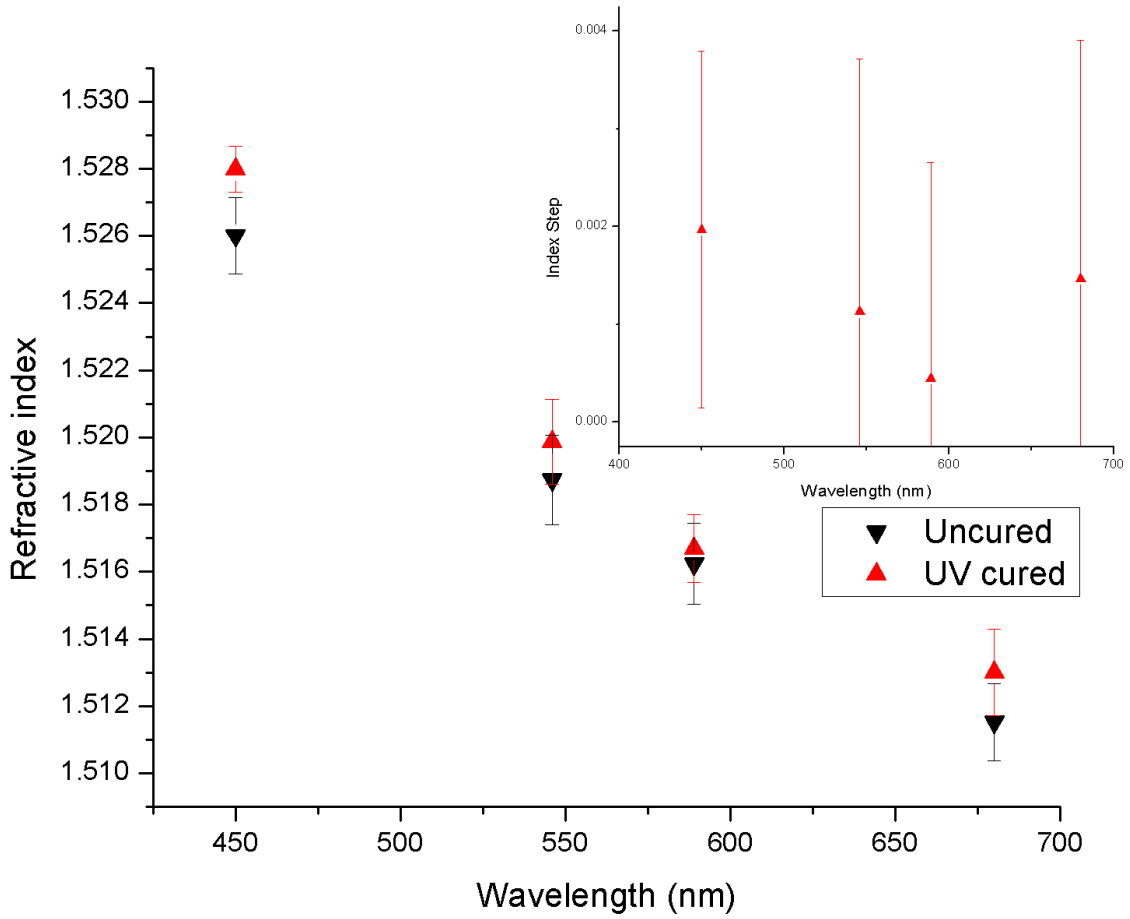


**Figure 3.10:** A plot representing the mean values of refractive indices of the UV cured and uncured MZ10-2.5 samples presented in Figures 3.8 and 3.9, and the refractive index step induced by the UV curing (Inset).

Since we will use our waveguides at  $635\text{ nm}$ , it is important to know the refractive index at this wavelength. In order to do this, we fit the results with the empirical Cauchy model that is applicable in the region of transparency of our material:

$$n = n_1 + \frac{n_2}{\lambda^2} \quad (3.4)$$

$n_1$  and  $n_2$  are empirically defined constants. The results of this fit are presented in Figure 3.11.

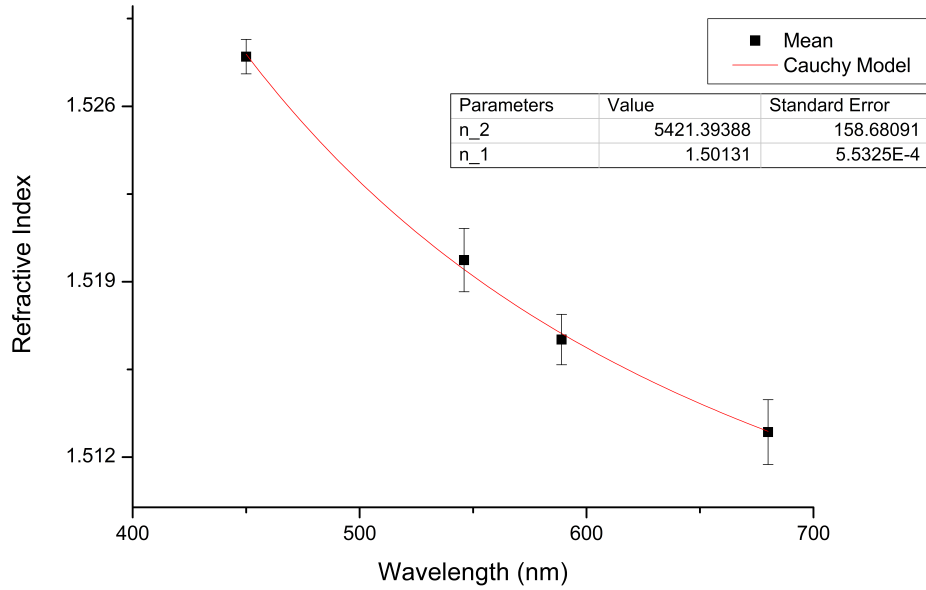


**Figure 3.11:** The Cauchy model’s fit of the cured samples of MZ10-2.5+ experimental results and the corresponding parameters.

We found  $n_1 = 1.501 \pm 0.001$ ,  $n_2 = 5500 \pm 200 \text{ nm}^2$ , and a refractive index of 1.515 at  $633 \text{ nm}$  which corresponds to values already measured as we can see in Figure 3.12. We can conclude that fitting the measured values using the Cauchy model is a valid method to estimate the refractive index at  $633 \text{ nm}$ .

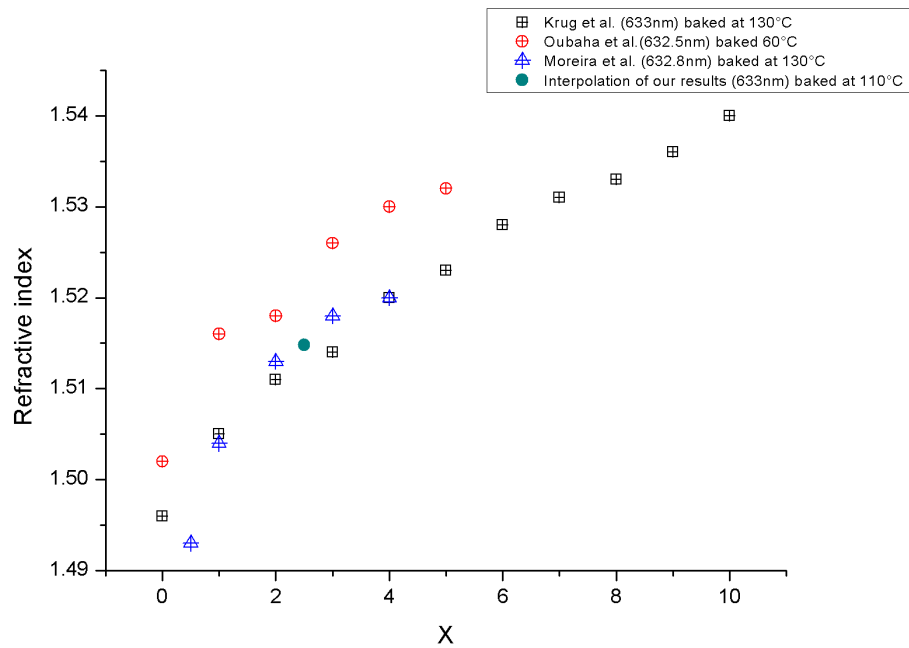


**Figure 3.12:** A comparison of the extrapolated value for MZ10-2.5+ with the existing literature.

### 3.4.2 MZ10-2.5 with Irgacure 189

In order to produce a higher refractive index contrast we opted for a photoinitiator, that is similar in structure to the one in the Irgacure 1800 formulation. We proceeded in the same manner to measure the refractive indices of the cured and uncured sets of 12 samples each. The results with their Cauchy model's fits are presented in Figure 3.13.

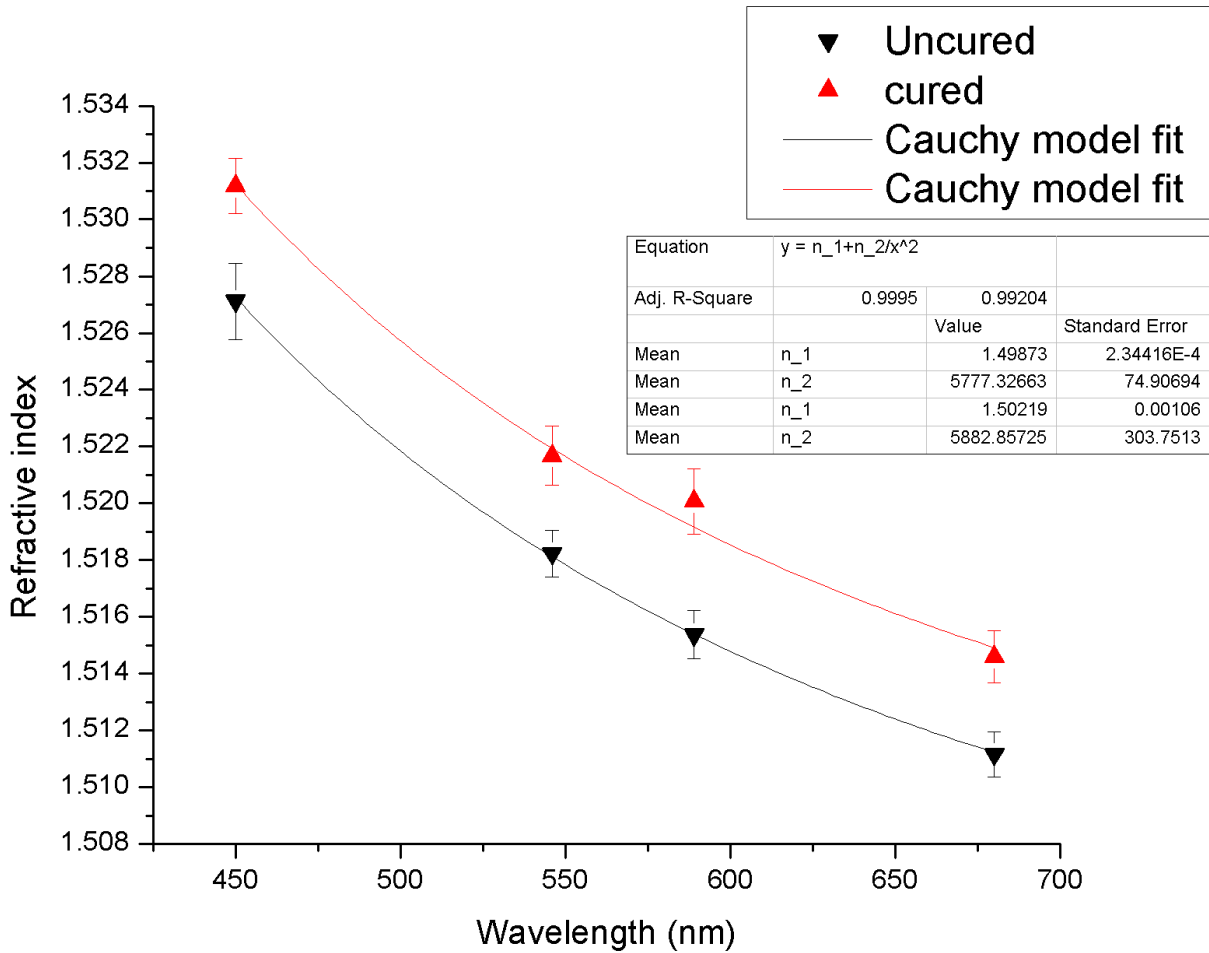


**Figure 3.13:** Refractive index of cured and uncured MZ10-2.5 formulation, along with the Cauchy model fit of each one of them

The refractive indices of the cured and uncured layers of this composition are respectively 1.517 and 1.513 at 633 nm. The refractive index step of around 0.004 is presented in Figure 3.14. We can clearly see higher refractive index step than the case of the MZ10-2.5 with Irgacure 184.

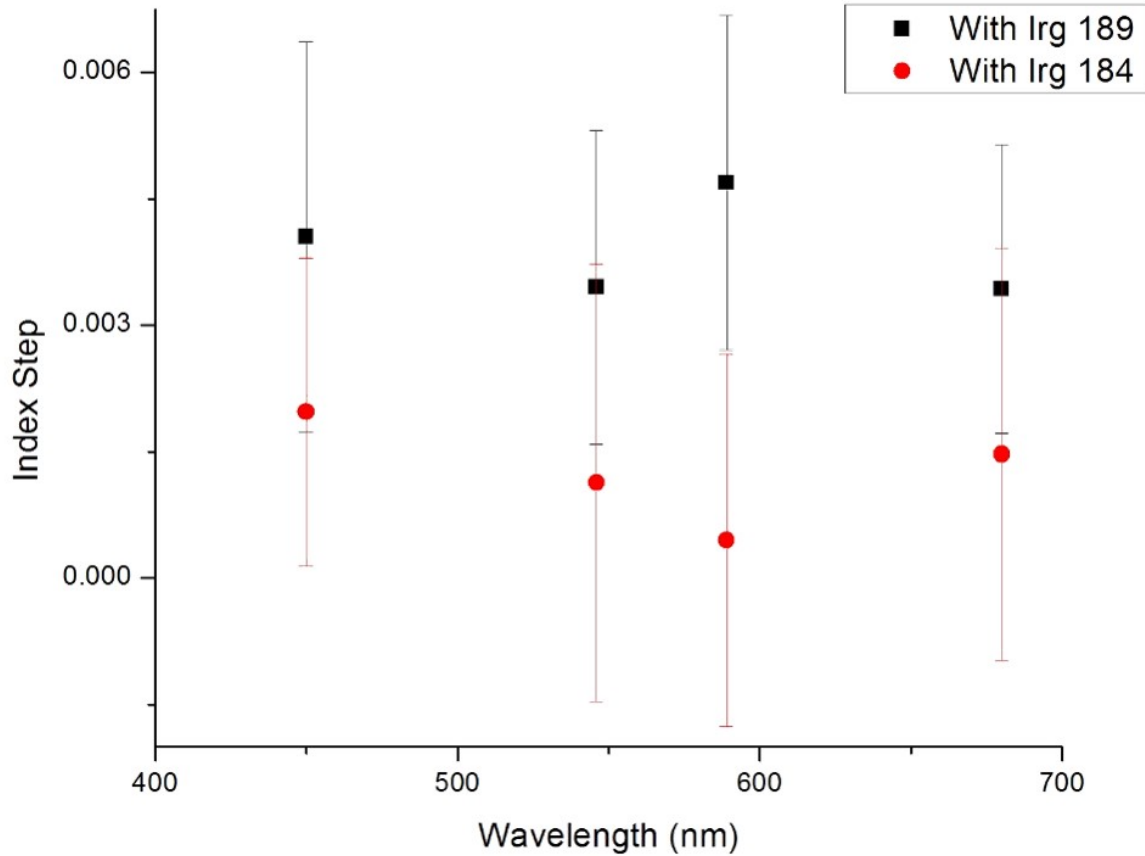


**Figure 3.14:** The associated refractive index step for the MZ10-2.5 composition with Irgacure 189 and 184 as photoinitiators.

### 3.4.3 MZ10-1 refractive index

For the buffer layer a composition with a lower refractive index is prepared. The molar ratio of MAPTMS to  $Zr(OPr)_4$  is 10 to 1. This composition of the sol doesn't need any PI. MZ10-1 coated samples (5000rpm 10s) were baked for 1h30min at  $110^\circ C$ , and the refractive indices were measured in the same way as for the previous samples. The results, the Cauchy model fit, and the corresponding parameters are represented in Figure 3.15. The Cauchy model fit gives the following dispersion relation:

$$n = (1.489 \pm 0.001) + \frac{6300 \pm 400}{\lambda^2} \quad (3.5)$$

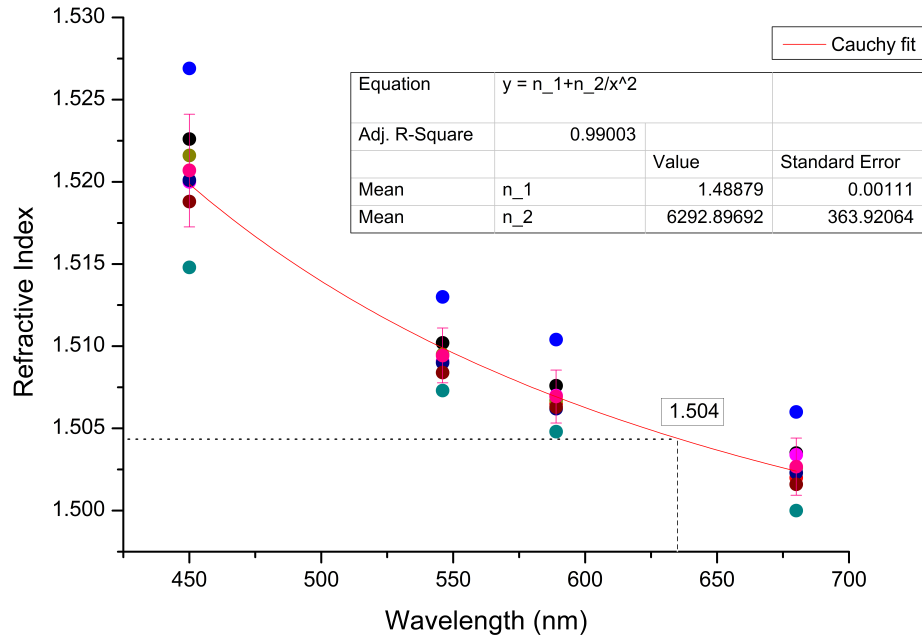


**Figure 3.15:** The refractive index of MZ10-1 with the associated cauchy model fit. Marked on the graph is the expected refractive index of the layer at 633 nm

A refractive index of 1.504 was found for this composition of the photoresist. Once again we can confirm that the interpolation of the results are in perfect accordance with the literature as seen in Figure 3.16.

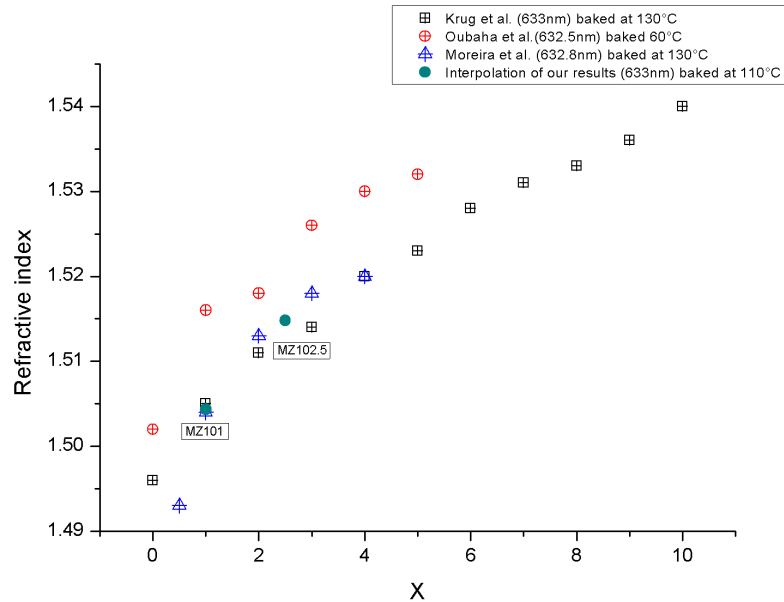


**Figure 3.16:** Validation of the extrapolated values for MZ10-1 with the existing literature.

## 3.5 Laser writing

In order to fabricate waveguides of varying width using a negative photoresist, we should be able to tailor and control this dimension as much as possible. Thus, it is important to draw a correspondence between the writing parameters and the linewidth for each photoresist. In order to constitute this mapping from the laser writing parameters space to the linewidth space, we will briefly introduce the laser writer that we use, before proceeding with the experiment.

### 3.5.1 The Dilase laser writer piloting

The laser writing machine used in our labs (Dilase 650) is designed by Kloe-France and equipped with 2 laser beams (407 nm and 375 nm). Each one of these lasers can be focused into two beam sizes  $1\ \mu\text{m}$  and  $10\ \mu\text{m}$ . The switching between the two laser spot sizes can be done automatically. However, this is not the case for switching from one wavelength to another. The machine is piloted by a software called Dilase Soft. Using this software we can adjust the parameters that define the patterns: power, focus, positions. In order to load a file into the Dilase Soft, a CAD file should be generated either by the associated CAD software Kloe design, or by any other software that is capable of producing a file compatible with Kloe Design.

The optical path of the lasers is static, and the writing of the patterns is enabled by a 2D moving stage, that moves at a speed  $v$ . The laser power  $P$  can be adjusted in 3 different ways:

- by mounting absorptive neutral density filters that can attenuate light in the near UV, and the visible range while reducing back reflections. The available filters in our facility have optical densities (*O.D.s*) of 0.6, 1.0, 1.3, and 2.0. Multiple filters can be mounted at once, giving an O.D. that is equal to the sum of those of the associated filters,
- through the piloting software, by including a modulation  $M$  in the file description,
- and finally, the least used method is the scrolling bar embedded in user interface of the Dilase Soft.

Subsequently  $P$  can be expressed as:

$$P = MP_0 10^{-O.D.} \quad (3.6)$$

Where  $M$  is the modulation, expressed as a percentage.  $P_0$  the laser power before entering the filter. O.D. the optical density of the mounted filter(s).

The dose received by the photoresist can be approximately estimated as the power density  $\frac{P}{\pi w^2}$  received during a time lapse  $dt$ , where  $dt$  is the time it takes for the spot to travel outside of its initial area, thus for its center to travel a distance  $2w$ ,  $w$  being the laser beam radius or waist. Which gives a time  $t = \frac{2w}{v}$ . This way the dose can be expressed in [ $\text{mJ}/\text{cm}^2$ ] as:

$$D = \text{power density} \times t = \frac{P}{\pi w^2} \frac{2w}{v} = \frac{2}{\pi w} \frac{P}{v} = \frac{2}{\pi w} \Omega \quad (3.7)$$

It is important to note that the dose as presented here cannot be compared to that of a UV masking system, nevertheless we prefer to use this approximation of the dose, because it offers a more tangible physical quantity than the ratio of  $\Omega = P/v$ . Finally, The dependence of the linewidth on the dose will be the same as its dependence on  $\Omega$ , thus we will use these two terms interchangeably in the rest of this section.

### 3.5.2 Laser writing parameters for MZ10-2.5

In order to control the linewidth of a cured laser written line we proceeded into what we call a dose test. This can be done in the same manner for any photoresist: we write identical lines at different speeds and different modulations. Afterwards, we need to find a correlation between the linewidth and the dose received  $D$ .

Using MZ10-2.5 cast over a buffer layer of MZ10-1, three different sets of lines written at different speeds (2, 1, and 0,75 mm/s) and laser modulation (0 – 100%) are prepared. The sample is soft baked for 5 min at 80°C, then developed for 1 – 2 min in butanol. Finally, it is rinsed in deionised water and blow dried using compressed air.

The linewidth  $L$  was measured using the automatic shape detection of a Keyence VHX 7 microscope, to avoid user bias. In addition, all the photos were taken with a 500 × 500 magnification. It is important to note that, the measurements of the linewidth were only done on revealed samples due to the difficulty to determine the boundaries of the waveguide with precision in unrevealed waveguides, due to limited penetration depth for high magnification objectives. We consider the linewidth to be the same in both cases.

Post measurement, the dose that corresponds to each  $P$  and  $v$  combination was calculated based on the approximation of the dose in Equation 3.7, given that the initial laser power  $P_0$  for the 1 μm diameter is 6.3 mW. The raw results for the MZ10-2.5 with Irgacure 189 are presented in figure 3.17.

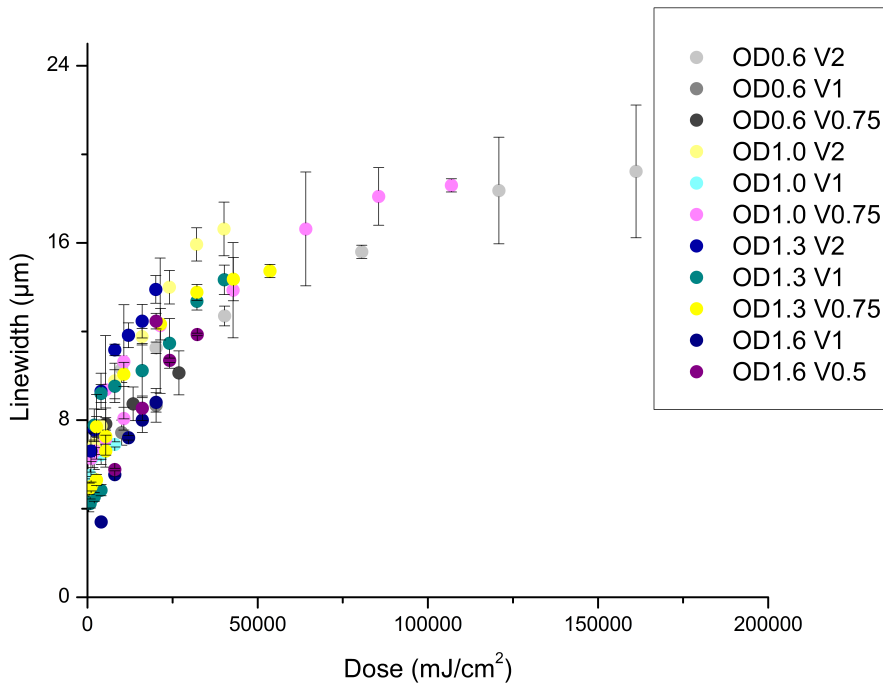


**Figure 3.17:** The cured linewidth as a function of the dose for the MZ10-2.5, for different combinations of filter's ODs and laser scanning speeds  $V$ .

The scatter plot shows the same trend as that presented in the experimental validation of Salgueiro [199] for truncated beam, and for high values of  $D$ , as seen in Figure 3.18. This relationship suggests that the linewidth changes as the square root of the dose. In order to verify this dependence we used  $L = a + b \times D^c$  in order to perform the fit. In fact we found a value of  $c$  that is equal to  $0.5 \pm 0.1$ , which is the value predicted by the model.

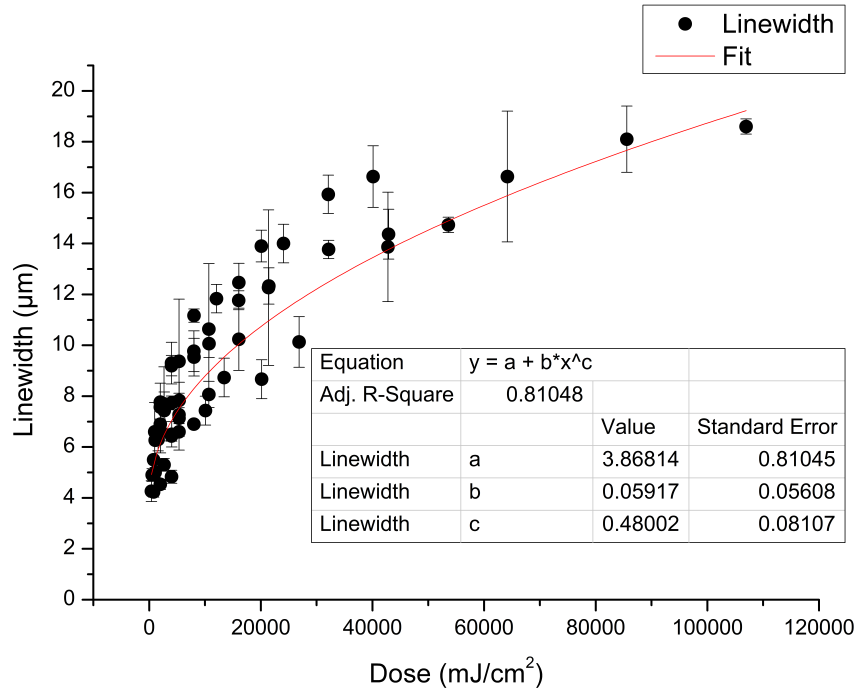


**Figure 3.18:** The cured linewidth as a function of the dose for the MZ10-2.5, with the corresponding fit.

This plot constitutes a working curve that can help us deduce the dose to be applied in order to create a line of specific width. Similar working curves can also be constituted for other types of photoresists in the same manner. Acquiring of sufficient number of measurements for  $L$  can be used to constitute a similar working curve, thus facilitating the prediction of the required dose to produce a certain linewidth.

We can also note that, for high doses, the linewidth reaches a certain threshold above which it will not increase drastically. In addition, the fact that with a  $1 \mu m$  diameter beam we are able to attain line widths as high as  $18 \mu m$ , is in perfect agreement with the observations in the literature. As seen in Figure 3.17, for extremely high values of  $D$  there is a big fluctuation in the measured values of the linewidth, as expected by the model for the truncated beam:

$$L_a = \frac{1}{\alpha} \Phi^{-1}\left(\frac{1}{k_a \Omega}\right) \quad (3.8)$$

where  $\Phi^{-1}$  fluctuates for extremely high values of  $\Omega$ , i.e. for high values of  $D^2$ . Thus in this range it is more difficult to predict the linewidth for a set of parameters.

---

<sup>2</sup>the subscript a refers to the case of a truncated beam with an Airy irradiance profile as explained in section 2.6.2 of chapter 2

### 3.6 Waveguides morphological characterisation

A single mode rectangular dielectric waveguide’s dimensions depends on the refractive index contrast between the core and the surrounding media. Figure 3.19 summarises the two different cases that we can encounter in our work, and that we have mentioned previously: either a waveguide created by refractive index increase, which we can call a diffused waveguide or one that is created by developing the photoresist to obtain a ridge waveguide.

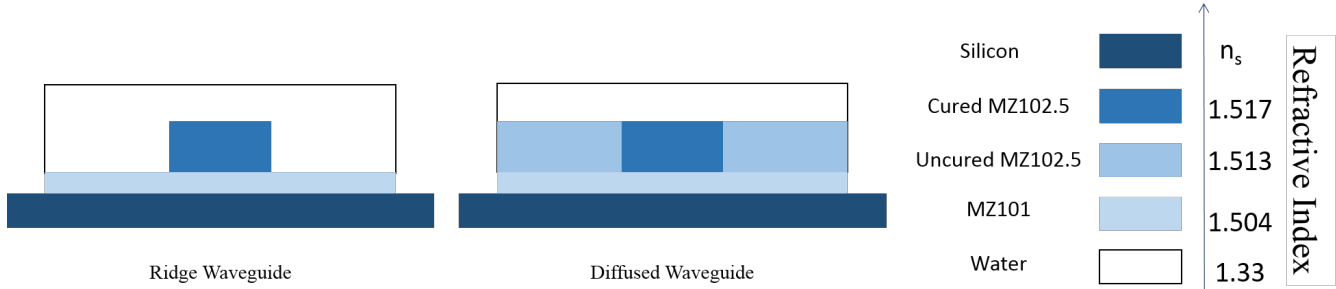


**Figure 3.19:** Summary of the waveguide’s core and surrounding media refractive indices.

Revealed waveguides implemented in MZ10-2.5, that have an index step of 0.2 with their surrounding medium<sup>3</sup> will lead to a better light confinement and will support the implementation of complex designs including bends. Nevertheless, we are also interested in index contrast waveguides due to the fact that they have smooth waveguide walls which might lead to less propagation losses in the visible range<sup>4</sup>. It is important to note that, the refractive index of the silicon substrate does not have any effect on the mode propagation in the waveguide core as long as the MZ10-1 buffer layer is thick enough to shield the core from this high refractive index of the substrate [163, 203]. Table 3.2 presents values of the channel width that support single mode operation. These values are estimated using Marcatilli’s closed form equations for  $E_{pq}^y$  presented in Chapter 1.a and  $b$  are the waveguides width and height respectively as introduced in Chapter 1.

	a=2b	a=b
Ridge Waveguide	3 $\mu m$	3 $\mu m$
Diffused Waveguide	6 $\mu m$	4 $\mu m$

**Table 3.2:** Values of the waveguide width  $a$  for different refractive index contrast and waveguide ratio.

#### 3.6.1 Dimensions and geometry of revealed waveguides

According to the section 3.5.2, the combinations of modulation and speed that can be used in order to produce single mode, or few modes waveguides are limited, especially if we need to use a low speed scanning. Some of these combinations are illustrated in table 3.3.

<sup>3</sup>assuming most microfluidic samples are aqueous samples

<sup>4</sup>This assumption will be addressed in the following section

		Filter $O.D. = 1.3$		Filter $O.D. = 1.0$
		$1\text{ mm/s}$	$0.75\text{ mm/s}$	$1\text{ mm/s}$
Modulation	10%	$4.8 \pm 0.3$	$6.6 \pm 0.7$	$6.9 \pm 0.1$
	5%	$4.5 \pm 0.2$	$5.3 \pm 0.3$	$6.4 \pm 0.2$
	2%	$4.2 \pm 0.2$	$5.0 \pm 0.2$	$6.3 \pm 0.5$
	1%	$4.3 \pm 0.4$	$4.9 \pm 0.3$	$5.5 \pm 0.2$

**Table 3.3:** Possible combinations for writing single mode waveguides.

We are able to write single mode waveguides using the above mentioned combinations as seen in Figure 3.20.

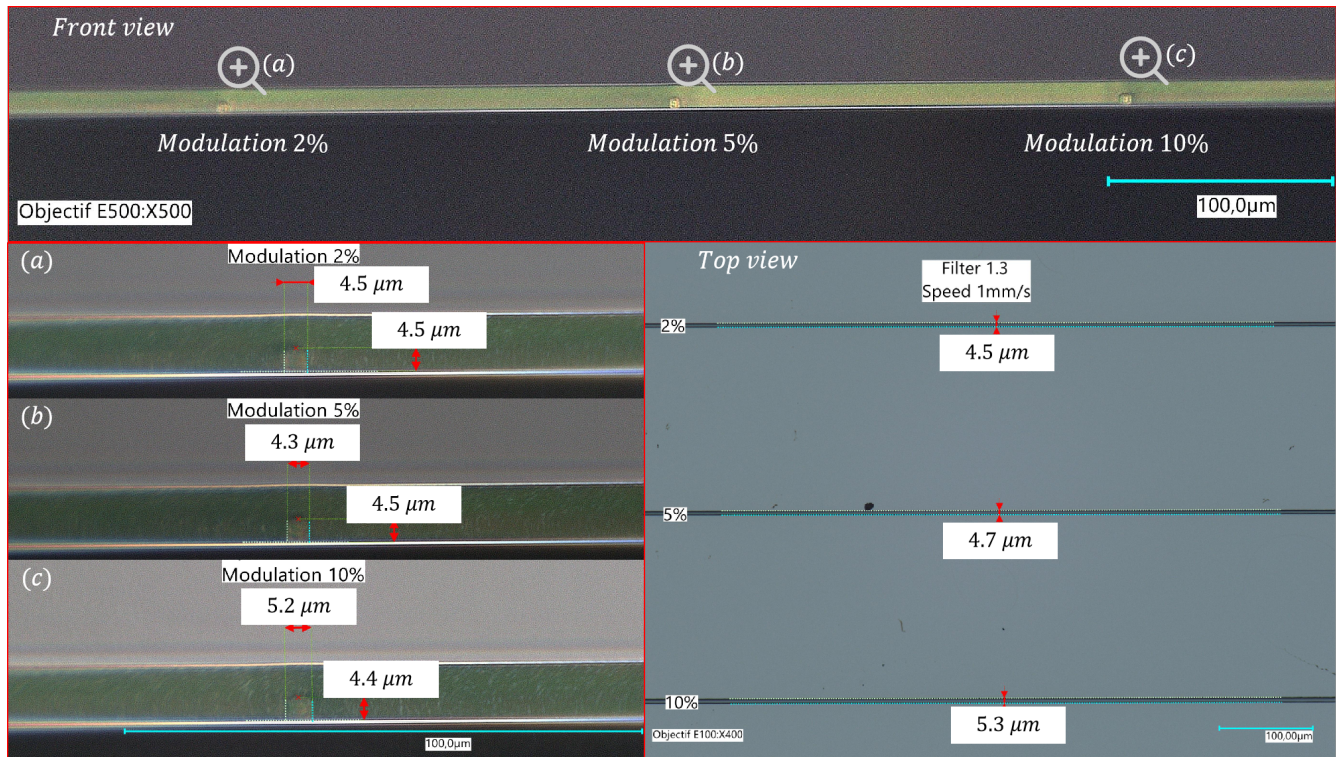


**Figure 3.20:** Waveguides fabricated with different combinations of modulation and speed using a Filter with an  $O.D.=1.3$ . On the top is the front view of the waveguides, on the bottom left is a zoom into each of the 3 waveguides, and finally the bottom right shows the top view of the waveguides. All the dimensions are indicated as well as the scale bars.

For example, a combination  $M = 5\%$  and  $v = 1\text{ mm/s}$  with a filter having an  $OD=1.3$  can be used to produce a waveguide having a width of around  $4.5 \pm 0.2\ \mu\text{m}$  (Figure 3.21). The taper of a width  $10.3 \pm 0.4$  is written by 2 passage of the laser beam.

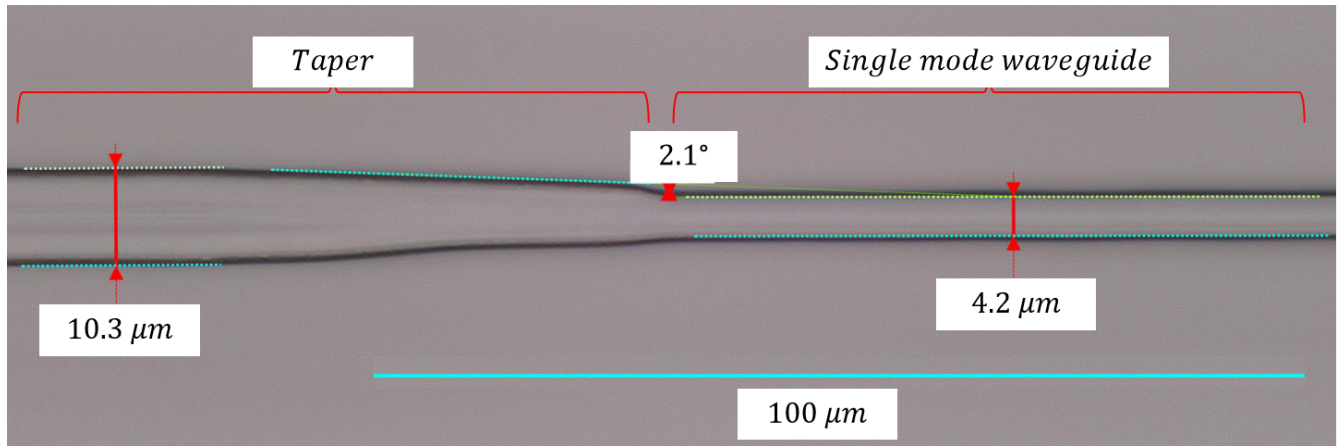


**Figure 3.21:** Optical microscope photos of the revealed waveguide structures, taken by optical microscope Keyence VHX7000. Writing parameters are  $M = 5\%$ ,  $v = 1\text{mm/s}$ ,  $OD = 1.3$

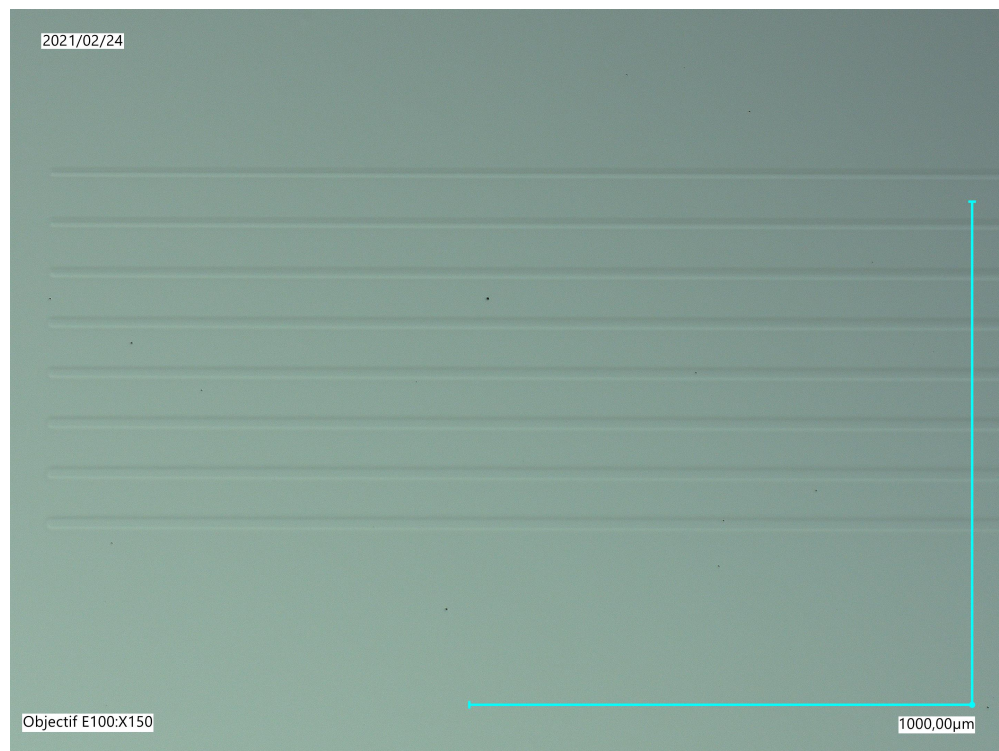
Tapered waveguide with wider input aperture provides the optimum solution for wide tolerance to source misalignment and excellent modal behaviour. Thus, in order to maximize the light coupled into the waveguide, our strategy is to use a slowly varying tapered waveguide entry as presented in chapter 1. Radiation losses and Back reflection losses were found to decrease as the taper length increase [29]. Longer taper length means small taper slopes, this would prevent the mode from perceiving an abrupt change in its path. Taper's angle is usually around  $1^\circ$  for dielectric waveguides that have an index of 1.54 [206]. Thus, we fixed the taper length to  $50 \mu\text{m}$ , which produced a slope of  $2.2 \pm 0.3^\circ$ .

### 3.6.2 Dimension and geometry of unrevealed waveguides

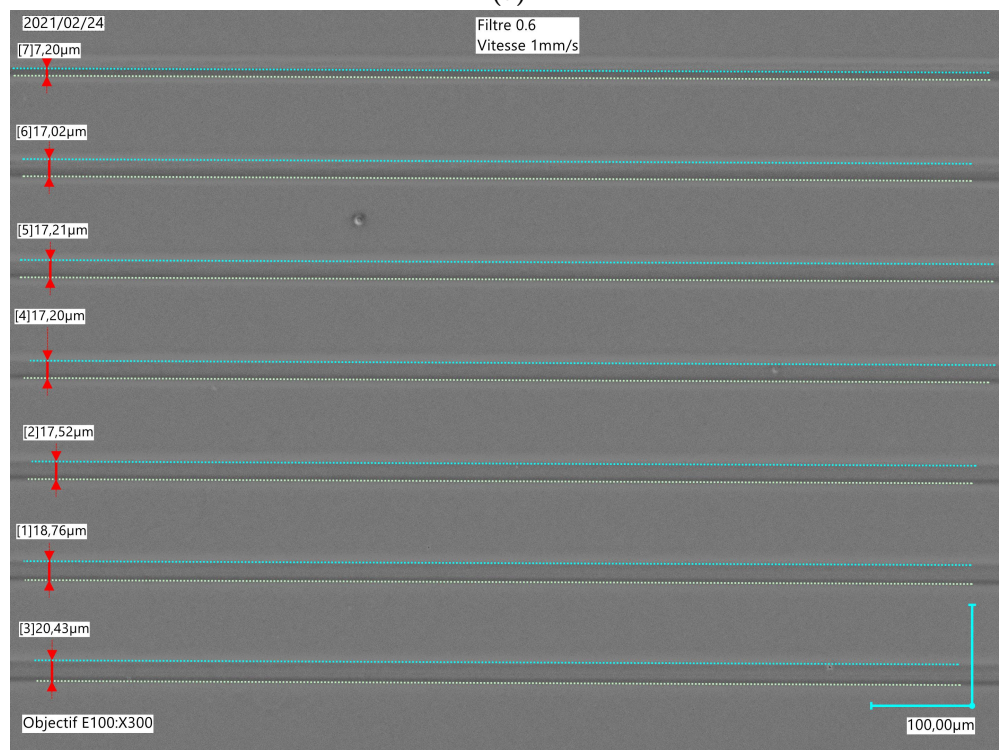
Waveguides fabricated using refractive index increase in the photoresist were observed under an optical microscope. The observation of these waveguides is challenging, due to the slight refractive index difference. They are only visible under partial coaxial illumination. This is probably due to the fact that the light is reflected by the waveguide's lateral walls under lateral illumination. SEM didn't demonstrate to be of good use to this task because there is no contrast between the chemical composition of the waveguide and its surrounding.

In Figure 3.22a, we can see the optical microscope image taken using partial coaxial illumination of the sample. In Figure 3.22b, we can see the same sample, imaged using the HD functionality<sup>5</sup> of the digital microscope. This gives good quality images of the waveguides expect for high magnification, due to the limited depth of the field, without the need to use a phase contrast microscope, which was expected to enhance the sharpness of the image in the same manner.

<sup>5</sup>It is a function that reconstructs the image from other ones taken at different illumination angles.



(a)



(b)

**Figure 3.22:** Optical microscope photos of the written waveguides, by refractive index increase in MZ10-2.5, at different power modulation, at a scanning velocity of 1mm/s and using an OD=0.6. Seen under a) partial coaxial illumination, and b) the using the HD functionality of the optical microscope Keyence VHX700.

The observation of these waveguides profile is not possible with neither SEM nor the optical microscope. Their width can be tailored using the same parameters as it is for the case of revealed waveguides, as in Table 3.3.

### 3.7 Power transmission and optical losses

Our purpose in this section is to assess the quality of the power transmission and the light coupling into the waveguide. In addition, since side wall roughness leads to scattering loss which is dominant in the visible range, we need to estimate the power transmission in a revealed waveguide structure, and compare it to another waveguide elaborated by refractive index increase in the photoresist. This will help us determine if there is a certain trade off that can be made between the propagation losses and the refractive index contrast.

In order to measure the losses and visualise the far field modes in the visible range, we used a fiber coupled laser source (Thorlabs) operating at  $635\text{ nm}$  and with a nominal power of  $P_1 = 2.5\text{ mW}$ , a spectrum analyser (Agilent 86142B), and 2 single mode 630-HP optical fibers (Thorlabs) and a camera to visualise the far field profile.

#### 3.7.1 Light propagation in unrevealed waveguides

Even for refractive index contrast as low as 0.004, the propagation in refractive index contrast waveguides is confirmed as seen in the far field images of Figure 3.23.

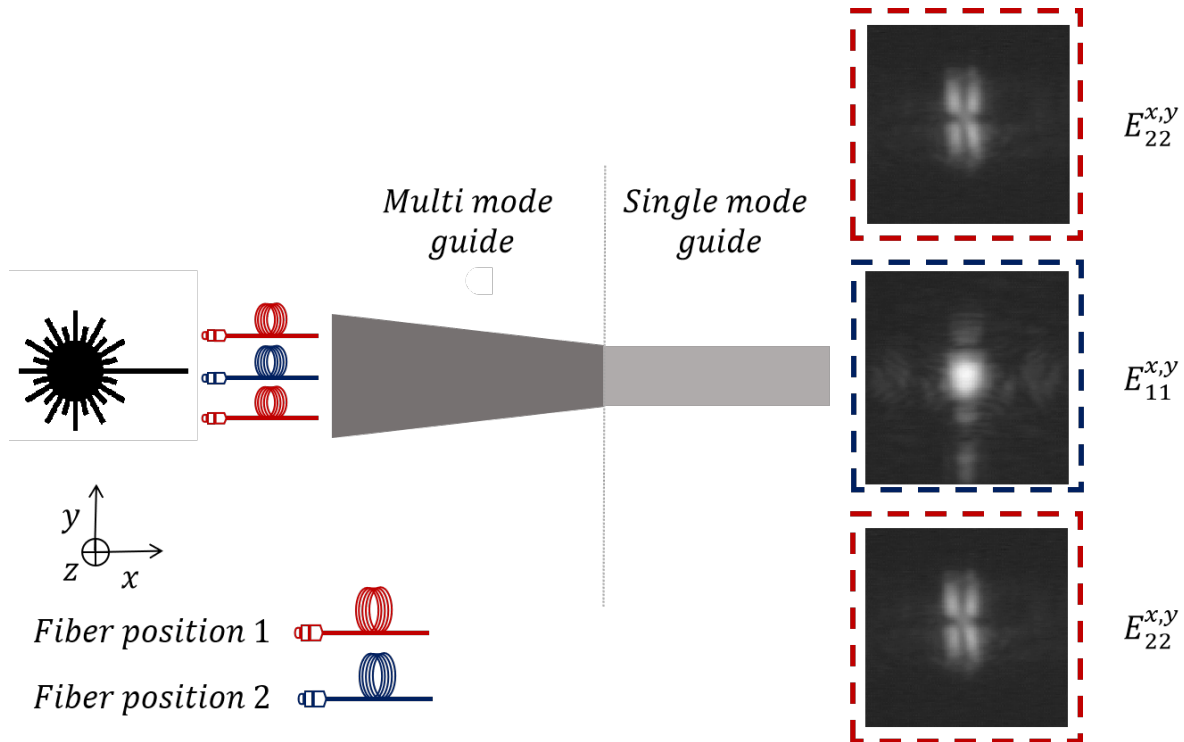


**Figure 3.23:** Far field photos of the different propagating modes that can be excited in the fabricated waveguides.

We could also observe that depending on the position of the fiber along the  $y$  axis, we can excite and propagate either the  $E_{11}$  or the  $E_{22}$ :

- if the fiber is aligned with the center of the taper the first order mode propagates,
- if the fiber's position is eccentric we can see that the fundamental mode cease to exist. Instead the  $E_{22}$  mode is excited and propagates in the waveguide. This is probably due to the fact that TIR occurs on the taper's walls before penetrating the waveguide.

The optical losses in these waveguides will be estimated in order to judge their importance when compared to revealed waveguides.

### 3.7.2 Propagation Losses at 365nm

One of this chapter's objectives is to compare the optical losses in refractive index induced waveguides and revealed waveguide structure. The aim being to know if the development step induces roughness on the surface that can increase the losses due to scattering. In addition, since scattering losses are most dominant in the visible range, and to avoid other sources of possible attenuation such as OH absorption in the IR, we chose to operate at 365  $nm$ .

To estimate the propagation loss we adopted the well-known cut-back measurement method that is based on optical transmission measurements of a set of waveguides with varying lengths. Cut back measurements therefore require in and out-coupling. The coupling is optimized by tuning the fiber position with respect to the sample position in order to maximise the transmitted power. The transmitted spectrum is visualised and measured by the spectrum analyser. The setup, equipment and sample are presented in Figure 3.24.

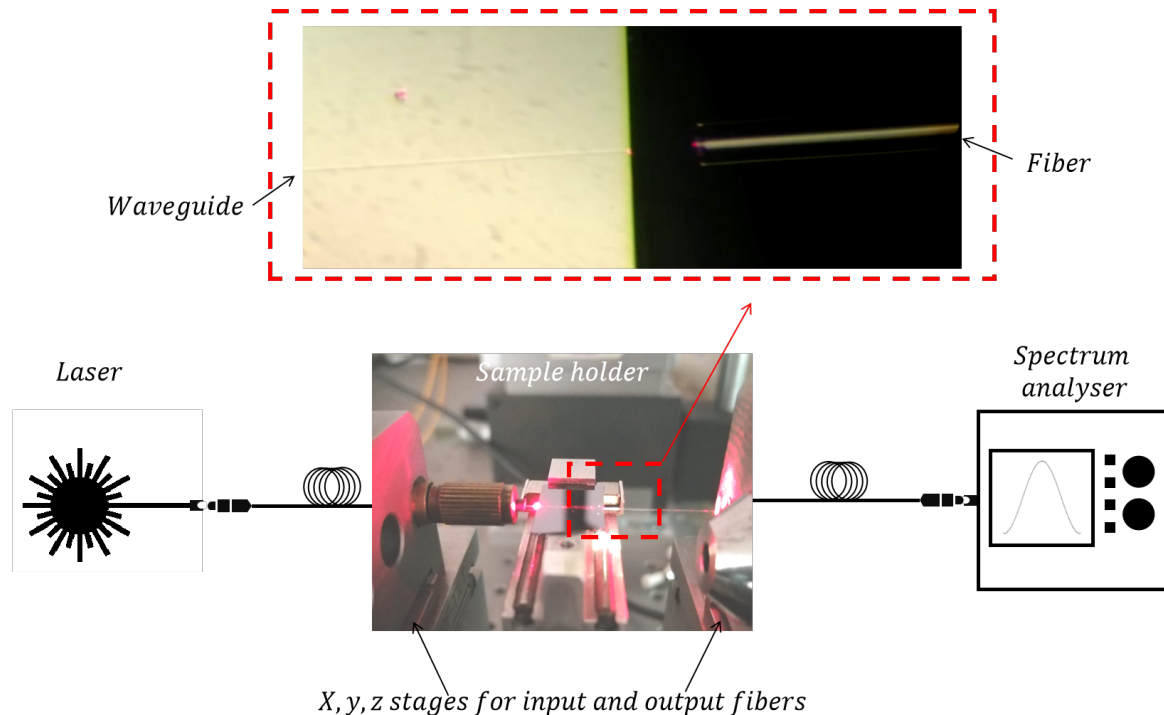


**Figure 3.24:** The setup used to measure the power transmission along the waveguides. The upper photo shows the exit facet coupling.

For this purpose two sets of 5 waveguides were prepared:

- the first set of waveguides was fabricated by UV induced refractive index change
- whereas the other is revealed after exposure, then covered with a  $5\ \mu\text{m}$  layer of the same photoresist in order to reproduce the same refractive index contrast, in a way to assess the effect of the revelation step on the waveguide's propagation loss.

Five measurements of the transmitted power are performed on each waveguide for different waveguide length. We started with a  $2.5\ \text{cm}$  length waveguide, the sample is reduced in length multiple times, and the length of the waveguide is measured after cleaving. The results were acquired in nW, and transformed into dBm. The mean values presented below are the mean of the dBm values. The power transmission in dBm vs. waveguide length for refractive index contrast waveguides is illustrated in Figure 3.25.

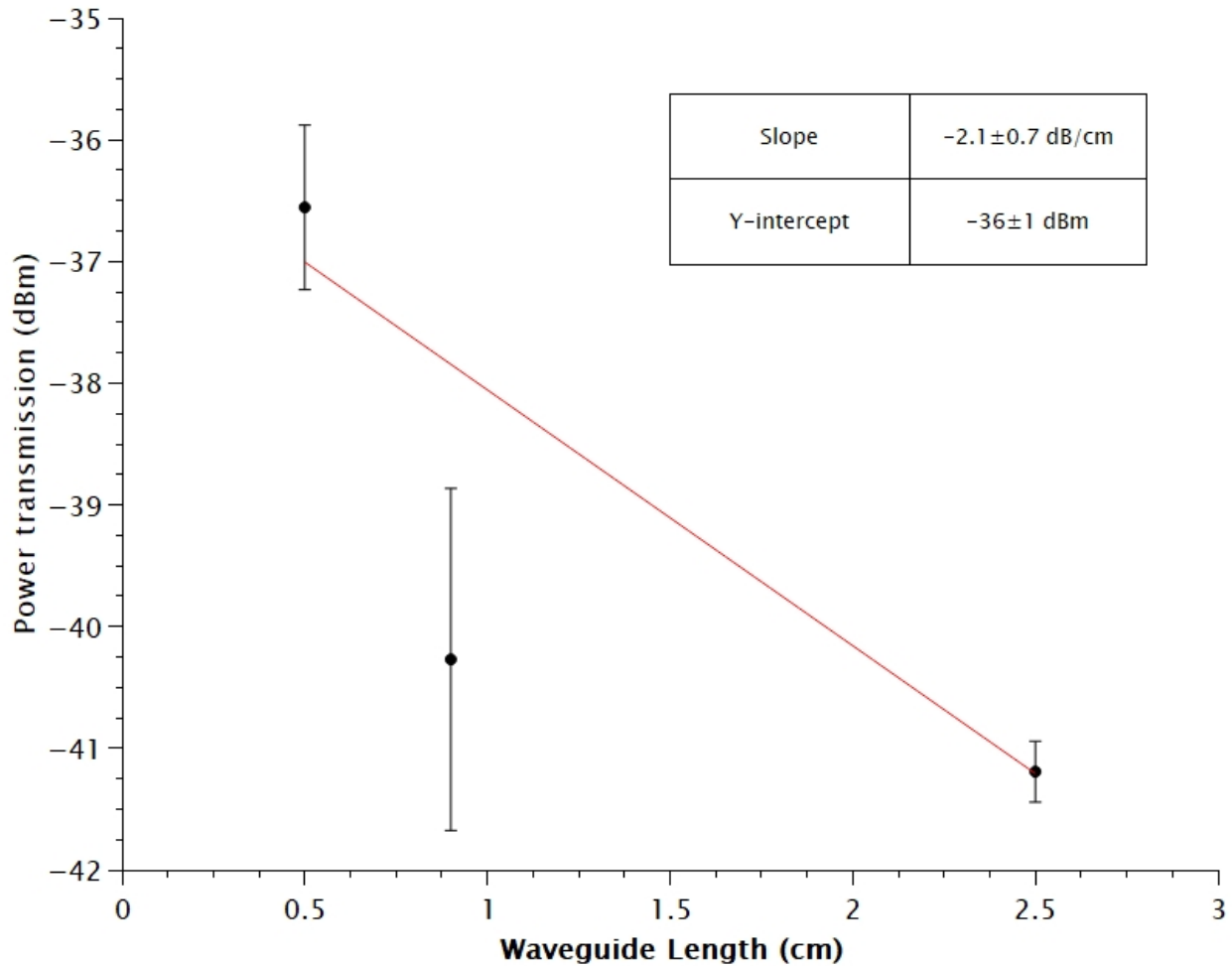


**Figure 3.25:** The power transmission plot in dBm for refractive index contrast waveguides.

Because we do not have the same error on all the measurements, a weighted linear fit was done to deduce the propagation losses. In this manner, less importance is given for the less precise

measurements. Propagation losses are estimated at  $2.1 \pm 0.7 \text{ dB/cm}$ , while the power coupled at the waveguide entry is  $-36 \pm 1 \text{ dBm}$ .

The same measurements for revealed waveguides can be seen in Figure 3.26. They also show propagation losses of  $2.5 \pm 1.1 \text{ dB/cm}$  and a value of the power coupled into the waveguide entry facet of  $-36 \pm 2 \text{ dBm}$ .

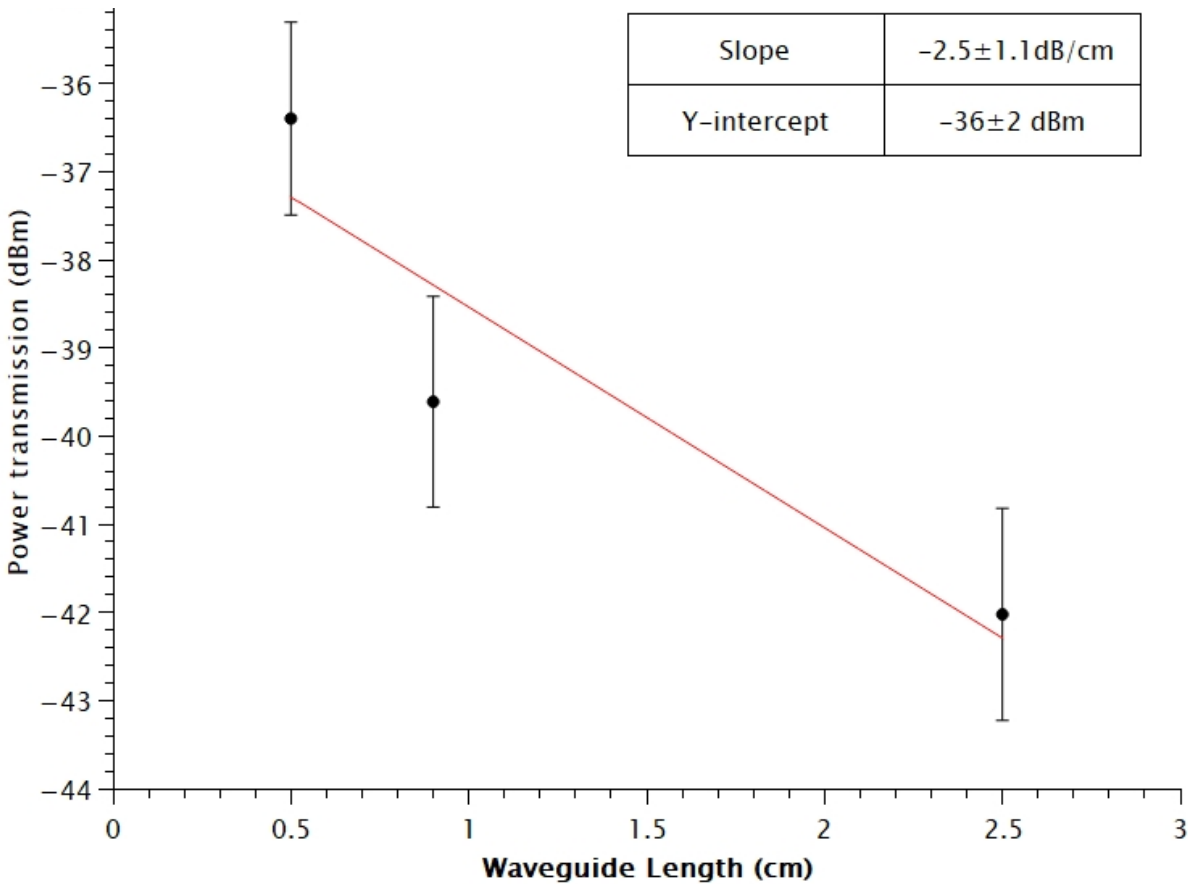


**Figure 3.26:** The power transmission plot in dBm for revealed waveguides.

We can deduce from the above results that there is no difference between the revealed and unrevealed waveguides in terms of propagation losses in the visible range. These values are slightly higher than those mentioned in the existing literature [203] for the same type of waveguides. We should note that the relative errors on the measurements and subsequently on the propagation losses values are high. The first explanation that might come to mind is that, it is difficult to reproduce the same coupling quality every time the sample is cleaved, without influencing the measured value of the transmitted power. In fact, the cut-back method highly depends on the coupling, because the estimation of the propagation losses is normally done after assuming that the coupling is identical at each measurement. However, the fact that the estimated power coupled into the waveguide does not change for both experiments seems to eliminate this hypothesis.

### 3.7.3 Coupling losses at the connections

In order to have an insight into the losses at the level of the laser/fiber and fiber/analyser connectors, we measured the power transmitted from the laser to the spectrum analyser without a sample. Ideally it is preferred to use the same fibers' lengths for all the experiments, but given that coupling losses are much higher than propagation losses, we didn't control the length of the fiber.

This being said, the power transmitted from the laser (having a nominal  $P_1 = 2.5 \text{ mW}$ ) to the spectrum analyser was monitored for 2 minutes with a sampling done every 5 seconds and it resulted in an average transmitted power  $P_3 = 22 \pm 2 \mu\text{W} = -16.6 \pm 0.5 \text{ dBm}$ .

If we consider that the two connectors are identical and that the propagation losses in the fibre ( $< 1.5 * 10^{-2} \text{ dB/m}$  at  $630 \text{ nm}$  [207]) are negligible compared to the losses at the connections, we can formulate a relation between the laser power  $P_1$ , the power  $P_2$  propagation in the fiber, the power  $P_3$  measured by the analyser:

$$10 \times \text{Log}\left(\frac{P_2}{P_1}\right) = 10 \times \text{Log}\left(\frac{P_3}{P_2}\right) \quad (3.9)$$

As such we can deduce the following quantities, that are illustrated in Figure 3.27:

- The power  $P_2$  transmitted to the fiber is equal to  $23.4 \pm 0.11 \times 10^2 \mu\text{W} = -6.3 \pm 0.3 \text{ dBm}$
- The coupling losses at the fiber/connector interface can be estimated at:  $10.3 \pm 0.8 \text{ dB}$

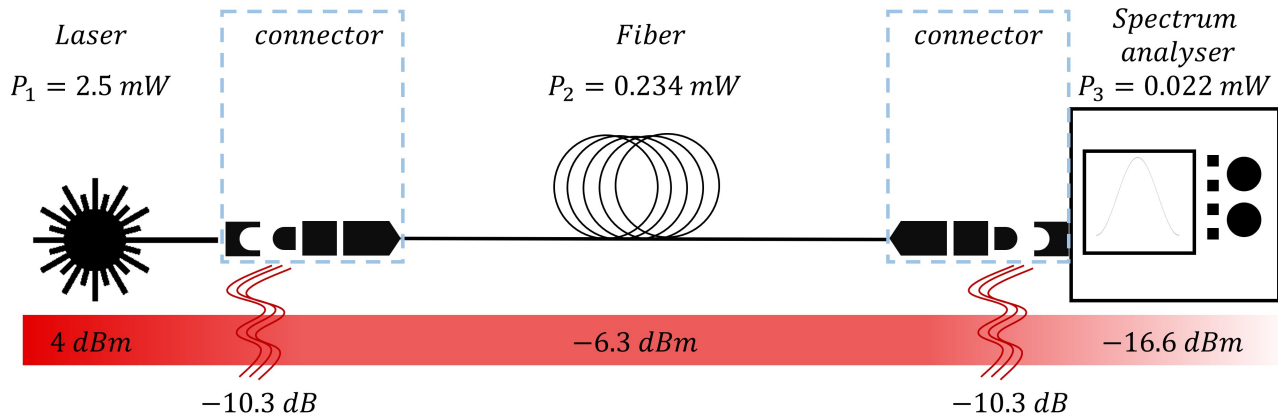


Figure 3.27: Schematic illustration of the setup used to measure the power at different levels of the equipment

## 3.8 Conclusion

In this chapter we presented the different steps for creating and characterising optical waveguides in a negative tone hybrid photoresist that is the MZ10-X. We used the Phenylbis(2,4,6-trimethylbenzoyl)phosphine oxide as a PI in order to implement waveguides either by refractive index increase or by developing the photoresist. We validated a framework for tailoring the linewidth of the written waveguides in hybrid photoresist and we found a tendency that agrees very well

with the proposed model for laser writing using a truncated Gaussian beam. The linewidth of the written waveguides was found to vary as the square root of the dose. Finally, we characterised the waveguides morphology and power transmission in the structure. We confirmed that waveguides with a refractive index contrast as low as 0.004 can be used to confine light, for lab on chip application as we have seen in section 2.3 of Chapter 2. We also found propagation losses as low as  $2\text{ dB/cm}$  for unrevealed waveguides. However, in the context of LoC for optical manipulation a high refractive index difference should be used. Thus, revealed waveguiding structure having a refractive index difference of around 0.2 with the surrounding medium (being water) are more adapted, especially that they do not show higher losses than unrevealed waveguides.



# Chapter 4

## The positive working resist

### 4.1 Introduction

Negative-working resists are in widespread use, nevertheless positive-working resists have inherent advantages over negative photoresists. In the context of the present work, a photosensitive positive-working resist is highly advantageous, when it comes to decreasing laser writing time, for LoCs R&D. The prototyping materials for the fluidic channels of the chip, should be identical to those used for mass production, in order to avoid the extra effort, time and cost that will be needed for redesign. Therefore a positive resist is equally adapted for R&D and production. Other benefits of positive resists includes higher resolution, stability in the presence of oxygen (when compared with radically polymerised negative resists), and less swelling upon development. Elaborating the microfluidic layer with a hybrid photosensitive resist allows us to harness the full potential of these materials. Moreover it facilitates the alignment task, that can be routinely integrated within the laser writing process.

For this reason, this chapter will be directed towards the elaboration of a thick photosensitive positive tone resist suitable for the fabrication of microfluidic channels walls. We are going to explore the potential to use a positive tone hybrid resist based on a polyamic acid (PAA) and vinyl ether (VE) crosslinkers for the microfluidic layer of the chip. In section 4.2, we address the characteristics of a photoresist that can be used for microfluidic chips elaboration, and for optofluidic integration. This will be followed in section 4.3, by a discussion about the limitations of this resist and the methodology to follow in order to enhance its performance. Afterwards, in section 4.4, we assess the transparency of this photoresist to the available insulation wavelength. Later, in section 4.5 we characterise the polymer using NMR: we determine the chemical shifts and estimate its molecular weight. We will also briefly discuss its stability over time at room temperature. Section 4.6 is dedicated to the investigation of two different ways in order to increase the solid content of the resist. Finally and most importantly, in Section 4.7 we are going to investigate the reactivity of the carboxylic acids and VE groups and we are going to propose a reactive model that is expected to reflect the activity of poly(pyromellitic dianhydride-co-4,4'-oxydianiline) (*PMDA-ODA*) and 1,3,5-tris[(2-vinyloxy)ethoxy]benzene (*TVEB*).

## 4.2 The requirements for a resist used to fabricate microchannels

In order for any resist to be utilised for microfluidic applications achieving high wall thickness is essential. Thick resists can be classified based on the thickness that they can attain as follows:

- moderately thick resists, produce layers between 5 and 10  $\mu m$  thick
- thick resists can attain 25  $\mu m$
- very thick resists can reach 50  $\mu m$
- and finally ultra thick resists can reach 100  $\mu m$  or even higher layer thickness.

Preferably it is important to be able to attain 100  $\mu m$ , because this is the maximum channel walls height usually used in microfluidics. Lower thickness values can be easily obtained by diluting the resist in additional solvent. In general the requirements for elaborating such a thick photoresists are:

- high solid content of the copolymer in the application solvent, in order to enable higher layer thickness deposition by spin coating
- high transparency of the copolymer at the exposure wavelength, in order to allow higher penetration depth of the UV light
- the association of the copolymer with a chemically suitable photosensitive compound, that should also procure a high photosensitivity at the operating wavelength.

Other prerequisites are application specific. In the case of optofluidic lab on chip, the requirements extend to:

- good adhesion to the optical layer
- the chemical inertia between the optical layer material and the application solvent on one hand
- the chemical resistance of the optical layer to the development solvent of the microfluidic layer
- the compatibility of the optical layer material with the process parameters of the microfluidic layer, most notably the baking temperatures
- lower refractive index than that of the optical waveguides.
- and finally biocompatibility

## 4.3 Statement of the problem

In the work of Mechref et al [167, 186], channel walls of  $3\ \mu\text{m}$  are fabricated, using a composition of PMDA-ODA: TVEB: VEPTES: PTMA, having a molar ratio of 10:3:5:3. Afterwards we faced some complications while trying to attain higher channel walls, because longer soft baking times (at  $110^\circ\text{C}$ ) did not lead to lower dissolution rate of the unexposed film. In the present work we will further investigate the limitations and capabilities of this resist, for the use in microfluidic channels fabrication. Multiple reasons are suspected to induce such difficulties:

- the limited transparency of the precursor (PMDA-ODA) to the i-line wavelengths,
- the low molecular weight of the polymer,
- reactivity problems arising from:
  - the competition of the copolymerisation of the PAA and the VE reaction, with imidisation and the VE cationic polymerisation,
  - the low acidity of the COOH groups of the PAA, which doesn't enable the opening of the VE double bond,
  - the protection of the COOH by the solvent (NMP specifically) until  $165^\circ\text{C}$  [208], thus inhibiting the reactivity of the COOH groups at the SB temperature  $110^\circ\text{C}$ .

In order to identify which one of these constraints is limiting the performance of this resist, we will proceed as follows:

- first we acquire the absorptance spectrum of the precursor, this will be helpful in choosing the optimal laser writing wavelength to be used for this resist
- afterwards we tackle the reactivity problem, after presenting our approach for characterizing the precursors and following the copolymerisation reaction kinetics.
- we also investigate the possibility to increase the solid content of the precursor in the photoresist, in order to attain higher wall thickness.

## 4.4 Transmittance spectrum of PMDA-ODA

Evaluating the Transmittance of PMDA-ODA in the UV range helps us to choose the most appropriate insulation wavelength. Two lasers are available in our facility. They operate at  $375\ \text{nm}$  and  $407\ \text{nm}$ . Before performing the absorptance measurements, we elaborate a spin coating calibration curve for the polymer.

### 4.4.1 Spin coating deposition of PMDA-ODA

Multiple PMDA-ODA (15% wt. in NMP, purchased from Sigma-Aldrich) films were deposited on a silicon substrate at varying spin speeds (ranging between 1000 and 5000 *RPM* with an increment of 1000 *RPM*) for 30 seconds. They are baked at  $165^\circ\text{C}$  for 30 minutes to evaporate the solvent. The sample is cleaved and observed under a microscope. The PMDA-ODA film thickness curve as a function of the spin speed is presented in Figure 4.1.

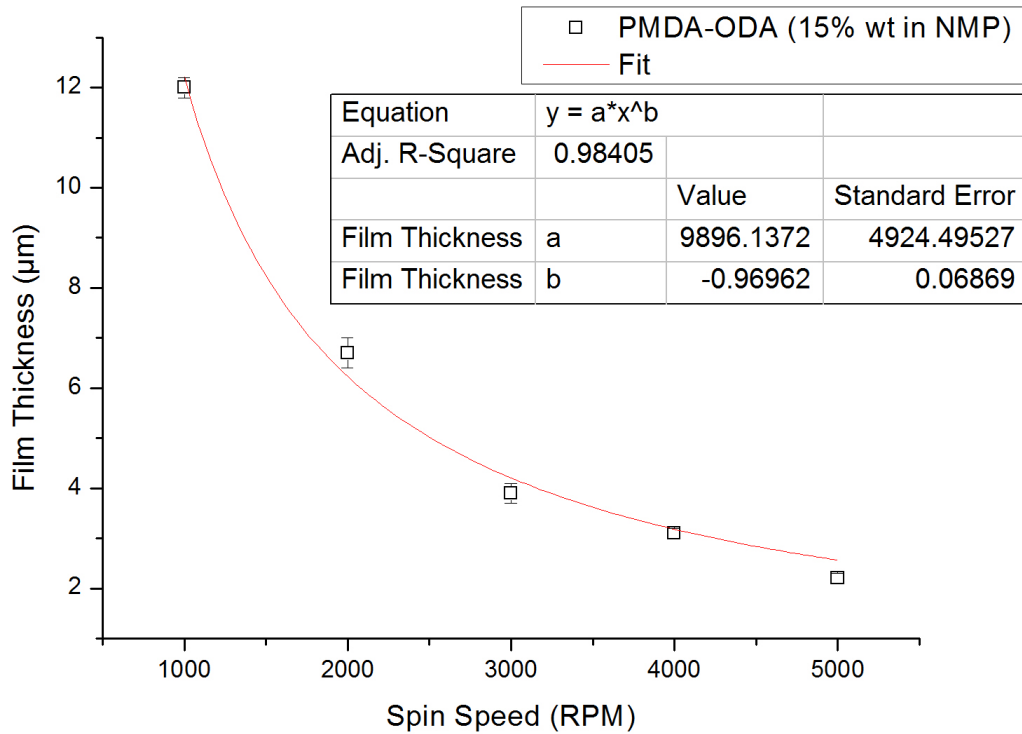


**Figure 4.1:** Thickness versus spin speed for PMDA-ODA, with a 15% wt. in NMP.

We can note that for a 15%wt of PMDA in the solution we are only able to cast a 12  $\mu m$  film. Therefore if we need to elaborate thicker films, higher solid content in the solvent is required. In addition the experimental curve of PMDA-ODA spin coating curve follows the same trend as a  $1/\omega$  function:

$$h_f = (10^4 \pm 5.10^3)\omega^{(-1\pm 0.1)} \quad (4.1)$$

As such the deviation between the spin coating model of Meyerhofer and the measured value could not be explained by a wrong estimation of the evaporation rate. Because in such case,  $e$  will vary as  $1/\omega$  in order for the model to remain true. Which means that the higher the spin speed is, the less the evaporation rate. The fact that the evaporation rate decreases with increasing spin speed seems counter-intuitive.

#### 4.4.2 Spectrophotometry measurements

The transparency at the exposure wavelength is an essential requirement in order to elaborate a thick photoresist. To deduce the absorbance spectrum of PMDA-ODA in the UV, we acquire the transmittance and reflectance spectra of PMDA-ODA films. First we cast PMDA-ODA films at different spin speeds ranging from 1000 to 5000  $RPM$  for 30 seconds and with an increment of 1000  $RPM$ . A series of UV-Visible spectra are recorded on these films of varying thickness deposited on a microscope slide using a UV-visible Aquila nkd 7000 spectrometer. The microscope slide spectra are also acquired. These results are presented in Figure 4.2. We can note the appearance of interference fringes in the visible for thinner films.

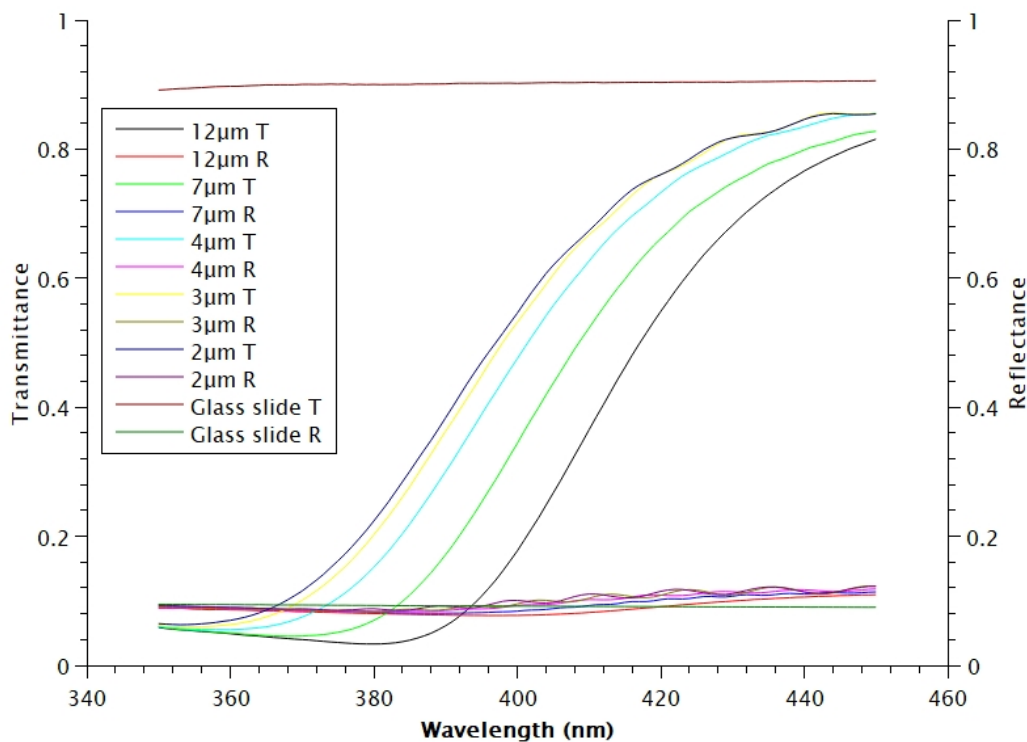


**Figure 4.2:** UV-Visible reflectance and transmittance spectra of PMDA-ODA films of different thickness.

Under the assumption that no scattering takes place in the film nor in the substrate, the absorbance was computed from the transmittance and reflectance spectra of each sample according to the formula:

$$A(\lambda) = 1 - T(\lambda) - R(\lambda) \quad (4.2)$$

The resulting spectra are presented in Figure 4.3 and show an absorbance maximum around the i-line.

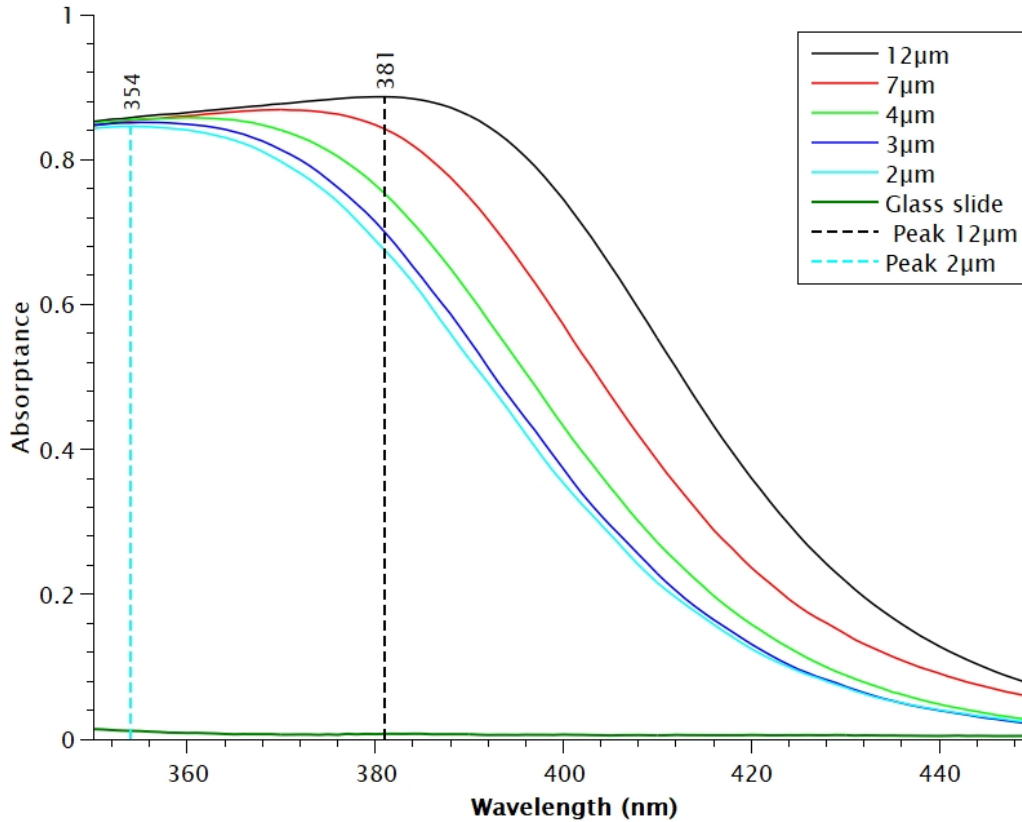


**Figure 4.3:** UV-Visible absorbance spectra of PMDA-ODA films of different thickness, as well as that of the glass slide used as a substrate.  $354\text{ nm}$  and  $381\text{ nm}$  are the wavelengths that correspond to maximum absorbance for the  $2\text{ }\mu\text{m}$  and the  $12\text{ }\mu\text{m}$  thick films respectively.

The absorbance maximum, shifts from  $353 \pm 1\text{ nm}$  for  $2\text{ }\mu\text{m}$  thick film to  $380 \pm 1\text{ nm}$  for  $12\text{ }\mu\text{m}$ . This shift is also accompanied by a same behavior of the reflectance minimum as seen in Figure 4.2.

Even though this cannot be considered as the absorbance ( $-Ln(T)$ ) spectrum of the PMDA-ODA it can be a good indicator of the absorption behavior of a film of the polymer in the UV range. Therefore the use of PMDA-ODA at an insulation wavelength of  $375\text{ nm}$  will not be possible, especially for thick layer, due to the high absorption of the polymer at this wavelength. However, at  $407\text{ nm}$  the absorbance is lower than in the i-line as shown in Figure 4.4.

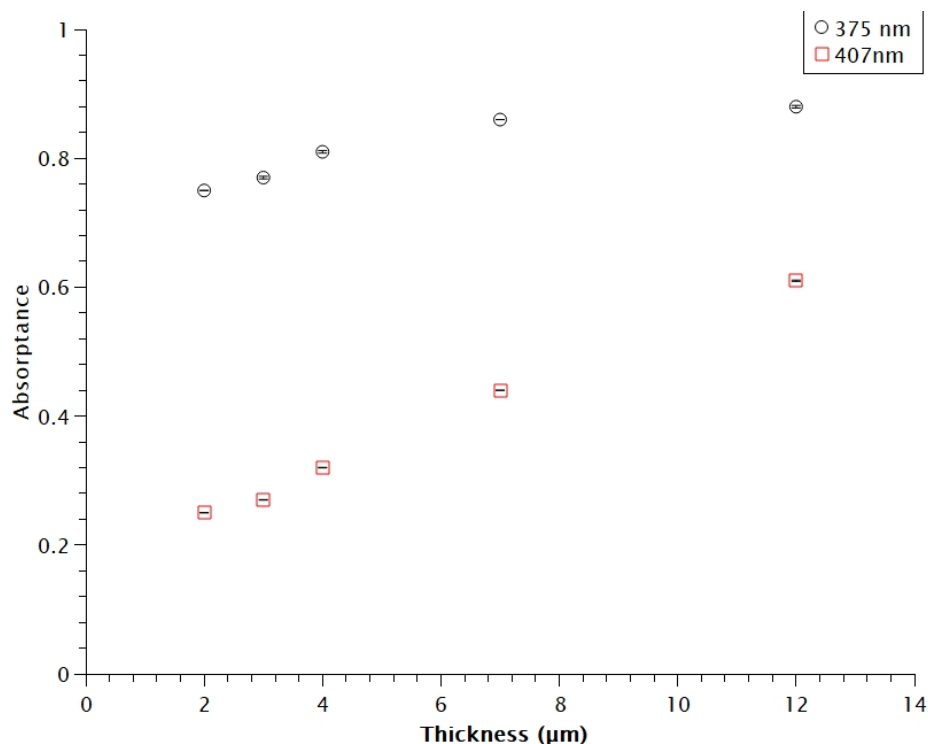


**Figure 4.4:** UV-Vis absorbances of PMDA-PDA films as a function of the film thickness for different wavelengths of interest.

Thus PMDA-ODA is more adapted for the use as a photoresist precursor at 407 nm. Nevertheless even at this wavelength, realising moderately thick (5 – 10 μm) layers with a resist based on PMDA-ODA, is challenging because the UV light cannot pass through the layer without being extremely attenuated. On the other hand one study showed that by decreasing the ODA content in a polyamic acid composition (PMDA; 2,5(6)-bis(aminomethyl)bicyclo[2.2.1]heptane (*NBDA*); ODA) the transparency window may be shifted or extended. This means that other polyamic acids may be used in order to have an i-line sensitive polyamic acid resists [195].

## 4.5 Characterization of the “as received” polyamic acid

Suitable characterisation methods should be chosen in order to fulfill multiple requirements:

- the determination of chain length of the polymer as it has a significant influence on its dissolution rate [192]. This is a primordial step in the fabrication of a working photoresist.
- following the aging of the precursor, and guarantying reproducibility of the resist in case of a future change of the supplier.
- the investigation of the crosslinking and decrosslinking reactions for different parameters.

### 4.5.1 The choice of the characterisation method

Two methods of characterisation are usually used to follow the reactivity of a system: nuclear magnetic resonance (NMR) spectroscopy and IR spectroscopy. As we said in section 2.4.4, the reaction kinetics between the VE and the carboxylic acids of the PMDA-ODA, was already studied

using FTIR in the work of Mechref et al. [167,186]. It showed a  $43 \pm 2\%$  conversion rate of amide C=O groups after 15 minutes thermal bake at  $110^\circ C$ , for a composition of molar ratio 10:3:3 (PMDA-ODA:TVEB:PTMA).

In our photoresist synthesis we use a  $15\% wt$  PMDA-ODA solution, in NMP from Sigma-Aldrich. On one hand we need to characterise it, without further processing to be able to follow its aging, ensure reproducibility over time, and estimate its molecular mass. All of which should be done without further processing, such as baking or drying. This is not possible using IR spectroscopy because the integrals of a peak is proportional to the concentration of the bond to which the corresponding vibration belongs. Therefore the IR spectrum of the PMDA-ODA is completely masked by that of the NMP.

On the other hand we need to follow its reactivity with VEs crosslinkers. IR spectroscopy is a great method to accomplish this task. Nevertheless since it was shown that proton NMR is a quantitatively precise characterisation method for PAA's and PI's, as well as for the transition between them [209], we decided to adopt this method.

A series of proton NMR spectrum was done on multiple samples of PMDA-ODA. They offered an insight into the reactions kinetics as well as the possibility to estimated the molecular mass of the polymer. All of which can be done through the analysis of a single  $H^1$  NMR measurement.

## 4.5.2 Assignment of the chemical shifts to the corresponding protons

Before being able to estimate the chain lengths or studying any possible reaction, it was essential to determine the chemical shifts of PMDA-ODA protons. It is well known from the literature that the polyamic acid prepared from a mixture of PMDA and ODA in NMP consists of repeating units of two different configurations, a meta-PMDA-ODA and a para-PMDA-ODA as illustrated in Figure 4.5 which will also be called Isomer A and B respectively in the remainder of the document. According to Chu and Huang [209], these isomers are approximately present in comparable amounts: 46% of the repeating units are those of isomer A and 54% are units of isomer B. These values were deduced from a proton NMR study.

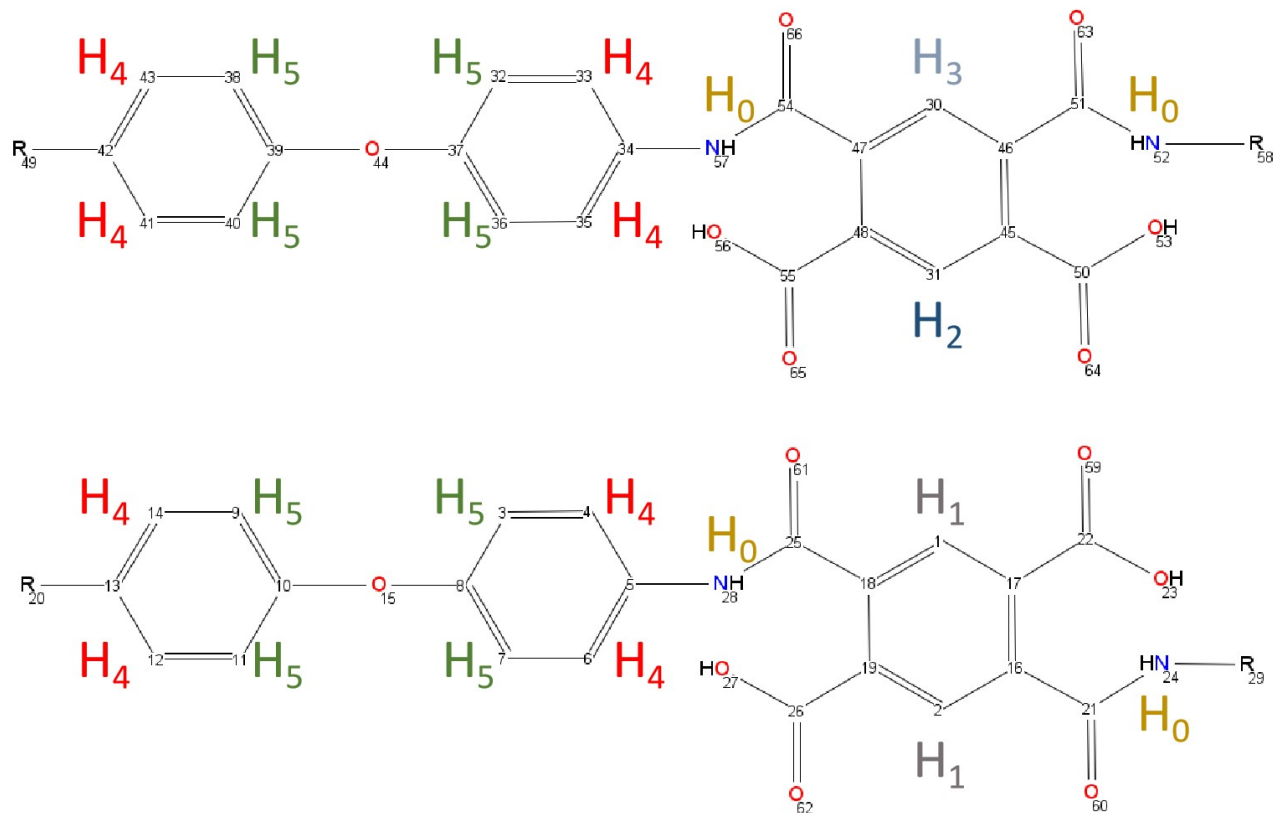


**Figure 4.5:** PMDA-ODA configurations, the meta-PMDA-ODA configuration, which will also be called isomer A (top) and the para-PMDA-ODA configuration, which will also be called isomer B (bottom).

The hydrogen atoms are annotated ( $H_0 - > H_5$ ) and color coded depending on their electromagnetic equivalence. The atoms numbering (1 - > 64) refers to non hydrogen atoms such as carbon, oxygen and hydrogen.

The first step in structural characterization of the precursor is 1-dimensional proton  $H^1$  NMR. The assignment is based on the chemical shift, multiplicity, coupling constants, and integration. The proton NMR spectrum of PMDA-ODA is presented in Figure 4.6, along with the shifts assignment in the corresponding Table 4.1. All the peaks are singlets except for  $H_4$  and  $H_5$ , that are both doublets. In theory they should appear as such. In practice  $H_0$  appears as two singlets,  $H_4$  and  $H_5$  appear as a two doublets. This is due to the fact that each one of these atom's spins, slightly vary between the meta and the para configuration. Nevertheless this will not change anything in our interpretation.

Peak	$\nu(F1)$ [ppm]	Intensity [abs]	Corresponding Atom Number	Annotation
1	10.59, and 10.56	72943 and 79691	24; 28; 52; 57	$H_0$
2	8.33	93646	30	$H_3$
3	7.98	187060	1; 2	$H_1$
4	7.73	144460	31	$H_2$
5	7.71	187594	4; 6; 12; 14; 33; 35; 43; 41	$H_4$
6	7.04	184536	3; 7; 9; 11; 32; 36; 38; 40	$H_5$

**Table 4.1:** Chemical shifts assignment of PMDA-ODA protons

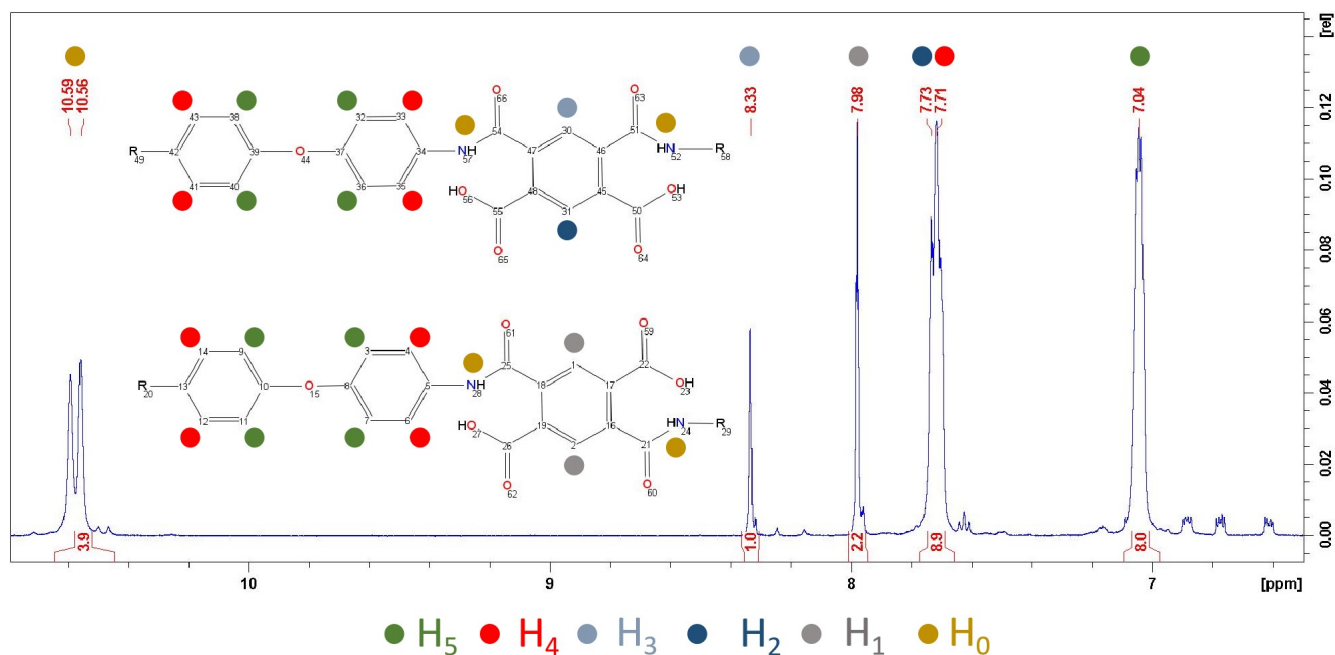


**Figure 4.6:** Proton NMR spectrum of the as received PMDA-ODA and chemical shifts assignment

The relative integrals of the peaks (normalised with respect to  $H_3$ ) agree with the corresponding number of hydrogen atoms as well, as seen in table 4.2. These attributions are in agreement with the bibliography [209]<sup>1</sup>.

Corresponding Proton	Integral [rel]	Number of peaks	$\nu(F1)$ [ppm]
$H_0$	3.9	2	10.56 and 10.59
$H_3$	1.0	1	8.33
$H_1$	2.2	1	7.98
$H_2$ and $H_4$	8.9	2	7.72
$H_5$	8.0	1	7.04

**Table 4.2:** Relative integrals of the peaks that appear in the PMDA-ODA spectrum

Since  $H_1$  and  $H_3$  are characteristic protons of isomers B and A respectively, and since they have isolated peaks we can deduce the composition of the polymer by comparing their relative intensities. The integrals of each peak ( $H_1$ ) and ( $H_3$ ) are indicated by  $S(H_1)$  and  $S(H_3)$ .  $S(H)$  is the contribution of one proton to the integral.  $n(\text{Isomer A})$  and  $n(\text{Isomer B})$  is the number of isomers A and B responsible for the chemical shift.

$$S(H_1) = 2S(H) \times n(\text{Isomer B}) \quad (4.3)$$

$$S(H_3) = S(H) \times n(\text{Isomer A}) \quad (4.4)$$

$$\frac{S(H_1)}{S(H_3)} = \frac{2 \times n(\text{Isomer B})}{n(\text{Isomer A})} \quad (4.5)$$

<sup>1</sup>Except for the attribution of  $H_2$  and  $H_3$ . As per our interpretation, since oxygen is more electronegative than nitrogen,  $H_2$  having 4 oxygen atoms in the vicinity should be more shielded than  $H_3$  having 2 oxygens and 2 nitrogens

$$\frac{n(\text{Isomer B})}{n(\text{Isomer A})} = 1.12 \quad (4.6)$$

As such, we find a composition of 52% of isomer B and 48% of isomer A, which is coherent with other studies [209]. In fact the integration of the peaks is done manually and 4% difference can be due to the delimitation of the integral limits. It is more appropriate to say that these two isomers exist approximately in equal amounts in the solution.

### 4.5.3 Chain length and molecular mass estimation

Here it is important to be reminded that the fabrication of the PMDA-ODA polymer is done by adding the anhydride and the oxidianiline into a strong polar solvent and mixing under specific conditions that will be later explained in details. Depending on the ratio of PMDA to ODA added into the solvent to make the corresponding PAA, we can end up with either of the following chain ends:

- If PMDA to ODA ratio is slightly higher than 1, the chain ends will be blocked by the excess PMDA and we will have what we called here a type 1 chain end represented in figure 4.7a.
- If PMDA to ODA ratio is slightly lower than 1, it is the excess ODA that will block the chain ends as illustrated in figure 4.7b.
- If the ratio is equal to 1, meaning the synthesis was done in stoichiometric conditions. We expect to find equal concentration of both and a constant change in the molar mass unless the PMDA-ODA was stored at  $-20^{\circ}C$ .

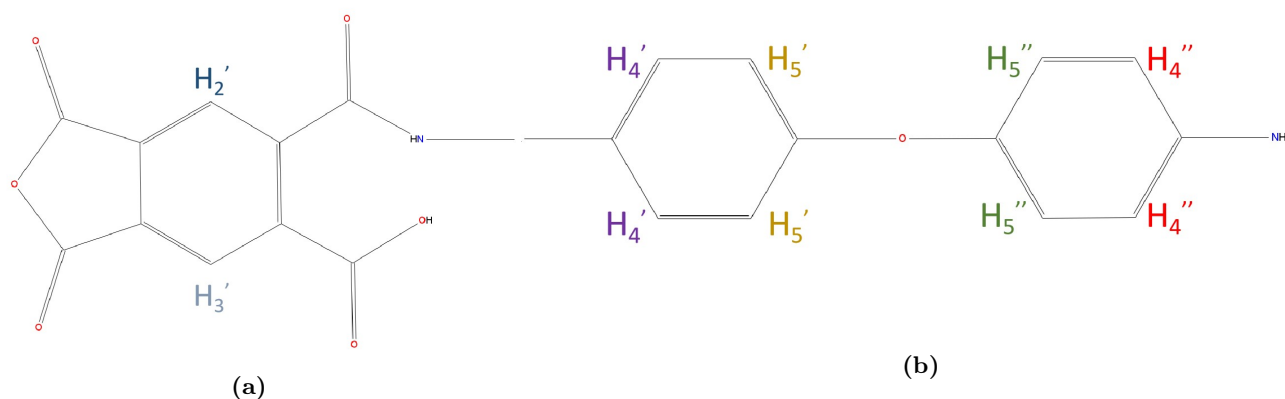


**Figure 4.7:** Possible chain ends in PMDA-ODA:(a)Type 1 chain end, resulting from excess PMDA. (b)Type 2 chain end, resulting from excess ODA.

In order to determine the average molecular weight of the resulting polymer, we need to determine the chemical shifts that corresponds to the protons of the molecular chain termination. To be able to assign chemical shifts to respective protons of chain ends, 2D  $H^1 - H^1$  correlation spectroscopy ( $COSY$ )<sup>2</sup> and,  $H^1 - C^{13}$  heteronuclear single quantum coherence ( $HSQC$ )<sup>3</sup> and

<sup>2</sup>It determines coupling between protons separated by one or more bonds, up to J3

<sup>3</sup>It determines proton-carbon single bond correlations

the heteronuclear multiple bond correlation (*HMBC*)<sup>4</sup> spectra were also acquired. They will be presented in the Appendix C, and we will only present the results in this chapter. These 2D correlations confirm the assignments as presented in Figure 4.8 and Table 4.3. The peaks centered around 6.78 and 6.61 ppm are those of protons  $H'_4$  and  $H'_5$  respectively and those at 7.62 and 6.88 ppm are those of  $H''_4$  and  $H''_5$  respectively. We can see that no chemical shifts can be assigned to protons 16 and 17 that are  $H'_3$  and  $H'_2$  respectively. This indicates that the polymer was elaborated with an excess amount of ODA.

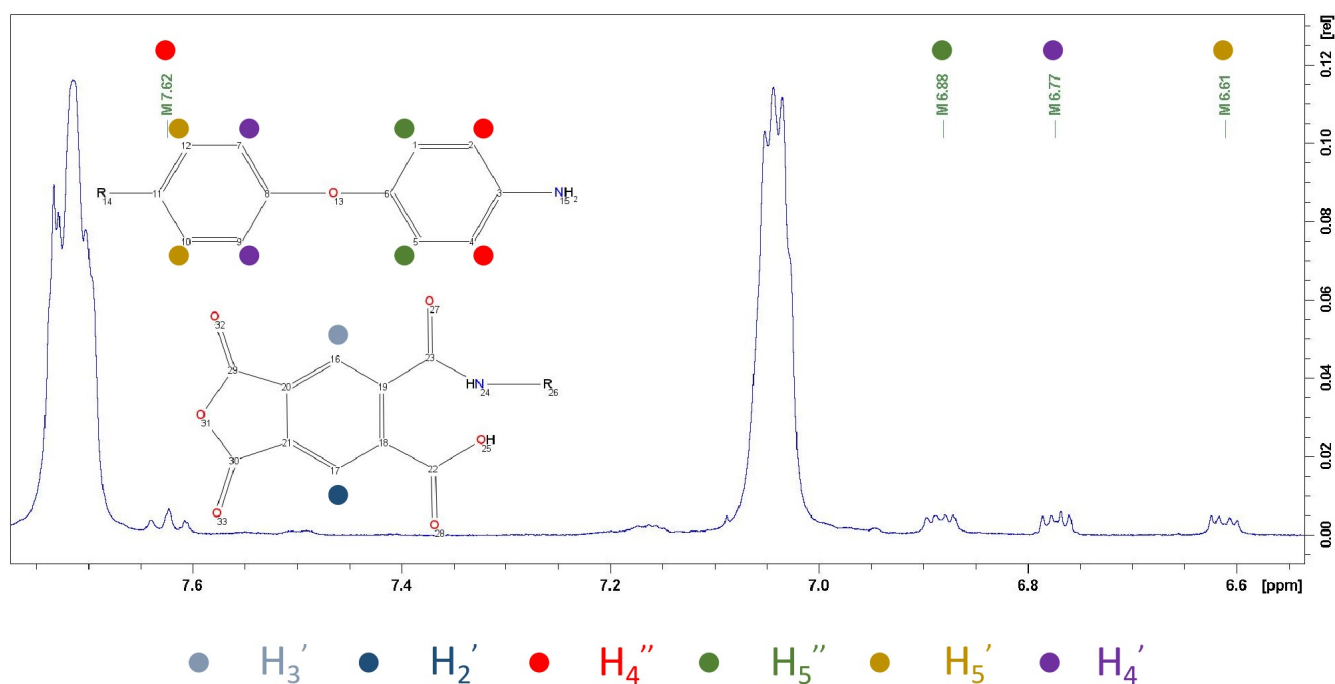


**Figure 4.8:** NMR spectrum showing the assignment of the end of chains of PMDA-ODA.

Corresponding proton	Integral [rel]	$\nu(F1)$ [ppm]	Assignment
$H''_4$	0.8397	7.6221	2; 4
$H_5$	34.6947	7.0353	see Table 4.1
$H''_5$	1.1413	6.8816	1; 5
$H'_4$	1.0873	6.7733	7; 9
$H'_5$	1.0000	6.6110	10; 12

**Table 4.3:** Assignment of end of chains protons according to carbon numbers in figure 4.8. The relative integral of the proton  $H_5$  is also mentioned because it is going to be used in the calculation of the molecular mass. The normalisation of the integrals is done with respect to  $H'_5$ .

As said earlier the intensity<sup>5</sup> of an NMR peak is proportional to the number of protons that give rise to the chemical shift. Thus the average molecular mass can be estimated by determining the ratio of the intensities of central protons to those of terminal protons. Accordingly we choose the peaks that corresponds to  $H_5$  and  $H'_5$ , the protons marked with green and gold dots in Figure

<sup>4</sup>It correlates carbons and protons that are separated by two, three bonds. Direct one-bond correlations are suppressed.

<sup>5</sup>When used in reference to NMR signals, intensity indicates the area under the peak

4.9. We can as well use any other integral, those ones were the most convenient because they have a horizontal and well defined baseline.

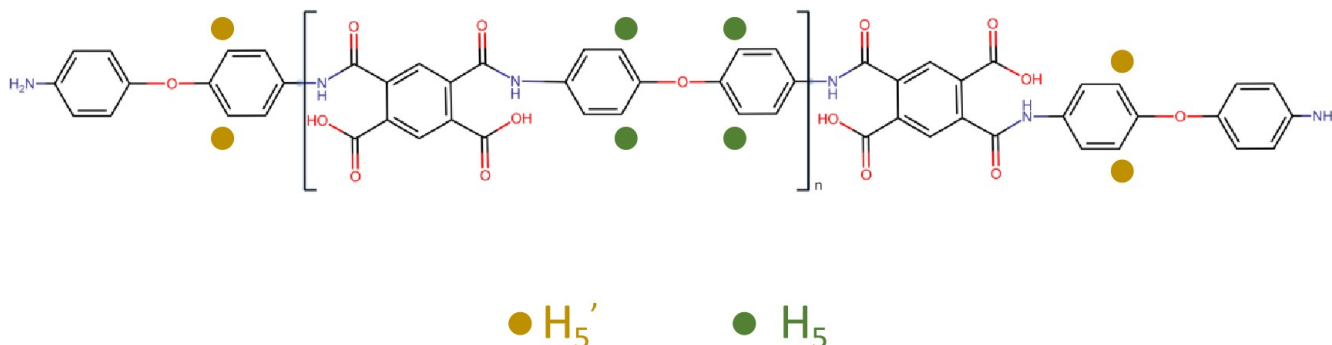


**Figure 4.9:** The structure of a PMDA-ODA polymer having  $n$  repetitive units and terminated with oxidianiline. The repetitive unit is illustrated as a para-PMDA-ODA, but in fact it should indeed be a combination of both configuration. This will not affect the molecular mass estimation.

Given that  $n$  is the average number of repetitive units of PMDA-ODA polymer chain,  $S(H_5)$ , and  $S(H_5')$  are the surface under the peaks of  $H_5$ , and  $H_5'$  :

$$S(H_5) = 4n * S(H) \quad (4.7)$$

$$S(H_5') = 4 * S(H) \quad (4.8)$$

$$n = \frac{S(H_5)}{S(H_5')} \quad (4.9)$$

This sample has an average number of repetitive PAA units of 36, hence a molecular weight of 15048  $g/mol$ . This is an estimate of the average molecular weight and it gives no idea about the distribution around this average, nevertheless, it allows us to assess a product as received and to follow its evolution over time.

#### 4.5.4 Evolution of PMDA-ODA at room temperature

We followed the evolution of the same PAA after 15 days of product's reception to see if the molecular mass will increase, or if the chains will degrade into anhydride and diamine at room temperature. If the molar mass of PAA is found to increase over time we can for example let it age before use in order to achieve molar mass values similar to those used in commercial positive resists.

For this purpose we analysed a sample of a newly received PMDA-ODA and kept another one in a hermetically sealed container and away from sunlight for 15 days, after which we acquired an  $H^1$  NMR spectrum of the aforementioned sample. These spectra presented in Figures 4.10a and 4.10b respectively, show an average number of repetitive units of  $27 \pm 1$  and  $28 \pm 1$ , as it can be estimated from Equation 4.9. However, the difference between the relative integrals is not very significant to consider that this slight change indicates a clear evolution of the molecular mass. Thus the molecular weight is around 11500  $g/mol$  for this newly received precursor.

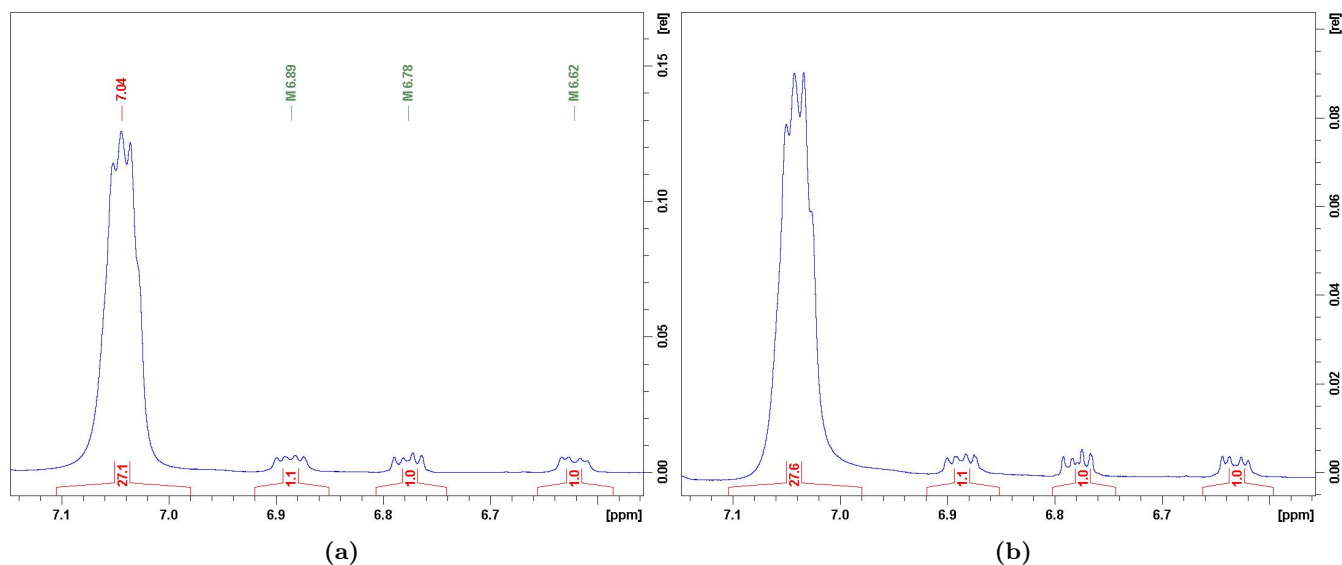


**Figure 4.10:** Evolution of PMDA-ODA sample:(a)received sample, (b)same sample after 15 days

Over the 15 days period there was no significant change in the molecular weight. This backs up the assumption we made in section 4.5.3: the purchased products consists of a non stoichiometric mixture of PMDA and ODA, ODA is in slight excess, resulting in what we earlier called a type 2 chain termination.

## 4.6 Increasing the solid content of the photoresist

In order to meet the requirements for a thick resist, the PAA content in the precursor solution should be increased. In addition there is also the need to replace NMP with DMSO. In fact NMP was identified as a substance of very high concern (*SVHC*) due to its reproductive toxicity [210], while DMSO has no toxicity<sup>6</sup>. This can be accomplished in two different ways:

- PMDA-ODA extraction from commercial sample dissolved in NMP and a re-dissolution in the solvent of choice and with a higher solid content (the physical route).
- A direct synthesis of PMDA-ODA in the solvent of choice, and with the desired solid content (the chemical route).

### 4.6.1 The physical route

As per multiple studies, Polyamic acids <sup>7</sup>can be extracted by precipitation in methanol [209], water [193,215,216] or a mixture of both [213,214] then filtered, washed thoroughly and vacuum dried at room temperature [209] or in mild temperature conditions notably less than 80°C [215] to avoid imidisation<sup>8</sup>. Vacuum drying can be done for couple of hours to couple of days as per the references cited above. This process is usually done to purify the polymer from remaining reactant, byproducts and other impurities.

<sup>6</sup>It is used in cell freezing for example [211].

<sup>7</sup>as well as polyimides and PAE [212–214]

<sup>8</sup>However in the case of polyimides the drying temperature can vary widely

After multiple attempts and procedures we found that the adequate one was to dilute the commercial solution of 15% wt of PAA, to 7.5%wt, then to pour it drop-wise into excess water. A white yellowish fibrous solid precipitated. The mixture is filtered and dried under vacuum at room temperature for 12 hours or until translucent yellow.

In order to compare the resulting mixture to the commercial solution and to validate the procedure an  $H^1$  NMR was done. 5mg of the solid was diluted into 6mL of DMSO-d6 for the analysis. A qualitative comparison of the two spectra shows that the structure of the polymer is preserved as seen in figure 4.11

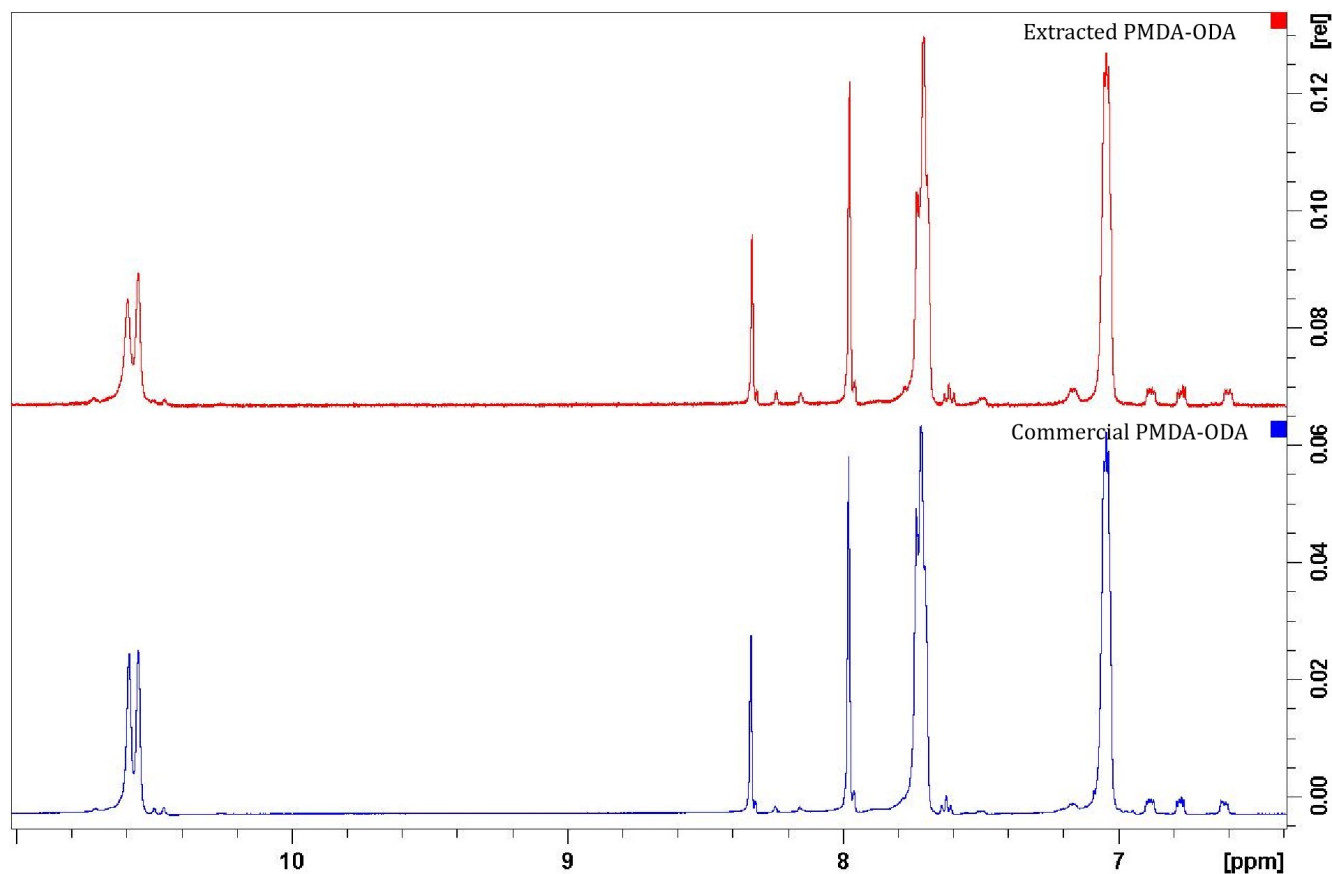


**Figure 4.11:** NMR spectra of a commercial PMDA-ODA sample and the extracted polymer from the same sample

On the other hand, there may be a risk of chain scission because the reaction of formation of polyamic acid from an anhydride and an oxydianiline is reversible and is favored by the presence of traces of water. For this reason, a comparison of the average molar masses can be informative. As seen the Table 4.4 and Figure 4.12 no significant change in the polymer molecular weight is found.

Sample	Average Molecular Weight (g/mol)
JE070120PAA-NMP (Commercial)	15048 ( $n = 36 \pm 1$ )
JE070120PAA1(Extracted)	14630 ( $n = 35 \pm 1$ )

**Table 4.4:** Average estimation of the polymers molecular weight

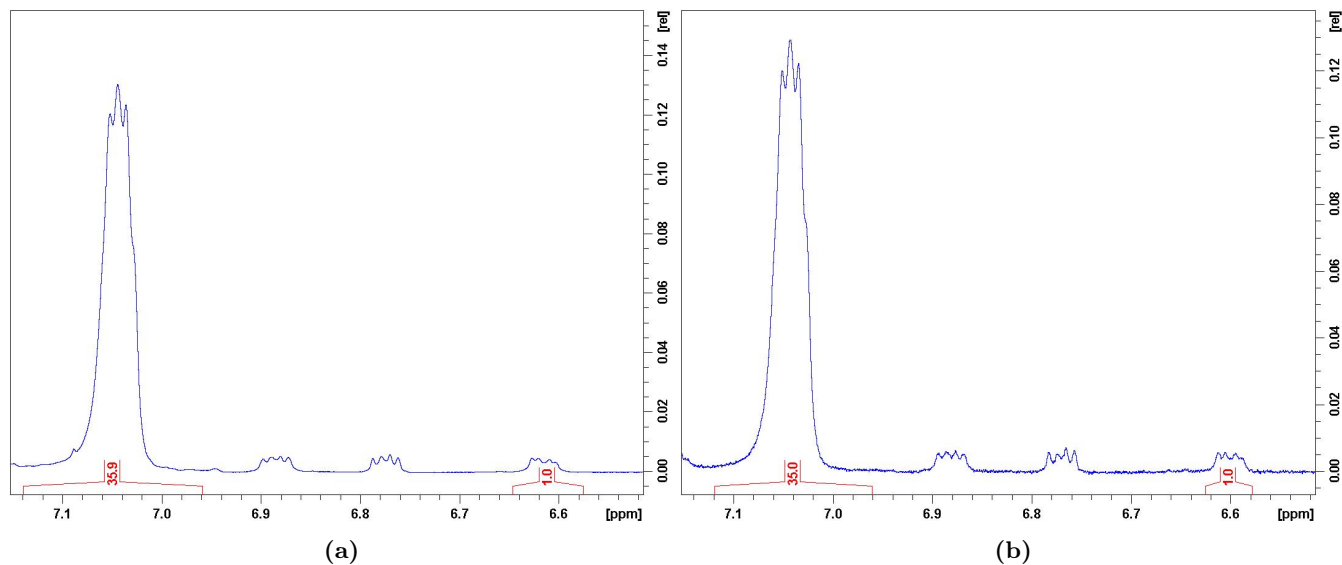


**Figure 4.12:** Evolution of PMDA-ODA chain length:(a)commercial sample, (b)extracted sample

## 4.6.2 The chemical route

Here we explain the procedure for PMDA-ODA synthesis in DMSO. As seen in the bibliography [187] the parameters for PAA synthesis can differ slightly as per different references. Temperature is generally kept low, mostly room temperature [217, 218], sometimes at  $0^{\circ}C$  [219], because the poly(amic acid) formation is exothermic and the equilibrium is favored at lower temperatures.

As per several references [220,221], increasing the monomer concentration favors high molecular weight products. It was also found that the order and the mode of the monomer addition strongly influences the final molecular weight, with the highest ones obtained when solid dianhydrides were added to a solution of diamines. The use of solid dianhydride can play a role in increasing the molecular weight of the resulting polymer [222]. Common dipolar aprotic solvents utilized are Dimethylformamide (DMF), Dimethylacetamide (DMAc), and N-Methyl-2-pyrrolidone (NMP) or a mixture of them. All these solvents share a common feature, as they are all Lewis' bases. To our knowledge less bibliography exists about the synthesis in DMSO, yet it seems a good alternative to NMP since they have the same physical and chemical properties, as DMSO is a polar aprotic solvent as well.

PMDA and ODA were purchased from abcr chemicals. All products are utilized as received without further purification. A solution of 23 % wt. of PMDA-ODA in DMSO solution is targeted. We proceeded into the synthesis of PMDA-ODA in DMSO as per the following method:

- We dissolve ODA in DMSO at room temperature with the beaker placed in an oil reactor
- We keep it under agitation for half an hour or until total dissolution of ODA
- once dissolved we slowly add a stoichiometric amount of PMDA into the beaker to avoid thermal heating
- we maintain the PMDA-ODA mixture under agitation for 4h.

We investigate the structure of the resulting polymer by the means of proton NMR and we compare it with the commercial sample. NMR acquisitions were done on the reactants as received

and on the PMDA-ODA mixture within half an hours of agitation and after 4hours.

#### 4.6.2.1 Characterization of the reactants: PMDA and ODA

We can see in figure 4.13 that the chemical shifts at 6.532 ppm are those of protons attached to carbons 2,4,7 and 11. The one at 6.627 ppm being more deshielded are those of protons attached to carbons 1,5,8, and 10. Normally the protons attached to atoms 14 and 15 are labile and hardly seen on the spectrum. The peak at 4.8 ppm is that of water. The peak at 3.4 ppm is probably methanol residues left from the fabrication of ODA.

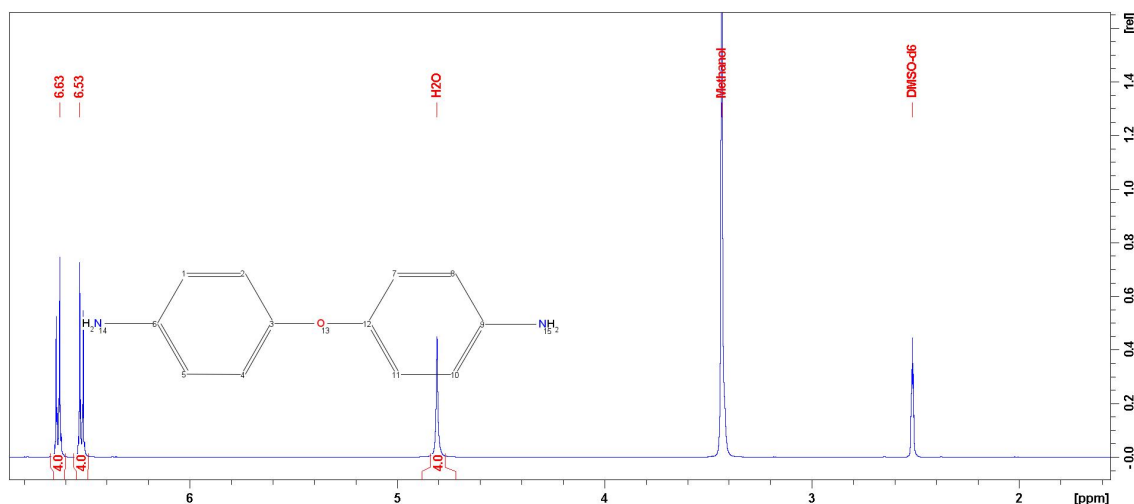


Figure 4.13: NMR proton spectrum of ODA purchased from abcr chemicals

As per the spectrum of PMDA, in figure 4.14, the product seems to be pure with only one peak that corresponds to the proton attached to carbons 1 and 2. We can however see a broad peak around 3.68ppm, indicating a contamination with deuterated water (HOD).

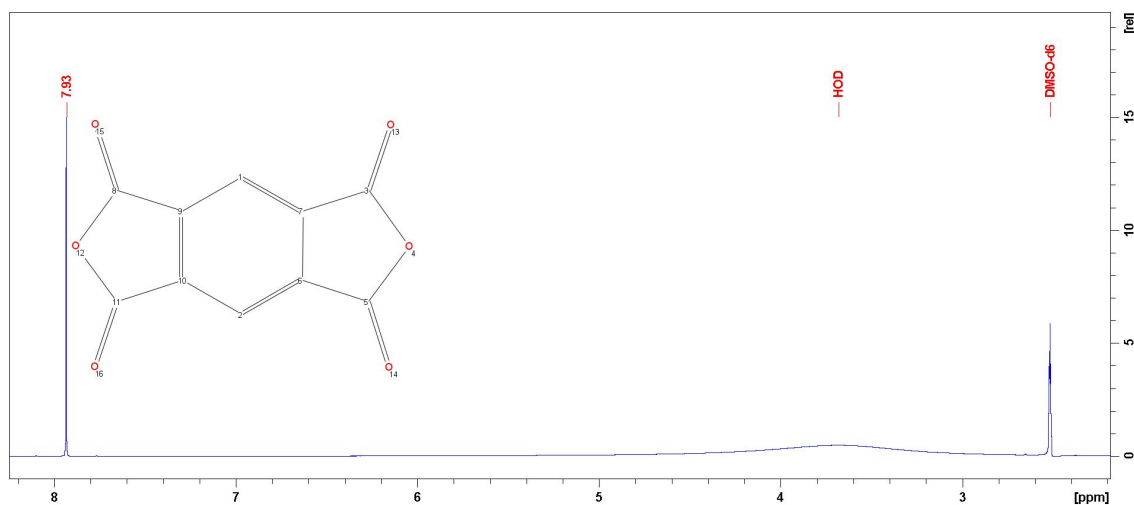
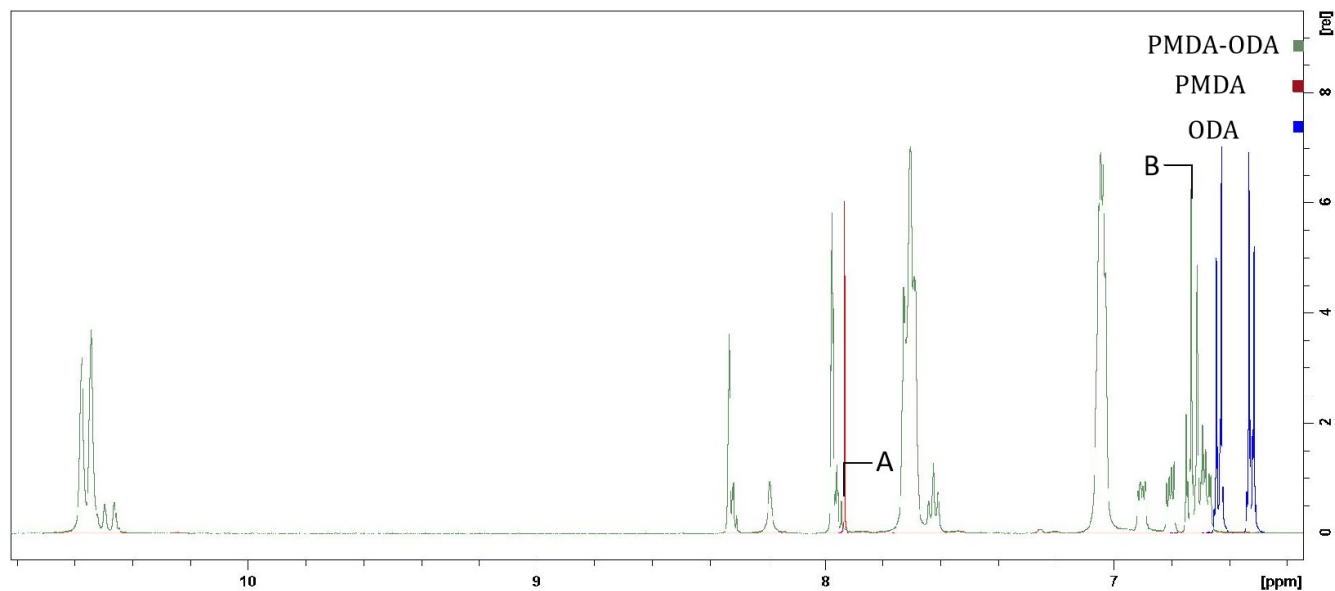


Figure 4.14: NMR proton spectrum of PMDA purchased from abcr chemicals

#### 4.6.2.2 Study of the PMDA-ODA reaction to form the polyamic acid

A sample taken right at the time where the mixture became homogeneous ( $t=0h$ ) was compared to PMDA and ODA spectra to see if there are any residual signals from either of their protons. We can note from figure 4.15 that the singlet (A) at  $7.94\text{ ppm}$  is that of residual PMDA. The peaks (B) that appear between  $6.70$  and  $6.74\text{ ppm}$  are those of residual ODA. A zoom into the region of interest is presented in Figure 4.16. These residual reactants can be eliminated by washing the polymer in water in the same way it is done for the extraction.



**Figure 4.15:** NMR proton spectrum of PMDA-ODA mixture compared to purchased reactants from abcr chemicals: in green the spectrum of the resulting PMDA-ODA sampled at  $t = 0h$  in red that of PMDA and in blue that of ODA.

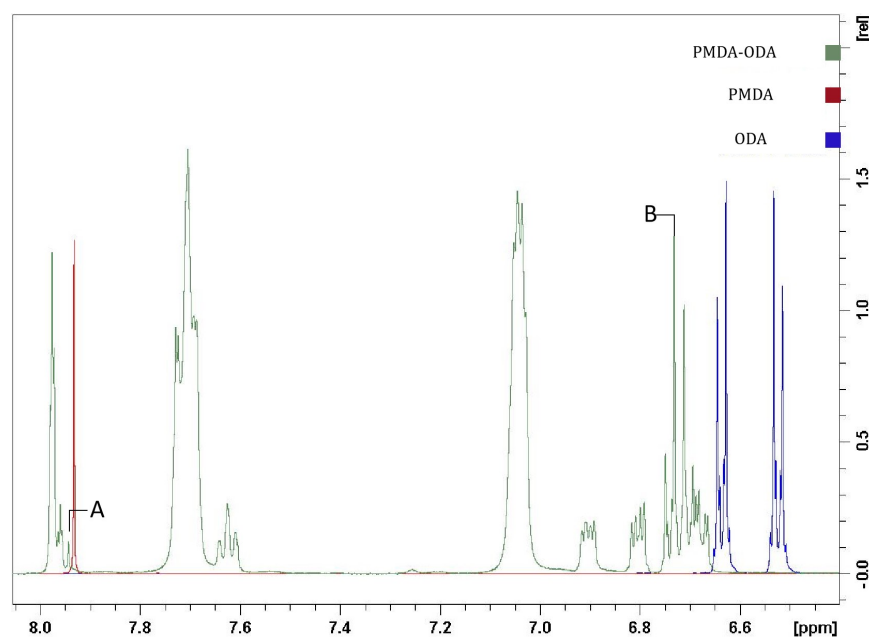


**Figure 4.16:** A zoom into the region of interest of Figure 4.15.

In order to kinetically study this reaction, 3 NMR spectra of the same sample presented in Figure 4.15 were taken at intervals of 2h between successive acquisitions as well as a sample taken after 4 hours of agitation in the mother solution (23%wt. of PMDA-ODA in DMSO). They show no difference when compared to the spectrum acquired at  $t = 0h$  as presented in Figure 4.15, neither in their chemical shifts nor in their relative intensities. This means that the reaction is quasi-instantaneous.

If we examine meticulously the spectrum of the resulting polymer as presented in Figure 4.17, we can identify a polymer that resembles the commercial one but with the particularity of having a singlet at 8.19 ppm probably due to the presence of PMDA terminations because the reactants are in stoichiometric amount.

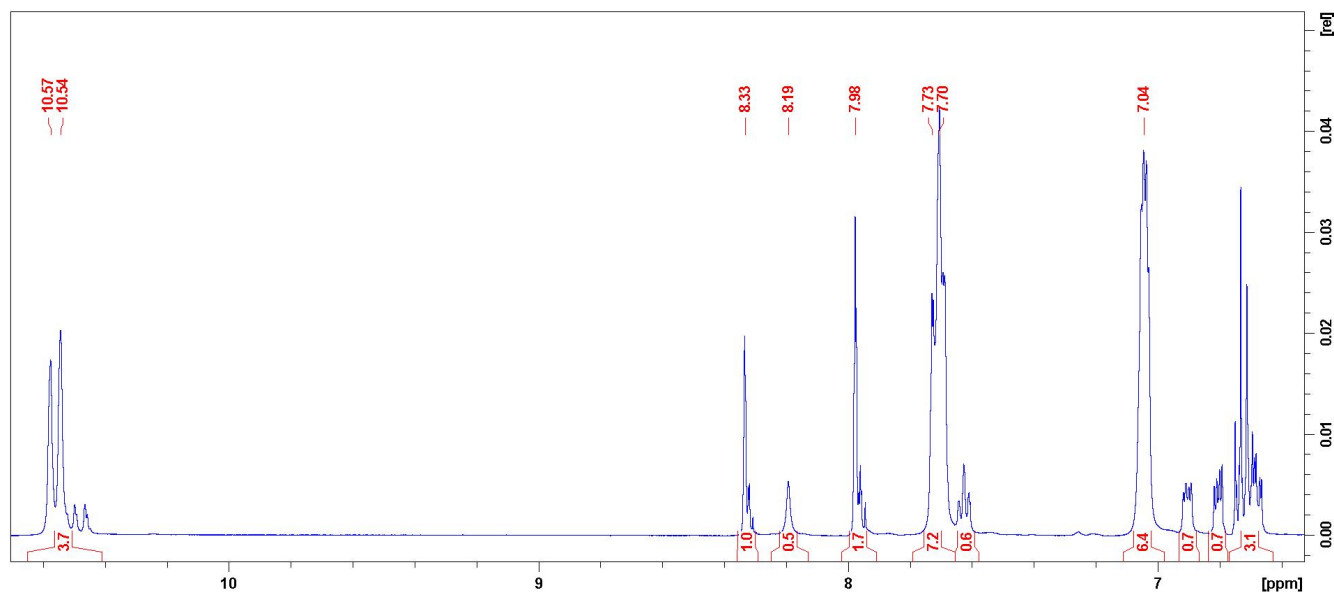


**Figure 4.17:** The  $H^1$  NMR spectrum of the resulting PMDA-ODA sampled at  $t = 0h$ .

Accordingly, only half of the terminations are of type 2. As such the average number of repetitive units  $n$  of PMDA-ODA polymer chain can be calculated as follows:

$$S(H_5) = 4n * S(H) \quad (4.10)$$

$$S(H_4') = 2 * S(H) \quad (4.11)$$

$$n = \frac{S(H_5)}{2S(H_4')} = 5 \quad (4.12)$$

This gives us a polymer having a molecular weight of 2090 g/mol, a very low one when compared to commercial samples. We can see that even though the reaction is instantaneous the equilibrium is not favored towards the right and the resulting polymer cannot be used in its present form, for the fabrication of the resist. The same process should be done in NMP to be able to judge if this is the effect of the DMSO or if the reaction parameters should be changed.

## 4.7 Reactivity of PMDA-ODA with the VE

In order to follow the copolymerisation reaction between the VEs and the carboxylic acids of the PMDA-ODA, we simplified the reactive mixture and kept the TVEB as the only precursor providing the VE. As such it is essential to assign the chemical shifts of the TVEB. As these protons, notably those of the VE, will serve as a indicator for the reactivity, because the protons of the carboxylic acid are labile and represented in the PMDA-ODA spectrum by a broad peak around 13 ppm.

### 4.7.1 TVEB $H^1$ NMR spectrum

The NMR spectrum of the TVEB<sup>9</sup> is presented in the Figure 4.18. The protons assignment and relative intensities are detailed in the Table 4.5. We can note that the relative integrals agree well with the number of protons giving rise to the NMR signals.

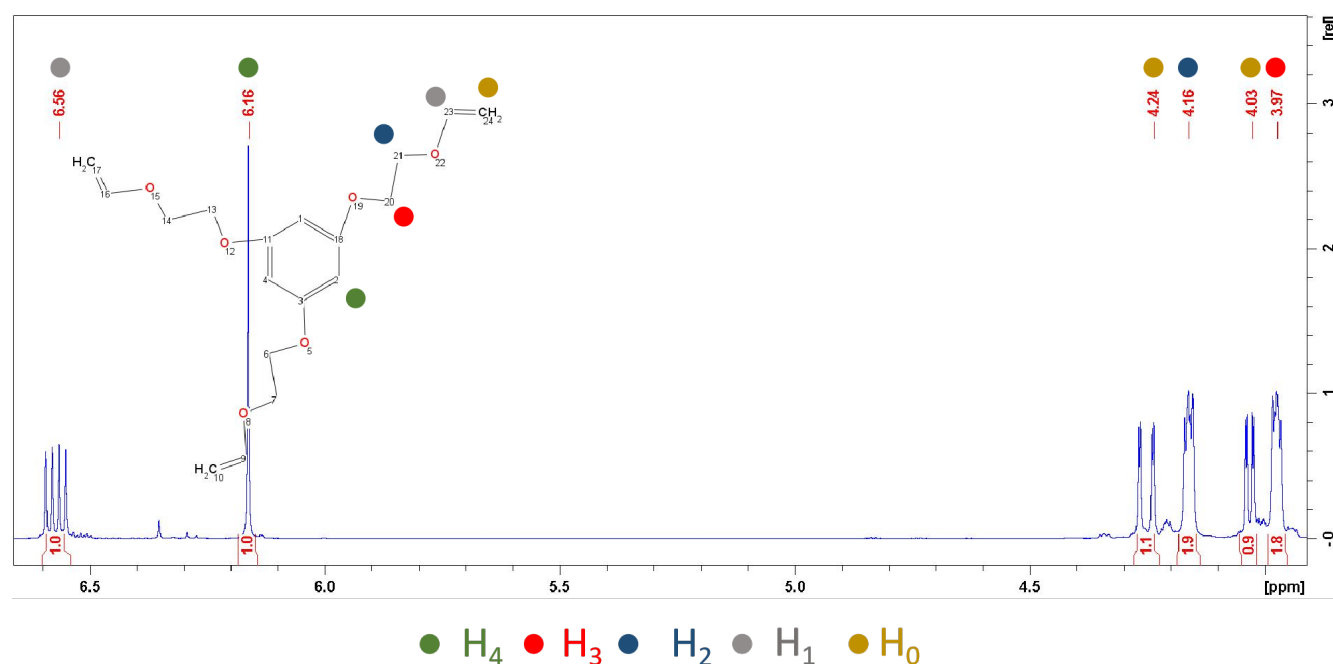


**Figure 4.18:**  $H^1$  NMR spectrum of TVEB. The atoms N, O, and C are indicated by a number. The protons are coloured coded and indexed from 0 to 4.

**Table 4.5:** Chemical shifts assignment and relative intensities (integrals) of TVEB protons

Corresponding proton	$\nu(F1)$ [ppm]	Integral [rel]
$H_1$	6.56	0.97
$H_4$	6.16	1.00
$H_0$	4.24	1.10
$H_2$	4.16	1.93
$H_0$	4.03	0.92
$H_3$	3.97	1.84

<sup>9</sup> kindly provided by colleagues from the Institute Charles Gerhardt Montpellier (ICGM)

$H_0$  and  $H_1$  are the protons that can inform us about the reactivity of the VE. They are all three represented in the NMR spectrum by a doublet of doublets. Those of  $H_0$  are centered around 4.03 and 4.24 *ppm*. That of  $H_1$  is centered around 6.56 *ppm*. The aromatic proton  $H_4$  whose peak is centered around 6.16 *ppm* will be used for normalisation as it is hardly affected. Upon reaction of the VE with carboxylic acid, we expect that the signal from these protons will diminish, along with the emergence of a doublet and quadruplet as schematically illustrated in Figure 4.19. Accordingly, by following the relative intensities from these protons we can follow the reaction kinetics.

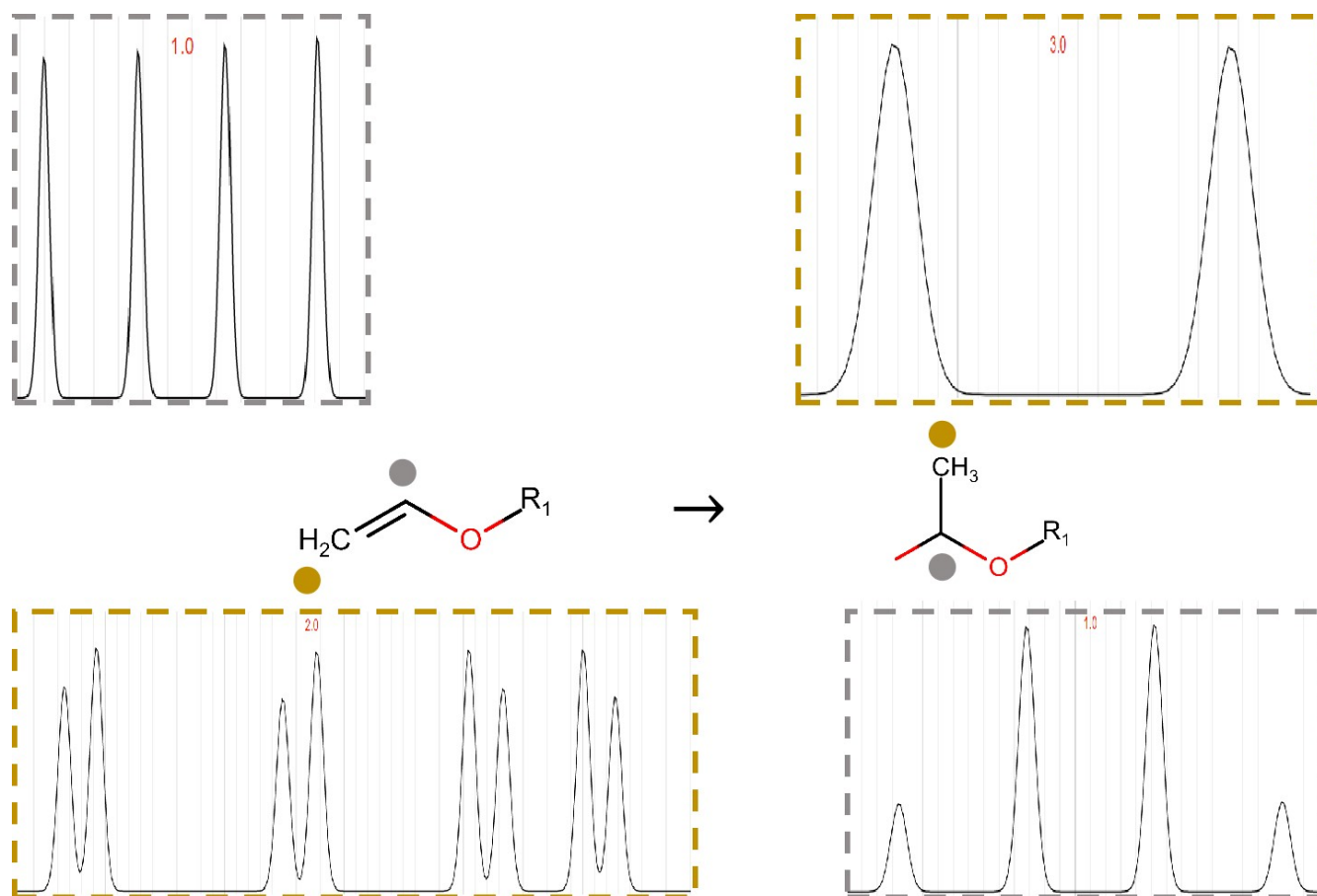


**Figure 4.19:** A schema illustrating the changes in the proton NMR spectrum of the PMDA-ODA and TVEB composition upon polymerisation of the VE and the COOH groups.

### 4.7.2 Co-polymerisation kinetics

Following the polymerisation kinetics, at varying temperatures, or using different solvents can inform us about the adequate processing conditions. As such we elaborated a mixture of PMDA-ODA and TVEB in NMP, with a molar ratio of 3 PAA units to 2 TVEB molecules (stoichiometric ratio). It was stirred for 2 hours at three different temperatures 25° C, 130° C and 165° C. The 25° C sample will serve as a control sample at ambient temperature. The 130° C sample will serve in order to check if at a slightly higher temperature than 110° C we will see a reactivity<sup>10</sup>. And finally the 165° C sample will serve in order to check if the reactivity is limited by the solvent complexation with the COOH groups.

<sup>10</sup>The suitable soft bake region for a VE and a COOH is between 110 – 130° C [178, 223]

By comparing the reaction mixtures treated at  $25^{\circ}\text{C}$ , and  $130^{\circ}\text{C}$ , we notice the disappearance of the peaks corresponding to the vinyl protons of TVEB (at  $6.56\text{ ppm}$ ) in the mixture at higher temperatures, but also the slight deshielding of the aromatic proton (at  $6.16\text{ ppm}$ ) as seen in Figure 4.20.

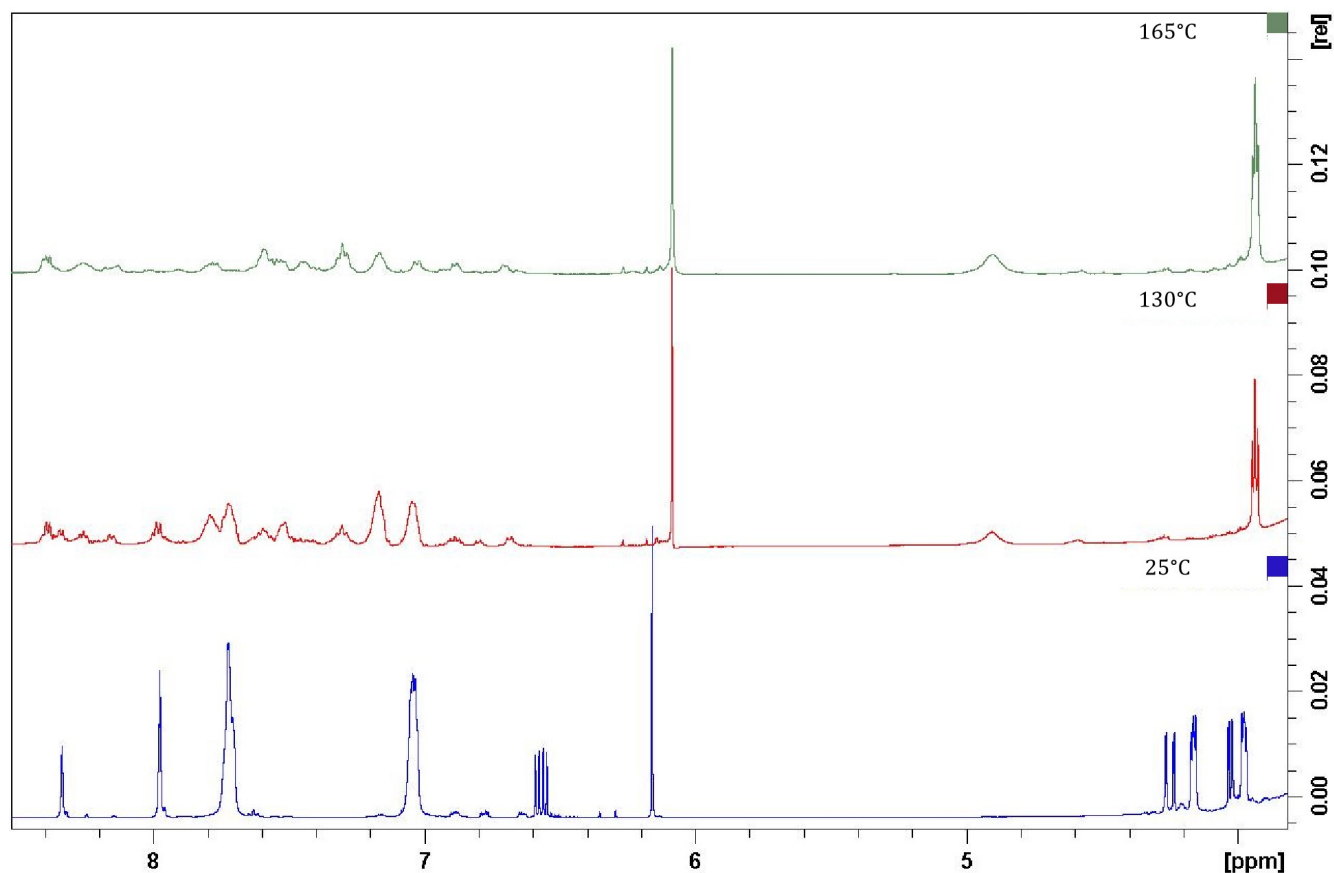


**Figure 4.20:** Proton NMR spectrum of the TVEB and PMDA-ODA mixture at  $25^{\circ}\text{C}$  (in blue) ,  $130^{\circ}\text{C}$  (in red) and  $165^{\circ}\text{C}$  (in green). Total disappearance of the vinyl proton peak at  $6.56\text{ ppm}$  and the shift of the aromatic proton peak at  $6.16\text{ ppm}$

On the other hand we can note the disappearance of  $H_2$  and  $H_3$  and the replacement of their peaks by a triplet at  $3.93\text{ ppm}$ . In addition the spectrum of the PMDA-ODA is disturbed. The compound is more anisotropic as the temperature increases. This non homogeneity is probably a result of the anisotropy of the solid phase proton field in the sample. This might be an indicator that, the imidisation of the PAA into PI might start at low temperature or it could indicate a chain scission as well because we can note a decrease in the molecular weight of the PMDA-ODA (to around  $2926\text{ g/mol}$  with 7 repetitive units). Since no important changes can be seen between the samples at  $130^{\circ}\text{C}$  and  $165^{\circ}\text{C}$ , we will only consider the sample at  $130^{\circ}\text{C}$ . The regions of interest of two spectra at  $25^{\circ}\text{C}$  and  $130^{\circ}\text{C}$  are presented below in Figure 4.21.

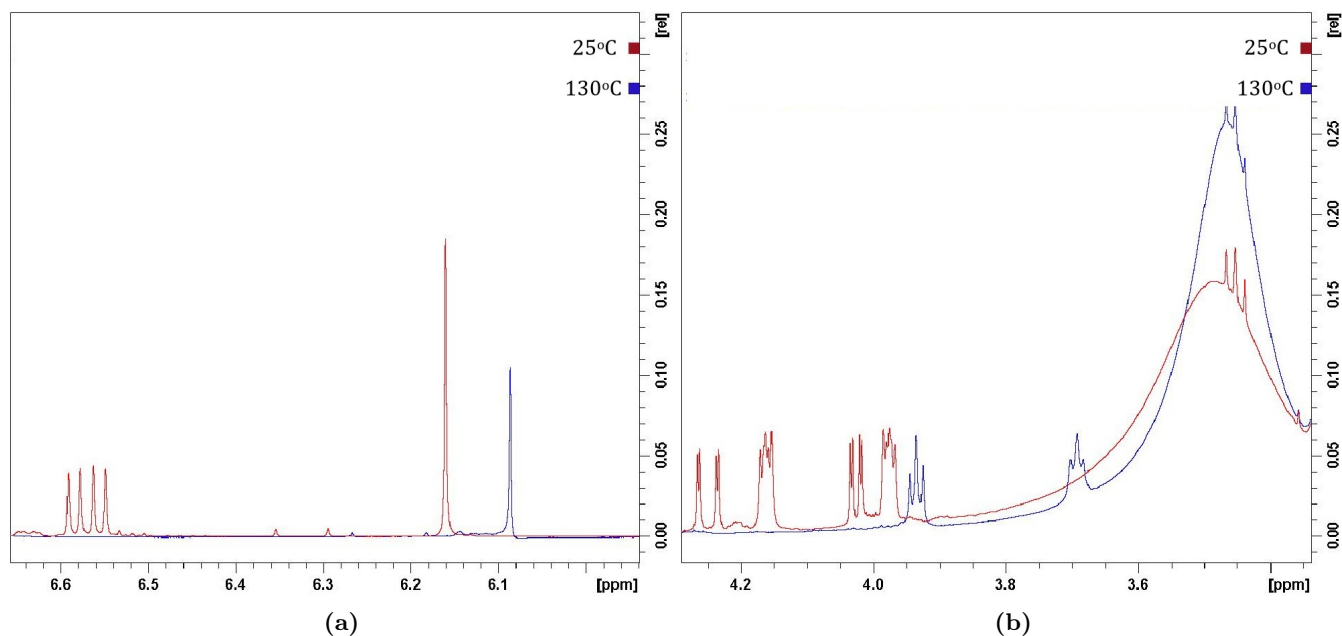


**Figure 4.21:** A comparison of the  $^1\text{H}$  NMR spectra of PMDA-ODA and TVEB thermally treated at  $25^\circ\text{C}$  (in red) and  $130^\circ\text{C}$  (in blue).

The TVEB has clearly transformed due to the presence of water generated by the imidisation reaction. The presence of the singlet at  $6.09\text{ ppm}$ , and the two triplets at  $3.94\text{ ppm}$  and  $3.69\text{ ppm}$  along with the disappearance of the two VE protons might suggest an acid catalyzed hydrolysis of vinyl ether, resulting in a 2,2',2''-[Benzene-1,3,5-triyltris(methyleneoxy)]triethanol, as illustrated in the NMR spectrum in Figure 4.22. The relative peak intensities agree perfectly with the number of hydrogen atoms in the molecule.

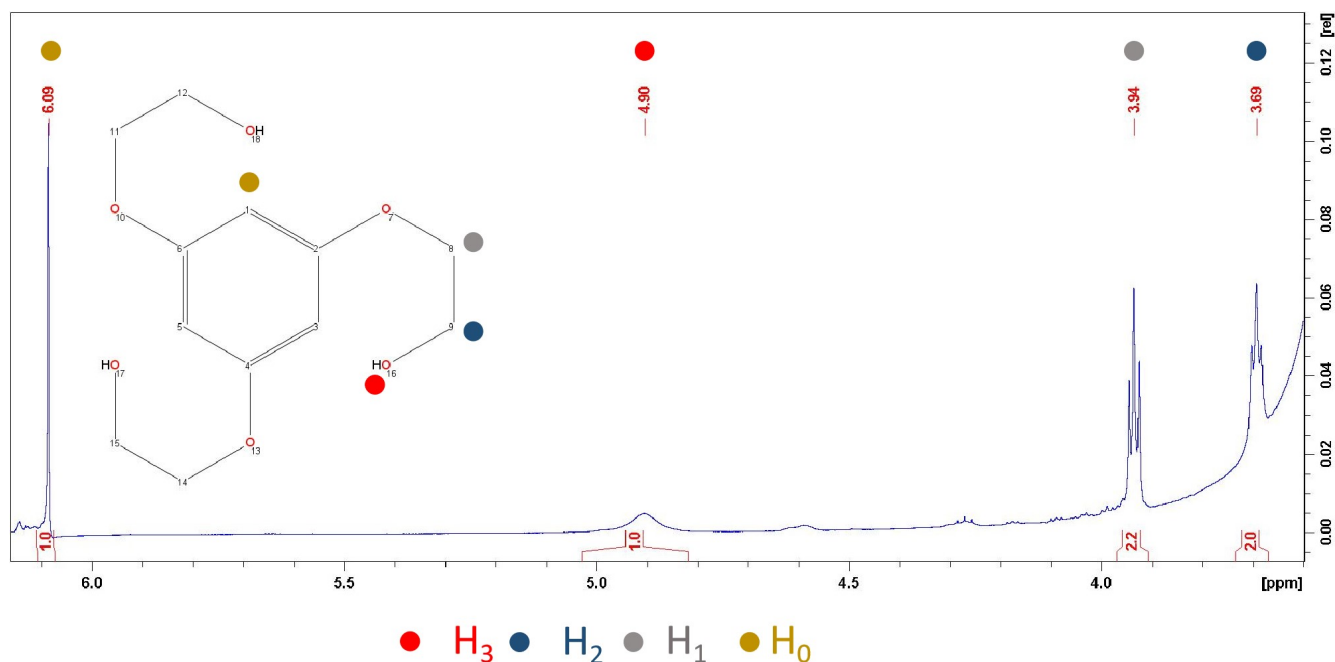


**Figure 4.22:** The NMR proton spectrum of the resulting molecule due to the hydrolysis of the TVEB.

### 4.7.3 The reactive model: Benzoic acid and TVEB

Based on these last results, the need for a reactive model that can replace the PAA-TVEB, arises. Benzoic acid is a good candidate to substitute the PAA, as it has a benzene to which a COOH is attached, thus representing the functional part of the PAA as seen in Figure 4.23. This will provide the information we need about the reactivity of the PAA with the VE without the risk of degrading the reactants.

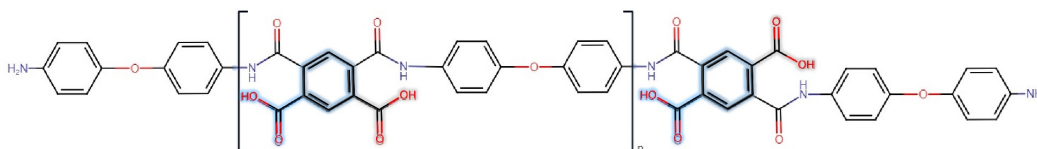


**Figure 4.23:** A schematic illustration showing four benzoic acid modules as functional group in the PMDA-ODA. Benzoic acid modules are highlighted in grey and blue.

Thus we use Benzoic acid with VE in DMSO to represent the more complex reaction of VE with PMDA-ODA. As explained in Section 4.7.1, the disappearance of the vinylic proton of the TVEB could be used as an indicator of this reaction. A stoichiometric amount of benzoic acid to TVEB (3:1) is added into a beaker containing DMSO. The sample was subject to a proton NMR analysis at  $25^{\circ}C$  then to another two acquisitions at  $110^{\circ}C$  and  $130^{\circ}C$  after 20 minutes of agitation at each temperature. These spectra are both presented in Figure 4.24.

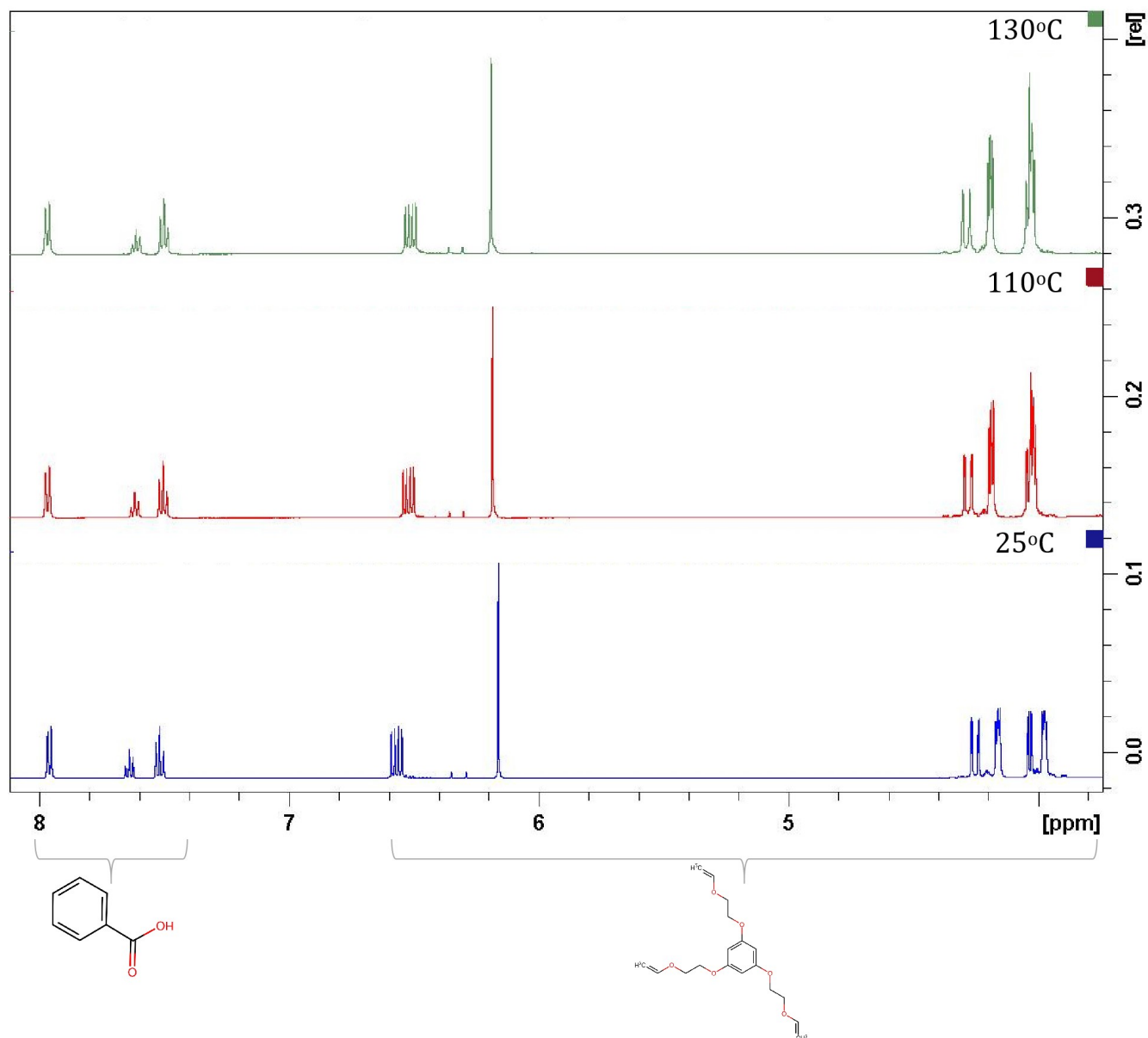


**Figure 4.24:** The  $H^1$  NMR spectra of the TVEB and benzoic acid reactive mixture at 25° C (blue) and 110° C (red), and 130° C (green).

They show no change in the overall spectrum of either of the two components, except for a slight shift of the proton at 3.97 ppm which we could not explain. In order to judge the reactivity of these components the ratio of the vinylic to the aromatic protons intensities of the TVEB should be quantified. These values are presented in Table 4.6.

**Table 4.6:** The ratio of the vinylic to aromatic proton intensities for the reactive model, benzoic acid and TVEB

Sample	Proton	Integral [rel]	$\nu(F1)$ [ppm]	vinylic/Aromatic Ratio
TVEB	vinylic H	0.97	6.57	0.97
	Aromatic H	1.0	6.16	
TVEB + Benzoic Acid	vinylic H	0.94	6.56	0.94
	Aromatic H	1.0	6.16	
TVEB + Benzoic Acid (110° C)	vinylic H	0.99	6.52	1.0
	Aromatic H	1.0	6.19	
TVEB + Benzoic Acid (130° C)	vinylic H	1.0	6.52	1.0
	Aromatic H	1.0	6.18	

The spectrum is normalised with respect to the aromatic protons as they are not affected. We can see that the TVEB + BA mixture shows no decrease in the quantity of VE protons neither at 110° C, nor at 130° C thus indicating a non reactivity of the two components and backing up the hypothesis that the acidity of the *COOH* is not sufficient to trigger the opening of the double bond. Accordingly we can conclude that the reactivity of the vinyl ether with a carboxylic acid could not be triggered by temperature solely. Thus the catalysis by a strong acid is essential to this process.

#### 4.7.4 Copolymerisation of TVEB and PMDA-ODA: Dissolution in TMAH

As seen in Section 4.7.3, no reactivity between the carboxylic acid and the VE can be seen in the reactive model even at 130° C. If this is the case what explains the functioning of this positive resist? The hypothesis is that the PAG103 acts as a TAG and dissociates at temperatures higher than 110° C, thus leading to the catalysis of the VE and COOH reaction. If we consider that the insolubility of the resist is an indicator of the occurrence of copolymerisation reaction, we can use this simple method to validate our hypothesis. Therefore, we need to confirm that the copolymerisation of TVEB and COOH does not take place, unless it is catalysed by a strong acid, which is generated by the PAG103 upon soft baking. For this purpose, we prepare a solution according to the molar ratios in Mechref's work [186], by adding 3 molar units of TVEB to 10 molar units of PAA and leaving under agitation for 30 *minutes*. To another preparation having the same composition we add 3 molar units of PTMA. We cast using the same spin parameters (5000 RPM 30 seconds) the two different preparations, as well as the PAA solution. The samples are baked 10 minutes at different baking temperatures (80° C, 110° C and 130° C). Afterwards we perform a dissolution test in 2.38% TMAH solution for 1 minute. The results are presented in Table 4.7.

**Table 4.7:** Dissolution in TMAH in of different copolymer reactants at 3 different temperatures. (+) is soluble (-) is insoluble.

Temperature ( $^{\circ}C$ )	Reactants		
	PAA	PAA+TVEB	PAA+TVEB+PAG
<b>80</b>	+	+	+
<b>110</b>	+	+	-
<b>130</b>	+	+	-

The fact that the only insoluble films are those containing the PAG 103, and baked for 10 minutes at temperatures higher than  $110^{\circ}C$ , suggests that the PAG decomposes at  $110^{\circ}C$ , thus generating a strong acid that is a sulfonic acid and triggering the copolymerisation reaction. This indicates a misunderstanding of the reaction mechanism by which the photoresist acquire it positive working aspect. This hypothesis should be further studied by an NMR study of Benzoic acid and TVEB with the addition of a catalytic amount of a sulfonic acid. Toluene sulfonic acid is a good candidate for this study, as it is the only solid acid that can be purchased and is adapted to our synthesis process because no aqueous acid can be added to the TVEB.

#### 4.7.5 Discussion and perspective

As we have shown by NMR study, the positive resist based on PMDA-ODA and VE, can only acquire its positive working aspect by the dissociation of the added photoacid generator. This claim is also backed up by the fact that, the FTIR studies that were done on this resist, and that showed a  $43 \pm 2\%$  conversion rate of amide C=O groups [167], contained the PAG (PTMA) in their composition. As a summary, the acidity of the COOH groups of the PMDA-ODA are not sufficient in order to provoke the thermal crosslinking. The dissociation of the photoacid generator procures the catalytic amount of acids in order to crosslink the COOH of PMDA-ODA and the VE of TVEB and form a hemiacetal. As soon as the reaction starts we have a reactive medium with carboxylic acids, VEs, hemiacetals and the photogenerated acid. Three reactions are able to take place:

- the acidolitic crosslinking of VEs and carboxylic acids,
- the acidolitic crosslinking of VEs,
- and finally the acidolitic decrosslinking of hemiacetals.

Therefore this reactive system is very complicated to manage, because as soon as the first acids start to appear in the system the crosslinking and the decrosslinking reaction succeed. As such, counter-intuitively a longer SB will not lead to a higher crosslinking, because at the same time the decrosslinking of the hemiacetal groups will occur.

## 4.8 Conclusion

In this chapter we formulated the requirements in order to elaborate a positive resist adapted for microfluidic channels fabrication. We proceeded accordingly in order to adapt a positive resist based on PMDA-ODA and VE crosslinkers, to the elaboration of the microfluidic layer. We first found that the polymer absorbs in the i-line which doesn't not make it a good candidate for thick

layer insulation at this wavelength. However it showed less absorption at  $407\text{ nm}$  which makes it more adapted for this wavelength. We were able to use NMR spectroscopy in order to estimate the molecular mass of the polymer used for the synthesis. As such a single NMR acquisition can be used to characterise the "as received" polymer. Also we attempted to increase the solid content of the polymer, which we did by extraction and re-dissolution and by elaborating the polymer from its precursor. The first method demonstrated to be more appropriate as it gave a higher molecular mass polymer. Finally and most importantly, we tried to solve the reactivity problem, which appeared to be a difficult task. Nevertheless, we identified the reason behind the counter-intuitive behavior of this material. Which is the complexity of the reactive system and the many competing reactions that are acid catalysis.

This part of this work will be undertaken by another PhD. student, in order to find a suitable formulation for an ultra-thick positive working resist that corresponds to the specification listed in section 4.2. By following the framework we formulated here, we should be able to achieve a performant resist. Due to the limited success with this resist formulation we decided to shift our attention to PDMS for the fabrication of the microfluidic layer. This will be presented in chapter 5.

# Chapter 5

## The optofluidic integration

### 5.1 Introduction

As seen in the previous chapter, we faced some difficulties while adapting the use of the positive resist based on PMDA-ODA, to the fabrication of thick microfluidic channels. Therefore, In order to accomplish the realisation of a demonstrator, we decide to use PDMS to fabricate the microfluidic channels by molding. As a consequence we use unrevealed waveguides in order to establish the integration, by bonding the microfluidic chip to the optical waveguide layer. In Section 5.2, we tackle the fabrication of the SU-8 mold and the casting of the PDMS, in order to realise the microfluidic layer. In section 5.3, we adjust the different parameters in order to accomplish a successful bonding between the PDMS and the MZ10-2.5, using an intermediate adhesive layer. Finally, in Section 5.4, we will present the alignment method using an optical microscope.

### 5.2 PDMS chip fabrication

The first approach that is the most widely used, as we have seen in chapter 2, is the mounting of a PDMS microfluidic chip on top of the optical layer. Mainly, the PDMS chip fabrication consists of 3 main steps:

- The mold fabrication,
- The molding of the PDMS,
- The inlets and outlets perforation.

After which the chip is ready to be assembled with the optical circuit.

#### 5.2.1 The mold fabrication

The mold was fabricated using the commercial epoxy based photoresist: SU-8-2025, purchased from microchemicals. It is especially attractive due the high coating thickness that can be applied, and the chemically and thermally stable patterns that can be produced. This composition of SU-8 with a 69% solid content permits a range of thickness between 20 and 80  $\mu m$  and respectively for spin speeds between 1000 and 4000 *RPM*. Concerning its UV sensitivity, it operates optimally under i-line exposure. Crosslinking proceeds in two step:

- acid generation during the exposure step,
- catalysis of the epoxy crosslinking, that is thermally provoked during the post exposure bake (PEB).

We pre-clean borosilicate substrates with acetone to remove organic contaminants. Afterwards, we expose the glass to  $O_2$  plasma using a Diener Femto PCCE (13.56 MHz power 0 – 200 W). It leads to the sputter removal of the upper layers of the substrate, resulting in a chemically active surface. Even if it also leads to a hydrophilic surface, we didn't see any delamination of the hydrophobic SU-8 after processing.

The spin coating of the resist happens in three phases:

- we dispense the SU-8 on the substrate surface,
- we spin at 500 RPM for 5 seconds with acceleration of 100 RPM/s to ensure of full coverage of the substrate,
- we ramp up at 300 RPM/s to attain 1000 RPM. This step has a 30 seconds duration and results in an 80  $\mu m$  layer thickness (as indicated in the SU-8 documentation).

Following the spin coating step, we perform a soft bake on a hotplate for 30 min at 95° C. In a similar way to MZ10-2.5, a dose test was done on SU-8 to set the optimal power and scanning speed to be used (Appendix D). Accordingly, a filter with  $O.D. = 0.6$  mounted on the 10  $\mu m$  line was used for this process. The laser writing parameters are summarised in Figure 5.1. The squares on the top right and bottom left are alignment marks, they are imprinted on the optical layer as well.

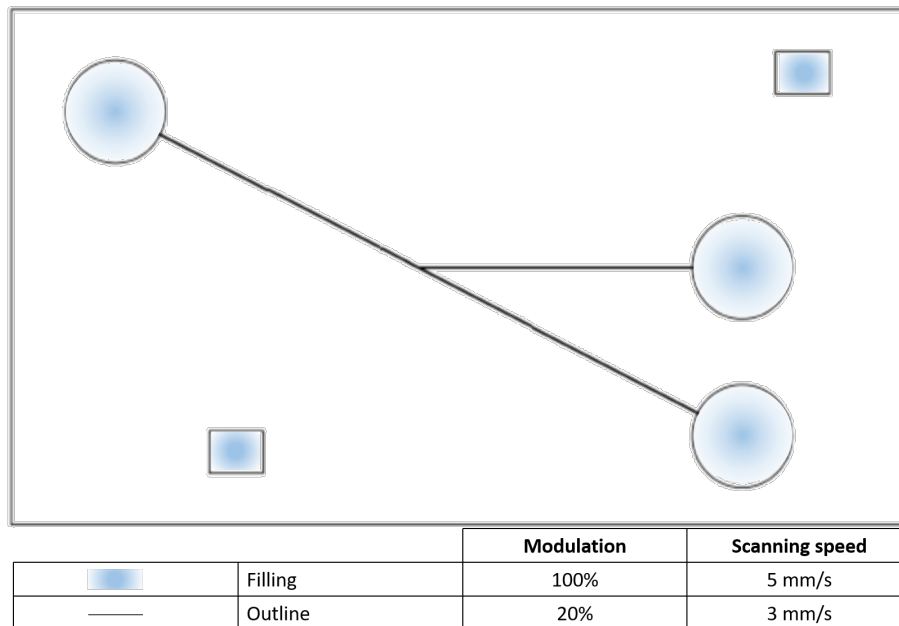


**Figure 5.1:** The 2D computer assisted design to be imprinted on SU-8, along with the laser writing parameters for the writing process.

The PEB is carried out for 1 min at 65° C, then for 5 min at 95° C on a hotplate, to avoid residual stress and to allow relaxation of the drawn patterns. If after this step we see a latent

image of the drawn pattern, this means that the exposure and baking parameters were adequate. The structure was developed in a bath of propylene glycol methyl ether acetate (PGMEA) for around 10 *min* after which it is cleaned in a bath of isopropanol. If a white film of edges appear during this rinse, it is an indication of underdevelopment.

The developed pattern is hard baked on a hot plate for 10 *min* at 210° *C* to ensure proper adhesion to substrate. After the mold has cooled, it is rinsed with ethanol and blow dried to be ready for the molding step. The mold is observed under a microscope, and the channel width is controlled. It showed a slight difference with respect to the CAD design as we can see in Figure 5.2, with a channel width of around 60  $\mu\text{m}$ .

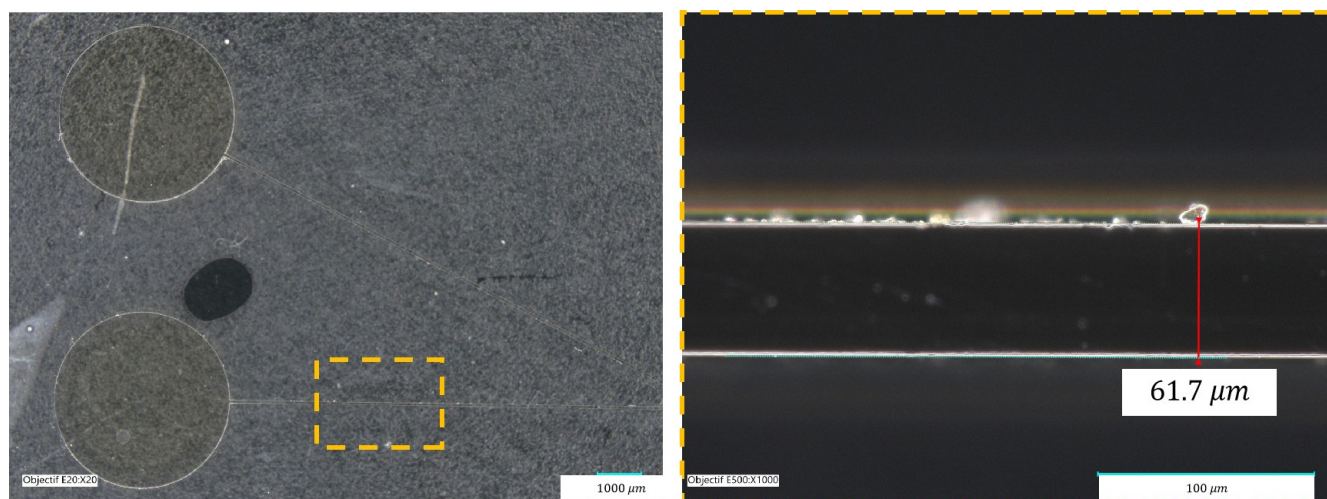


**Figure 5.2:** An optical microscope photo of the SU-8 mold fabricated, the width of the channel is indicated in the figure on the right.

### 5.2.2 PDMS Molding

A SYLGARD 184 kit, containing Polydimethylsiloxane, and its curing agent<sup>1</sup>, were purchased from Sigma Aldrich. The two component were thoroughly mixed according to the manufacturer's recommendation with a ratio of PDMS prepolymer to curing agent of 10 : 1. The mixture is left to de-air in a desiccator with an operating air pump for 20 minutes or until no air bubbles are expelled out of the mixture.

Afterwards, it is poured over the mold that is placed in an inert container and the PDMS is left to dry overnight at 50° *C*. This thermal crosslinking reaction, is a hydrosilylation between the vinyl ( $\text{Si} - \text{CH} = \text{CH}_2$ ) groups of the PDMS and hydrosilane ( $\text{Si} - \text{H}$ ) groups of the crosslinking agent, as illustrated in Figure 5.3.

<sup>1</sup>No further information is provided concerning the nature of the curing agent, but according to one of their patents [224] it is "an organopolysiloxane having at least two silicon-bonded hydrogen atoms per molecule". This is also backed up by articles [225].

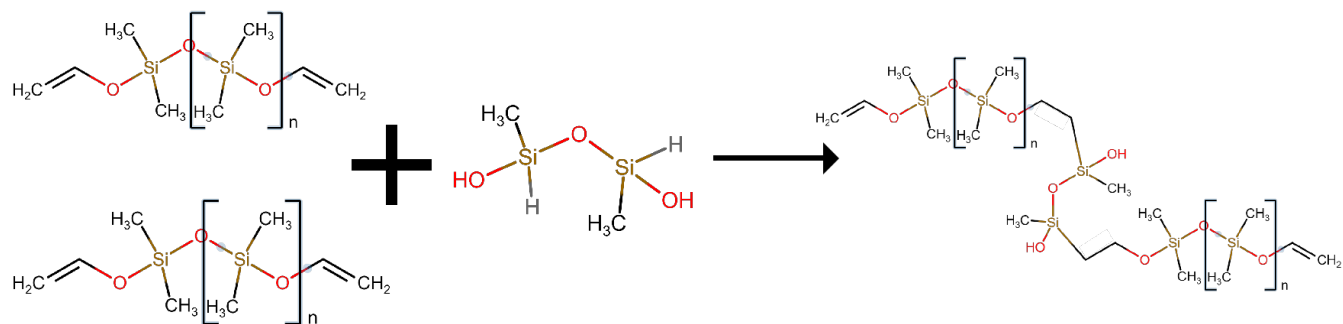


**Figure 5.3:** The crosslinking reaction between the PDMS prepolymer and the crosslinking agent, illustrated here as polymethylhydrosiloxane (*PMHS*), the most simple form that the curing agent may take.

Once it has completely crosslinked, the PDMS chip is demolded using a scalpel to cut out the chip edges, allowing it to be released from the glass substrate. Inlets and outlets holes are punched, after which it will be ready for the following steps. The resulting channels are observed under optical microscope as seen in Figure 5.4. The profile shows straight walls and a well defined rectangular profile with a width of around  $60\ \mu\text{m}$  and a height of around  $80\ \mu\text{m}$ , in agreement with the mold width and height.

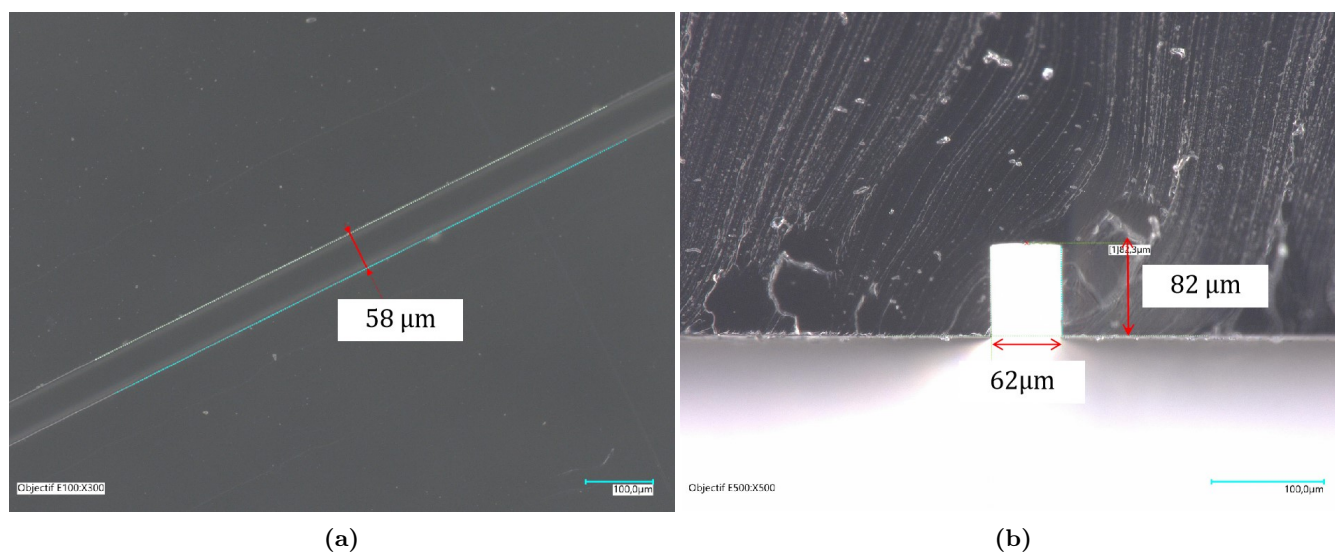


**Figure 5.4:** Optical microscope photo of the PDMS channel:(a) top view, (b) channel profile

## 5.3 The bonding step

Even though activation with oxygen plasma is a widely used method for bonding the PDMS to the optical layer. We are going to investigate another method to accomplish the bonding for a couple of reasons:

- the low mechanical properties of the MZ resist, and its low resistance to high temperature. Plasma induces roughness on the surface as seen in Figure 5.5<sup>2</sup>. As such, the contact between the two materials becomes harder to accomplish, which will lead to poor bonding. We did not have time to study the bonding quality depending on the plasma parameters (power, time, pressure), so we decided to switch to another method.
- in anticipation for the following step that is the alignment of the optical layer and the microfluidic layer, plasma-treated surfaces remain chemically reactive for only up to ten minutes after treatment, this is a limiting factor in our case because we might need additional time to accomplish the alignment between the two layers.

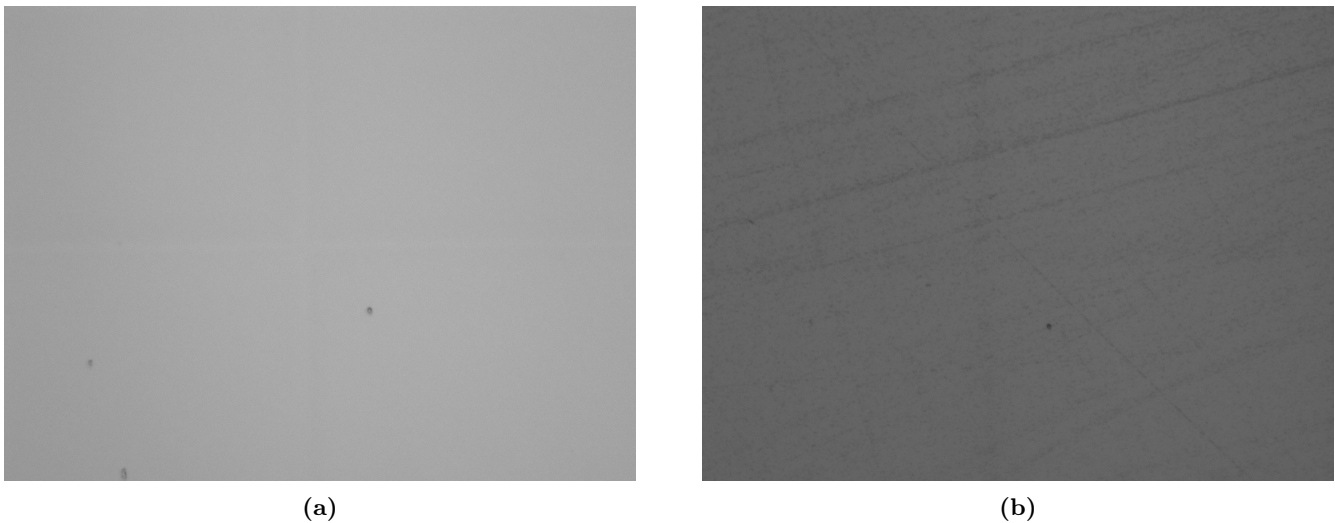


**Figure 5.5:** The plasma treatment effect on the MZ layer: (a) before and (b) after plasma treatment of the same location. The observation spot is marked by the UV imprint of a cross.

The alternative to plasma bonding is adhesive bonding. It is a type of intermediate layer bonding, that is usually applied when bonding glass to silicon [226], or PMDS to materials that may or may not support hydroxyl immobilisation on their surface [227]. It can be used for a wide range of materials, under the one condition that an adequate adhesive layer can be found. It utilizes low temperature when compared with thermal, or anodic bonding. It does not require high voltages, nor special equipment. Its only requirements are, the uniformity of the two surfaces to be put into contact, and a thin and uniform adhesive layer, that can be easily obtained by spin coating. The thickness of the adhesive should be adjusted in order to avoid channel clogging.

PDMS adhesive techniques were even found to be a better alternative to oxygen plasma for PDMS-PDMS devices [228]. In the light of these findings we will opt for a similar approach to the

<sup>2</sup>Plasma parameters: 140 W, 60 s

stamp and stick method presented in [227], which we will adapt to our materials.

In our case, the choice of the adhesive was made based on the fact that the MZ layer should have a better affinity with itself more than any other resist, and might be mechanically anchored within the PDMS matrix in addition to the formation of  $Si - O - Si$  bonds. The steps of the selective adhesive bonding are illustrated in Figure 5.6, and the process can generally be summarised as follows:

- the adhesive layer transfer process (steps 1 2 and 3)
- and the bonding of the top and bottom device (step 4).

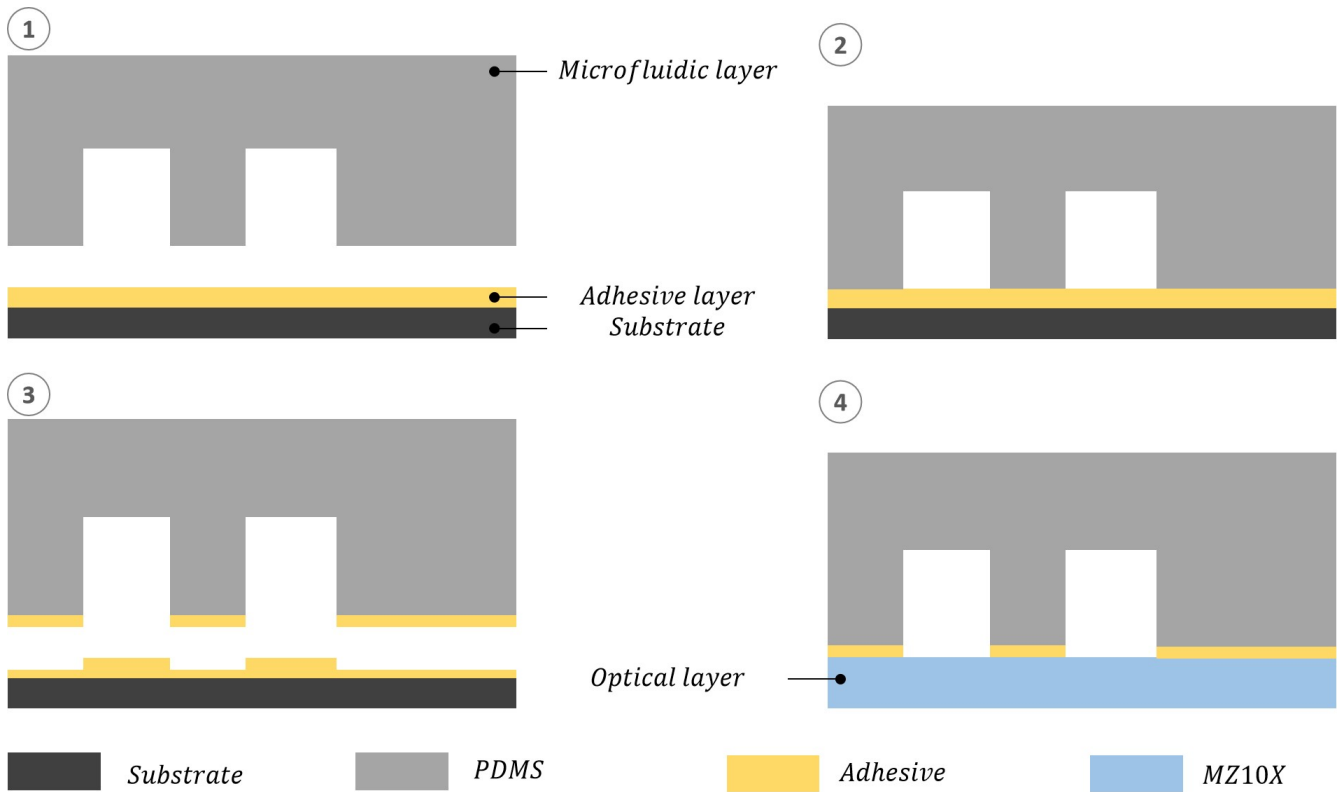


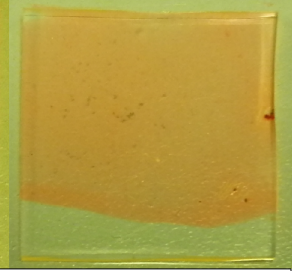
**Figure 5.6:** The adhesive transfer and bonding process.

The transfer process consists of multiple steps: it starts with the coating of a uniform adhesive layer on a substrate, after which the patterned top layer is brought into contact with the adhesive (steps 1 and 2). Afterwards, the top device is removed with the selectively patterned adhesive layer. Indeed, additional steps that are specific to the materials may be required, and will be investigated and adjusted in the following section.

### 5.3.1 Selective transfer of the adhesive

The transfer of the adhesive layer from the substrate to the PDMS is crucial to the success of this process. In order to optimize this step we used cured non patterned PDMS pieces, a composition of MZ10-1 as an adhesive, to which we added rodhamine G as a colouring agent to observe the transferred film with ease, and finally a silicon substrate.

An MZ10-1 layer is spun coated on a silicon substrate. Clean PDMS pieces were placed on top of the adhesive layer. They were baked at  $80^{\circ}C$  for 10, 20, and 30 minutes. Another PDMS piece was cleaned and plasma treated (60 s oxygen plasma 140 W power modulation), then placed into contact with the adhesive layer and baked for 30 minutes at  $80^{\circ}C$ , in order for the Si-O-Si bond to form between the adhesive and the PDMS. The results for the transferred layers are presented in Figure 5.7.

Plasma Treatment	No			Yes
				
Baking time	10 minutes	20 minutes	30 minutes	

**Figure 5.7:** Plasma treatment and baking time effect

Clearly the plasma treatment changes the surface properties of the PDMS, most importantly the wettability which enables the uniform transfer of the adhesive onto the PDMS layer. On the other hand, increasing the baking time without any plasma treatment does not enhance the spreading of the film.

### 5.3.2 The bonding of the two layers

The uniform transfer of the adhesive cannot be accomplished without a plasma treatment. Upon bonding, another adjustment was needed as the adhesive layer baked for 30 minutes exhibited poor adhesion to the optical layer, due to complete solvent evaporation. The baking was reduced to 15 minutes instead, in order to keep an acceptable trade off between a good and uniform transfer of the film onto the PDMS and the exhibition of sufficient adhesion. Accordingly, we proceed in the following process:

- We clean the patterned PDMS with isopropanol and air dry it. We then plasma treat the PDMS layer (60 s oxygen plasma with 140 W power), to enable the silanol formation on its surface.
- In the meanwhile, we cast the MZ10-1 layer on a clean silicon substrate. Soon after the plasma treatment is done we carefully drop off the PMDS layer (microstructured side down) without applying any pressure to avoid the channel walls deformation as illustrated in Figure 5.6 (1) and (2). We can instantly see that the sticking front spreads quickly and easily without any pressure.
- We then place the substrate with the adhesive and PDMS in an  $80^{\circ}C$  oven for 15 minutes to enable the formation of an Si-O-Si bond between the PDMS and the MZ10-1 adhesive.

- Afterwards, and as illustrated in Figure 5.6 (3) and (4) we remove the PDMS off the substrate and place it on the optical layer while applying a gentle and uniform pressure by the mean of a glass plate. Finally we leave the whole device at  $110^{\circ}C$  for 2 hours.

### 5.3.3 The adhesive layer thickness

In order to avoid clogging the adhesive layer thickness should be adjusted. Therefore, the steps presented in the previous section are applied to patterned PDMS chip and different adhesive layer. Two adhesive layers having different thicknesses were cast on a substrate. A  $5\mu m$  and a  $2\mu m$  layers were cast using MZ10-1 solutions having solid contents of 50% and 40% respectively<sup>3</sup>. The spin speed and time respectively are  $4000\text{ RPM}$  and  $2\text{ s}$  for both layers. Figure 5.8 shows the PDMS channels after bonding for both thicknesses.

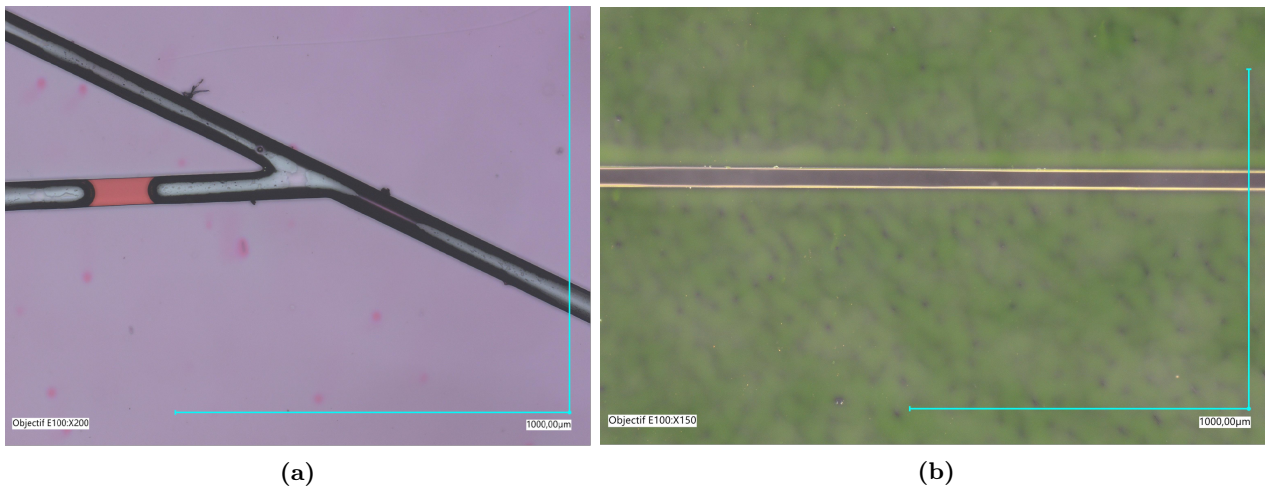


**Figure 5.8:** Optical microscope photo of the bonded PDMS channels: (a) with a  $5\mu m$ , and (b)  $2\mu m$  adhesive layer.

As seen in Figure 5.8a, the  $5\mu m$  adhesive layer infiltrated into the channel and lead to its obstruction. The thinner layer showed good adhesion while avoiding channel clogging. Fluid injection in the channels was successful, once again confirming the absence of any blockage due to the adhesive layer as seen in Figure 5.9.

<sup>3</sup>The solid content of the MZ10-1 is reduced to 40% by diluting the original sol with butanol

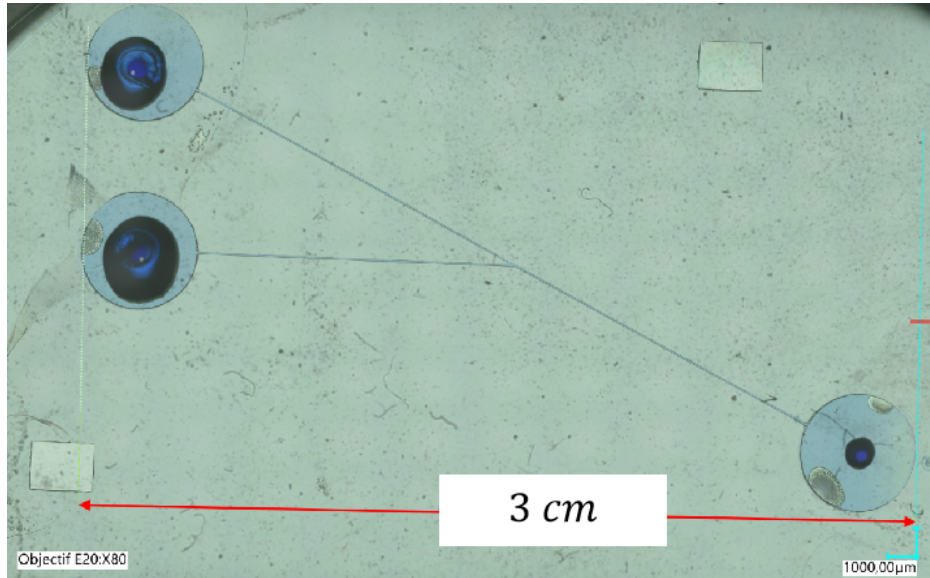


**Figure 5.9:** Fluid (in blue) injection in the bonded PDMS chip.

Finally, in order to verify the bonding strength a wrenching test was performed. The PDMS couldn't be detached from the bottom layer unless it was torn into pieces as we can see in Figure 5.10. This means that the bond strength is comparable or superior to that of bulk PDMS.

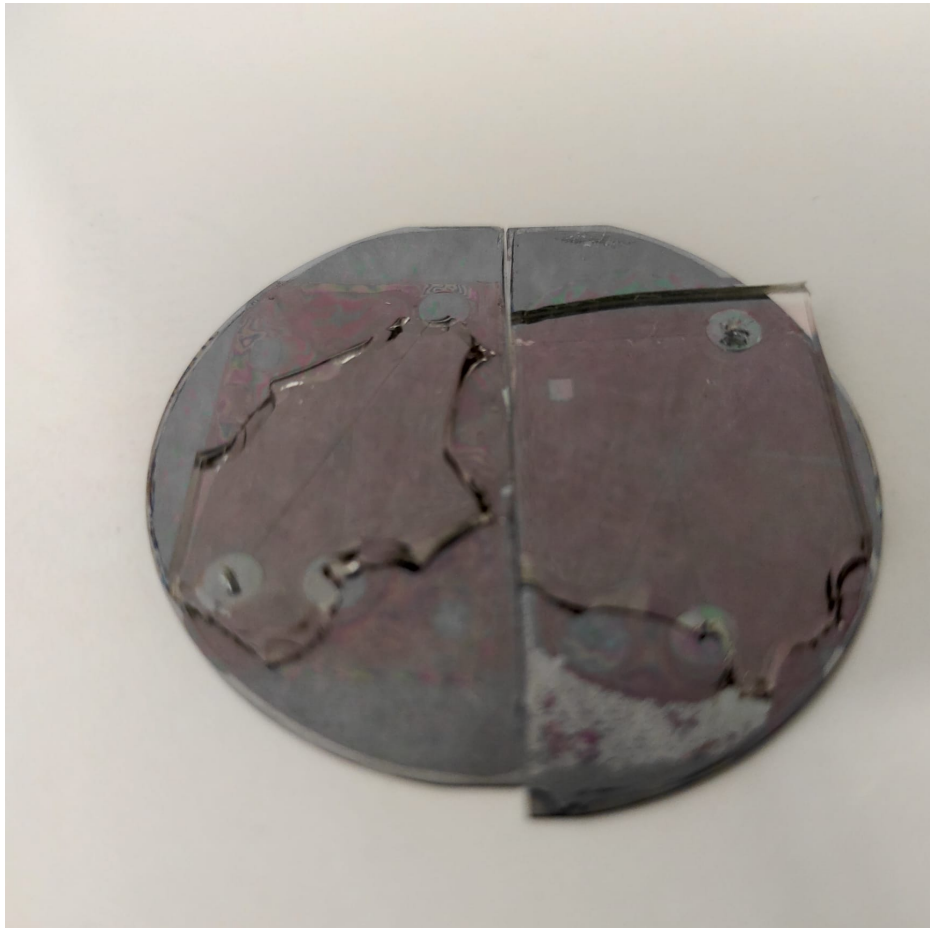


**Figure 5.10:** Two adhesive bonded chips that passed the dismantling test.

## 5.4 The alignment step

The alignment of the two layers can be accomplished in two different ways:

- The use of a commercial mask aligner, such as the UV Kub-3 fabricated by Kloe France.
- The use of an optical microscope, to which a special adjustment is made.

The first method even though feasible has some limitations, such as the working distance, i.e. the distance between the mask and the substrate plate. This working distance is only  $5\text{ mm}$  which imposes a PDMS layer thickness that cannot exceed  $4\text{ mm}$ . On the other hand, the penetration depth of the aligner camera doesn't provide equal focus on the bottom layer and on the PDMS chip.

The second method can be applied using a simple add on to the optical microscope as seen in Figure 5.11. Thus presenting a simplified version of the desktop aligner realised in [229].

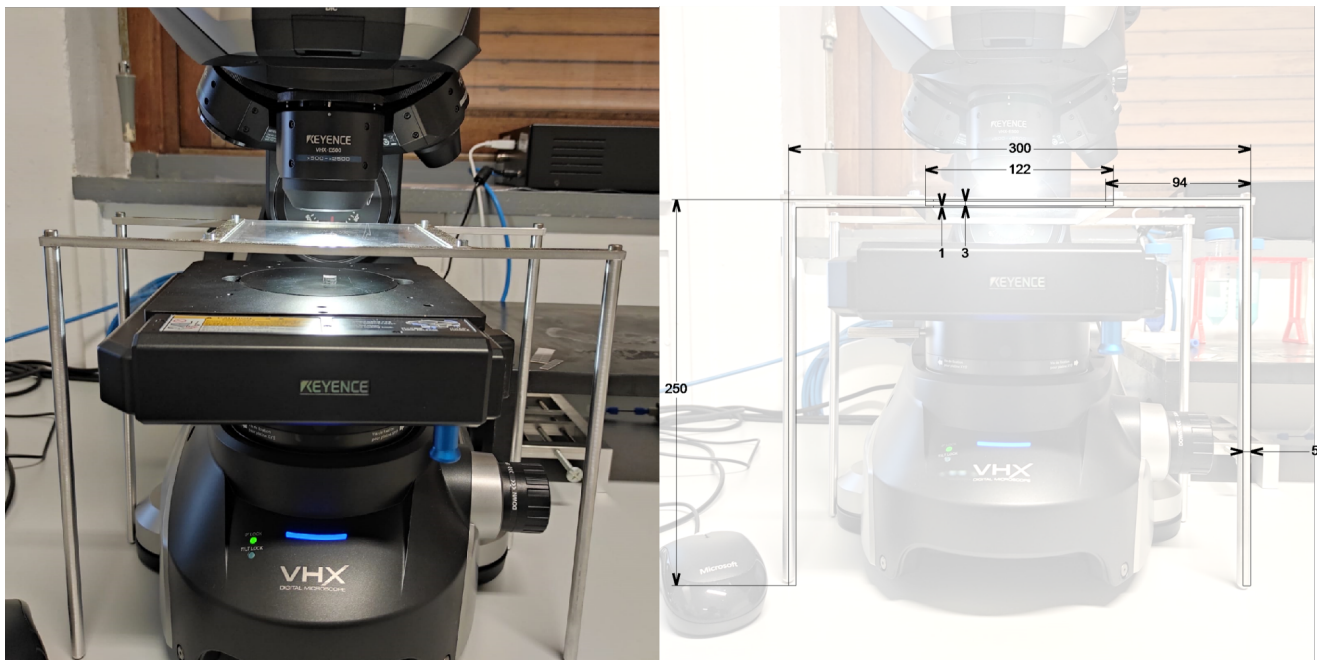


**Figure 5.11:** An alternative to a desktop aligner for PDMS/PDMS or PDMS/MZ: on the left, a photo of the setup that is the optical microscope and the upper layer mount, and on the right the same setup with the mounts dimensions in mm.

The alignment procedure illustrated in Figure 5.12 can be broken down into 6 steps as follows:

- Step 1: The reversible bonding of PDMS to glass by the mean of *van der Waals* forces<sup>4</sup>, is exploited in order to attach the upper PDMS layer to the glass plate. The PDMS should be placed in the center of the glass slide in order to facilitate the process.
- Step 2: The bottom layer (MZ on a silicon substrate, PDMS, or any other material) is placed in the center of the microscope stage, and the glass plate is slid into the holder. A rough  $(x,y,\theta)$  alignment between the two layers, is necessary, and can be easily achieved by placing

<sup>4</sup>Or by capillarity using a drop of water between the glass and the PDMS.

the two layers in the center of their corresponding holders, with the alignment marks as close as possible.

- Step 3: Now that the setup is ready, the focus of the microscope objective is adjusted on the top PDMS layer and the (z) motorised microscope stage is used to bring the two layers closer, in order to get a clear view of the bottom alignment mark as well. Afterwards, the (x,y) motorised positioning as well as the manual ( $\theta$ ) positioning is done.
- Step 4: the z position is adjusted to bring the layers closer while avoiding contact and a more precise (x, y,  $\theta$ ) alignment is done, with the use of a higher magnification objective.
- Step 5: the z axis is used to bring the two pieces to contact. The design of the holder will prevent the glass plate from touching the objective as the stage pushes up, nevertheless the lifting of the stage should be carefully done in order not to put any stress of the motorized stage.
- Step 6: Finally the stage is lowered and the glass plate with the aligned and bonded chip can be slid out of the holder. The chip can be detached using a thin razor blade to lift it off.

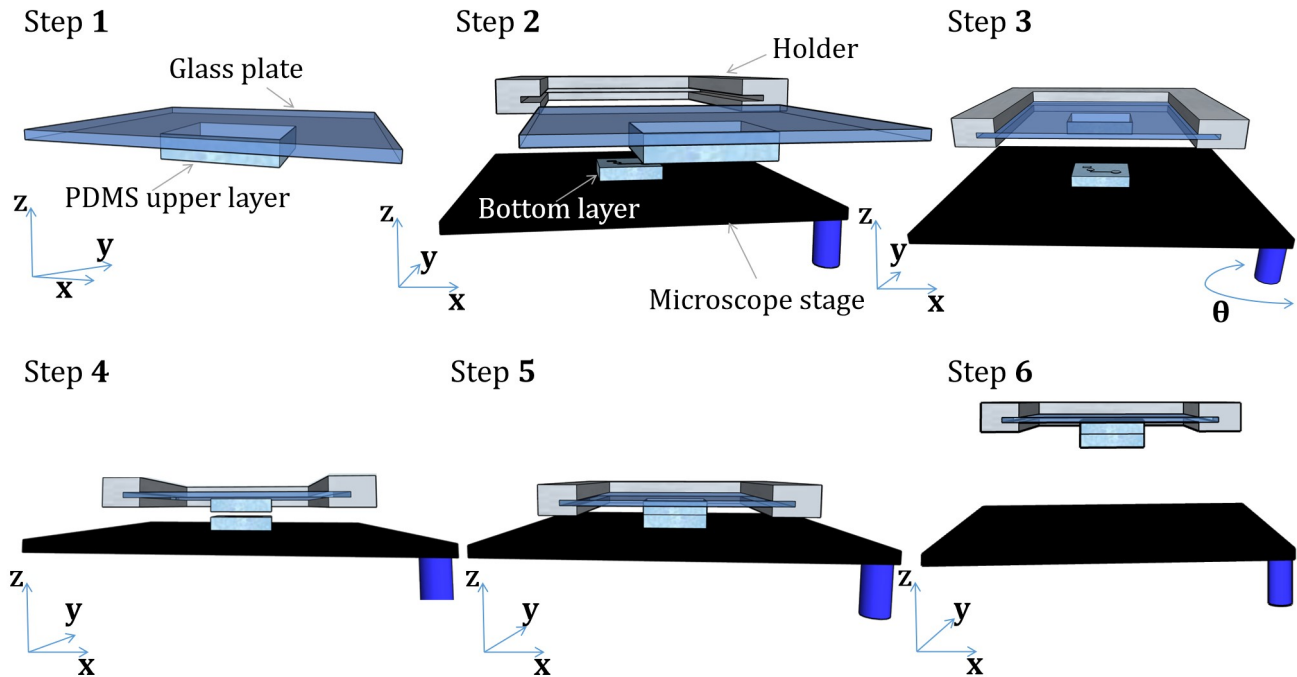
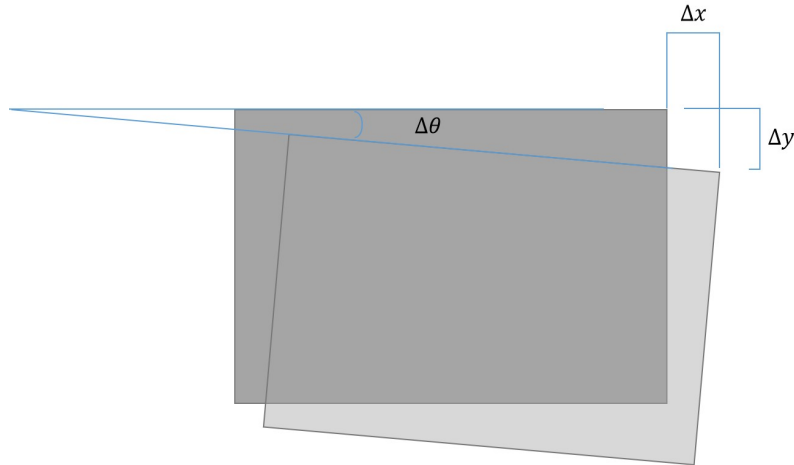


Figure 5.12: The alignment process steps.

The misalignment increases as the marks surfaces decreases below  $0.6 \text{ mm}^2$ , a value above which they found no significant change<sup>5</sup>. The alignment can be assessed by estimating the maximum translational shift  $\Delta l$ , as well as the rotational shift  $\Delta\theta$ . Such that  $2\Delta l = \Delta x + \Delta y$ , with  $\Delta x$  and  $\Delta y$  being the maximum shifts in both  $x$  and  $y$  directions respectively.

<sup>5</sup> Their results were validated for different users, with different degrees of experience.



**Figure 5.13:** A schema explaining the method we use to assess the alignment quality. The  $(\Delta x, \Delta y, \Delta\theta)$  model proposed by [229]

In order to assess the quality of the alignment, we used two PDMS chips with rectangular ( $2 \times 1.5 \text{ mm}$ ) alignment marks and we proceeded as explained in the steps above. Figure 5.14, shows the alignment marks before and after the alignment is accomplished.

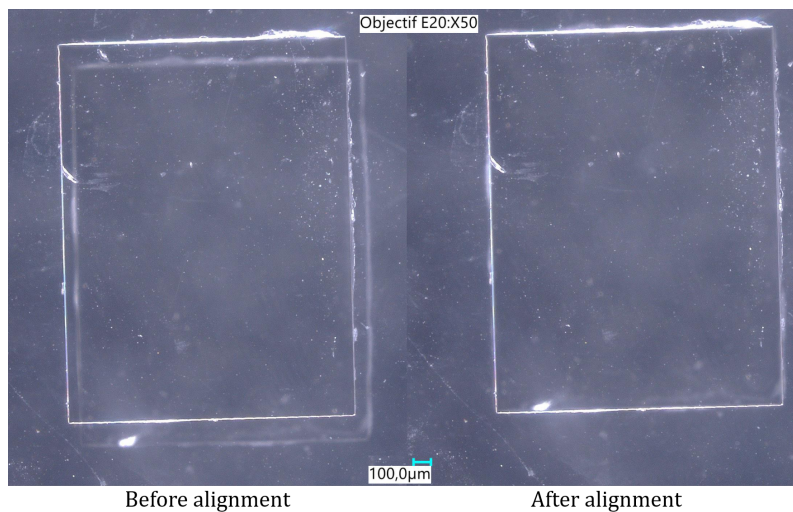


**Figure 5.14:** Photos taken of the alignment marks, before and after the alignment

After detaching the chips from the upper holder, we measured the  $(x, y$  and  $\theta)$  shifts. An average  $(x, y)$  translation shift of  $13 \pm 3 \mu\text{m}$  was found. Nevertheless, shifts as low as  $7 \mu\text{m}$  can be reached. The rotational shift was  $0.5 \pm 0.3^\circ$ . This variability, especially in the translational shift is probably due to the stability of the mount we fabricated. These results are comparable with those found using the desktop aligner in [229].

## 5.5 Conclusion

In this chapter, we demonstrated the integration of a PDMS chip on the optical waveguide layer. The bonding of the two layers can be accomplished using an intermediate adhesive layer of  $2 \mu\text{m}$

thickness. This layer is cast using MZ10-1 solution having 40% solid content, and transferred selectively on the molded PDMS chip. The alignment of the two layers was done using an optical microscope equipped with a special mount capable to hold the upper layer during the alignment. An average  $(x, y)$  translation shift of  $13 \pm 3 \mu m$  was found, while the rotational shift was  $0.5 \pm 0.3^\circ$ .



# General Conclusion

We presented in this manuscript an investigation of the potential of organic-inorganic photoresists, in order to respond to the needs of the R&D for optofluidic LoC fabrication. These resists can be rapidly patterned by laser writing: a negative tone resist for the fabrication of the optical waveguides and a positive tone resist for the fabrication of the microfluidic layer. For the prototype we proposed to implement an optical manipulation function on a chip that is a particle sorter in the same spirit of the work presented in the literature for 2D actuators. Manipulation functions on chip are usually elaborated using waveguides made of silicon (Si), silicon nitride ( $Si_3N_4$ ), silicon oxynitride ( $SiON$ ), and tantalum Pentoxide ( $Ta_2O_5$ ), deposited on a silicon dioxide  $SiO_2$  buffer layer. They can also be fabricated in polymer photoresists such as the commercial epoxy resist SU-8. In addition, they can be realised in glass even with much lower refractive index steps (0.005). Hybrid organic-inorganic materials are a good fit for this integration. On one hand, they are widely used for the realisation of optical circuits, and optical waveguides for sensing applications. On the other, the development of a positive tone photo-resist based on hybrid materials is in progress towards elaborating an ultra-thick resist. The combination of these materials is equally adapted for rapid prototyping by laser writing techniques, and for mass fabrication by UV masking techniques.

Negative tone hybrid resists are widely known for their outstanding optical properties. In particular a composition based on different molar ratios of MAPTMS and  $Zr(PrO)_4$  demonstrated to be an adjustable formulation for optical circuit as well as for optofluidic sensor fabrication. The interesting characteristic of this composition is the ability to tune its refractive index by changing the molar ratio between these two precursors. As such it is suitable for the casting of the guiding layer and the lower cladding layer. In these resists, waveguides can either be implemented by UV induced refractive index change, or by a standard photolithographic process (insulation, baking, development). Even at very low refractive index difference (0.002) the guiding of light was confirmed. The change of the photoactive compound was found to be able to increase this step in order to attain 0.004. The development step has no effect on the quality of the surface. Revealed and unrevealed waveguides showed an attenuation of around  $2\text{ dB/cm}$  in the visible range where the most pronounced scattering effects can take place. In order to be able to master the channels dimension as a function of the applied dynamic dose, we validated a model for laser writing using a truncated Gaussian beam. It predicts that the width of a cured line, vary as the square root of the dose, or as the square root of the ratio  $\frac{P}{v}$ . For future work, this model can be used to predict the laser writing parameters needed for a certain waveguide width. Also for other resists (positive and negative), we will only need a reduced set of points in order to constitute the curve. This can help us to choose a region of interest in terms of laser parameters to achieve a more targeted calibration. In general, we found that it is better to avoid using extremely high doses because the linewidth cannot be controlled with accuracy in this range. This was experimentally observed and is also predicted by the model.

We also tried to adapt the use of a positive resist composition to the fabrication of a microfluidic layer. Even though we had limited success, we were able to constitute a framework to follow in order to accomplish this task. The steps we followed are applicable while fabricating any type of thick photoresist. We started by evaluating the transparency of the polymer in the UV-visible region. This can be done by acquiring the UV-Vis reflectance and transmittance spectra and deducing the absorptance. This can give a good idea about the transparency of a deposited film of the photoresist. In our case this polymer was more adapted for an insulation at  $407\text{ nm}$ . Also, we were able to estimate the molecular weight of the polymer from an  $H^1$  NMR spectra. This can be applied to other polymers as well and it can enable the characterisation of newly received samples in order to ensure reproducibility. We also tried to increase the solid content of the polymer and change the solvent in which it is dissolved. This can be done either by extraction and re-dissolution, or by synthesizing the polymer from ODA and PMDA directly in the solvent of choice. The first method preserved the structure of the polymer and its molecular weight, while the second produced lower molecular weight polymer. In order to address the reactivity of the PMDA-ODA and the TVEB, we used NMR spectroscopy which appeared to be a very straightforward method to follow the reaction kinetics. However the polymer was replaced with benzoic acids in order to avoid the imidisation and a model based on benzoic acid and TVEB was used to follow the crosslinking reaction. We found that a resist based on PMDA-ODA and VE crosslinkers, cannot acquire its positive working aspect only by thermal crosslinking. An acid is essential to this process. The acidity of the COOH groups of the PMDA-ODA are not sufficient in order to provoke the thermal crosslinking. A catalytic amount of acid is provided by the decomposition of the PAG at temperatures higher than  $110^\circ\text{C}$ . This is what crosslinks the COOH of PMDA-ODA and the VE of TVEB and form hemiacetals. Therefore, this reactive system is very complicated to manage, because as soon as the first acids start to appear in the medium, the crosslinking and the decrosslinking reactions succeed. As such, three competing reactions are able to take place:

- the acidolitic crosslinking of VEs and carboxylic acids,
- the acidolitic crosslinking of VEs,
- and finally the acidolitic decrosslinking of hemiacetals.

Finally, we used PDMS in order to develop a microfluidic layer, because the positive resist needs further optimisation. This then obliged us to use unrevealed waveguide structures in order to be able to implement the integration by bonding the PDMS chip on the optical layer. For the bonding we used an adhesive bonding technique called stick and stamp. The alignment of the two layers was performed using an optical microscope to which we adapted a special mount that can hold the upper PDMS layer. The alignment was evaluated by measuring the translational and rotational shifts of the alignment marks.

This work constitutes a solid start to the project through establishing the basics of laser writing in photosensitive resists and the steps to follow in order to elaborate a reliable positive resist for the microfluidic layer fabrication. While we couldn't fully achieve the fabrication of the system and prototype formation with the desired materials, this work provides a strong basis for the continuation of the project. In future work, we will focus on the development of positive tone photoresists that fit the requirements stated in Chapter 3.

# Appendices



# Appendix A: Waveguides characteristics

Waveguides for optofluidic evanescent field sensing and control: materials, fabrication techniques and key properties.

Reference	Cladding material	Core material	Deposition /patterning	Refractive index increase	Core width ( $\mu m$ )	Core Height ( $\mu m$ )	Wavelength (nm)	Refractive index step	Losses ( $dB/cm$ )	Comments
[159]	PDMS	PDMS and photopolymerisable monomer	Molding bulk PDMS Direct waveguide writing	Multiphoton polymerisation	0.6 – 1	1.5-3	535 – 679	$\approx 0.005$	13	A multi-track waveguide strategy was implemented to increase the waveguide width and lower the losses from $13dB/cm$ to $0.1dB/cm$ at around $710nm$ .
[158]					1.3	1.3	650 – 700	$\geq 0.06$	0.03	Poor transmission below $600nm$ .
[160]		PDMS	Molding	Tailoring base to curing agent mixing ratio	125	125	460	$0.01 - 0.02$	1.1	Single mode waveguides fabrication is challenging. Optical fiber can be directly and permanently integrated
[161]				Modifying the curing process for the PDMS	125	125	460	0.02	0.40	
[230]	XP-07423A cladding	XP6701A core	Spin coating	Direct Laser Writing	4	4	1310	$\approx 0.034$ or lower	$0.34 \pm 0.04$	Low definition, round waveguide corners.
	Epo Clad	Epo Core			5	5	1550		$1.36 \pm 0.02$	
							1310	$\approx 0.007$	$0.49 \pm 0.07$	Vertical sidewalls good definition, higher absorption losses than siloxanes.
[231]	OE-4141 UV cladding	OE-4140 UV core		UV curing + different core and cladding material	5.5	5.5	1.3	0.009	0.28	Low losses
[232]	Lumogen OVD Varnish 311 (BASF)	UV-curable organic inorganic OrmoClear FX	Roll to plate imprint and doctor blade		6.5	6.5	1.55	0.008	0.92	Only multimode waveguides can be fabricated. Limited resolution.
[233]	InkOrmo	InkEpo	Inkjet printing		50	50	1308.2	0.04	0.56	
					100	20	NA	0.04	NA	Parabolic Waveguide profile. Only multimode waveguides can be fabricated.

[150]	PMMA	UV glue NOA72	Hot embossing of the PMMA + injection of core material	80	60	635	0.07	1	Only multimode waveguides can be fabricated.
[154]	$SiO_2$ (lower)	SUS	Lower $SiO_2$ is thermally grown on Si. SU 8 is Spin coated and UV patterned	30	100	633	0.13	1.4	Thermally unstable
	PDMIS (upper)						0.16		
[153]	$SiO_2$	SUS		2 – 6	0.8 – 1	980	0.11	$1.36 \pm 0.02$ (TE) $2.01 \pm 0.02$ (TM)	
[156]	$SiO_2$ (lower)	SUS		30	10	576	0.14	2.5	The laser is an RG6 distributed feedback dye laser. Details about the waveguide characteristics in [154]
	PMMA (upper)						0.11		
[91]	PMMA	SUS		2.8	0.560	975	0.101	$1.3 \pm 0.2$	$5.0 \pm 0.2 dB$ coupling losses
[148]	PMMA	PMMA	Bulk substrate	$\approx 4.5$	300	645	0.0075	NA	Graded index waveguide. RI decays in depth
[139]	soda-lime glass	$K^+$ Ion exchanged soda-lime glass	Bulk substrate for the core. Aluminum mask for selective ion exchange.	10	20 – 40	632.8	$4.8 \times 10^{-3}$ (TE) $5.3 \times 10^{-3}$ (TM)	NA	Time consuming, extreme temperature conditions. For [137] total system losses is 8 dB. For [77, 139] the core height is deduced from the modal size.
[137]		$Cs^+$ ion exchanged soda lime glass		2.5	NA	1082	0.03	NA	
[77]	BK7 glass	$Cs^+$ ion exchanged BK7 glass		5.5 – 10.5	5 – 8	$\approx 1000$	0.009	0.2	
[128, 134, 135]	$SiO_2$	SiON	Thermal growing of $SiO_2$ buffer and PECVD of SiON core and $SiO_2$ upper cladding	24 and 250 (only mentioned in [135])	6	633	0.013	NA	Time consuming (Thermal growing + annealing), High temperature.
[87]	$SiO_2$ (lower)	$Si_3N_4$	LPCVD/resist patterning /RIE	1 – 10	0.200	1064	0.52	2	Important insertion losses 10dB





## Appendix B: Polymerisation of VEs [180, 181]

The cationic chain polymerization of VEs can be initiated by a cation ( $A^+$ ), derived from an initiator ( $A^+, B^-$ ), and is illustrated in Figure 5.15.

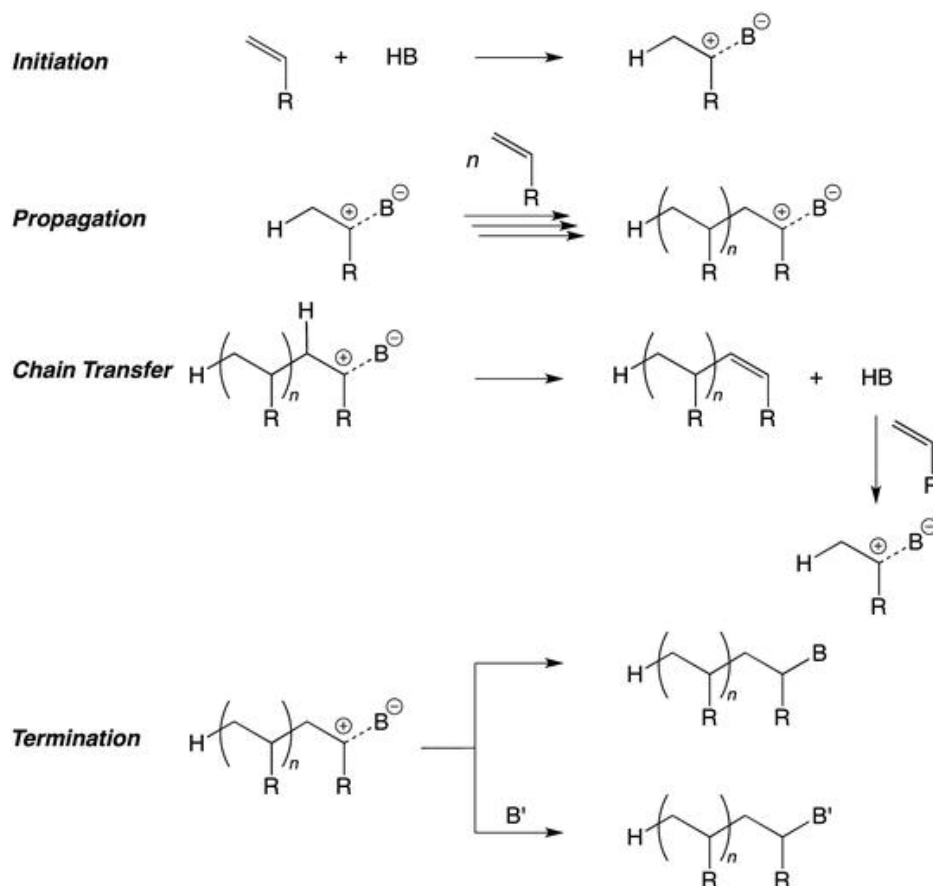


**Figure 5.15:** Cationic polymerisation mechanism of Vinyl groups. For VEs the R is an OR' [181].

The electrophilic addition of the cation, protonates the double bond carbon as illustrated in Figure 5.15, leading to the formation of a cationic active species. The propagation reaction that follows can be described as a series of carbocation, with the previously formed active species acting in the same manner as the initiating proton. Finally the growth of the molecular chain stops with:

- either a chain transfer to the counter ion ( $B^-$ ), that can restart the initiation process of new VE

- or with a termination, by a recombination with the counter ion or another species, which is less probable unless a basic compound is present in the medium.<sup>6</sup>

The cations can be provided by different types of initiators such as protonic acids<sup>7</sup>, or organic salts such as iodonium and sulfonium salts. The release of the cations can be done in different ways:

- either by localised UV excitation of a cationic photoinitiator, more precisely a photo acid generator (*PAG*) such as aryl sulfonium or iodonium salts for example.
- or by the excitation of a thermal acid generator (*TAG*) upon baking.

It is important to note that, in the presence of an acid, VE groups can also undergo a competing reactions of cationic polymerization [180,181] (see Appendix B for details), and an acidolysis by photogenerated acids depending on the process conditions [182] such as the soft baking temperature and the exposure. It was also demonstrated that unless acid groups of the polymer are 20 times the number of VEs of the crosslinker monomer the cationic polymerisation of VE is more probable than the copolymerisation with a COOH [177].

---

<sup>6</sup>The counter ion  $B^-$  shouldn't be very nucleophilic in order for the reaction to propagate, this is why the termination by a nucleophilic attack of the counter ion is not very probable.

<sup>7</sup>Hardly ever produces high polymers because of accompanying side reactions

# Appendix C: 2D NMR spectra

## $H^1 - H^1$ COSY spectrum

COSY is a useful technique for determining neighboring protons. Thus a J3 proton-proton correlation is marked by a cross peak in the resulting 2D spectrum. It will help us determine the protons that correspond to the low intensity signal in the  $H^1$  NMR spectrum. We know that these signals are those of terminal protons. We also know that the termination may be an ODA (Figure 5.16a) or a PMDA termination (Figure 5.16b).

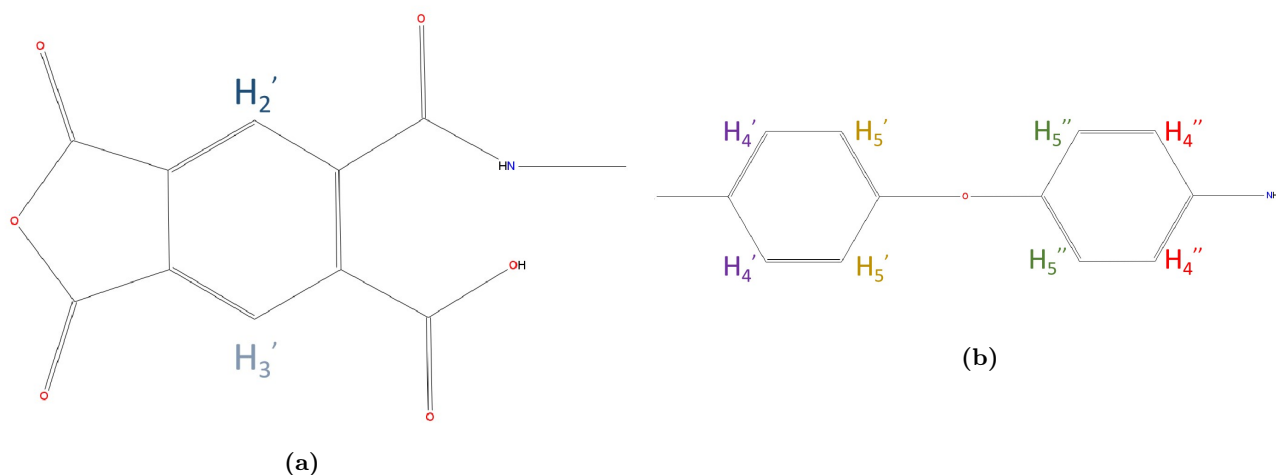


**Figure 5.16:** (a) ODA and (b) PMDA terminations.

The COSY NMR spectrum represented in Figure 5.17, confirms that the low intensity double doublets centered around 7.63, 6.90, 6.77 and 6.61ppm are respectively those for  $H_4''$ ,  $H_5''$ ,  $H_4'$  and  $H_5'$ .  $H_5'$  and  $H_5''$  are more shielded than their respective coupled protons  $H_4'$  and  $H_4''$ , in the same manner as it is for  $H_4$  and  $H_5$ . In addition the far most terminal protons marked by '' are also less shielded when compared to their closest homologous marked by ' because they are the farthest from the electronic cloud of the polymer. We can note that no uncoupled protons appear on the COSY, suggesting that all chain terminations are of PMDA type.

**Table 5.2:** COSY protons correlations and assignments

Peak	$\nu(F2)[ppm]$	Assignment	$\nu(F1)[ppm]$	Assignment
3	7.70	$H_4$	7.05	$H_5$
2	7.63	$H_4''$	6.90	$H_5''$
1	6.77	$H_4'$	6.61	$H_5'$

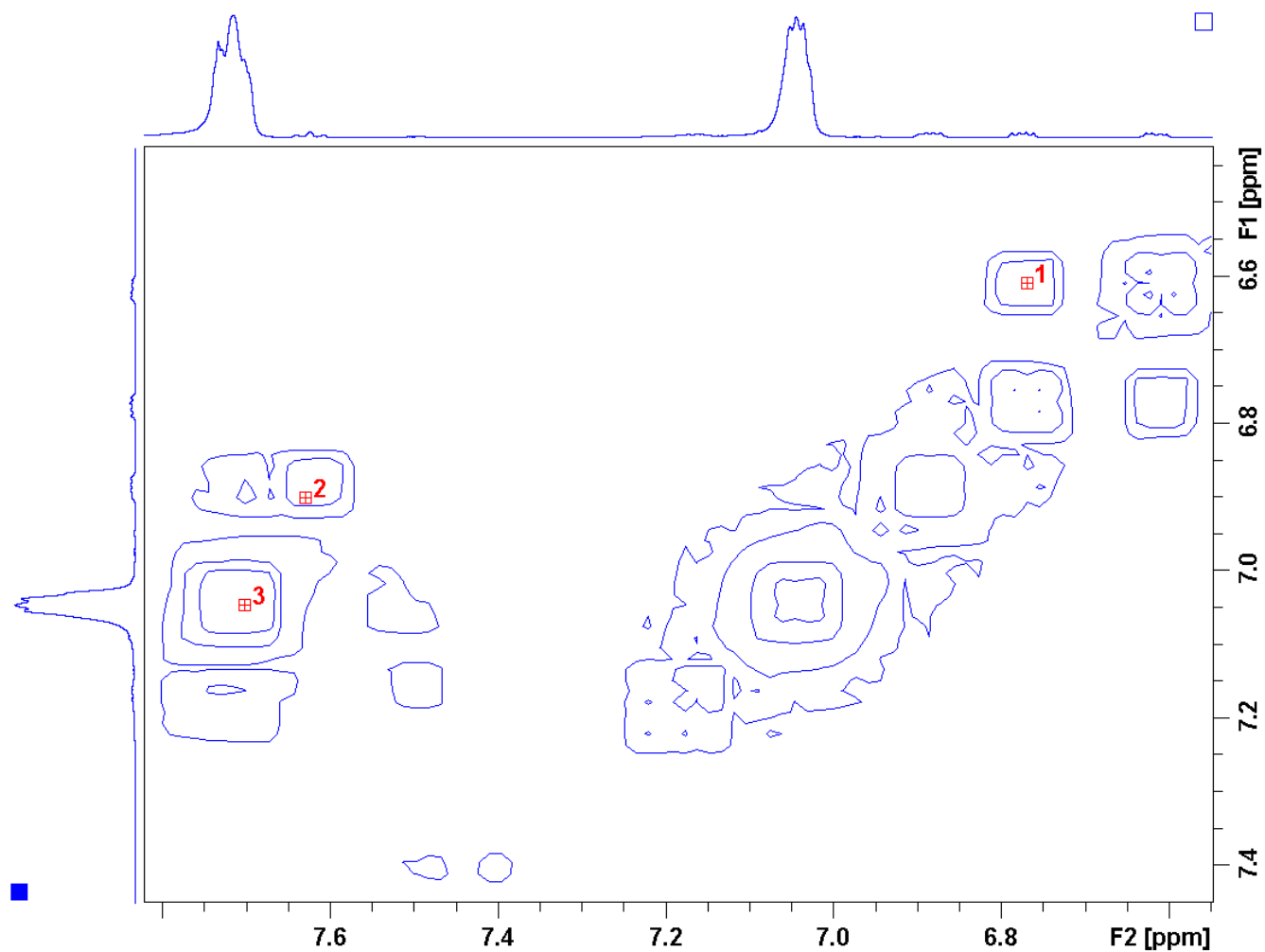


Figure 5.17:  $H^1 - H^1$  COSY spectrum of PMDA-ODA

## Protons and Carbons correlations

As complementary information, we also acquired carbon/protons correlations in order to fully characterise the polymer. This was done through HSQC and HMBC NMR measurements.

### HSQC $H^1/C^{13}$ NMR of PMDA-ODA

The HSQC experiment is used to determine proton-carbon single bond correlations. The data is presented as a 2D plot, where the protons lie along the horizontal F2 (X) axis and the carbons are along the vertical F1 (Y) axis. A  $J_1$  carbon proton correlation is marked by a cross peak on the plot. Thus HSQC will help us determine the peaks that are associated to the carbons directly attached to the protons  $H_1$  to  $H_5$  as seen in Figure 5.18.

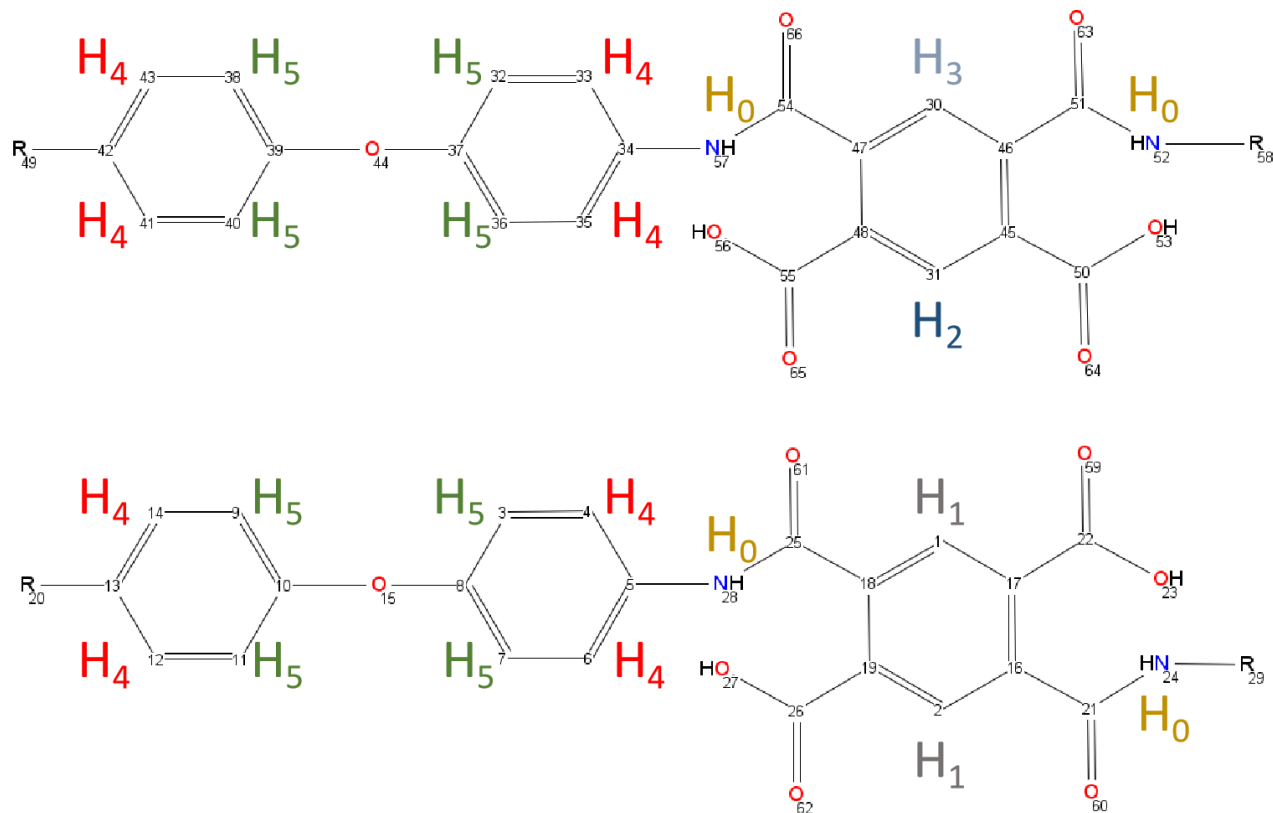


**Figure 5.18:** PMDA-ODA configurations, the meta-PMDA-ODA configuration, which will also be called isomer A (top) and the para-PMDA-ODA configuration, which will also be called isomer B (bottom). The hydrogen atoms are annotated ( $H_0 - > H_5$ ) and color coded depending on their electromagnetic equivalence. The atoms numbering (1 – > 64) refers to non hydrogen atoms such as carbon, oxygen and hydrogen.

In the acquired HSQC spectrum represented in Figure 5.19, we are able to easily attribute the carbons associated with the peaks 1 – 3, 5, and 6. These attributions are presented in table 5.3. The peaks 4 and 7 – 9 are those of terminal carbons and their corresponding protons.

**Table 5.3:** Carbon assignment according to HSQC correlation. Carbon annotation is done according to Figure 5.20.

Peak Number	$\nu(F2)[ppm]$	Proton	$\nu(F1)[ppm]$	Atom number as in Figure 5.18	Carbon annotation as in Figure 5.20
1	8.33	$H_3$	131.20	30	$C_5$
2	7.98	$H_1$	129.26	1, 2	$C_3$
3	7.73	$H_2$	127.97	31	$C_4$
5	7.71	$H_4$	121.82	33, 35, 43, 41, 4,6, 14, 12	$C_2$
6	7.05	$H_5$	119.23	32, 36, 38, 40, 3, 7, 9, 11	$C_1$

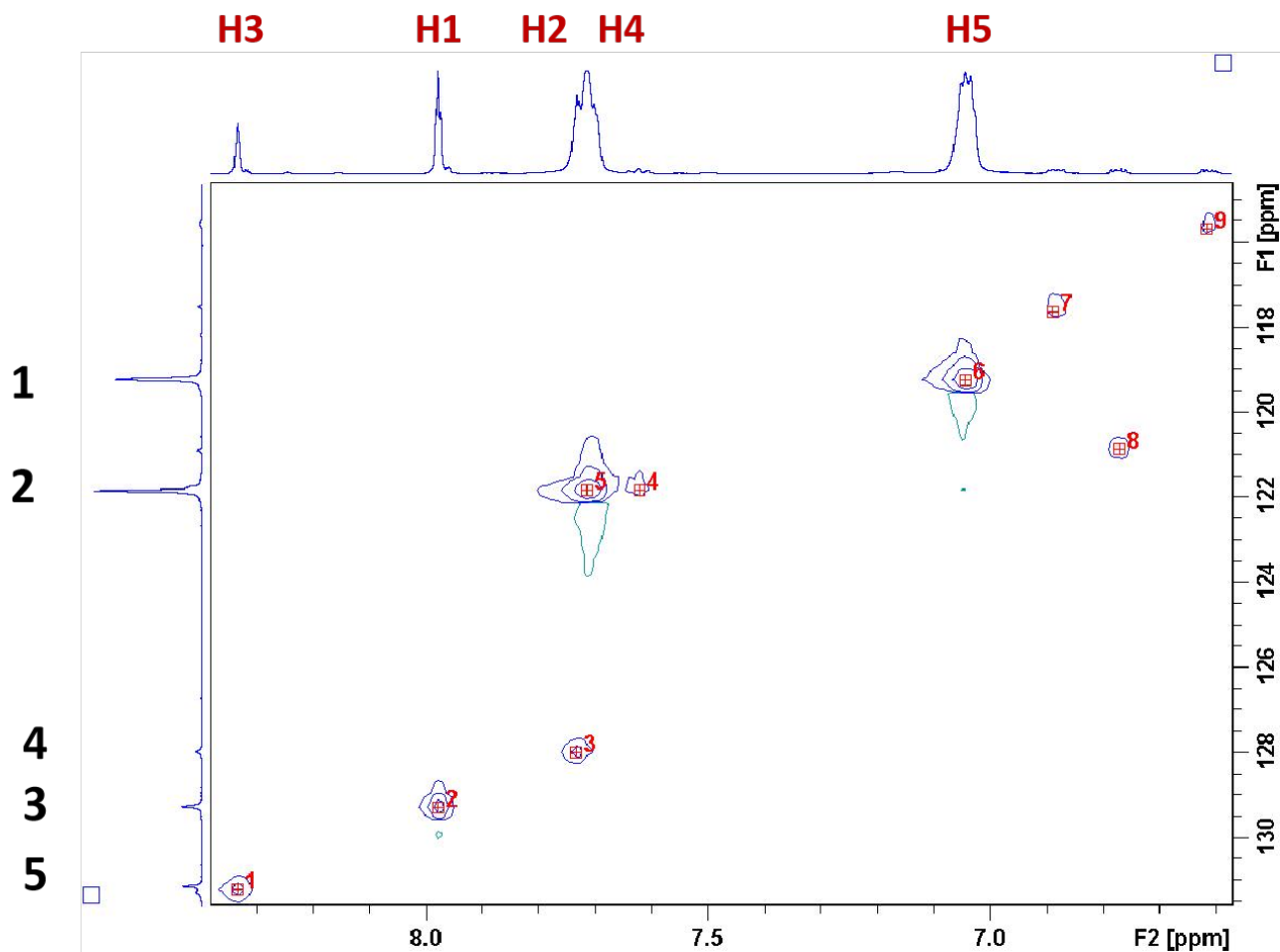


Figure 5.19: 2D HSQC NMR of PMDA-ODA. Protons on horizontal axis and carbons on the vertical one.

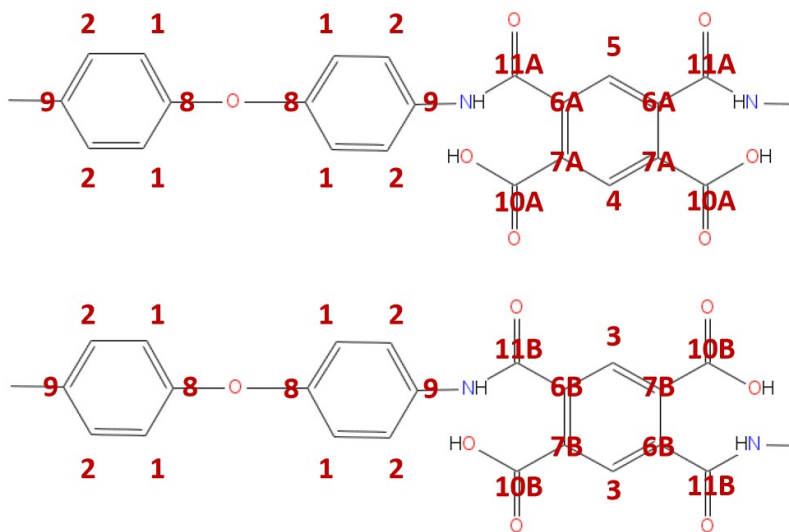
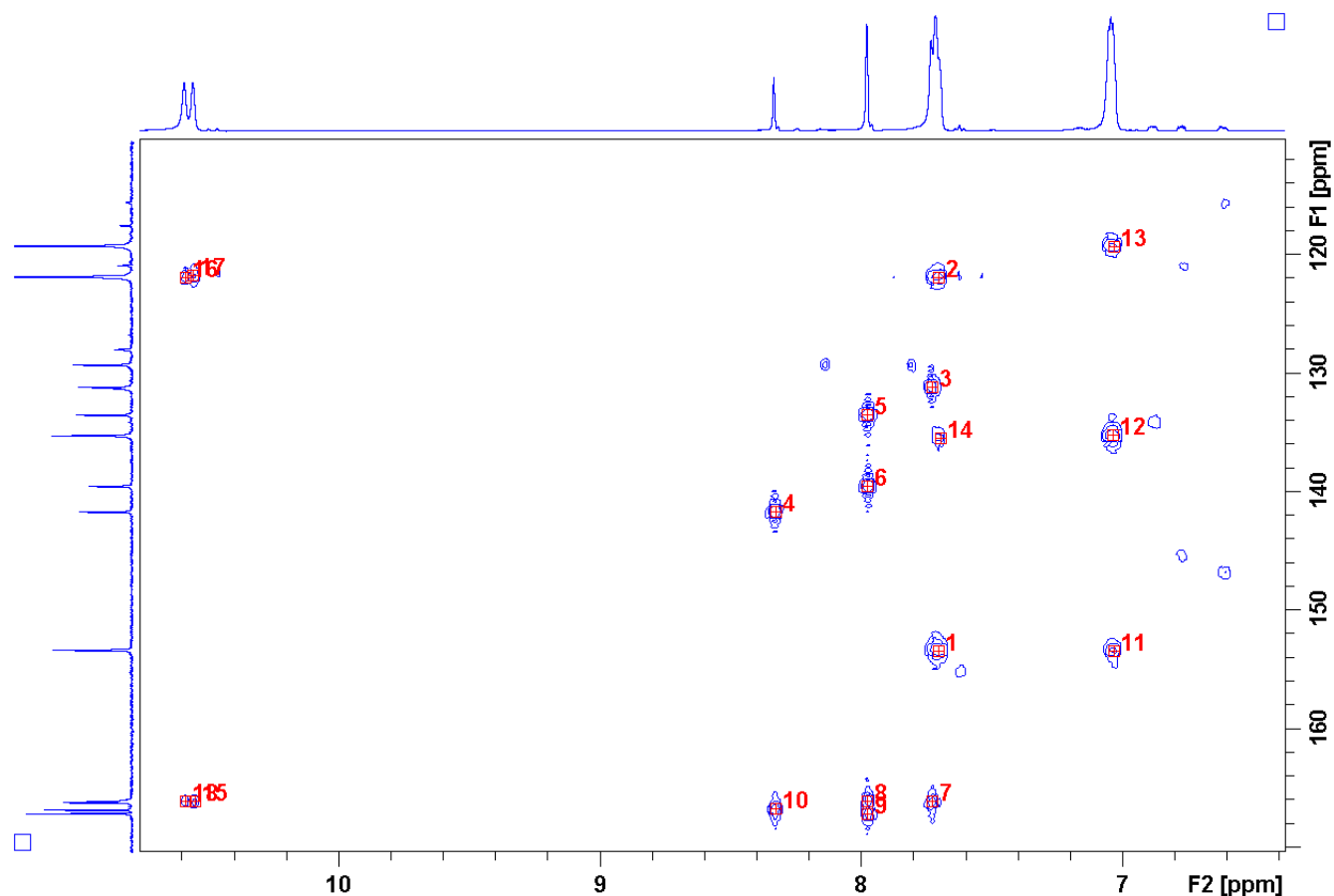


Figure 5.20: PMDA-ODA configurations, the isomer A (top) and isomer B (bottom). The Carbon atoms are annotated depending on their electromagnetic equivalence.

## HMBC $H^1/C^{13}$ NMR of PMDA-ODA

The HMBC experiment gives correlations between carbons and protons that are separated by two, or three bonds. Direct one-bond correlations are suppressed. The intensity of cross peaks depends on the coupling constant. HMBC will help in assigning the rest of the molecule carbons. The assignment will be done based on the correlation between the unknown carbons and the known protons. Given that the carbons in the carboxylic acid groups generate peaks located between 165 and 220 ppm [16], the four peaks between 166 and 168 ppm are those of carbons  $C_{10}$  and  $C_{11}$  of both isomers. Given that aromatic carbones generated peaks that are in the range of 120 – 140 ppm [16], the peaks between 131 and 142 ppm are those of carbons  $C_6$  and  $C_7$ .



**Figure 5.21:** 2D HMBC NMR of PMDA-ODA. Protons on horizontal axis and carbons on the vertical one.

**Table 5.4:** Carbon assignment according to HMBC correlation

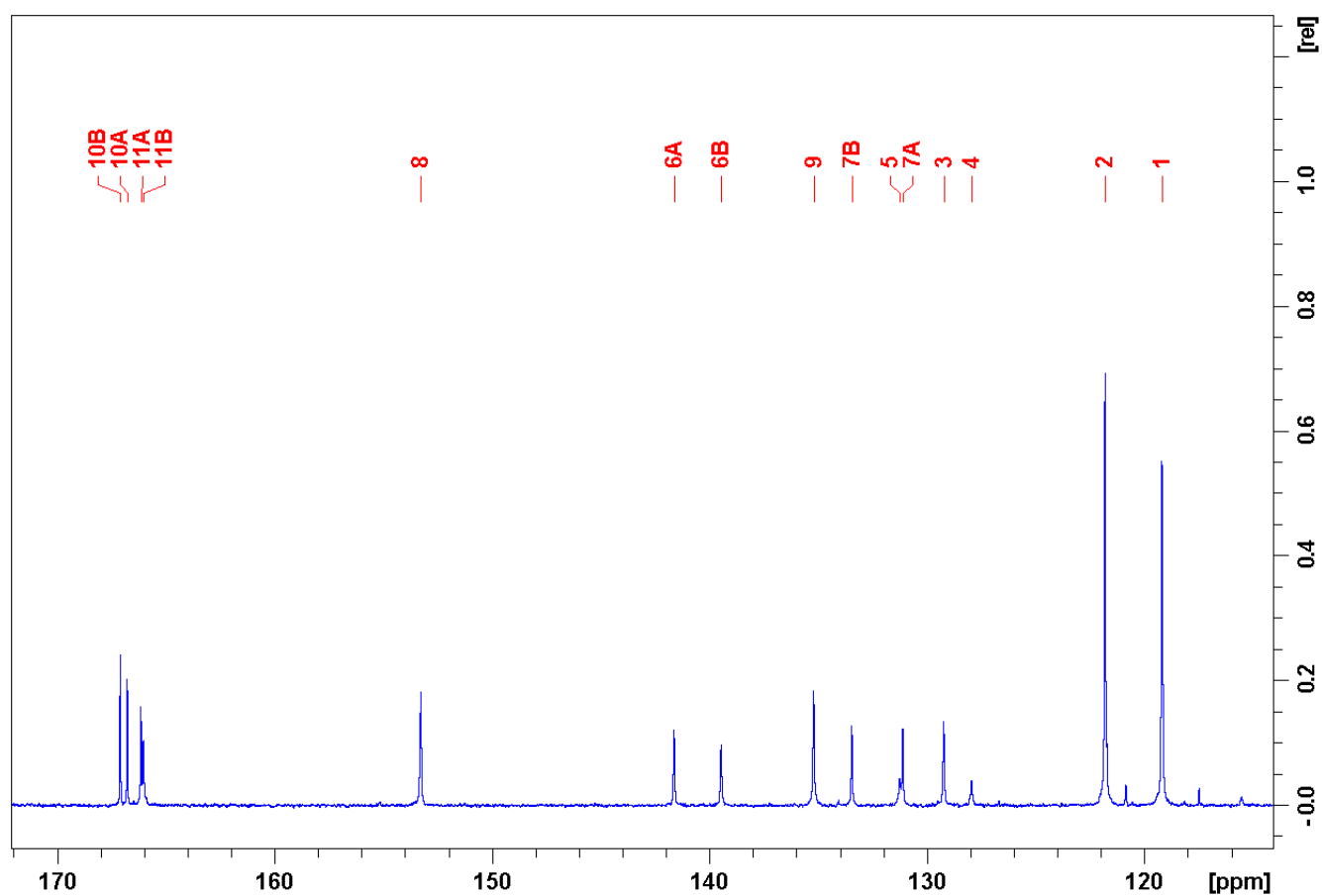
Peak number	$\mu(F2)[ppm]$	Proton	$\mu(F1)[ppm]$	Atom number	Carbon annotation
1	7.71	$H_4$	153.41	34, 42, 13, 5	$C_9$
2	7.71	$H_4$	121.88	33, 35, 43, 41, 4, 6, 14, 12	$C_2$
3	7.73	$H_2$	131.10	48, 45	$C_{7A}$
4	8.33	$H_3$	141.61	46, 47	$C_{6A}$
5	7.98	$H_1$	133.46	17, 19	$C_{7B}$
6	7.98	$H_1$	139.47	16, 18	$C_{6B}$
7	7.73	$H_2$	166.16	50, 55	$C_{11A}$
8	7.98	$H_1$	166.04	22, 26	$C_{11B}$
9	7.98	$H_1$	167.10	21, 25	$C_{10B}$
10	8.33	$H_3$	166.78	51, 54	$C_{10A}$
11	7.03	$H_5$	153.41	34, 42, 13, 5	$C_9$
12	7.03	$H_5$	135.18	8, 10, 37, 39	$C_8$
13	7.03	$H_5$	119.30	32, 36, 38, 40, 37, 9, 11	$C_1$
14	7.69	$H_4$	135.39	8, 10, 37, 39	$C_8$
15	10.55	$H_0$	166.16	51, 53 ou 21, 25	$C_{11A}$
16	10.58	$H_0$	121.88	33, 35, 43, 41, 4,6, 14, 12	$C_2$
17	10.56	$H_0$	121.66	33, 35, 43, 41, 4,6, 14, 12	$C_2$
18	10.58	$H_0$	166.07	51, 53 ou 21, 25	$C_{11B}$

## Carbon NMR spectrum

As a summary for the above HSQC and HMBC, we present the assignment of the molecules carbons for the NMR spectrum in Figure 5.22 and table 5.5. In the Figure and the table only the subscripts of the carbons are mentioned.

**Table 5.5:** Carbon NMR assignment

$\nu(F1)[ppm]$	Carbon annotation
119.20	1
121.81	2
127.94	4
129.23	3
131.11	7A
131.25	5
133.46	7B
135.22	9
139.47	6B
141.64	6A
153.27	8
166.04	11B
166.16	11A
166.78	10A
167.10	10B

**Figure 5.22:**  $C^{13}$  NMR spectrum of PMDA-ODA.



# Appendix D: The linewidth as a function of the dose for SU-8

A dose test was done to choose the optimal insulation parameter for SU-8 resist. It was performed in the same manner as it was done for MZ10-2.5 resist in Chapter 3. The results are presented in Figure 5.23. The beam used for the writing process has a  $10\mu\text{m}$  diameter. The linewidth shows a fair dependence on the square root of the dose even for low values of  $D$ .

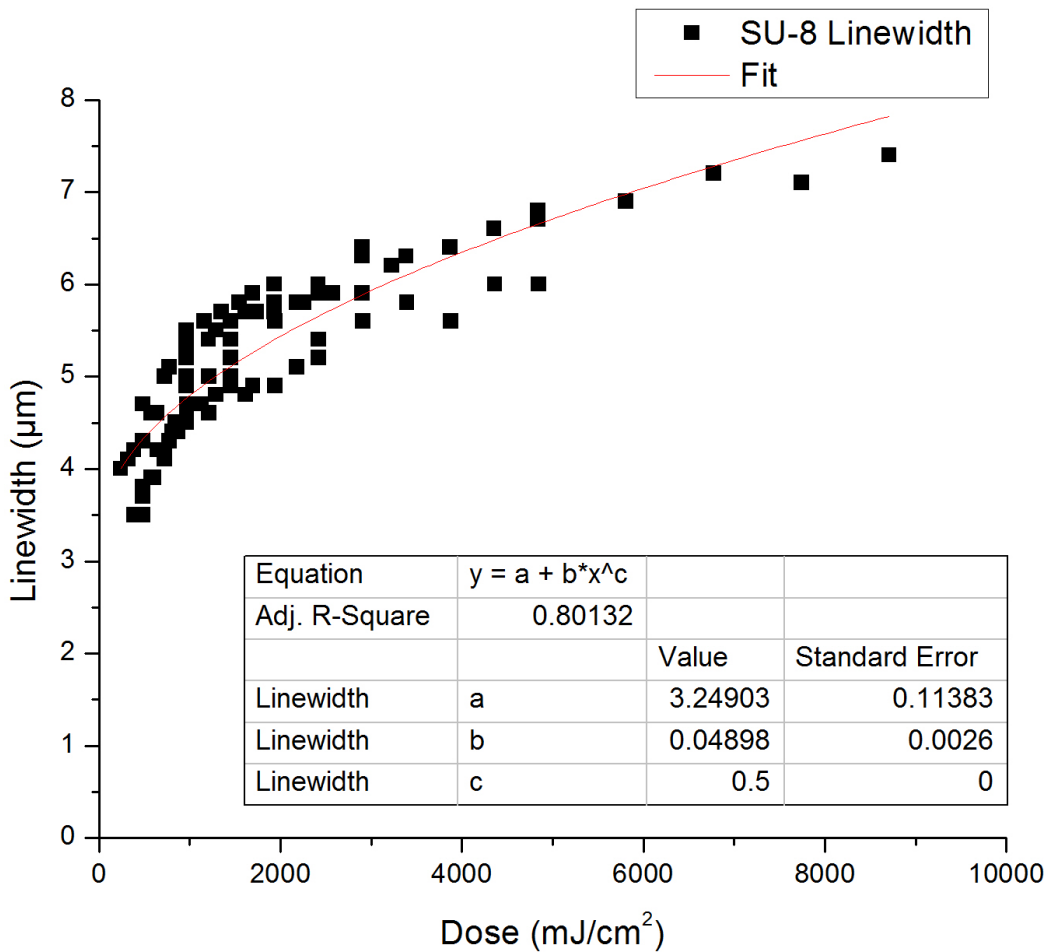


**Figure 5.23:** The cured linewidth as a function of the dose applied for SU-8.



# Bibliography

- [1] K. V. Sharp, “Liquid flows in microchannels,” *The MEMS handbook*, pp. 6–1, 2002.
- [2] S. C. Terry, J. H. Jerman, and J. B. Angell, “A gas chromatographic air analyzer fabricated on a silicon wafer,” *IEEE transactions on electron devices*, vol. 26, no. 12, pp. 1880–1886, 1979.
- [3] A. Manz, N. Graber, and H. á. Widmer, “Miniaturized total chemical analysis systems: a novel concept for chemical sensing,” *Sensors and actuators B: Chemical*, vol. 1, no. 1-6, pp. 244–248, 1990.
- [4] M. Koch, A. Evans, A. Brunnschweiler, A. Evans, and A. Brunnschweiler, *Microfluidic technology and applications*. Research Studies Press Baldock, 2000.
- [5] M. A. Unger, H.-P. Chou, T. Thorsen, A. Scherer, and S. R. Quake, “Monolithic micro-fabricated valves and pumps by multilayer soft lithography,” *Science*, vol. 288, no. 5463, pp. 113–116, 2000.
- [6] A. D. Stroock, S. K. Dertinger, A. Ajdari, I. Mezić, H. A. Stone, and G. M. Whitesides, “Chaotic mixer for microchannels,” *Science*, vol. 295, no. 5555, pp. 647–651, 2002.
- [7] J. C. McDonald, D. C. Duffy, J. R. Anderson, D. T. Chiu, H. Wu, O. J. Schueller, and G. M. Whitesides, “Fabrication of microfluidic systems in poly (dimethylsiloxane),” *ELECTROPHORESIS: An International Journal*, vol. 21, no. 1, pp. 27–40, 2000.
- [8] D. R. Stevens, C. J. Vrana, R. E. Dlin, and J. E. Korte, “A global review of hiv self-testing: themes and implications,” *AIDS and Behavior*, vol. 22, no. 2, pp. 497–512, 2018.
- [9] C. B. Hurt and K. A. Powers, “Self-testing for hiv and its impact on public health,” *Sexually transmitted diseases*, vol. 41, no. 1, p. 10, 2014.
- [10] A. Baghel, B. Singh, P. Pandey, and K. Sekhar, “A rapid field detection method for arsenic in drinking water,” *Analytical sciences*, vol. 23, no. 2, pp. 135–137, 2007.
- [11] A. Lace, D. Ryan, M. Bowkett, and J. Cleary, “Arsenic detection in water using microfluidic detection systems based on the leucomalachite green method,” *Analytical Methods*, vol. 11, no. 42, pp. 5431–5438, 2019.
- [12] C. Tymm, J. Zhou, A. Tadimety, A. Burklund, and J. X. Zhang, “Scalable covid-19 detection enabled by lab-on-chip biosensors,” *Cellular and Molecular Bioengineering*, vol. 13, no. 4, pp. 313–329, 2020.
- [13] A. R. Hawkins and H. Schmidt, *Handbook of optofluidics*. CRC Press, 2010.

- [14] Elveflow, “Ob1 mk3+ microfluidic flow controller.” <https://www.elveflow.com/microfluidic-products/microfluidics-flow-control-systems/ob1-pressure-controller/>, May 2021.
- [15] P. Kennedy, “Intel silicon photonics update at interconnect day 2019.” <https://www.servethehome.com/intel-silicon-photonics-update-at-interconnect-day-2019/>, May 2019.
- [16] D. R. Lide, *CRC handbook of chemistry and physics*, vol. 85. CRC press, 2004.
- [17] E. A. Marcatili, “Dielectric rectangular waveguide and directional coupler for integrated optics,” *Bell System Technical Journal*, vol. 48, no. 7, pp. 2071–2102, 1969.
- [18] J. Goell, “A circular-harmonic computer analysis of rectangular dielectric waveguides,” *Bell System Technical Journal*, vol. 48, no. 7, pp. 2133–2160, 1969.
- [19] R. Knox and P. Toullos, “Integrated circuits for the millimeter through optical frequency range,” in *Proc. Symp. Submillimeter Waves*, vol. 20, pp. 497–515, Brooklyn, NY, 1970.
- [20] K. Chiang, “Dual effective-index method for the analysis of rectangular dielectric waveguides,” *Applied optics*, vol. 25, no. 13, pp. 2169–2174, 1986.
- [21] K. Bierwirth, N. Schulz, and F. Arndt, “Finite-difference analysis of rectangular dielectric waveguide structures,” *IEEE Transactions on Microwave Theory and Techniques*, vol. 34, no. 11, pp. 1104–1114, 1986.
- [22] C. Yeh, S. Dong, and W. Oliver, “Arbitrarily shaped inhomogeneous optical fiber or integrated optical waveguides,” *Journal of Applied Physics*, vol. 46, no. 5, pp. 2125–2129, 1975.
- [23] C. Yeh, K. Ha, S. Dong, and W. Brown, “Single-mode optical waveguides,” *Applied Optics*, vol. 18, no. 10, pp. 1490–1504, 1979.
- [24] C. Yeh and F. Manshadi, “On weakly guiding single-mode optical waveguides,” *Journal of lightwave technology*, vol. 3, no. 1, pp. 199–205, 1985.
- [25] D. P. Hamilton, *Novel dispersion representation of rectangular dielectric guides with application to leaky-wave antennas*. PhD thesis, University of Warwick, 2007.
- [26] D. Lioubtchenko, S. Tretyakov, and S. Dudorov, “Dielectric waveguides: classical methods for propagation constant calculations,” *Millimeter-Wave Waveguides*, pp. 79–101, 2003.
- [27] P. Lecoy, *Fiber-Optic Communications*. John Wiley & Sons, 2013.
- [28] C. Pin, J.-B. Jager, M. Tardif, E. Picard, E. Hadji, F. de Fornel, and B. Cluzel, “Optical tweezing using tunable optical lattices along a few-mode silicon waveguide,” *Lab on a Chip*, vol. 18, no. 12, pp. 1750–1757, 2018.
- [29] G. Jin, S. Shi, A. Sharkawy, and D. W. Prather, “Polarization effects in tapered dielectric waveguides,” *Optics express*, vol. 11, no. 16, pp. 1931–1941, 2003.
- [30] E. Marcatili, “Bends in optical dielectric guides,” *Bell System Technical Journal*, vol. 48, no. 7, pp. 2103–2132, 1969.

- [31] Y. A. Vlasov and S. J. McNab, “Losses in single-mode silicon-on-insulator strip waveguides and bends,” *Optics express*, vol. 12, no. 8, pp. 1622–1631, 2004.
- [32] M. Kawachi, “Silica waveguides on silicon and their application to integrated-optic components,” *Optical and Quantum Electronics*, vol. 22, no. 5, pp. 391–416, 1990.
- [33] J. M. Ruano, A. Glidle, A. Cleary, A. Walmsley, J. S. Aitchison, and J. M. Cooper, “Design and fabrication of a silica on silicon integrated optical biochip as a fluorescence microarray platform,” *Biosensors and Bioelectronics*, vol. 18, no. 2-3, pp. 175–184, 2003.
- [34] B. E. Saleh and M. C. Teich, *Fundamentals of photonics*. John Wiley & sons, 2019.
- [35] M. W. Davidson, “Pioneers in optics: Giovanni battista amici and girolamo cardano,” *Microscopy Today*, vol. 18, no. 3, pp. 50–52, 2010.
- [36] A. Meschiari, “Schede tecniche e istruzioni per l’uso di 160 microscopi di giovanni battista amici,” *Atti Della Fondazione Giorgio Ronchi Anno LVII N. 5*, p. 795, 1857.
- [37] K. Tomimatsu, “Fluid immersion microscope objective lens,” Sept. 8 1998. US Patent 5,805,346.
- [38] B. K. Gibson, “Liquid mirror telescopes-history,” *Journal of the Royal Astronomical Society of Canada*, vol. 85, p. 158, 1991.
- [39] F. P. Schäfer, “1. principles of dye laser operation,” in *Dye lasers*, pp. 1–89, Springer, 1973.
- [40] D. Erickson, T. Rockwood, T. Emery, A. Scherer, and D. Psaltis, “Nanofluidic tuning of photonic crystal circuits,” *Optics letters*, vol. 31, no. 1, pp. 59–61, 2006.
- [41] Z. Li, Z. Zhang, A. Scherer, and D. Psaltis, “Mechanically tunable optofluidic distributed feedback dye laser,” *Optics express*, vol. 14, no. 22, pp. 10494–10499, 2006.
- [42] S. I. Shopova, H. Zhou, X. Fan, and P. Zhang, “Optofluidic ring resonator based dye laser,” *Applied physics letters*, vol. 90, no. 22, p. 221101, 2007.
- [43] K. De Vos, I. Bartolozzi, E. Schacht, P. Bienstman, and R. Baets, “Silicon-on-insulator microring resonator for sensitive and label-free biosensing,” *Optics express*, vol. 15, no. 12, pp. 7610–7615, 2007.
- [44] S. Mandal and D. Erickson, “Optofluidic transport in liquid core waveguiding structures,” *Applied physics letters*, vol. 90, no. 18, p. 184103, 2007.
- [45] A. Ashkin, “Acceleration and trapping of particles by radiation pressure,” *Physical review letters*, vol. 24, no. 4, p. 156, 1970.
- [46] A. Ashkin, “Atomic-beam deflection by resonance-radiation pressure,” *Physical Review Letters*, vol. 25, no. 19, p. 1321, 1970.
- [47] D. Psaltis, S. R. Quake, and C. Yang, “Developing optofluidic technology through the fusion of microfluidics and optics,” *nature*, vol. 442, no. 7101, p. 381, 2006.
- [48] C. Monat, P. Domachuk, and B. Eggleton, “Integrated optofluidics: A new river of light,” *Nature photonics*, vol. 1, no. 2, p. 106, 2007.

- [49] K. Jo, Y.-L. Chen, J. J. de Pablo, and D. C. Schwartz, "Elongation and migration of single dna molecules in microchannels using oscillatory shear flows," *Lab on a Chip*, vol. 9, no. 16, pp. 2348–2355, 2009.
- [50] B. S. Ahluwalia, P. McCourt, A. Oteiza, J. S. Wilkinson, T. R. Huser, and O. G. Hellesø, "Squeezing red blood cells on an optical waveguide to monitor cell deformability during blood storage," *Analyst*, vol. 140, no. 1, pp. 223–229, 2015.
- [51] A. van de Stolpe, K. Pantel, S. Sleijfer, L. W. Terstappen, and J. M. Den Toonder, "Circulating tumor cell isolation and diagnostics: toward routine clinical use," 2011.
- [52] X. Cheng, D. Irimia, M. Dixon, K. Sekine, U. Demirci, L. Zamir, R. G. Tompkins, W. Rodriguez, and M. Toner, "A microfluidic device for practical label-free cd4+ t cell counting of hiv-infected subjects," *Lab on a Chip*, vol. 7, no. 2, pp. 170–178, 2007.
- [53] S. L. Neale, M. P. MacDonald, K. Dholakia, and T. F. Krauss, "All-optical control of microfluidic components using form birefringence," *Nature materials*, vol. 4, no. 7, p. 530, 2005.
- [54] E. Biddiss, D. Erickson, and D. Li, "Heterogeneous surface charge enhanced micromixing for electrokinetic flows," *Analytical Chemistry*, vol. 76, no. 11, pp. 3208–3213, 2004.
- [55] P.-H. Huang, Y. Xie, D. Ahmed, J. Rufo, N. Nama, Y. Chen, C. Y. Chan, and T. J. Huang, "An acoustofluidic micromixer based on oscillating sidewall sharp-edges," *Lab on a Chip*, vol. 13, no. 19, pp. 3847–3852, 2013.
- [56] M. Kumemura, D. Collard, C. Yamahata, N. Sakaki, G. Hashiguchi, and H. Fujita, "Single dna molecule isolation and trapping in a microfluidic device," *ChemPhysChem*, vol. 8, no. 12, pp. 1875–1880, 2007.
- [57] M. M. Wang, E. Tu, D. E. Raymond, J. M. Yang, H. Zhang, N. Hagen, B. Dees, E. M. Mercer, A. H. Forster, I. Kariv, *et al.*, "Microfluidic sorting of mammalian cells by optical force switching," *Nature biotechnology*, vol. 23, no. 1, pp. 83–87, 2005.
- [58] A. Ozcelik, J. Rufo, F. Guo, Y. Gu, P. Li, J. Lata, and T. J. Huang, "Acoustic tweezers for the life sciences," *Nature methods*, vol. 15, no. 12, pp. 1021–1028, 2018.
- [59] L. R. Huang, J. O. Tegenfeldt, J. J. Kraeft, J. C. Sturm, R. H. Austin, and E. C. Cox, "A dna prism for high-speed continuous fractionation of large dna molecules," *Nature Biotechnology*, vol. 20, no. 10, pp. 1048–1051, 2002.
- [60] A. Rosenthal and J. Voldman, "Dielectrophoretic traps for single-particle patterning," *Biophysical journal*, vol. 88, no. 3, pp. 2193–2205, 2005.
- [61] A. Ashkin, J. M. Dziedzic, J. Bjorkholm, and S. Chu, "Observation of a single-beam gradient force optical trap for dielectric particles," *Optics letters*, vol. 11, no. 5, pp. 288–290, 1986.
- [62] T. Hatano, T. Kaneta, and T. Imasaka, "Application of optical chromatography to immunoassay," *Analytical chemistry*, vol. 69, no. 14, pp. 2711–2715, 1997.
- [63] T. Imasaka, "Optical chromatography. a new tool for separation of particles," *Analisis*, vol. 26, no. 5, pp. 53–53, 1998.

- [64] A. Terray, J. Arnold, and S. Hart, “Enhanced optical chromatography in a pdms microfluidic system,” *Optics Express*, vol. 13, no. 25, pp. 10406–10415, 2005.
- [65] A. Casner and J.-P. Delville, “Giant deformations of a liquid-liquid interface induced by the optical radiation pressure,” *Physical review letters*, vol. 87, no. 5, p. 054503, 2001.
- [66] A. Casner and J.-P. Delville, “Laser-induced hydrodynamic instability of fluid interfaces,” *Physical review letters*, vol. 90, no. 14, p. 144503, 2003.
- [67] A. Casner and J.-P. Delville, “Laser-sustained liquid bridges,” *EPL (Europhysics Letters)*, vol. 65, no. 3, p. 337, 2004.
- [68] A. Vogel, S. Busch, and U. Parlitz, “Shock wave emission and cavitation bubble generation by picosecond and nanosecond optical breakdown in water,” *The Journal of the Acoustical Society of America*, vol. 100, no. 1, pp. 148–165, 1996.
- [69] Z. Li, K. Ando, J. Yu, A. Liu, J. Zhang, and C. Ohl, “Fast on-demand droplet fusion using transient cavitation bubbles,” *Lab on a Chip*, vol. 11, no. 11, pp. 1879–1885, 2011.
- [70] Y. Chen, A. J. Chung, T.-H. Wu, M. A. Teitell, D. Di Carlo, and P.-Y. Chiou, “Pulsed laser activated cell sorting with three dimensional sheathless inertial focusing,” *Small*, vol. 10, no. 9, pp. 1746–1751, 2014.
- [71] P. N. Prasad, *Nanophotonics*. John Wiley & Sons, 2004.
- [72] S. Kawata, M. Ohtsu, and M. Irie, *Near-field optics and surface plasmon polaritons*, vol. 81. Springer Science & Business Media, 2001.
- [73] W. M. Irvine, “Light scattering by spherical particles: radiation pressure, asymmetry factor, and extinction cross section,” *JOSA*, vol. 55, no. 1, pp. 16–21, 1965.
- [74] A. Ashkin, “Forces of a single-beam gradient laser trap on a dielectric sphere in the ray optics regime,” *Biophysical journal*, vol. 61, no. 2, pp. 569–582, 1992.
- [75] W. Wright, G. Sonek, and M. Berns, “Radiation trapping forces on microspheres with optical tweezers,” *Applied Physics Letters*, vol. 63, no. 6, pp. 715–717, 1993.
- [76] L. N. Ng, B. J. Luff, M. N. Zervas, and J. S. Wilkinson, “Forces on a rayleigh particle in the cover region of a planar waveguide,” *Journal of lightwave technology*, vol. 18, no. 3, pp. 388–400, 2000.
- [77] L. Ng, B. Luff, M. Zervas, and J. Wilkinson, “Propulsion of gold nanoparticles on optical waveguides,” *Optics Communications*, vol. 208, no. 1-3, pp. 117–124, 2002.
- [78] G. Roosen, “La levitation optique de spheres,” *Canadian Journal of Physics*, vol. 57, no. 9, pp. 1260–1279, 1979.
- [79] E. Almaas and I. Brevik, “Radiation forces on a micrometer-sized sphere in an evanescent field,” *JOSA B*, vol. 12, no. 12, pp. 2429–2438, 1995.
- [80] J. Y. Walz, “Ray optics calculation of the radiation forces exerted on a dielectric sphere in an evanescent field,” *Applied optics*, vol. 38, no. 25, pp. 5319–5330, 1999.

- [81] Ø. I. Helle, B. S. Ahluwalia, and O. G. Hellesø, “Optical transport, lifting and trapping of micro-particles by planar waveguides,” *Optics express*, vol. 23, no. 5, pp. 6601–6612, 2015.
- [82] H. Y. Jaising and O. G. Hellesø, “Radiation forces on a mie particle in the evanescent field of an optical waveguide,” *Optics communications*, vol. 246, no. 4-6, pp. 373–383, 2005.
- [83] O. G. Hellesø, “Optical pressure and numerical simulation of optical forces,” *Applied optics*, vol. 56, no. 12, pp. 3354–3358, 2017.
- [84] S. Kawata and T. Sugiura, “Movement of micrometer-sized particles in the evanescent field of a laser beam,” *Optics letters*, vol. 17, no. 11, pp. 772–774, 1992.
- [85] S. Kawata and T. Tani, “Optically driven mie particles in an evanescent field along a channeled waveguide,” *Optics letters*, vol. 21, no. 21, pp. 1768–1770, 1996.
- [86] C. Bradac, “Nanoscale optical trapping: a review,” *Advanced Optical Materials*, vol. 6, no. 12, p. 1800005, 2018.
- [87] S. Gaugiran, S. Gétin, J.-M. Fedeli, G. Colas, A. Fuchs, F. Chatelain, and J. Dérourard, “Optical manipulation of microparticles and cells on silicon nitride waveguides,” *Optics Express*, vol. 13, no. 18, pp. 6956–6963, 2005.
- [88] V. R. Almeida, Q. Xu, C. A. Barrios, and M. Lipson, “Guiding and confining light in void nanostructure,” *Optics letters*, vol. 29, no. 11, pp. 1209–1211, 2004.
- [89] A. H. Yang, S. D. Moore, B. S. Schmidt, M. Klug, M. Lipson, and D. Erickson, “Optical manipulation of nanoparticles and biomolecules in sub-wavelength slot waveguides,” *Nature*, vol. 457, no. 7225, pp. 71–75, 2009.
- [90] A. H. Yang, T. Lerdsuchatawanich, and D. Erickson, “Forces and transport velocities for a particle in a slot waveguide,” *Nano letters*, vol. 9, no. 3, pp. 1182–1188, 2009.
- [91] B. S. Schmidt, A. H. Yang, D. Erickson, and M. Lipson, “Optofluidic trapping and transport on solid core waveguides within a microfluidic device,” *Optics Express*, vol. 15, no. 22, pp. 14322–14334, 2007.
- [92] K. Grujic, O. G. Hellesø, J. P. Hole, and J. S. Wilkinson, “Sorting of polystyrene microspheres using a y-branched optical waveguide,” *Optics Express*, vol. 13, no. 1, pp. 1–7, 2005.
- [93] D. Erickson, X. Serey, Y.-F. Chen, and S. Mandal, “Nanomanipulation using near field photonics,” *Lab on a Chip*, vol. 11, no. 6, pp. 995–1009, 2011.
- [94] X. Zhao, N. Zhao, Y. Shi, H. Xin, and B. Li, “Optical fiber tweezers: A versatile tool for optical trapping and manipulation,” *Micromachines*, vol. 11, no. 2, p. 114, 2020.
- [95] S. Mandal, X. Serey, and D. Erickson, “Nanomanipulation using silicon photonic crystal resonators,” *Nano letters*, vol. 10, no. 1, pp. 99–104, 2010.
- [96] R. Quidant and C. Girard, “Surface-plasmon-based optical manipulation,” *Laser & Photonics Reviews*, vol. 2, no. 1-2, pp. 47–57, 2008.

- [97] M. Righini, G. Volpe, C. Girard, D. Petrov, and R. Quidant, “Surface plasmon optical tweezers: tunable optical manipulation in the femtonewton range,” *Physical review letters*, vol. 100, no. 18, p. 186804, 2008.
- [98] M. Soltani, J. Lin, R. A. Forties, J. T. Inman, S. N. Saraf, R. M. Fulbright, M. Lipson, and M. D. Wang, “Nanophotonic trapping for precise manipulation of biomolecular arrays,” *Nature nanotechnology*, vol. 9, no. 6, p. 448, 2014.
- [99] N. Bellini, K. Vishnubhatla, F. Bragheri, L. Ferrara, P. Minzioni, R. Ramponi, I. Cristiani, and R. Osellame, “Femtosecond laser fabricated monolithic chip for optical trapping and stretching of single cells,” *Optics Express*, vol. 18, no. 5, pp. 4679–4688, 2010.
- [100] S. Arnold, D. Keng, S. Shopova, S. Holler, W. Zurawsky, and F. Vollmer, “Whispering gallery mode carousel—a photonic mechanism for enhanced nanoparticle detection in biosensing,” *Optics Express*, vol. 17, no. 8, pp. 6230–6238, 2009.
- [101] C. Pin, C. Renaut, M. Tardif, J.-B. Jager, E. Delamadeleine, E. Picard, D. Peyrade, E. Hadji, F. de Fornel, and B. Cluzel, “On-chip photonic tweezers for photonics, microfluidics, and biology,” in *Optical Manipulation Conference*, vol. 10252, p. 1025212, International Society for Optics and Photonics, 2017.
- [102] O. G. Hellesø, P. Løvhaugen, A. Z. Subramanian, J. S. Wilkinson, and B. S. Ahluwalia, “Surface transport and stable trapping of particles and cells by an optical waveguide loop,” *Lab on a Chip*, vol. 12, no. 18, pp. 3436–3440, 2012.
- [103] L. Novotny, R. X. Bian, and X. S. Xie, “Theory of nanometric optical tweezers,” *Physical Review Letters*, vol. 79, no. 4, p. 645, 1997.
- [104] M. Righini, A. S. Zelenina, C. Girard, and R. Quidant, “Parallel and selective trapping in a patterned plasmonic landscape,” *Nature Physics*, vol. 3, no. 7, pp. 477–480, 2007.
- [105] A. Grigorenko, N. Roberts, M. Dickinson, and Y. Zhang, “Nanometric optical tweezers based on nanostructured substrates,” *Nature Photonics*, vol. 2, no. 6, pp. 365–370, 2008.
- [106] W. Zhang, L. Huang, C. Santschi, and O. J. Martin, “Trapping and sensing 10 nm metal nanoparticles using plasmonic dipole antennas,” *Nano letters*, vol. 10, no. 3, pp. 1006–1011, 2010.
- [107] K. Wang, E. Schonbrun, P. Steinvurzel, and K. B. Crozier, “Trapping and rotating nanoparticles using a plasmonic nano-tweezer with an integrated heat sink,” *Nature communications*, vol. 2, no. 1, pp. 1–6, 2011.
- [108] D. Yoo, K. L. Gurunatha, H.-K. Choi, D. A. Mohr, C. T. Ertsgaard, R. Gordon, and S.-H. Oh, “Low-power optical trapping of nanoparticles and proteins with resonant coaxial nanoaperture using 10 nm gap,” *Nano letters*, vol. 18, no. 6, pp. 3637–3642, 2018.
- [109] J.-H. Kang, K. Kim, H.-S. Ee, Y.-H. Lee, T.-Y. Yoon, M.-K. Seo, and H.-G. Park, “Low-power nano-optical vortex trapping via plasmonic diabolite nanoantennas,” *Nature communications*, vol. 2, no. 1, pp. 1–6, 2011.

- [110] A. Ivinskaya, M. I. Petrov, A. A. Bogdanov, I. Shishkin, P. Ginzburg, and A. S. Shalin, “Plasmon-assisted optical trapping and anti-trapping,” *Light: Science & Applications*, vol. 6, no. 5, pp. e16258–e16258, 2017.
- [111] J. Guck, R. Ananthakrishnan, T. Moon, C. Cunningham, and J. Käs, “Optical deformability of soft biological dielectrics,” *Physical review letters*, vol. 84, no. 23, p. 5451, 2000.
- [112] J. Guck, R. Ananthakrishnan, H. Mahmood, T. J. Moon, C. C. Cunningham, and J. Käs, “The optical stretcher: a novel laser tool to micromanipulate cells,” *Biophysical journal*, vol. 81, no. 2, pp. 767–784, 2001.
- [113] J. Guck, S. Schinkinger, B. Lincoln, F. Wottawah, S. Ebert, M. Romeyke, D. Lenz, H. M. Erickson, R. Ananthakrishnan, D. Mitchell, *et al.*, “Optical deformability as an inherent cell marker for testing malignant transformation and metastatic competence,” *Biophysical journal*, vol. 88, no. 5, pp. 3689–3698, 2005.
- [114] I. Sraj, C. D. Eggleton, R. Jimenez, E. E. Hoover, J. A. Squier, J. Chichester, and D. W. Marr, “Cell deformation cytometry using diode-bar optical stretchers,” *Journal of biomedical optics*, vol. 15, no. 4, p. 047010, 2010.
- [115] S. Henon, G. Lenormand, A. Richert, and F. Gallet, “A new determination of the shear modulus of the human erythrocyte membrane using optical tweezers,” *Biophysical journal*, vol. 76, no. 2, pp. 1145–1151, 1999.
- [116] J. Sleep, D. Wilson, R. Simmons, and W. Gratzer, “Elasticity of the red cell membrane and its relation to hemolytic disorders: an optical tweezers study,” *Biophysical journal*, vol. 77, no. 6, pp. 3085–3095, 1999.
- [117] M. Dao, C. T. Lim, and S. Suresh, “Mechanics of the human red blood cell deformed by optical tweezers,” *Journal of the Mechanics and Physics of Solids*, vol. 51, no. 11-12, pp. 2259–2280, 2003.
- [118] R. Martinez Vazquez, G. Nava, M. Vegliione, T. Yang, F. Bragheri, P. Minzioni, E. Bianchi, M. Di Tano, I. Chiodi, R. Osellame, *et al.*, “An optofluidic constriction chip for monitoring metastatic potential and drug response of cancer cells,” *Integrative Biology*, vol. 7, no. 4, pp. 477–484, 2015.
- [119] N. Bellini, F. Bragheri, I. Cristiani, J. Guck, R. Osellame, and G. Whyte, “Validation and perspectives of a femtosecond laser fabricated monolithic optical stretcher,” *Biomedical optics express*, vol. 3, no. 10, pp. 2658–2668, 2012.
- [120] R. W. Applegate, J. Squier, T. Vestad, J. Oakey, and D. W. Marr, “Optical trapping, manipulation, and sorting of cells and colloids in microfluidic systems with diode laser bars,” *Optics express*, vol. 12, no. 19, pp. 4390–4398, 2004.
- [121] B. S. Ahluwalia, P. McCourt, T. Huser, and O. G. Hellesø, “Optical trapping and propulsion of red blood cells on waveguide surfaces,” *Optics Express*, vol. 18, no. 20, pp. 21053–21061, 2010.
- [122] G. Testa, G. Persichetti, P. M. Sarro, and R. Bernini, “A hybrid silicon-pdms optofluidic platform for sensing applications,” *Biomedical optics express*, vol. 5, no. 2, pp. 417–426, 2014.

- [123] J. W. Parks, H. Cai, L. Zempoaltecatl, T. D. Yuzvinsky, K. Leake, A. R. Hawkins, and H. Schmidt, "Hybrid optofluidic integration," *Lab on a Chip*, vol. 13, no. 20, pp. 4118–4123, 2013.
- [124] T. Wall, J. McMurray, G. Meena, V. Ganjalizadeh, H. Schmidt, and A. R. Hawkins, "Optofluidic lab-on-a-chip fluorescence sensor using integrated buried arrow (barrow) waveguides," *Micromachines*, vol. 8, no. 8, p. 252, 2017.
- [125] R. Osellame, H. J. Hoekstra, G. Cerullo, and M. Pollnau, "Femtosecond laser microstructuring: an enabling tool for optofluidic lab-on-chips," *Laser & Photonics Reviews*, vol. 5, no. 3, pp. 442–463, 2011.
- [126] G. Bettella, R. Zamboni, G. Pozza, A. Zaltron, C. Montevecchi, M. Pierno, G. Mistura, C. Sada, L. Gauthier-Manuel, and M. Chauvet, "Linbo3 integrated system for opto-microfluidic sensing," *Sensors and Actuators B: Chemical*, vol. 282, pp. 391–398, 2019.
- [127] Y. Özbakır, A. Jonas, A. Kiraz, and C. Erkey, "Aerogels for optofluidic waveguides," *Micro-machines*, vol. 8, no. 4, p. 98, 2017.
- [128] K. B. Mogensen, P. Friis, J. Hübner, N. Petersen, A. M. Jørgensen, P. Telleman, and J. P. Kutter, "Ultraviolet transparent silicon oxynitride waveguides for biochemical microsystems," *Optics letters*, vol. 26, no. 10, pp. 716–718, 2001.
- [129] E. Shkondin, O. Takayama, M. A. Panah, P. Liu, P. V. Larsen, M. D. Mar, F. Jensen, and A. Lavrinenko, "Large-scale high aspect ratio al-doped zno nanopillars arrays as anisotropic metamaterials," *Optical Materials Express*, vol. 7, no. 5, pp. 1606–1627, 2017.
- [130] S. K. Selvaraja, D. Vermeulen, M. Schaeckers, E. Sleenckx, W. Bogaerts, G. Roelkens, P. Dumon, D. Van Thourhout, and R. Baets, "Highly efficient grating coupler between optical fiber and silicon photonic circuit," in *2009 Conference on Lasers and Electro-Optics and 2009 Conference on Quantum electronics and Laser Science Conference*, pp. 1–2, IEEE, 2009.
- [131] M. Soltani, J. T. Inman, M. Lipson, and M. D. Wang, "Electro-optofluidics: achieving dynamic control on-chip," *Optics express*, vol. 20, no. 20, pp. 22314–22326, 2012.
- [132] W. Bogaerts, P. Dumon, D. Taillaert, V. Wiaux, S. Beckx, B. Luyssaert, J. Van Campenhout, D. Van Thourhout, and R. Baets, "Soi nanophotonic waveguide structures fabricated with deep uv lithography," *Photonics and Nanostructures-Fundamentals and Applications*, vol. 2, no. 2, pp. 81–86, 2004.
- [133] H. Cai and A. W. Poon, "Optical trapping of microparticles using silicon nitride waveguide junctions and tapered-waveguide junctions on an optofluidic chip," *Lab on a chip*, vol. 12, no. 19, pp. 3803–3809, 2012.
- [134] K. B. Mogensen, N. J. Petersen, J. Hübner, and J. P. Kutter, "Monolithic integration of optical waveguides for absorbance detection in microfabricated electrophoresis devices," *Electrophoresis*, vol. 22, no. 18, pp. 3930–3938, 2001.
- [135] N. J. Petersen, K. B. Mogensen, and J. P. Kutter, "Performance of an in-plane detection cell with integrated waveguides for uv/vis absorbance measurements on microfluidic separation devices," *Electrophoresis*, vol. 23, no. 20, pp. 3528–3536, 2002.

- [136] B. S. Ahluwalia, A. Z. Subramanian, O. G. Hellso, N. M. Perney, N. P. Sessions, and J. S. Wilkinson, "Fabrication of submicrometer high refractive index tantalum pentoxide waveguides for optical propulsion of microparticles," *IEEE Photonics Technology Letters*, vol. 21, no. 19, pp. 1408–1410, 2009.
- [137] K. Grujic, O. G. Hellesø, J. S. Wilkinson, and J. P. Hole, "Optical propulsion of microspheres along a channel waveguide produced by cs<sup>+</sup> ion-exchange in glass," *Optics Communications*, vol. 239, no. 4-6, pp. 227–235, 2004.
- [138] K. B. Mogensen and J. P. Kutter, "Optical detection in microfluidic systems," *Electrophoresis*, vol. 30, no. S1, pp. S92–S100, 2009.
- [139] R. Mazurczyk, J. Vieillard, A. Bouchard, B. Hannes, and S. Krawczyk, "A novel concept of the integrated fluorescence detection system and its application in a lab-on-a-chip microdevice," *Sensors and Actuators B: Chemical*, vol. 118, no. 1-2, pp. 11–19, 2006.
- [140] K. Miura, H. Inouye, J. Qiu, T. Mitsuyu, and K. Hirao, "Optical waveguides induced in inorganic glasses by a femtosecond laser," *Nuclear Instruments and Methods in Physics Research Section B: Beam interactions with materials and atoms*, vol. 141, no. 1-4, pp. 726–732, 1998.
- [141] K. M. Davis, K. Miura, N. Sugimoto, and K. Hirao, "Writing waveguides in glass with a femtosecond laser," *Optics letters*, vol. 21, no. 21, pp. 1729–1731, 1996.
- [142] R. Taylor, C. Hnatovsky, and E. Simova, "Applications of femtosecond laser induced self-organized planar nanocracks inside fused silica glass," *Laser & Photonics Reviews*, vol. 2, no. 1-2, pp. 26–46, 2008.
- [143] R. Osellame, V. Maselli, R. M. Vazquez, R. Ramponi, and G. Cerullo, "Integration of optical waveguides and microfluidic channels both fabricated by femtosecond laser irradiation," *Applied physics letters*, vol. 90, no. 23, p. 231118, 2007.
- [144] V. Maselli, R. Osellame, G. Cerullo, R. Ramponi, P. Laporta, L. Magagnin, and P. L. Cavallotti, "Fabrication of long microchannels with circular cross section using astigmatically shaped femtosecond laser pulses and chemical etching," *Applied physics letters*, vol. 88, no. 19, p. 191107, 2006.
- [145] Y. Xia and G. M. Whitesides, "Soft lithography," *Annual review of materials science*, vol. 28, no. 1, pp. 153–184, 1998.
- [146] A. Baum, P. J. Scully, W. Perrie, D. Liu, and V. Lucarini, "Mechanisms of femtosecond laser-induced refractive index modification of poly (methyl methacrylate)," *JOSA B*, vol. 27, no. 1, pp. 107–111, 2010.
- [147] M. Kagami, A. Kawasaki, and H. Ito, "A polymer optical waveguide with out-of-plane branching mirrors for surface-normal optical interconnections," *Journal of Lightwave Technology*, vol. 19, no. 12, p. 1949, 2001.
- [148] C. Vannahme, S. Klinkhammer, U. Lemmer, and T. Mappes, "Plastic lab-on-a-chip for fluorescence excitation with integrated organic semiconductor lasers," *Optics express*, vol. 19, no. 9, pp. 8179–8186, 2011.

- [149] R. Suriano, A. Kuznetsov, S. M. Eaton, R. Kiyon, G. Cerullo, R. Osellame, B. N. Chichkov, M. Levi, and S. Turri, “Femtosecond laser ablation of polymeric substrates for the fabrication of microfluidic channels,” *Applied Surface Science*, vol. 257, no. 14, pp. 6243–6250, 2011.
- [150] M. Fleger, D. Siepe, and A. Neyer, “Microfabricated polymer analysis chip for optical detection,” in *IEE Proceedings-Nanobiotechnology*, vol. 151, pp. 159–161, IET, 2004.
- [151] D. W. Van Krevelen and K. Te Nijenhuis, *Properties of polymers: their correlation with chemical structure; their numerical estimation and prediction from additive group contributions*. Elsevier, 2009.
- [152] K. Denbigh, “The polarisabilities of bonds—i,” *Transactions of the Faraday Society*, vol. 36, pp. 936–948, 1940.
- [153] B. Bêche, N. Pelletier, E. Gaviot, and J. Zyss, “Single-mode te<sub>00</sub>–tm<sub>00</sub> optical waveguides on su-8 polymer,” *Optics Communications*, vol. 230, no. 1-3, pp. 91–94, 2004.
- [154] K. B. Mogensen, J. El-Ali, A. Wolff, and J. P. Kutter, “Integration of polymer waveguides for optical detection in microfabricated chemical analysis systems,” *Applied Optics*, vol. 42, no. 19, pp. 4072–4079, 2003.
- [155] J. Kim and J. H. Shin, “Stable, free-space optical trapping and manipulation of sub-micron particles in an integrated microfluidic chip,” *Scientific reports*, vol. 6, no. 1, pp. 1–9, 2016.
- [156] S. Balslev and A. Kristensen, “Microfluidic single-mode laser using high-order bragg grating and antiguiding segments,” *Optics Express*, vol. 13, no. 1, pp. 344–351, 2005.
- [157] J. C. McDonald and G. M. Whitesides, “Poly (dimethylsiloxane) as a material for fabricating microfluidic devices,” *Accounts of chemical research*, vol. 35, no. 7, pp. 491–499, 2002.
- [158] G. Panusa, Y. Pu, J. Wang, C. Moser, and D. Psaltis, “Photoinitiator-free multi-photon fabrication of compact optical waveguides in polydimethylsiloxane,” *Optical Materials Express*, vol. 9, no. 1, pp. 128–138, 2019.
- [159] G. Panusa, Y. Pu, J. Wang, C. Moser, and D. Psaltis, “Fabrication of sub-micron polymer waveguides through two-photon polymerization in polydimethylsiloxane,” *Polymers*, vol. 12, no. 11, p. E2485, 2020.
- [160] Z. Cai, W. Qiu, G. Shao, and W. Wang, “A new fabrication method for all-pdms waveguides,” *Sensors and Actuators A: Physical*, vol. 204, pp. 44–47, 2013.
- [161] D. A. Chang-Yen, R. K. Eich, and B. K. Gale, “A monolithic pdms waveguide system fabricated using soft-lithography techniques,” *Journal of lightwave technology*, vol. 23, no. 6, p. 2088, 2005.
- [162] S. K. Tang and G. M. Whitesides, “Basic microfluidic and soft lithographic techniques,” 2010.
- [163] P. Coudray, P. Etienne, Y. Moreau, J. Porque, and S. Najafi, “Sol-gel channel waveguide on silicon: fast direct imprinting and low cost fabrication,” *Optics communications*, vol. 143, no. 4-6, pp. 199–202, 1997.

- [164] P. Moreira, P. Marques, and A. Leite, "Hybrid sol-gel channel waveguide patterning using photoinitiator-free materials," *IEEE photonics technology letters*, vol. 17, no. 2, pp. 399–401, 2005.
- [165] M. Oubaha, *Elaboration de systèmes photoniques à partir de matériaux hybrides organiques et inorganiques préparés par voie sol-gel*. PhD thesis, Montpellier 2, 2003.
- [166] S. Aura, T. Sikanen, T. Kotiaho, and S. Franssila, "Novel hybrid material for microfluidic devices," *Sensors and Actuators B: Chemical*, vol. 132, no. 2, pp. 397–403, 2008.
- [167] E. Mechref, J. Jabbour, S. Calas-Etienne, K. Amro, A. Mehdi, R. Tauk, D. Zaouk, and P. Etienne, "Synthesis and characterization of a photosensitive organic–inorganic, hybrid positive resin type material: application to the manufacture of microfluidic devices by laser writing," *RSC advances*, vol. 6, no. 5, pp. 3951–3959, 2016.
- [168] A. Gorin, R. Copperwhite, S. Elmaghrum, C. Mc Donagh, and M. Oubaha, "Hybrid zirconium sol-gel thin films with high refractive index," in *International Symposium on Photoelectronic Detection and Imaging 2011: Sensor and Micromachined Optical Device Technologies*, vol. 8191, p. 81911Q, International Society for Optics and Photonics, 2011.
- [169] S. Elmaghrum, A. Gorin, R. K. Kribich, B. Corcoran, R. Copperwhite, C. McDonagh, and M. Oubaha, "Development of a sol–gel photonic sensor platform for the detection of biofilm formation," *Sensors and Actuators B: Chemical*, vol. 177, pp. 357–363, 2013.
- [170] M. Oubaha, A. Gorin, C. McDonagh, B. Duffy, and R. Copperwhite, "Development of a multianalyte optical sol–gel biosensor for medical diagnostic," *Sensors and Actuators B: Chemical*, vol. 221, pp. 96–103, 2015.
- [171] G. Kickelbick, "Introduction to hybrid materials," *Hybrid materials*, vol. 1, p. 2, 2007.
- [172] W. A. Green, *Industrial photoinitiators: a technical guide*. CRC Press, 2010.
- [173] C. E. Hoyle, "An overview of oxygen inhibition in photocuring," in *Technical Conference Proceedings-UV & EB Technology Expo & Conference, Charlotte, NC, United States*, pp. 892–899, 2004.
- [174] C. Decker, "The use of uv irradiation in polymerization," *Polymer International*, vol. 45, no. 2, pp. 133–141, 1998.
- [175] C. Decker, B. Elzaouk, and D. Decker, "Kinetic study of ultrafast photopolymerization reactions," *Journal of Macromolecular Science, Part A: Pure and Applied Chemistry*, vol. 33, no. 2, pp. 173–190, 1996.
- [176] C. Decker and K. Moussa, "Real-time kinetic study of laser-induced polymerization," *Macromolecules*, vol. 22, no. 12, pp. 4455–4462, 1989.
- [177] S. Moon, "K. kamenosono, s. kondo, a. umehara, t. yamaoka: "three-component photopolymers based on thermal cross-linking and acidolytic de-cross-linking of vinyl ether groups. effects of binder polymers on photopolymer characteristics",," *Chem. Mater*, vol. 6, no. 10, pp. 1854–1860, 1994.

- [178] S. Moon, K. Kamenosono, S. Kondo, A. Umehara, and T. Yamaoka, "Three-component photopolymers based on thermal crosslinking and acidolytic de-crosslinking of vinyl ether groups. effects of binder polymers on photopolymer characteristics," *Chemistry of materials*, vol. 6, no. 10, pp. 1854–1860, 1994.
- [179] T. Mukaiyama and H. Nohira, "A kinetic study of addition reaction of vinyl ether with carboxylic acids," *Bulletin of the Chemical Society of Japan*, vol. 33, no. 12, pp. 1716–1720, 1960.
- [180] T. Higashimura and M. Sawamoto, "Carbocationic polymerization: Vinyl ethers," *Pergamon Press plc, Comprehensive Polymer Science: the Synthesis, Characterization, Reactions & Applications of Polymers.*, vol. 3, pp. 673–696, 1989.
- [181] M. Sawamoto and M. Ouchi, "Cationic addition polymerization (fundamental)," 2014.
- [182] S. Moon, K. Naitoh, and T. Yamaoka, "Novel dual-mode photoresist based on cationic polymerization and acidolysis," *Chemistry of materials*, vol. 5, no. 9, pp. 1315–1320, 1993.
- [183] H. Krug, F. Tiefensee, P. W. Oliveira, and H. K. Schmidt, "Organic-inorganic composite materials: Optical properties of laser-patterned and protective-coated waveguides," in *Sol-Gel Optics II*, vol. 1758, pp. 448–455, International Society for Optics and Photonics, 1992.
- [184] M. Oubaha, P. Etienne, S. Calas, P. Coudray, J.-M. Nedelec, and Y. Moreau, "Sol-gel derived organic and inorganic hybrid materials for photonic applications: contribution to the correlation between the material structure and the transmission in the near infrared region," *Journal of sol-gel science and technology*, vol. 33, no. 2, pp. 241–248, 2005.
- [185] D.-L. Versace, O. Soppera, J. Lalevée, and C. Croutxé-Barghorn, "Influence of zirconium propoxide on the radical induced photopolymerisation of hybrid sol-gel materials," *New Journal of Chemistry*, vol. 32, no. 12, pp. 2270–2278, 2008.
- [186] E. Mechref, J. Jabbour, S. Calas-Etienne, K. Amro, A. Mehdi, R. Tauk, and P. Etienne, "New organic-inorganic hybrid material based on a poly (amic acid) oligomer: a promising opportunity to obtain microfluidic devices by a photolithographic process," *RSC advances*, vol. 6, no. 93, pp. 90666–90673, 2016.
- [187] T. Ogura, T. Higashihara, and M. Ueda, "Direct patterning of poly (amic acid) and low-temperature imidization using a crosslinker, a photoacid generator, and a thermobase generator," *Journal of Polymer Science Part A: Polymer Chemistry*, vol. 47, no. 13, pp. 3362–3369, 2009.
- [188] T. Nakano, H. Iwasa, N. Miyagawa, S. Takahara, and T. Yamaoka, "Positive-type photopolyimide based on vinyl ether crosslinking and de-crosslinking," *Journal of Photopolymer Science and Technology*, vol. 13, no. 5, pp. 715–718, 2000.
- [189] M. J. Plater, W. T. Harrison, and A. Raab, "Photochemical fragmentation of irgacure pag 103," *ACS omega*, vol. 4, no. 22, pp. 19875–19879, 2019.
- [190] C. P. Constantin, M. Aflori, R. F. Damian, and R. D. Rusu, "Biocompatibility of polyimides: A mini-review," *Materials*, vol. 12, no. 19, p. 3166, 2019.

- [191] F. J. Loprest and E. F. McInerney, "Positive working thermally stable photoresist composition, article and method of using," June 6 1978. US Patent 4,093,461.
- [192] M. G. Moss, T. Brewer, R. M. Cuzmar, D. W. Hawley, and T. D. Flaim, "Positive working polyamic acid/imide photoresist compositions and their use as dielectrics," Aug. 9 1994. US Patent 5,336,925.
- [193] M. Tomikawa, S. Yoshida, and N. Okamoto, "Novel partial esterification reaction in poly (amic acid) and its application for positive-tone photosensitive polyimide precursor," *Polymer journal*, vol. 41, no. 8, pp. 604–608, 2009.
- [194] M. Okazaki, H. Onishi, W. Yamashita, and S. Tamai, "Positive-working photosensitive alkaline-developable polyimide precursor based on semi-alicyclic poly (amide acid), vinyl ether crosslinker, and a photoacid generator," *Journal of Photopolymer Science and Technology*, vol. 19, no. 2, pp. 277–280, 2006.
- [195] M. Okazaki, H. Onishi, W. Yamashita, and S. Tamai, "Positive-type photosensitive polyimide based on poly (amide acid), vinyl ether crosslinker, and a photoacid generator," *Journal of Photopolymer Science and Technology*, vol. 21, no. 1, pp. 119–123, 2008.
- [196] S.-Y. Moon, C.-M. Chung, and T. Yamaoka, "Three-component photoresists based on thermal crosslinking and acidolytic cleavage," *Polymer*, vol. 41, no. 11, pp. 4013–4019, 2000.
- [197] S. Hellstrom, "Published course work for physics 210," 2007.
- [198] D. Meyerhofer, "Characteristics of resist films produced by spinning," *Journal of Applied Physics*, vol. 49, no. 7, pp. 3993–3997, 1978.
- [199] J. R. Salgueiro, V. Moreno, and J. Linares, "Model of linewidth for laser writing on a photoresist," *Applied optics*, vol. 41, no. 5, pp. 895–901, 2002.
- [200] P. F. Jacobs, "Fundamentals of stereolithography," in *1992 International Solid Freeform Fabrication Symposium*, 1992.
- [201] P. F. Jacobs, *Rapid prototyping & manufacturing: fundamentals of stereolithography*. Society of Manufacturing Engineers, 1992.
- [202] H. Schmidt, "Inorganic-organic composites for optoelectronics," in *Sol-Gel Optics*, pp. 451–481, Springer, 1994.
- [203] P. Etienne, P. Coudray, Y. Moreau, and J. Porque, "Photocurable sol-gel coatings: channel waveguides for use at 1.55  $\mu\text{m}$ ," *Journal of sol-gel science and technology*, vol. 13, no. 1, pp. 523–527, 1998.
- [204] D. P. Birnie, S. K. Hau, D. S. Kamber, and D. M. Kaz, "Effect of ramping-up rate on film thickness for spin-on processing," *Journal of Materials Science: Materials in Electronics*, vol. 16, no. 11-12, pp. 715–720, 2005.
- [205] D. E. Haas, J. N. Quijada, S. J. Picone, and D. P. Birnie III, "Effect of solvent evaporation rate on skin formation during spin coating of complex solutions," in *Sol-Gel Optics V*, vol. 3943, pp. 280–284, International Society for Optics and Photonics, 2000.

- [206] A. M. Rashed and D. R. Selviah, “Modelling of polymer taper waveguide for optical back-plane,” SIOE’04, 2004.
- [207] Thorlabs, “Single mode fiber: 633 -780 nm.” <https://www.thorlabs.com/drawings/900c756c252f3620-EE4B9D1A-BAE1-7A1B-2BF4C0C063AC7303/SM600-SpecSheet.pdf>, May 2019.
- [208] S.-Y. Yang and L.-L. Yuan, “Advanced polyimide films,” in *Advanced Polyimide Materials*, pp. 1–66, Elsevier, 2018.
- [209] N.-J. Chu and J.-W. Huang, “Reactivity of poly (amic acid) isomers in thermal imidization,” *Polymer journal*, vol. 22, no. 8, pp. 725–732, 1990.
- [210] M. S. C. of the ECHA, “1-methyl-2-pyrrolidone as a substance of very high concern because of its cmr properties,” svhc support document, ECHA, May 2011.
- [211] S. A. Merck, “Sds: Cell culture freezing medium w/ dms0.”
- [212] H. Hou, J. Jiang, and M. Ding, “Ester-type precursor of polyimide and photosensitivity,” *European polymer journal*, vol. 35, no. 11, pp. 1993–2000, 1999.
- [213] W. H. Mueller and D. N. Khanna, “Hydroxy polyimides and high temperature positive photoresists therefrom,” May 22 1990. US Patent 4,927,736.
- [214] M. S. Jung, S. M. Lee, and L. Jingyu, “Photosensitive polyimide composition, polyimide film and semiconductor device using the same,” June 29 2010. US Patent 7,745,096.
- [215] Y. Koyama, Y. Shoji, K. Hashimoto, Y. Masuda, H. Araki, and M. Tomikawa, “Development of novel low-temperature curable positive-tone photosensitive dielectric materials with high reliability,” in *2019 IEEE 69th Electronic Components and Technology Conference (ECTC)*, pp. 346–351, IEEE, 2019.
- [216] W. A. Reinerth, S. Malik, and B. B. De, “Process for the production of polyimide and polyamic ester polymers,” Apr. 11 2017. US Patent 9,617,386.
- [217] S. Tead, E. Kramer, T. Russell, and W. Volksen, “Ion beam analysis of the imidization kinetics of polyamic ethyl ester,” *Polymer*, vol. 31, no. 3, pp. 520–523, 1990.
- [218] P. Sysel, V. Šindelář, E. Chánová, and B. Wallin, “Preparation of polyimides by using mixtures of tetrahydrofuran and methanol and their properties,” *Polymer journal*, vol. 34, no. 2, pp. 54–56, 2002.
- [219] H.-C. Yu, J.-W. Jung, J.-Y. Choi, and C.-M. Chung, “Kinetic study of low-temperature imidization of poly (amic acid) s and preparation of colorless, transparent polyimide films,” *Journal of Polymer Science Part A: Polymer Chemistry*, vol. 54, no. 11, pp. 1593–1602, 2016.
- [220] F. Harris, D. Wilson, H. Stenzenberger, and P. Hergenrother, “Polyimides,” *D. Wilson, HD Stenzenberger, PM Hergenrother, Chapman and Hall edt., New York*, pp. 23–96, 1990.
- [221] R. Dine-Hart and W. Wright, “Preparation and fabrication of aromatic polyimides,” *Journal of Applied Polymer Science*, vol. 11, no. 5, pp. 609–627, 1967.

- [222] S. Kim, K.-S. Jang, H.-D. Choi, S.-H. Choi, S.-J. Kwon, I.-D. Kim, J. A. Lim, and J.-M. Hong, "Porous polyimide membranes prepared by wet phase inversion for use in low dielectric applications," *International Journal of Molecular Sciences*, vol. 14, no. 5, pp. 8698–8707, 2013.
- [223] K. Tsuchiya, Y. Shibasaki, and M. Ueda, "A positive type alkaline developable thermally stable and photosensitive polymer based on partially o-methylated poly (2, 6-dihydroxy-1, 5-naphthylene), an acidolytic de-cross-linker, and a photoacid generator," *Polymer*, vol. 45, no. 20, pp. 6873–6878, 2004.
- [224] T. Kato and M. Isshiki, "Curable organopolysiloxane composition, use of the cured product of the composition, and semiconductor device," Sept. 18 2007. US Patent 7,271,232.
- [225] N. Tucher, *Analysis of photonic structures for silicon solar cells*. Fraunhofer Verlag, 2017.
- [226] R. S. Lima, P. A. Leão, M. H. Piazzetta, A. M. Monteiro, L. Y. Shiroma, A. L. Gobbi, and E. Carrilho, "Sacrificial adhesive bonding: a powerful method for fabrication of glass microchips," *Scientific reports*, vol. 5, p. 13276, 2015.
- [227] S. Satyanarayana, R. N. Karnik, and A. Majumdar, "Stamp-and-stick room-temperature bonding technique for microdevices," *Journal of Microelectromechanical Systems*, vol. 14, no. 2, pp. 392–399, 2005.
- [228] M. A. Eddings, M. A. Johnson, and B. K. Gale, "Determining the optimal pdms–pdms bonding technique for microfluidic devices," *Journal of Micromechanics and Microengineering*, vol. 18, no. 6, p. 067001, 2008.
- [229] X. Li, Z. T. F. Yu, D. Geraldo, S. Weng, N. Alve, W. Dun, A. Kini, K. Patel, R. Shu, F. Zhang, *et al.*, "Desktop aligner for fabrication of multilayer microfluidic devices," *Review of Scientific Instruments*, vol. 86, no. 7, p. 075008, 2015.
- [230] A. Elmogi, E. Bosman, J. Missinne, and G. Van Steenberge, "Comparison of epoxy-and siloxane-based single-mode optical waveguides defined by direct-write lithography," *Optical Materials*, vol. 52, pp. 26–31, 2016.
- [231] E. Zraggen, I. M. Soganci, F. Horst, A. La Porta, R. Dangel, B. J. Offrein, S. A. Snow, J. K. Young, B. W. Swatowski, C. M. Amb, *et al.*, "Laser direct writing of single-mode polysiloxane optical waveguides and devices," *Journal of Lightwave Technology*, vol. 32, no. 17, pp. 3036–3042, 2014.
- [232] V. Prajzler, V. Chlupaty, P. Kulha, M. Neruda, S. Kopp, and M. Mühlberger, "Optical polymer waveguides fabricated by roll-to-plate nanoimprinting technique," *Nanomaterials*, vol. 11, no. 3, p. 724, 2021.
- [233] T. Wolfer, P. Bollgruen, D. Mager, L. Overmeyer, and J. G. Korvink, "Flexographic and inkjet printing of polymer optical waveguides for fully integrated sensor systems," *Procedia Technology*, vol. 15, pp. 521–529, 2014.

# Abstract

Microfluidics is the set of technologies allowing the manipulation and characterization of fluids at the micrometric or nanometric scales. It can be viewed both as a science aimed at studying the behavior of fluids within microchannels, and as a technology for the manufacture and the use of microfluidic devices. These devices consist of a flat surface on which capillaries and reaction chambers are formed by photolithography, molding or stamping... Liquids in micrometric or nanometric volumes are then inserted into these capillaries where they are actuated, separated or mixed to obtain chemical reactions. In addition to the low reagent consumption, the advantage of working with micrometric volumes, lies in the acceleration and automation of the process. Microfluidic chips and reactors can be simple or instrumented (electrodes, sensors, optics, pumps, etc.). The overall trend being towards a comprehensive miniaturization and more complex devices, integrating multiple functionalities, without a cost increase. When an optical integration is carried out on a chip we are in the realm of opto-microfluidics. This work aims at prototyping an opto-microfluidic device with a dual objective:

- The improvement of the resolution of microfluidic circuits by the use of high resolution 2D and 3D laser writing technology,
- and to push the integration by combining on the same chip both the microfluidic circuit and an integrated optical component using hybrid organic-inorganic photoresists.

**Keywords:** Hybrid Materials, Photolithography, Photonic Circuits, Microfluidics, Lab-on-Chip.

# Résumé

La microfluidique est l'ensemble de technologies permettant la manipulation et la caractérisation de fluides à des échelles micrométriques ou nanométriques. Elle peut être considérée à la fois comme une science visant à l'étude du comportement des fluides à l'intérieur de ces micro-canaux, et une technologie permettant la fabrication et l'utilisation de dispositifs microfluidiques. Ces dispositifs sont constitués d'une surface plane sur laquelle des capillaires et des chambres de réactions sont formés par photolithographie, moulage ou emboutissage. Des liquides en volumes micrométriques ou nanométriques sont ensuite insérés dans ces capillaires où ils sont déplacés, fractionnés, séparés ou mélangés pour obtenir des réactions chimiques. L'intérêt de travailler avec des volumes micrométriques, outre l'économie de moyens utilisés, réside dans l'accélération et l'automatisation du processus. Les puces et réacteurs microfluidiques peuvent être simples ou instrumentés (électrodes, capteurs, optiques, pompes...), la tendance étant à la complexification des outils, intégrant de plus en plus d'instruments sans pour autant être accompagnée d'une augmentation du prix. Lorsqu'une intégration optique est effectuée, on parle d'opto-microfluidique. Le travail proposé sera de construire un prototype de dispositif avec un double objectif:

- l'amélioration de la résolution des circuits de microfluidique par utilisation des nouvelles technologies de photoinscription Laser 2D et 3D haute résolution,
- et pousser l'intégration en implantant sur la même puce, à la fois le circuit microfluidique et un composant d'optique intégré, en utilisant des résines hybrides organiques-inorganiques

**Mots-clés :** Matériaux Hybrides, Photolithographie, Circuits Photoniques, Microfluidique, Laboratoire sur Puce